RICE UNIVERSITY

ISOTROPIC MODELING OF TRANSVERSELY ISOTROPIC WEDGE INDENTATION

by

Tom Stanley Marshall

A THESIS SUBMITTED
IN PARTIAL FULFILLMENT OF THE
REQUIREMENTS FOR THE DEGREE OF

Master of Science

THESIS DIRECTOR'S SIGNATURE:

JB Cheatham Jr

HOUSTON, TEXAS

December 1976

ABSTRACT

ISOTROPIC MODELING OF TRANSVERSELY ISOTROPIC WEDGE INDENTATION

by Tom Stanley Marshall

The need has become evident for a more thorough understanding of the causes of hole deviation when drilling through stratified formations. The approach to this problem herein is to analyze the forces between the bit teeth and rock and how they might affect horizontal deflection of the drill bit. This study is specifically concerned with methods of modeling the rock and bit tooth interaction so that valid predictions can be made of the actual behavior.

The rock and bit tooth interaction is modeled by a vertical wedge indentation into the flat, level surface of an arbitrarily oriented transversely isotropic rigid - perfectly plastic medium. The transversely isotropic wedge is itself modeled by vertical wedge indentation into the flat, inclined surface of an isotropic medium with arbitrary orientation of the direction of maximum slope. An upper bound approximation method for predicting horizontal and vertical loads is developed using fundamental principles of plasticity theory and an experimental study conducted as verification of the method. It is demonstrated herein that the experimental behavior has been satisfactorily predicted by the theoretical analysis and that a limit analysis solution to the isotropic wedge indentation problem has been obtained. An approach to the analysis of the transversely isotropic problem is outlined as a possible introduction to further work on this problem.

Acknowledgments

The author wishes to express his gratitude to Dr. John B. Cheatham, Jr., for his dedicated guidance and support throughout the development of this thesis.

The support of this work through the National Science Foundation, Grant No. ENG74-03957 is also greatly appreciated.

Table of Contents

List of Figures

Force-Deflection Tests

Figure	Test No.	β	ψ_x	ψ_y	Page
F-21	62	30°	30°	0	159
F-22	63	30°	45°	0	160
F-23	65	45°	15°	0	161
F-24	66	45°	30°	0	162
F-25	97	45°	30°	0	163
F-26	67	15°	0	15°	164
F-27	95	15°	0	15°	165
F-28	68	15°	0	30°	166
F-29	69	15°	0	45°	167
F-30	70	15°	0	54°	168
F-31	75	22.5°	0	5°	169
F-32	72	22.5°	0	15°	170
F-33	73	22.5°	0	15°	171
F-34	76	15°	30°	5°	172
F-35	88	15°	30°	20°	173
F-36	89	15°	45°	20°	174
F-37	90	22.5°	30°	20°	175
F-38	91	22.5°	30°	45°	176
F-39	84	30°	15°	20°	177
F-40	87	30°	15°	45°	178
F-41	78	30°	30°	5°	179
F-42	94	30°	30°	5°	180
F-43	79	30°	30°	10°	181
F-44	80	30°	30°	20°	182
F-45	81	30°	30°	30°	183
F-46	82	30°	30°	45°	184
F-47	83	30°	30°	55°	185
F-48	86	30°	45°	20°	186
F-49	85	30°	45°	45°	187
F-50	92	45°	30°	20°	188
F-51	93	45°	30°	45°	189

List of Tables and Charts

Page

Tables

Charts

To my wife

Jan

Whose undying faith and
support made this thesis possible

Nomenclature

Introduction

$\underset{\sim}{i},\underset{\sim}{j},\underset{\sim}{k}$	reference coordinate system
$\underset{\sim}{i}',\underset{\sim}{j}',\underset{\sim}{k}',$	principal axes of anisotropy
Ψ_x,Ψ_y	inclination angles with respect to the i,j,k coordinates
$\sigma,\sigma_{yp},\sigma,\sigma_2,$ $\underset{\sim}{\sigma},\sigma^*,\sigma_{ij},\tau_m,\sigma_m$	stresses
$\epsilon,\epsilon_1,\epsilon_2,\underset{\sim}{\epsilon}^p,$ $\underset{\sim}{\epsilon},\underset{\sim}{\epsilon}^e,\epsilon_{ij}$	strains
$f, f_1, f_2,\ldots,f_{12}$	yield conditions
θ_1,θ_2	stability discussion parameters
λ	plastic potential parameter
I,J_2,J_3	stress tensor and deviatoric stress tensor invariants
$R_i,S_i,T_i,n_i,\gamma,$ $A,B,\ldots,M,N$	yield function parameters
k	yield in pure shear
$\underset{\sim}{T}_i$	surface traction
F_i	body force
v_i,u,v	velocities
$A_1,A_2,B_1,B_2,\ldots,E_1,E_2,$ n,a,b,c	parameters in "method of characteristics"
p	hydrostatic pressure
θ	angle from $\underset{\sim}{i}'$ - axis to direction of maximum principal stress
ϕ_c,ϕ_+,ϕ_-	characteristic directions
C_+,C_-	characteristic curves
ξ	velocity characteristics solution parameter
s_+,s_-	length coordinates along characteristics

θ_T, θ_n	surface traction parameters
θ_+	characteristic direction with respect to stress discontinuity
P_1, P_2, Q_1, Q_2	points in physical plane
P_1', P_2', Q_1', Q_2'	poles in stress plane
$P_1'', P_2'', Q_1'', Q_2''$	points in hodograph

<u>Theoretical Solution</u>

$\underset{\sim}{i}, \underset{\sim}{j}, \underset{\sim}{k}$	reference coordinate system
ψ_x, ψ_y	inclination angles with respect to $\underset{\sim}{i}, \underset{\sim}{j}, \underset{\sim}{k}$ coordinates
β	half wedge angle
δ_V	indentation depth
μ	wedge friction coefficient
$O, A, B, C, \ldots, M$	points in physical plane of slip line field
$(\overline{OM}), (\overline{OL}), (\overline{OA}), (\overline{OE}),$ $(\overline{BI}), (\overline{FI}), d_1, d_2,$ $b_1, b_2, \varkappa$	lengths in slip line field
$\gamma_1, \gamma_2, \lambda_1, \lambda_2,$ $\alpha_1, \alpha_2, \epsilon$	angles in slip line field
O'', C'', D'', G'', H''	points in hodograph
t	hodograph parameter of time
G', H', C', D'	poles in stress plane
$\sigma_{OE}, \sigma_{OA}, \tau_{OE}, \tau_{OA}$	stress on surface of wedge
k	yield in pure shear
P, W, b	external loads on "infinite" wedge of "width" b
Q, R, S, T, Q'', R''	points in physical and hodograph planes for stress discontinuity
$a, b, c, d, e, f, g, h, m, n$	areas in physical plane for stress discontinuity
ϕ', $\angle OCB$, $\angle COB, \ldots$	angles in physical plane for stress discontinuity
v, v_a, v_b, v_n	velocities for stress discontinuity

$F_x, F_y, F_z{}', F_z{}'', F_z, \underset{\sim}{F}_o$	forces medium exerts on actual wedge
x	length coordinate along wedge
$\delta_V(x)$	indentation depth
$A(x)$	indentation cross-sectional area
$g_1, g_2, \tau_o, \tau_b, \sigma_o, \sigma_b$	infinite wedge solutions applied to actual wedge problem
ϕ	orientation of $\underset{\sim}{F}_o$
P_V, P_H	external loads applied to actual wedge
$\overline{ABCDE}, A_1, A_2, \ldots, A_7$	areas in plane strain slip line field
$v_1, v_2, \ldots, v_7$	velocities in slip line field
r	radial coordinate of centered fan
$P_V{}'$	upper bound correction to P_V
n, e	parameters in $P_V{}'$ calculation

Experimental Solution

ψ_x, ψ_y	inclination angles
$\epsilon, \epsilon_{24}, \epsilon_{31}$	strain readings
C_{13}, C_{24}	load cell calibration parameters
1,2,3,4	labelling of strain gages
$P_x, P_x{}', P_y, P_y{}'$	horizontal forces
e_{13}, e_{24}	correction angles in load cell calibration
x_δ	location of horizontal deflection calibration
F_c, p, x_o	hydraulic jack calibration parameters
Θ	friction test angle parameter
L, D, δ, t	compression test parameters
σ, σ_{yp}	stress in compression test
$\delta_\phi, \delta_\perp$	horizontal deflection readings in wedge indentation tests
m_V, m_H	data reduction parameters

other nomenclature same as in Theoretical Solution

Transversely Isotropic Analysis

$\underset{\sim}{i},\underset{\sim}{j},\underset{\sim}{k}$	reference coordinate system
$\underset{\sim}{i}',\underset{\sim}{j}',\underset{\sim}{k}'$	principal axes of anisotropy
$\underset{\sim}{e}_i'$	material coordinates
$\underset{\sim}{e}_j$	reference coordinates
a_{ij}	directional cosines
$\sigma_{ij}')_y$	yield strength parameters
ϕ_τ	shearing plane orientation with respect to the reference system
τ	shear stress
P_H,P_V	external loads
λ_1,λ_2	assumed velocity field parameters
v_1,v_2,v_3	velocities
β	wedge angle
ϵ	wedge travel direction from vertical
$\overline{ABCD}$, $\overline{AGHD}$,...	areas
F_1,F_2	upper bound solution functions

Appendix A

same as in Theoretical Solution

Appendix B

by inspection

Appendix C

same as in Experimental Solution

Introduction

Drill Bit Deviation Problem

Hole deviation when drilling through a stratified formation is a phenomenon which has aroused considerable interest and concern, but has yet to be fully understood. The mechanics of a flexible drill string and the anisotropic characteristics of the formation may both play important roles in causing horizontal deviation. This study will concentrate on hole deviation behavior caused by the bottom hole forces between the bit teeth and the anisotropic formation.

Transversely Isotropic Wedge Indentation

The rock and bit tooth interaction when drilling vertically through a bedded formation is modeled by a two dimensional wedge indentation into a transversely isotropic plastic medium (Figure 1). The axis of transverse isotropy ($\underset{\sim}{i}'$) is normal to the bedding planes of the actual formation. The actual mechanics of the bit tooth indentation, scraping action, and the drill bit design make the actual problem quite complex and the simplification of the two dimensional model considerable. Plasticity theory is utilized in the analysis of the problem, the applicability to mechanical testing of rock at high pressure having been justified by previous experimental work [2, 4, 7, 14, 20, 23, 32].

Isotropic Model

An isotropic model has been developed for the transversely isotropic wedge indentation problem to gain a qualitative knowledge of the rock and bit tooth problem and to determine a satisfactory analytical method. A wedge is forced vertically into an isotropic medium, the flat surface of which is inclined with respect to the horizontal (Figure 2). The direction of maximum slope varies arbitrarily with respect to the orientation of the wedge. In the course of this study an analytical method has been developed and verified experimentally for the vertical and horizontal external loads required to force the wedge in a vertical direction. The isotropic model is considered a qualitatively accurate analogy to the transversely isotropic wedge indentation problem.

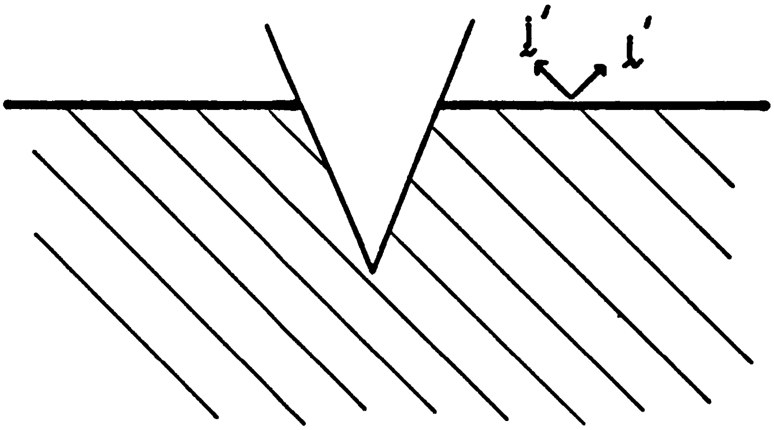

Figure 1 Transversely Isotropic Wedge Indentation

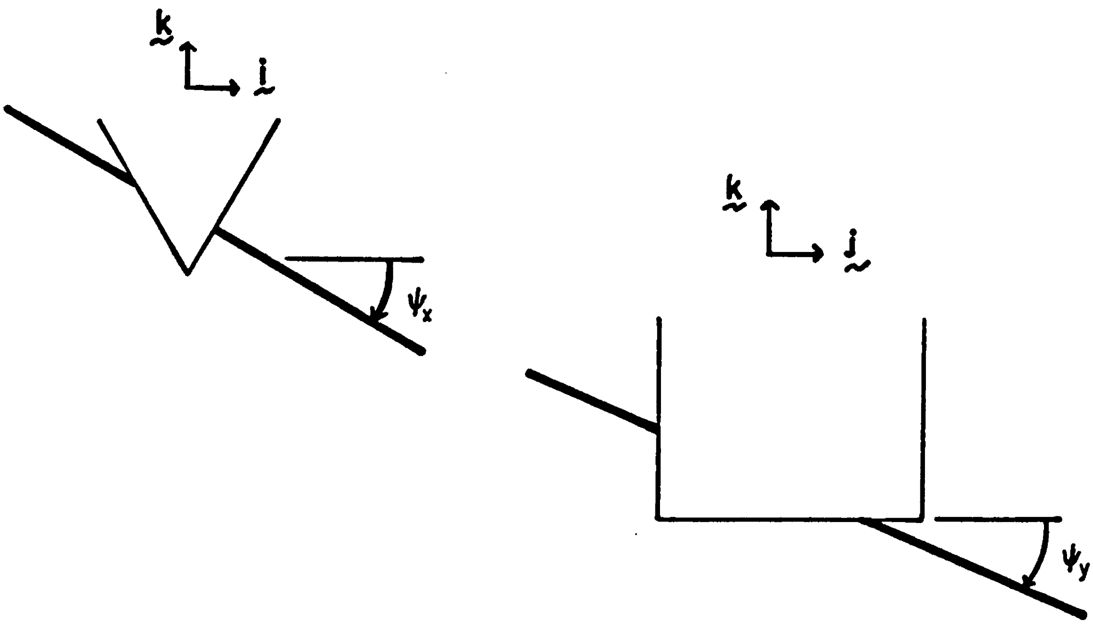

Figure 2 Isotropic Indentation Model

Introduction to Principles of Plasticity

Some fundamentals of plasticity theory should be mentioned before a discussion of this experimental study may be continued. The discussion to follow includes some principles of yield conditions, limit analysis, method of characteristics and its application to a slip line field solution for plane strain, velocity and stress discontinuities and Prager's mapping technique from the physical plane to the stress and velocity planes.

Yield Conditions

Consider a simple uniaxial tensile test which gives a typical experimental true stress - true strain curve as shown in Figure 3. The material is linearly elastic - plastic with an initial yield stress σ_{yp} and plastic work hardening evident. An elastic - perfectly plastic material would exhibit a level curve beyond the yield point and the curve for a rigid - perfectly plastic material would be vertical in the elastic region showing no elastic strain. In general, a material may exhibit elastic behavior (either linear or non-linear) and a non-decreasing plastic curve beyond the yield point. A yield function is a mathematical description of conditions which must be satisfied for plastic deformation to occur. For initial yielding in the uniaxial tensile test a possible yield function would be: $\sigma - \sigma_{yp} = 0$.

A complete yield criterion for an isotropic material can be represented by a surface in the three dimensional principal stress space. For the purpose of convenient illustration the yield condition is represented by a two dimensional curve in a principal stress plane. As shown in Figure 4 the principal stress plane may then be superimposed onto the principal strain plane such that the stress and strain axes are mutually parallel. This two dimensional representation is convenient for describing the various stress and strain parameters and yield behavior as depicted in Figure 5. The diagram shows a general work hardening behavior under yield; the shape and position of the yield curve may change when undergoing plastic deformation. The yield curve must everywhere be convex and the increment of plastic strain ($\Delta \underset{\sim}{\varepsilon}^p$) must be normal to the surface. These two fundamental properties of yield functions can be rigorously proven [8, 10], but only a brief clarification will follow.

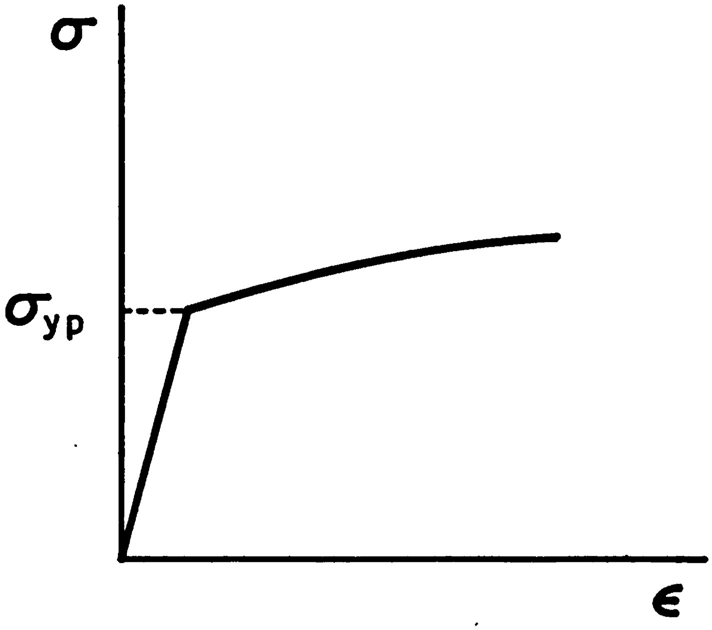

Figure 3 Uniaxial Stress-Strain Curve

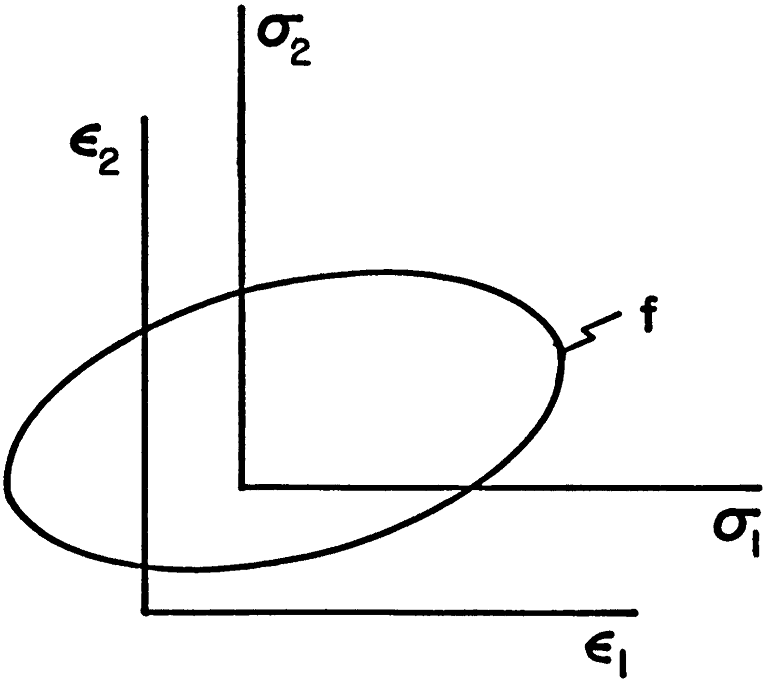

Figure 4 Two Dimensional Yield Condition Model

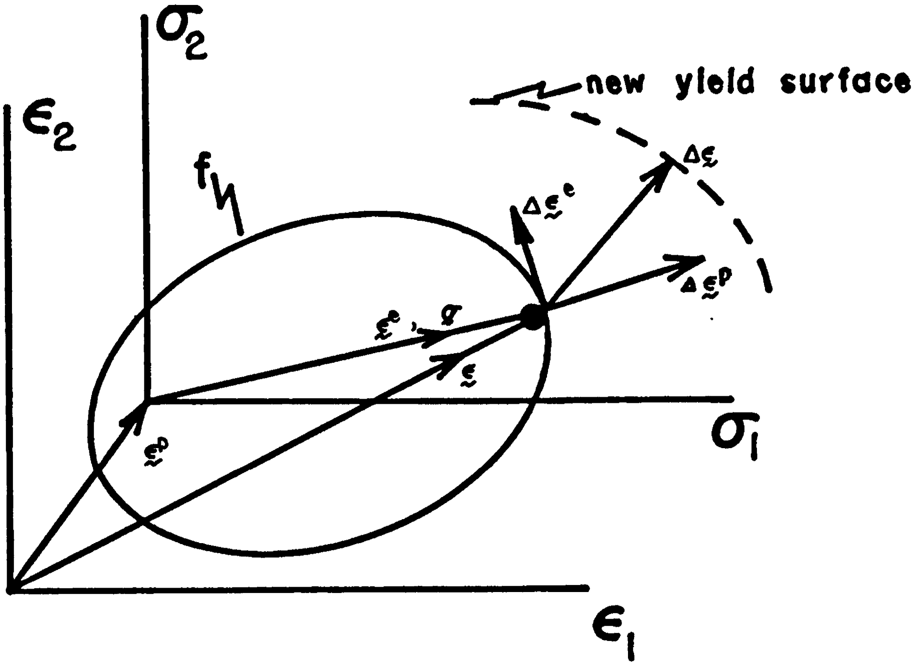

Figure 5 Behavior of Two Dimensional Yield Condition Model

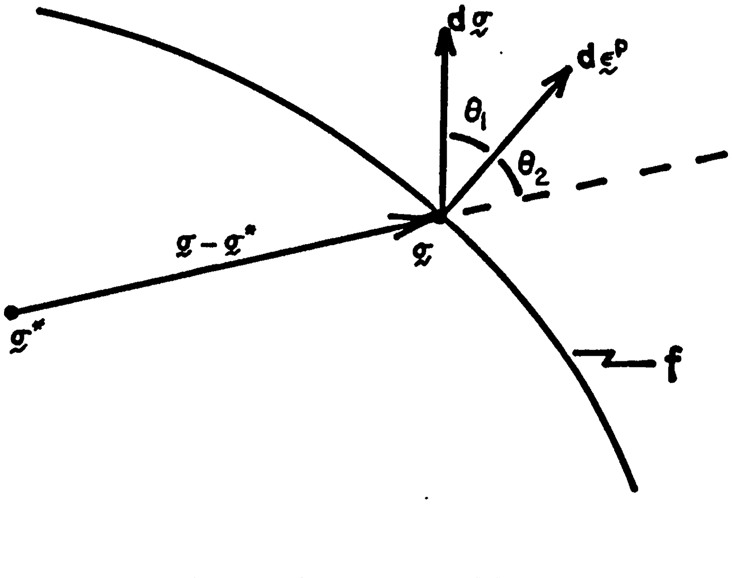

Figure 6 Convexity and Normality of Yield Function

Drucker's postulate for mechanical stability states that the work done by external forces on a body in a state of yield must be positive [8, 10]. An equivalent mathematical statement is:

$$(\underset{\sim}{\sigma} - \underset{\sim}{\sigma}^*) \cdot d\underset{\sim}{\varepsilon}^P > 0 \qquad \text{and} \qquad d\underset{\sim}{\sigma} \cdot d\underset{\sim}{\varepsilon}^P > 0$$

where $\underset{\sim}{\sigma}^*$ is an initial state of stress before external loads are applied. (See Figure 6.)

The two fundamental requirements for a yield function follow directly from the stability criterion.

1. The yield surface is convex.

$$d\underset{\sim}{\sigma} \cdot d\underset{\sim}{\varepsilon}^P = |d\underset{\sim}{\sigma}||d\underset{\sim}{\varepsilon}^P| \cos\theta_2 \geq 0$$

$$-\frac{\pi}{2} \leq \theta_2 \leq \frac{\pi}{2}$$

2. The plastic strain increment is always normal to the yield surface where the surface is smooth and between normals to the surface at a corner.

$$(\underset{\sim}{\sigma} - \underset{\sim}{\sigma}^*) \cdot d\underset{\sim}{\varepsilon}^P = |\underset{\sim}{\sigma} - \underset{\sim}{\sigma}^*||d\varepsilon^P| \cos\theta_1 \geq 0$$

$$-\frac{\pi}{2} \leq \theta_1 \leq \frac{\pi}{2}$$

A necessary consequence of normality is the principle of plastic potential, $d\varepsilon^P_{ij} = \lambda \frac{\partial f}{\partial \sigma_{ij}}$, where λ is a proportionality constant.

Before various yield conditions are presented a note must be made on material symmetries. A material is said to be anisotropic if the mechanical properties of a body are in some way dependent upon the orientation of the material within the body. If there exist three mutually orthogonal planes of anisotropic symmetry then the material is said to be orthotropic and the intersections of these planes are the principal axes of anisotropy. If a principal axis of anisotropy is also an axis of rotational symmetry with respect to the state of anisotropy the material is said to be transversely isotropic. If there exist two axes of rotational symmetry the material must be isotropic.

In the analysis to follow elastic strains will be neglected and it will be assumed that no work hardening takes place. In other words, the analysis will assume a rigid - perfectly plastic mechanical behavior.

Yield conditions will be prescribed in the form $f = f(\sigma_{ij})$. If $f < 0$ the material is below yield. Yielding occurs when $f = 0$. In all cases $f \leq 0$.

The familiar Tresca yield condition states that plastic flow will take place when the maximum shear stress reaches yield.

$$f_1 = \tau_m - R_1 = 0$$

In terms of an arbitrary state of stress this can be written in a more rigorous form [27].

$$f_1 = 4J_2^3 - 27J_3^2 - 36R_1^2 J_2^2 + 96R_1^4 J_2 - 64R_1^6 = 0$$

where J_2 and J_3 are the second and third deviatoric stress invariants. The Mohr-Coulomb yield condition is a modification of the Tresca criterion and accounts for a mean stress dependency.

$$f_2 = \tau_m - R_2 - S_2\sigma_m$$

Experimental evidence of hydrostatic pressure compaction suggests a quadratic relationship for some materials [32].

$$f_3 = \tau_m - R_3 - S_3\sigma_m - \tau_3\sigma_m^2$$

The von Mises yield condition states that yielding occurs when a maximum distortion strain energy is reached.

$$f_4 = J_2^{\frac{1}{2}} - k = 0$$

An extended von Mises yield condition can be formulated as

$$f_5 = J_2^{\frac{1}{2}} - k - n_1 I$$

where I is the first stress tensor invariant [9]. A further extension of the von Mises condition gives the following relationship [32].

$$f_6 = J_2^{\frac{1}{2}} - k - n_2 I - n_3 I^2$$

All of the yield conditions above describe the behavior of an isotropic medium. Anisotropic yield conditions can be formulated which for the case of infinitesimal anisotropy reduce to the isotropic criteria.

$$f_1 = \tau_m - R_1 \quad \Rightarrow \quad f_7 = \tau_M - R_1(\gamma) \quad [32]$$

γ describes the orientation of the principal axes of anisotropy

$$f_2 = \tau_m - R_2 - S_2\sigma_m \quad \Rightarrow \quad f_8 = \tau_m - R_2(\gamma) - S_2(\gamma)\sigma_m \qquad [32]$$

$$f_3 = \tau_m - R_3 - S_3\sigma_m - T_3\sigma_m^2 \Rightarrow f_9 = \tau_m - R_3(\gamma) - S_3(\gamma)\sigma_m - T_3(\gamma)\sigma_m^2 \qquad [32]$$

$$f_4 = J_2^{\frac{1}{2}} - k \quad \Rightarrow \quad f_{10} = [A(\sigma_y-\sigma_z)^2 + B(\sigma_z-\sigma_x)^2 + C(\sigma_x-\sigma_y)^2 + + D\tau_{yz}^2 + E\tau_{zx}^2 + F\tau_{xy}^2]^{\frac{1}{2}} - 1 \qquad [16]$$

$$f_5 = J_2^{\frac{1}{2}} - k - n_1 I \quad \Rightarrow \quad f_{11} = [A(\sigma_y-\sigma_z)^2 + B(\sigma_z-\sigma_x)^2 + C(\sigma_x-\sigma_y)^2 + + D\tau_{yz}^2 + E\tau_{zx}^2 + F\tau_{xy}^2]^{\frac{1}{2}} + - (G\sigma_x + H\sigma_y + K\sigma_z) - 1 \qquad [21]$$

$$f_6 = J_2^{\frac{1}{2}} - k - n_2 I - n_3 I^2 \quad \Rightarrow \quad f_{12} = [A(\sigma_y-\sigma_z)^2 + B(\sigma_z-\sigma_x)^2 + + C(\sigma_x-\sigma_y)^2 + D\tau_{yz}^2 + E\tau_{zy}^2 + + F\tau_{xy}^2]^{\frac{1}{2}} - (G\sigma_x + H\sigma_y + K\sigma_z) + - (L\sigma_x + M\sigma_y + N\sigma_z)^2 - 1 \qquad [32]$$

As with the isotropic yield conditions, f_7 is a simplification of f_8 which is likewise of f_9, and f_{10} is a simplification of f_{11} which is likewise of f_{12}. For the case of plane strain $f_4 = f_1$, $f_5 = f_2$, $f_6 = f_3$, $f_{10} = f_7$, $f_{11} = f_8$ and $f_{12} = f_9$. For the purposes of analysis of the wedge indentation problem the von Mises isotropic yield condition will be utilized solely.

Limit Analysis [11,12]

A brief word must be said on the application of limit analysis to problems in plasticity. Three constraints define a statically admissible stress field for a body. A statically admissible stress field must

1. satisfy force equilibrium
2. be everywhere below yield ($f(\sigma_{ij}) < 0$), and
3. satisfy boundary conditions where surface tractions are specified

A body cannot undergo plastic yield as long as there exists a statically admissible stress field. Restated, the surface tractions and body forces associated with a statically admissible stress field constitute a lower bound to the loads necessary for plastic flow to occur. A kinematically admissible velocity field for a body must satisfy the following constraints.

1. The velocities $\underset{\sim}{v}$ and their first spatial derivatives $\nabla \cdot \underset{\sim}{v}$ must be continuous everywhere except along a finite number of surfaces of discontinuity. Along these surfaces only velocity components tangential to the surface may be discontinuous.
2. Incompressibility must be satisfied everywhere.
3. The rate of energy dissipation by surface tractions T_i must be positive.

$$\int_s T_i v_i ds > 0$$

s denotes the surface of the body

The principle of virtual work can be stated as follows.

$$\int_s T_i v_i ds + \int_V F_i v_i dV = \int_V \sigma_{ij} \varepsilon_{ij} \; dV$$

where T_i = component of surface traction

v_i = component of body force

V denotes the volume of the body

and s denotes the surface of the body

$\int_V \sigma_{ij}\varepsilon_{ij} \; dV$ is often called the "power dissipation". A body must undergo yield if the loading system of surface tractions and body forces satisfy the principle of virtual work for a kinematically admissible velocity field and a state of stress satisfying the criterion for yielding. Restated, for a kinematically admissible velocity field and stress state under yield, a system of surface tractions and body forces satisfying the principle of virtual work will be an upper bound for the loading system necessary for yield. A fundamental approach to solution of problems in plasticity is to seek a greatest lower bound and least upper bound solution for the actual loading system at yield. The analysis to follow will be primarily concerned with determining a reasonable upper bound solution for the wedge indentation problem.

Method of Characteristics [1]

To obtain an exact solution of the partial differential equations in plasticity the "Method of Characteristics" is employed [10]. Assume we have the following system of two linear first order partial differential equations in the xy plane.

$$A_1\frac{\partial u}{\partial x} + B_1\frac{\partial u}{\partial y} + C_1\frac{\partial v}{\partial x} + D_1\frac{\partial v}{\partial y} = E_1$$

$$A_2\frac{\partial u}{\partial x} + B_2\frac{\partial u}{\partial y} + C_2\frac{\partial v}{\partial x} + D_2\frac{\partial v}{\partial y} = E_2$$

The goal is to solve for u and v in terms of x and y. Since u and v are functions of x and y,

$$du = \frac{\partial u}{\partial x}\,dx + \frac{\partial u}{\partial y}\,dy$$

$$dv = \frac{\partial v}{\partial x}\,dx + \frac{\partial v}{\partial y}\,dy$$

The above four equations may be combined into a matrix form

$$\begin{bmatrix} A_1 & B_1 & C_1 & D_1 \\ A_2 & B_2 & C_2 & D_2 \\ dx & dy & 0 & 0 \\ 0 & 0 & dx & dy \end{bmatrix} \begin{bmatrix} \frac{\partial u}{\partial x} \\ \frac{\partial u}{\partial y} \\ \frac{\partial v}{\partial x} \\ \frac{\partial v}{\partial y} \end{bmatrix} = \begin{bmatrix} E_1 \\ E_2 \\ du \\ dv \end{bmatrix}$$

The requirement for the system of equations to be linear means that the coefficients A_1, A_2, $B_1, \ldots, E_1$, E_2 are all functions of x and y only. If for the case of nonlinearity $E_1 = E_2 = 0$ and $A_1, A_2, \ldots, D_2$ are functions of u and v only then the system may be transformed to a linear system by interchanging the roles of dependent and independent variables. Thus, the system of equations must be either linear or reducible to linearity for the solution method to apply. In the xy plane there exist certain lines or directions characteristic to the solution of u(x,y) and v(x,y) called, simply, characteristics. The characteristics may be described as the lines along which the partial differential equations become ordinary differential equations with respect to a spatial coordinate tangential to the characteristic line. The derivatives of u and v with respect to x and y may be indeterminate only along a characteristic line. Discontinuities in the derivatives of u and v must propagate in the xy plane only along characteristics. Restated, wherever discontinuities in the derivatives of u and v exist, a continuous solution occurs only in the characteristic direction. The derivatives of u and v may be indeterminate, but for a solution to exist must be mutually related. To satisfy this condition the following (n+1) X n matrix must be of rank (n-1).

$$\begin{bmatrix} A_1 & B_1 & C_1 & D_1 & E_1 \\ A_2 & B_2 & C_2 & D_2 & E_2 \\ dx & dy & 0 & 0 & du \\ 0 & 0 & dx & dy & dv \end{bmatrix} \qquad n = 4$$

This condition can be satisfied only if

$$\begin{vmatrix} A_1 & B_1 & C_1 & D_1 \\ A_2 & B_2 & C_2 & D_2 \\ dx & dy & 0 & 0 \\ 0 & 0 & dx & dy \end{vmatrix} = 0$$

and

$$\begin{vmatrix} A_1 & B_1 & C_1 & E_1 \\ A_2 & B_2 & C_2 & E_2 \\ dx & dy & 0 & du \\ 0 & 0 & dx & dv \end{vmatrix} = 0$$

The first relationship determines the characteristic directions and the second determines the solution of the ordinary differential equation along the characteristics. The first relationship yields the solution

$$\frac{dy}{dx} = \frac{-b \pm \sqrt{b^2 - 4ac}}{2a}$$

where $a = A_1C_2 - A_2C_1$

$b = B_2C_1 - B_1C_2 + A_2D_1 - A_1D_2$

$c = B_1D_2 - B_2D_1$

The system of equations is classified according to the value $b^2 - 4ac$.

$$b^2 - 4ac > 0 \Rightarrow \text{hyperbolic}$$

$$b^2 - 4ac = 0 \Rightarrow \text{parabolic}$$

$$b^2 - 4ac < 0 \Rightarrow \text{ellyptic}$$

Only for a hyperbolic system of linear first order partial differential equations does the method provide a useful solution.

Solution for Plane Strain [1]

For most solutions of problems in plasticity to be mathematically tractable the constraint to problems of plane strain must be employed. The analysis following will be restricted to plane strain in the xy plane and body forces will be considered negligible. The von Mises isotropic yield condition $f = 1/6\,[(\sigma_x - \sigma_y)^2 + (\sigma_y - \sigma_z)^2 + (\sigma_z - \sigma_x)^2] + {}$ $+ \tau_{xy}{}^2 + \tau_{yz}{}^2 + \tau_{zx}{}^2 - k^2 = 0$ and the principle of plastic potential $\dot{\epsilon}^p_{ij} = \lambda \frac{\partial f}{\partial \sigma_{ij}}$ yield, for plane strain

$$\dot{\epsilon}^p_z = \tfrac{1}{3}\lambda\,(2\sigma_z - \sigma_x - \sigma_y) = 0$$

$$\dot{\epsilon}^p_{yz} = 2\,\lambda\tau_{yz} = 0$$

$$\dot{\epsilon}^p_{zx} = 2\,\lambda\tau_{zx} = 0$$

Solving for σ_z, τ_{yz} and τ_{zx} and substituting into the yield condition gives

$$\sigma_z = \tfrac{1}{2}(\sigma_x + \sigma_y) \qquad \tau_{yz} = \tau_{zx} = 0$$

$$f = \left(\frac{\sigma_x - \sigma_y}{2}\right)^2 + \tau_{xy}{}^2 - k^2 = 0$$

The yield condition can be represented by the Mohr Circle diagram (Figures 7,8).

$$\sigma_x = p + k\cos 2\theta$$

$$\sigma_y = p - k\cos 2\theta$$

$$\tau_{xy} = k\sin 2\theta \qquad (1)$$

p = hydrostatic pressure

θ = angle from the $\underset{\sim}{i}'$ - axis to the direction of maximum principal stress

The equations of equilibrium are,

$$\frac{\partial\sigma_x}{\partial x} + \frac{\partial\tau_{xy}}{\partial y} = 0$$

$$(2)$$

$$\frac{\partial\tau_{xy}}{\partial x} + \frac{\partial\sigma_y}{\partial y} = 0$$

Substitute (1) into (2) to obtain

$$\frac{\partial p}{\partial x} - 2k\sin 2\theta\,\frac{\partial\theta}{\partial x} + 2k\cos 2\theta\,\frac{\partial\theta}{\partial y} = 0$$

$$\frac{\partial p}{\partial y} + 2k\cos 2\theta\,\frac{\partial\theta}{\partial x} + 2k\sin 2\theta\,\frac{\partial\theta}{\partial y} = 0$$

p and θ are to be solved in terms of x and y

$$dp = \frac{\partial p}{\partial x}dx + \frac{\partial p}{\partial y}dy$$

$$d\theta = \frac{\partial\theta}{\partial x}dx + \frac{\partial\theta}{\partial y}dy$$

The four equations combine to form a system of linearly reducible first order partial differential equations.

$$\begin{bmatrix} 1 & 0 & -2k\sin 2\theta & 2k\cos 2\theta \\ 0 & 1 & 2k\cos 2\theta & 2k\sin 2\theta \\ dx & dy & 0 & 0 \\ 0 & 0 & dx & dy \end{bmatrix} \begin{bmatrix} \frac{\partial p}{\partial x} \\ \frac{\partial p}{\partial y} \\ \frac{\partial\theta}{\partial x} \\ \frac{\partial\theta}{\partial y} \end{bmatrix} = \begin{bmatrix} 0 \\ 0 \\ dp \\ d\theta \end{bmatrix}$$

By the method of characteristics, the stress characteristics are defined by

$$\begin{vmatrix} 1 & 0 & -2k\sin 2\theta & 2k\cos 2\theta \\ 0 & 1 & 2k\cos 2\theta & 2k\sin 2\theta \\ dx & dy & 0 & 0 \\ 0 & 0 & dx & dy \end{vmatrix} = 0$$

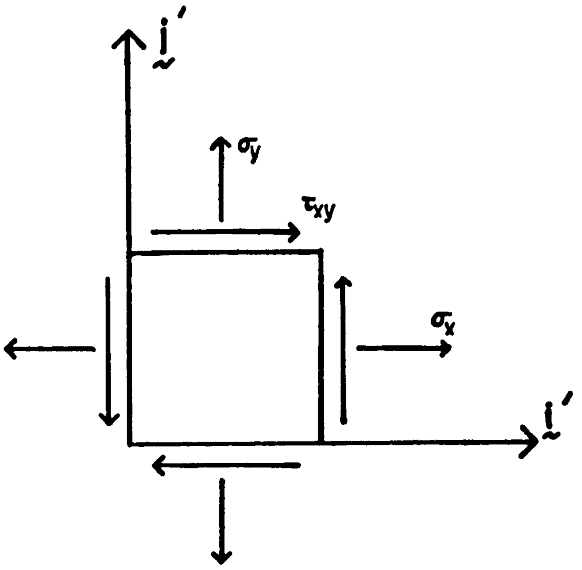

Figure 7 Representation of Stress in Physical Plane

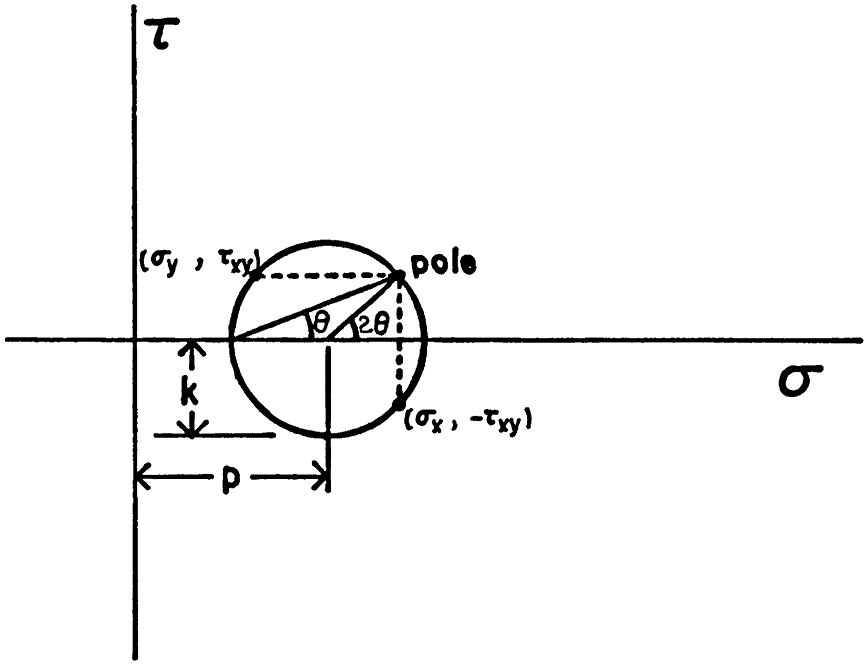

Figure 8 Mohr's Circle Representation of Stress

Let ϕ_c be the angle between $\underset{\sim}{i}'$ - axis and a characteristic direction. Then $\frac{dy}{dx} = \tan\phi_c$ and

$$\begin{vmatrix} 1 & 0 & -2k\sin 2\theta & 2k\cos 2\theta \\ 0 & 1 & 2k\cos 2\theta & 2k\sin 2\theta \\ 1 & \tan\phi_c & 0 & 0 \\ 0 & 0 & 1 & \tan\phi_c \end{vmatrix} = 0$$

Subtract the third row from the first,

$$\begin{vmatrix} 0 & -\tan\phi_c & -2k\sin 2\theta & 2k\cos 2\theta \\ 0 & 1 & 2k\cos 2\theta & 2k\sin 2\theta \\ 1 & \tan\phi_c & 0 & 0 \\ 0 & 0 & 1 & \tan\phi_c \end{vmatrix} = 0$$

$$\begin{vmatrix} -\tan\phi_c & -2k\sin 2\theta & 2k\cos 2\theta \\ 1 & 2k\cos 2\theta & 2k\sin 2\theta \\ 0 & 1 & \tan\phi_c \end{vmatrix} = 0$$

$$-2k\cos 2\theta\tan^2\phi_c + 2k\cos 2\theta + 4k\sin 2\theta\tan\phi_c = 0$$

$$\tan^2\phi_c - 2\tan 2\theta\tan\phi_c - 1 = 0 \qquad (3)$$

$$\tan\phi_c = \tan 2\theta \pm \sec 2\theta$$

$$= \frac{\tan\theta}{1-\tan^2\theta} \pm \frac{1+\tan^2\theta}{1-\tan^2\theta}$$

$$= \frac{(1 \pm \tan\theta)(\tan\theta \pm 1)}{(1 \pm \tan\theta)(1 \mp \tan\theta)}$$

$$= \frac{\tan\theta \pm 1}{1 \mp \tan\theta}$$

or $\quad \tan\phi_c = \tan(\theta \pm \frac{\pi}{4})$

The stress field solution along the characteristics is defined by

$$\begin{vmatrix} 1 & 0 & -2k\sin 2\theta & 0 \\ 0 & 1 & 2k\cos 2\theta & 0 \\ 1 & \tan\phi_c & 0 & \frac{dp}{dx} \\ 0 & 0 & 1 & \frac{d\theta}{dx} \end{vmatrix} = 0$$

A similar procedure is utilized to determine the solution of the velocity field of a body undergoing plane plastic strain. The assumption of incompressibility implies

$$\frac{\partial v_x}{\partial x} + \frac{\partial v_y}{\partial y} = 0 \tag{4}$$

The strain increments are

$$\dot{\epsilon}_x = \lambda(\sigma_x - \sigma_y) = \frac{\partial v_x}{\partial_x}$$

$$\dot{\epsilon}_y = \lambda(\sigma_y - \sigma_x) = \frac{\partial v_x}{\partial y}$$

$$\dot{\epsilon}_{xy} = 2\lambda\tau_{xy} = \tfrac{1}{2}\left(\frac{\partial v_x}{\partial y} + \frac{\partial v_y}{\partial x}\right) = \tfrac{1}{2}\,\dot{\gamma}_{xy}$$

$$\frac{\dot{\epsilon}_x - \dot{\epsilon}_y}{\dot{\gamma}_{xy}} = \frac{2\lambda(\sigma_x - \sigma_y)}{4\lambda\tau_{xy}} = \frac{\sigma_x - \sigma_y}{2\tau_{xy}}$$

$$\frac{\partial v_x}{\partial x} - \frac{\partial v_y}{\partial y} = \frac{\sigma_x - \sigma_y}{2\tau_{xy}}\left(\frac{\partial v_x}{\partial y} + \frac{\partial v_y}{\partial x}\right) \tag{5}$$

The velocities are functions of x and y.

$$dv_x = \frac{\partial v_x}{\partial x}\,dx + \frac{\partial v_x}{\partial y}\,dy$$

$$dv_y = \frac{\partial v_y}{\partial x}\,dx + \frac{\partial v_y}{\partial y}\,dy \tag{6}$$

The equations (4), (5), and (6) can be combined in matrix form.

$$\begin{bmatrix} 1 & 0 & 0 & 1 \\ 1 & -\xi & -\xi & -1 \\ dx & dy & 0 & 0 \\ 0 & 0 & dx & dy \end{bmatrix} \begin{bmatrix} \frac{\partial v_x}{\partial x} \\ \frac{\partial v_x}{\partial y} \\ \frac{\partial v_y}{\partial x} \\ \frac{\partial v_y}{\partial y} \end{bmatrix} = \begin{bmatrix} 0 \\ 0 \\ dv_x \\ dv_y \end{bmatrix}$$

where $\xi = \dfrac{\sigma_x - \sigma_y}{2\tau_{xy}}$

The velocity characteristics are defined by,

$$\begin{vmatrix} 1 & 0 & 0 & 1 \\ 1 & -\xi & -\xi & -1 \\ dx & dy & 0 & 0 \\ 0 & 0 & dx & dy \end{vmatrix} = 0$$

$$[-dx\ dy + \xi\ dy^2] - [dy\ dx] + dx[-\xi dx] = 0$$

$$\left(\frac{dy}{dx}\right)^2 - \frac{2}{\xi}\left(\frac{dy}{dx}\right) - 1 = 0$$

$$\left(\frac{dy}{dx}\right)^2 - \frac{4\tau_{xy}}{\sigma_x - \sigma_y}\left(\frac{dy}{dx}\right) - 1 = 0$$

$$\left(\frac{dy}{dx}\right)^2 - 2\tan 2\theta\left(\frac{dy}{dx}\right) - 1 = 0$$

This relationship is the same as (3). Thus the velocity characteristics coincide with the stress characteristics. The velocity field along the characteristics is defined by

$$\begin{vmatrix} 1 & 0 & 0 & 0 \\ 1 & -\xi & -\xi & 0 \\ dx & dy & 0 & dv_x \\ 0 & 0 & dx & dv_y \end{vmatrix} = 0$$

$$\xi\ dx\ dv_x + \xi\ dy\ dv_y = 0$$

$$dv_x + dv_y\left(\frac{dy}{dx}\right) = 0$$

Let s_+ and s_- be length coordinates along the characteristics, with orientations ϕ_+ and ϕ_- with respect to the $\underset{\sim}{i}'$ - axis. Then

$$\begin{aligned} \cos\phi_+ \frac{dv_x}{ds_+} + \sin\phi_+ \frac{dv_y}{ds_+} &= 0 \\ \sin\phi_+ \frac{dv_x}{ds_-} - \cos\phi_+ \frac{dv_y}{ds_-} &= 0 \end{aligned} \qquad (7)$$

$$\begin{bmatrix} v_x \\ v_y \end{bmatrix} = \begin{bmatrix} \cos\phi_+ & -\sin\phi_+ \\ \sin\phi_+ & \cos\phi_+ \end{bmatrix} \begin{bmatrix} v_+ \\ v_- \end{bmatrix} \qquad (8)$$

With some mathematical manipulation substitution of (8) into (7) yields the Geiringer Relationships.

$$\frac{dv_+}{ds_+} - v_- \left(\frac{d\phi_+}{ds_+}\right) = 0$$

$$\frac{dv_-}{ds_-} + v_+ \left(\frac{d\phi_+}{ds_-}\right) = 0$$

The transpose of (8) gives

$$\begin{aligned} dv_+ &= \cos\phi_+ \, dv_x + \sin\phi_+ \, dv_y \\ dv_- &= -\sin\phi_+ \, dv_x + \cos\phi_+ \, dv_y \end{aligned} \qquad (9)$$

Inspection of (7) and (9) yields the condition that the characteristics are inextensible.

$$dv_+ = dv_- = 0$$

To solve an actual problem in plane strain a slip line field is determined by the solution for the characteristics and the known boundary conditions [24]. The state of stress is then known throughout the field due to the stress relationships along the characteristics.

Stress and Velocity Discontinuities

Velocity discontinuities can occur only along slip lines, the velocity (and stress) characteristics. Incompressibility requires that only velocities tangential to the line of discontinuity may be discontinuous. The Geiringer Relationships require that the jump in tangential velocity be constant along a line of discontinuity (Figure 9).

$$dv_+^{\,1} - v_- \, d\phi_+ = 0$$

$$dv_+^{\,2} - v_- \, d\phi_+ = 0$$

$$\therefore \quad dv_+^{\,1} - dv_+^{\,2} = 0$$

There are two possible states of stress at yield due to an arbitrary surface traction (Figures 10, 11). Whether the weak or strong solution is appropriate is determined by the boundary conditions as a whole. A line of stress discontinuity cannot coincide with a slip line (Figures 12 and 14). The slip line field on either side of a line of stress dis-

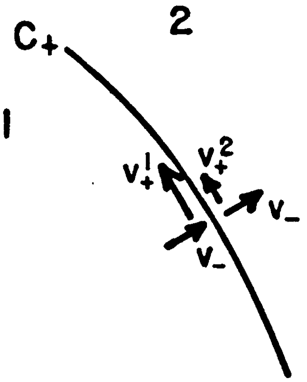

Figure 9 Velocity Discontinuity

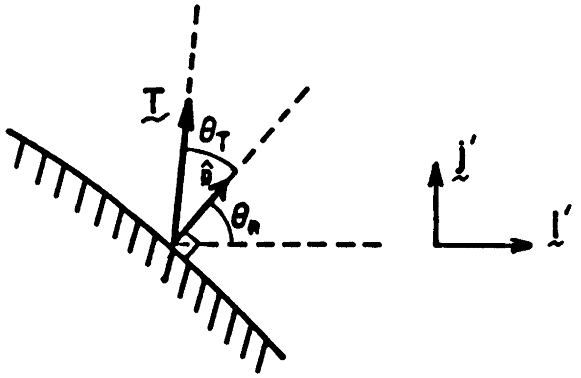

Figure 10 Surface Traction

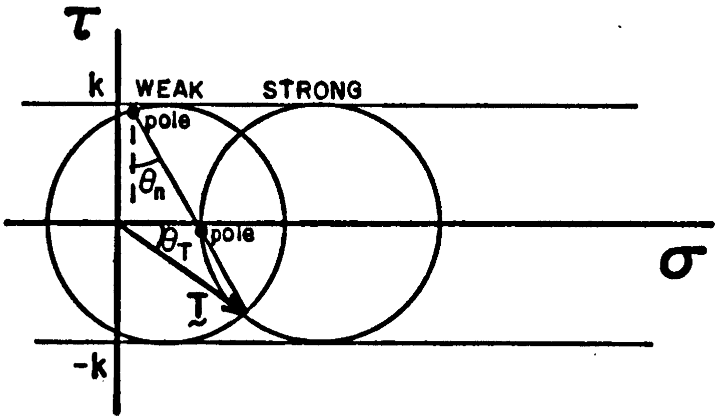

Figure 11 Stress Plane Representation of Surface Traction

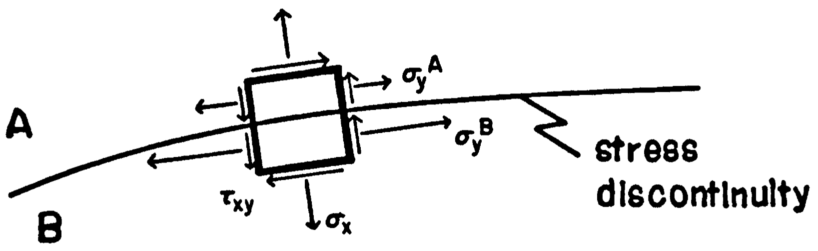

Figure 12 Stress Discontinuity

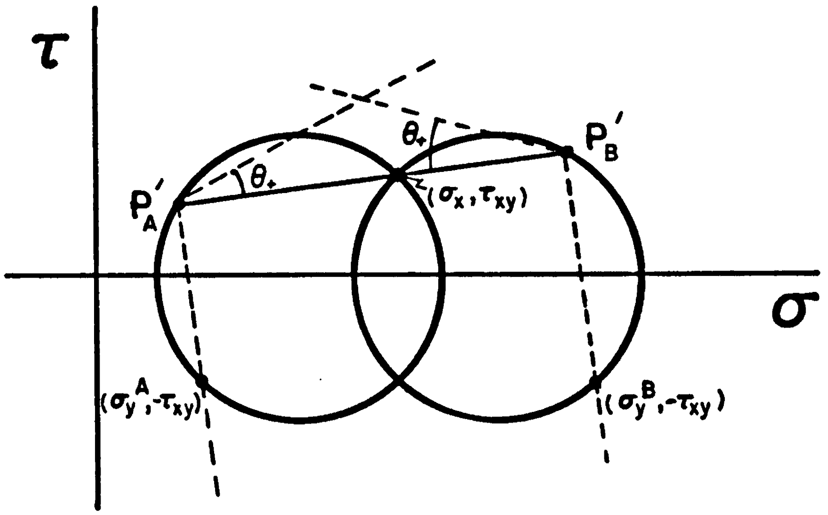

Figure 13 Stress Plane Representation of Stress Discontinuity

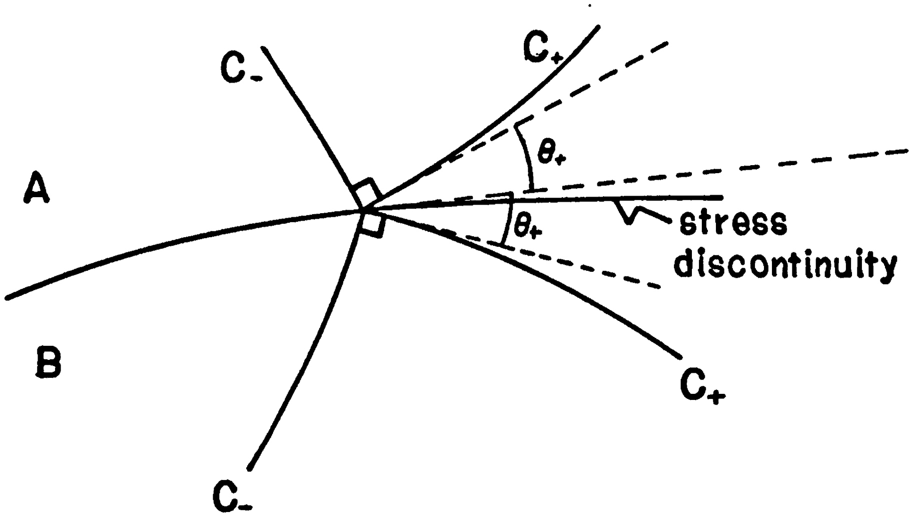

Figure 14 Slip Line Field Near Stress Continuity

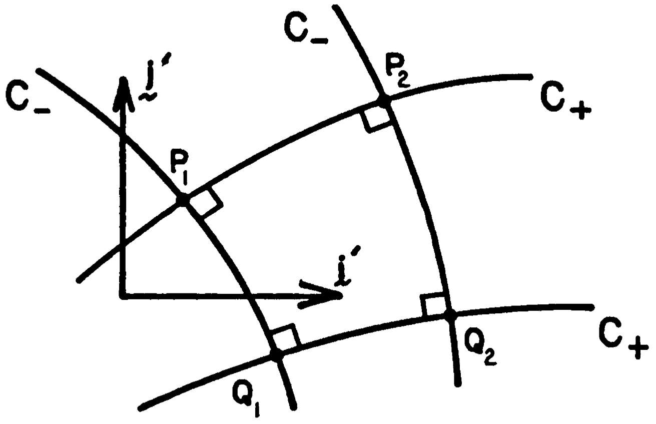

Figure 15 Mapping Technique - Physical Plane

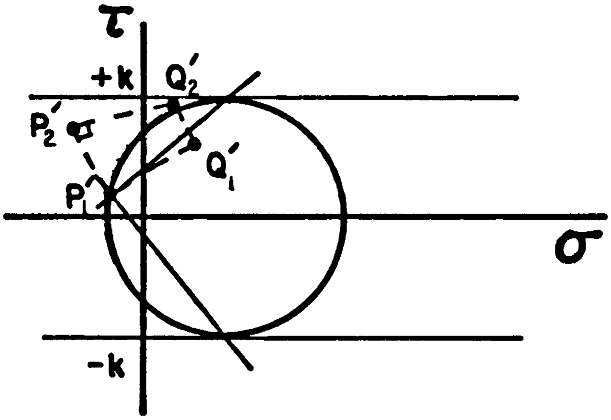

Figure 16 Mapping Technique - Stress Plane

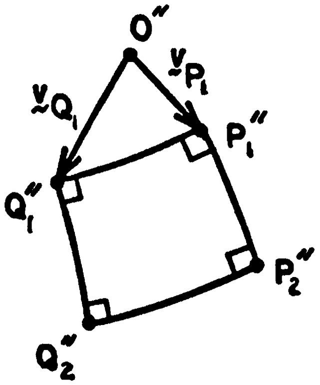

Figure 17 Mapping Technique- Velocity Plane (Hodograph)

continuity will be symmetric with respect to the line of stress discontinuity. Equilibrium requires that only the normal stress component tangential to the line of stress discontinuity may be discontinuous. From the Mohr Circle diagram the stress jump across the line of stress discontinuity is readily obtained.

$$\sigma_y^B - \sigma_y^A = 4\sqrt{k^2 - \tau_{xy}^2}$$

The inextensibility of the slip lines requires that lines of stress discontinuity be inextensible.

Mapping Techniques [24]

Prager has developed a mapping technique which serves as a useful aid in studying plane strain plasticity (Figures 15 - 17). Slip lines in the physical plane are mapped into cycloidal curves in the stress plane generated by the pole of the Mohr Circle as the circle rolls without sliding along either the line $\tau = k$ or $\tau = -k$. The direction of the cycloidal tangent is perpendicular to the corresponding slip line field direction. A point in the physical plane is mapped into a pole of a Mohr Circle. A mapping is generated by first deciding upon a "weak" or "strong" stress state solution for a particular point in the physical plane and simply "rolling" the Mohr Circle according to the corresponding slip line field. A hodograph is a mapping of the physical plane into the velocity plane. The mapping of a slip line is a line whose tangent is always perpendicular to the slip line direction. A slip line field with one family of slip lines straight (called a centered fan) maps into a single cycloid in the stress plane and a single circular arc in the hodograph. A slip line field where all the slip lines are straight maps into a single point in both the stress and velocity planes.

The discussion above constitutes a brief summary of the fundamentals of plasticity theory necessary for the practical analysis to follow.

Theoretical Isotropic Wedge Indentation Solution

An upper bound solution is desired for the horizontal and vertical forces necessary to force a wedge of finite width vertically into an inclined isotropic medium with arbitrary orientation of wedge and direction of maximum slope. The problem will be divided into two parts. A solution will be found for the plane strain indentation of a wedge of infinite width and $\psi_y = 0$. These results will then be used to determine the solution for the actual wedge and arbitrary ψ_y assuming a plane strain slip line field on all sides of the wedge. As will be shown later in this discussion the analysis constitutes an upper bound for the horizontal load, but not for the vertical. The necessary correction will be described and calculated for several cases.

Plane Strain Infinite Wedge Solution

In the course of this study solutions were found for smooth, rough, and frictional wedge conditions using both Prandtl - type (no lip formation) and Hill - type (lip formation) slip line fields. The analysis to follow assumes the least number of simplifying constraints and is proposed as the most meaningful prediction of physical behavior. A vertically symmetric two dimensional infinite width frictional wedge is assumed to move in a non - vertical direction (for sake of generality) into a semi - infinite incompressible non - work hardening isotropic medium whose smooth flat surface is inclined with respect to the horizontal. The resulting slip line field is one which predicts lip formation on each side of the wedge. The other solutions are described in Appendix A to this report.

The physical plane slip line field determined by application of the boundary conditions to the solution for the characteristics is shown along with the corresponding mappings in the stress and velocity planes (Figures 18 - 21). The known parameters in the physical plane are β, ψ_x, μ, δ_V, b, k, and ϵ. In actual numerical calculations for vertical indentation, $\epsilon = 0$. Relationships for the other physical plane parameters are determined geometrically.

$$(\overline{OM}) = \delta_V \cos\psi_x + d_1 \sin\gamma_1$$

$$(\overline{OL}) = \delta_V \cos\psi_x + d_2 \sin\gamma_2$$

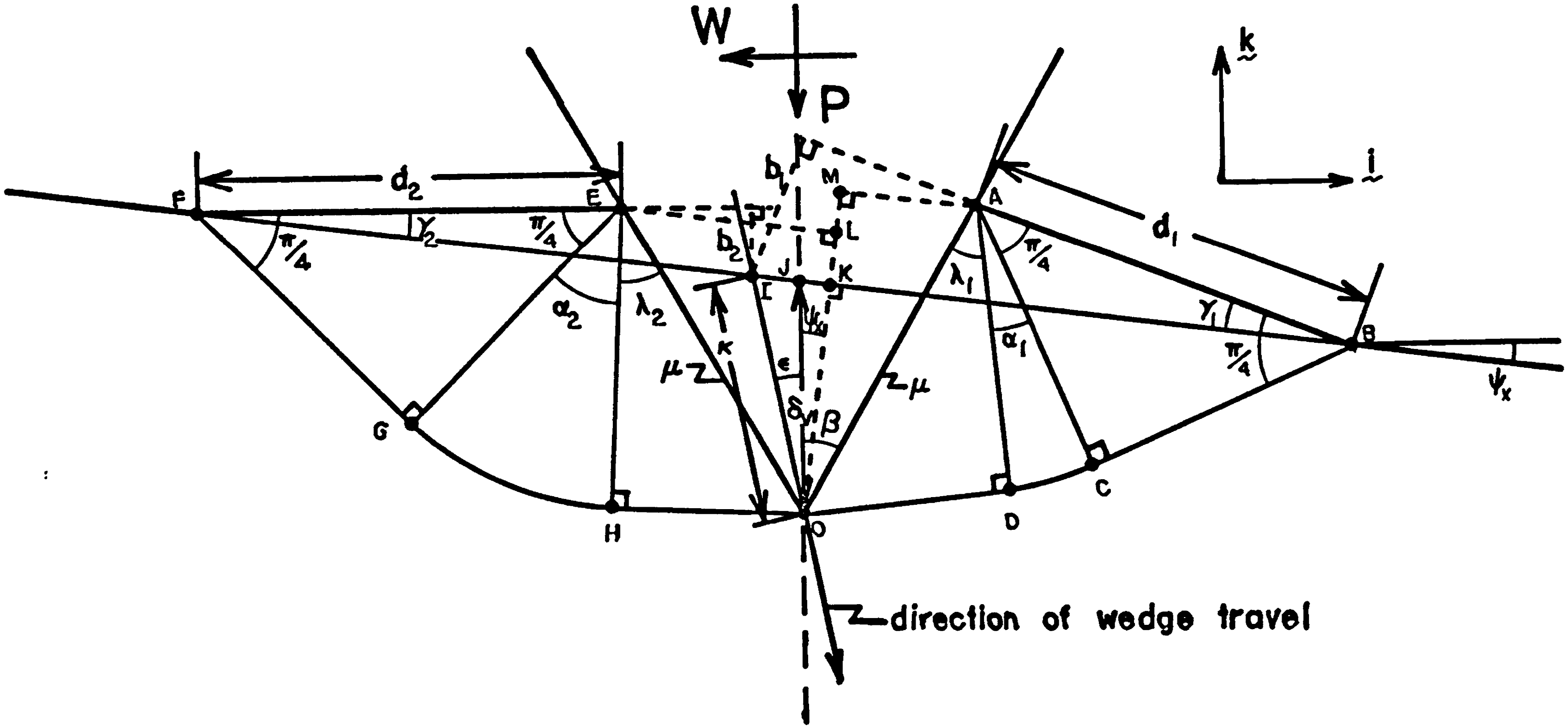

Figure 18 Slip Line Field for Frictional Wedge with Lip Formation

Also,

$$(\overline{OM}) = (\overline{OA})\cos(\beta - \psi_x) = \frac{1}{\sqrt{2}} d_1 \sec\lambda_1 \cos(\beta - \psi_x)$$

$$(\overline{OL}) = (\overline{OE})\cos(\beta + \psi_x) = \frac{1}{\sqrt{2}} d_2 \sec\lambda_2 \cos(\beta + \psi_x)$$

Combine the equations above to obtain

$$\frac{1}{\sqrt{2}} d_1 \sec\lambda_1 \cos(\beta - \psi_x) = \delta_V \cos\psi_x + d_1 \sin\gamma_1$$

$$\frac{1}{\sqrt{2}} d_2 \sec\lambda_2 \cos(\beta + \psi_x) = \delta_V \cos\psi_x + d_2 \sin\gamma_2$$

or,

$$\frac{d_1}{\delta_V} = \frac{\sqrt{2}\cos\psi_x}{\sec\lambda_1 \cos(\beta - \psi_x) - \sqrt{2}\sin\lambda_1}$$

$$\frac{d_2}{\delta_V} = \frac{\sqrt{2}\cos\psi_x}{\sec\lambda_2 \cos(\beta + \psi_x) - \sqrt{2}\sin\gamma_2} \qquad (10)$$

It can be seen by inspection that

$$b_1 = (\overline{BI})\sin\gamma_1$$

$$b_2 = (\overline{FI})\sin\gamma_2$$

and

$$(\overline{BI}) = d_1\cos\gamma_1 + (\overline{OA})\sin(\beta - \psi_x) + \delta_V \cos\psi_x \tan(\psi_x + \varepsilon)$$

$$(\overline{FI}) = d_2\cos\gamma_2 + (\overline{OE})\sin(\beta + \psi_x) - \delta_V \cos\psi_x \tan(\psi_x + \varepsilon)$$

Then

$$b_1 = [d_1\cos\gamma_1 + \frac{1}{\sqrt{2}} d_1 \sec\lambda_1 \sin(\beta - \psi_x) + \delta_V \cos\psi_x \tan(\psi_x + \varepsilon)]\sin\lambda_1$$

$$b_2 = [d_2\cos\gamma_2 + \frac{1}{\sqrt{2}} d_2 \sec\lambda_2 \sin(\beta + \psi_x) - \delta_V \cos\psi_x \tan(\psi_x + \varepsilon)]\sin\lambda_2$$

or

$$\frac{b_1}{\delta_V} = \left[\left(\cos\gamma_1 + \frac{\sin(\beta - \psi_x)}{\sqrt{2}\cos\lambda_1}\right)\frac{d_1}{\delta_V} + \cos\psi_x\tan(\psi_x + \epsilon)\right]\sin\gamma_1$$

(11)

$$\frac{b_2}{\delta_V} = \left[\left(\cos\gamma_2 + \frac{\sin(\beta + \psi_x)}{\sqrt{2}\cos\lambda_2}\right)\frac{d_2}{\delta_V} - \cos\psi_x\tan(\psi_x + \epsilon)\right]\sin\gamma_2$$

The following relationships can be discerned from the hodograph (Figure 21).

$$v_1 = v\sin(\beta + \epsilon)\sec\lambda_1$$

$$v_2 = v\sin(\beta - \epsilon)\sec\lambda_2$$

Let $t \equiv \frac{\varkappa}{v}$

Then $b_1 = \frac{v_1 t}{\sqrt{2}} = \frac{vt\sin(\beta - \epsilon)}{\sqrt{2}\cos\lambda_2}$

$$b_2 = \frac{v_2 t}{\sqrt{2}} = \frac{vt\sin(\beta - \epsilon)}{\sqrt{2}\cos\lambda_2}$$

From the physical plane,

$$vt = \varkappa = \delta_V\cos\psi_x\sec(\psi_x + \epsilon)$$

Then

$$\frac{b_1}{\delta_V} = \frac{\cos\psi_x(\sin(\beta + \epsilon)}{\sqrt{2}\cos(\psi_x + \epsilon)\cos\lambda_1}$$

(12)

$$\frac{b_2}{\delta_V} = \frac{\cos\psi_x\sin(\beta - \epsilon)}{\sqrt{2}\cos(\psi_x + \epsilon)\cos\lambda_2}$$

From the physical plane, a summation of angles at A and E yields

$$\frac{\pi}{4} + \alpha_1 + \lambda_1 + \left(\frac{\pi}{2} - \beta\right) + \psi_x + \gamma_1 = \pi$$

$$\frac{\pi}{4} + \alpha_2 + \lambda_2 + \left(\frac{\pi}{2} - \beta\right) - \psi_x + \gamma_2 = \pi$$

or

$$\gamma_1 = \frac{\pi}{4} + \beta - \psi_x - \alpha_1 - \lambda_1$$

(13)

$$\gamma_2 = \frac{\pi}{4} + \beta + \psi_x - \alpha_2 - \lambda_2$$

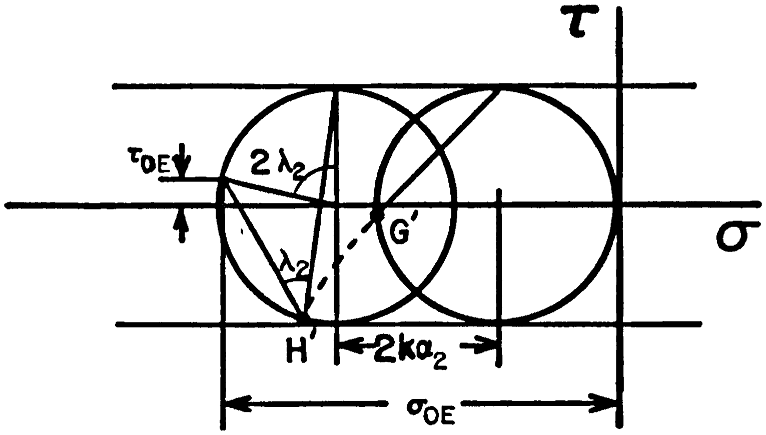

Figure 19 Upslope Stress Diagram for Frictional/Lip Hypothesis

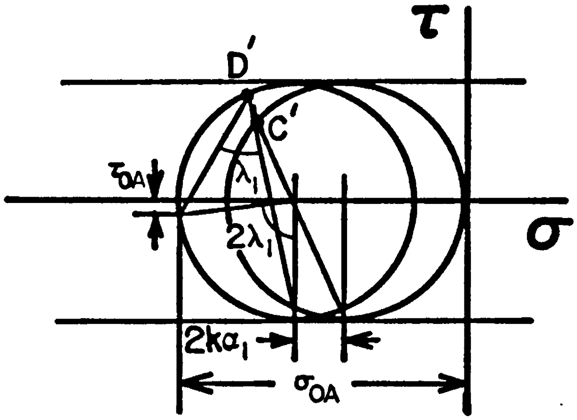

Figure 20 Downslope Stress Diagram for Frictional/Lip Hypothesis

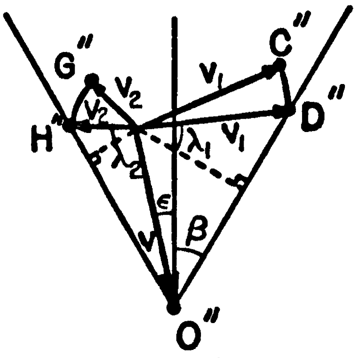

Figure 21 Frictional/Lip Hodograph

The Mohr Circle diagrams in the stress plane yield the following relationships.

$$\sigma_{OA} = k(2\alpha_1 + 1 + \sin 2\lambda_1) \ , \ \tau_{OA} = k\cos 2\lambda_1$$

$$\sigma_{OE} = k(2\alpha_2 + 1 + \sin 2\lambda_2) \ , \ \tau_{OE} = k\cos 2\lambda_2$$

From the definition of coefficient of friction,

$$\tau = \mu\sigma$$

Then

$$\cos 2\lambda_1 = \mu(2\alpha_1 + 1 + \sin 2\lambda_1)$$

$$\cos 2\lambda_2 = \mu(2\alpha_2 + 1 + \sin 2\lambda_2)$$

or

$$\alpha_1 = \frac{1}{2}\left(\frac{\cos 2\lambda_1}{\mu} - 1 - \sin 2\lambda_1\right)$$

$$\alpha_2 = \frac{1}{2}\left(\frac{\cos 2\lambda_2}{\mu} - 1 - \sin 2\lambda_2\right) \qquad (14)$$

An iterative numerical procedure must be used to determine the various parameters in the solution:

1. Choose λ_i.
2. Calculate α_i from (14).
3. Calculate λ_i from (13).
4. Calculate $\frac{d_i}{\delta_V}$ from (10).
5. Calculate $\frac{b_i}{\delta_V}$ from (11) and (12), compare.
6. Repeat the procedure until (11) and (12) give the same $\frac{b_i}{\delta_V}$.

When these parameters have been determined the forces that must be exerted on the wedge by an external source can be calculated.

$$P = b(\overline{OA})[\sigma_{OA}\sin\beta + \tau_{OA}\cos\beta] + b(\overline{OE})[\sigma_{OE}\sin\beta + \tau_{OE}\cos\beta]$$

$$W = b(\overline{OA})[-\sigma_{OA}\cos\beta + \tau_{OA}\sin\beta] + b(\overline{OE})[\sigma_{OE}\cos\beta - \tau_{OE}\sin\beta]$$

where

$$(\overline{OA}) = \frac{d_1}{\sqrt{2}\cos\lambda_1} = \frac{\delta_V}{\sqrt{2}\cos\lambda_1}\left(\frac{d_1}{\delta_V}\right)$$

$$(\overline{OE}) = \frac{d_2}{\sqrt{2}\cos\lambda_2} = \frac{\delta_V}{\sqrt{2}\cos\lambda_2}\left(\frac{d_2}{\delta_V}\right)$$

and

$$\sigma_{OA} = \frac{\tau_{OA}}{\mu} = \frac{k\cos 2\lambda_1}{\mu}$$

$$\sigma_{OE} = \frac{\tau_{OE}}{\mu} = \frac{k\cos 2\lambda_2}{\mu}$$

Substitution above gives

$$P = \frac{b\delta_V}{\sqrt{2}\cos\lambda_1}\left(\frac{d_1}{\delta_V}\right)\left[k\cos 2\lambda_1\left(\frac{\sin\beta}{\mu} + \cos\beta\right)\right] + \frac{b\delta_V}{\sqrt{2}\cos\lambda_2}\left(\frac{d_2}{\delta_V}\right)\left[k\cos 2\lambda_2\left(\frac{\sin\beta}{\mu} + \cos\beta\right)\right]$$

$$W = \frac{b\delta_V}{\sqrt{2}\cos\lambda_1}\left(\frac{d_1}{\delta_V}\right)\left[k\cos 2\lambda_1\left(\sin\beta - \frac{\cos\beta}{\mu}\right)\right] - \frac{b\delta_V}{\sqrt{2}\cos\lambda_2}\left(\frac{d_2}{\delta_V}\right)\left[k\cos 2\lambda_2\left(\sin\beta - \frac{\cos\beta}{\mu}\right)\right]$$

or

$$\frac{P}{b\delta_V k} = \left[\frac{\cos 2\lambda_1}{\cos(\beta - \psi_x) - 2\cos\lambda_1\sin\gamma_1} + \frac{\cos 2\lambda_2}{\cos(\beta + \psi_x) - 2\cos\lambda_2\sin\gamma_2}\right]\left(\frac{\sin\beta}{\mu} + \cos\beta\right)\cos\psi_x$$

$$\frac{W}{b\delta_V k} = \left[\frac{\cos 2\lambda_1}{\cos(\beta - \psi_x) - 2\cos\lambda_1\sin\gamma_1} - \frac{\cos 2\lambda_2}{\cos(\beta + \psi_x) - 2\cos\lambda_2\sin\gamma_2}\right]\left(\sin\beta - \frac{\cos\beta}{\mu}\right)\cos\psi_x$$

For the special case where $\beta < \psi_x + \lambda_1 + \gamma_1 - \frac{\pi}{4}$ a stress discontinuity is found on the down slope side of the wedge (Figures 22 - 24). The pattern of velocity discontinuities in the physical plane becomes an infinitesimally fine mesh near A. Inspection of the physical plane slip line field will yield a derivation for ϕ'. Summing angles about C gives

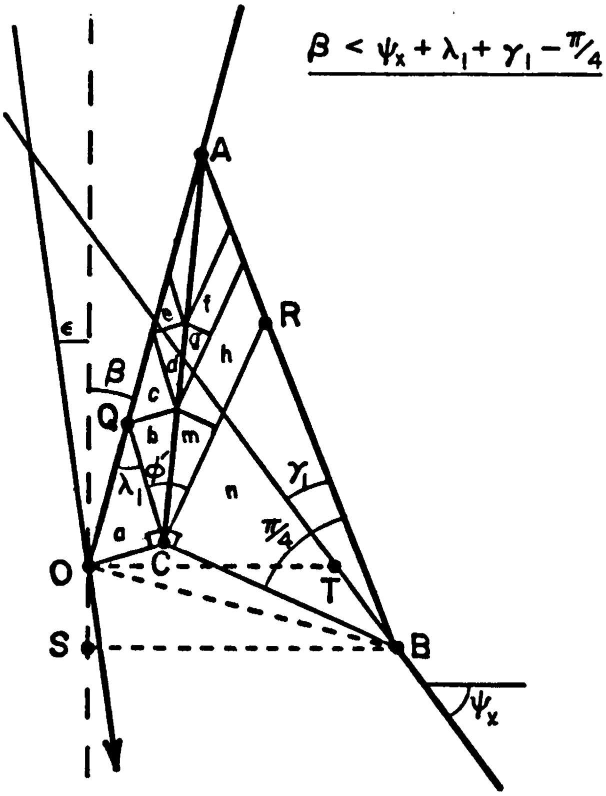

Figure 22 Frictional/Lip Slip Line Field with Stress Discontinuity

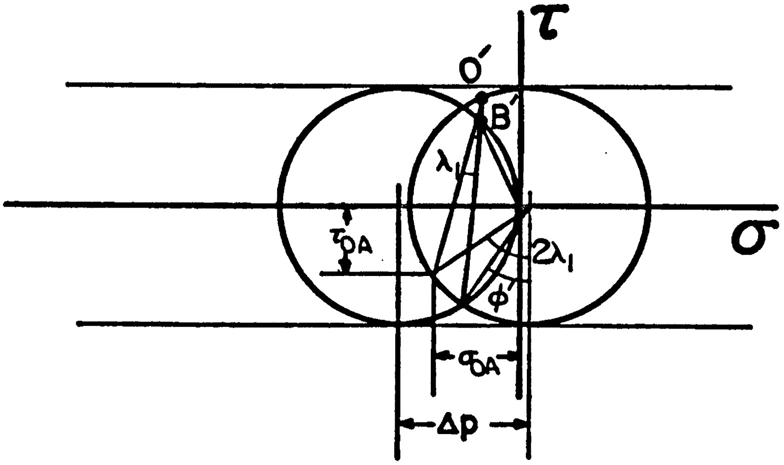

Figure 23 Frictional/Lip Stress Diagram for Stress Discontinuity

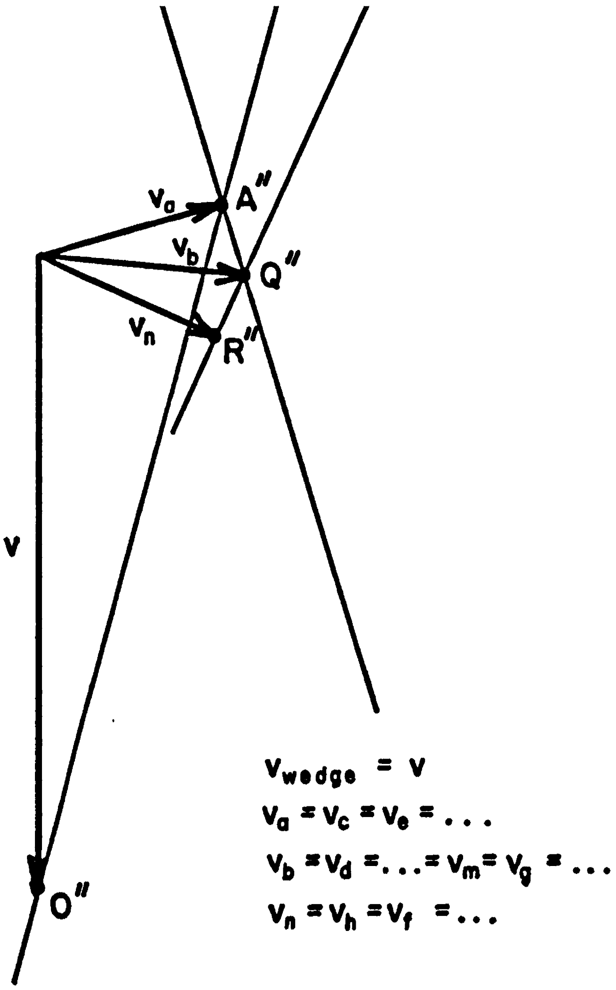

Figure 24 Frictional/Lip Hodograph for Stress Discontinuity

$$\angle OCB + \frac{\pi}{2} + \phi' + \frac{\pi}{2} = 2\pi$$

$$\angle OCB + \phi' = \pi$$

$$\phi' = \angle COB + \angle CBO \tag{16}$$

Summing angles about B gives

$$(\frac{\pi}{4} - \gamma_1) + \angle CBO + \angle OBS = \psi_x \tag{17}$$

Summing angles about 0 gives

$$\beta + (\frac{\pi}{2} - \lambda_1) + \angle COT = \frac{\pi}{2}$$

$$\angle COB - \angle TOB = \lambda_1 - \beta \tag{18}$$

Using $\angle TOB = \angle OBS$, (18) and (17) become, respectively,

$$\angle TOB = \angle COB + \beta - \lambda_1$$

$$\frac{\pi}{4} - \gamma_1 + \angle CBO + \angle COB + \beta - \lambda_1 = \psi_x \tag{19}$$

(16) and (19) combine to yield

$$\frac{\pi}{4} - \gamma_1 + \phi' + \beta - \lambda_1 = \psi_x$$

or

$$\phi' = \psi_x - \beta - \frac{\pi}{4} + \gamma_1 + \lambda_1 \tag{20}$$

Inspection of the stress plane will yield the following relationships.

$$\Delta p = 2k\sin\phi'$$

$$\sigma_{OA} = k\sin2\lambda_1 - (\Delta p - k) = k(\sin2\lambda_1 - 2\sin\phi' + 1)$$

$$\tau_{OA} = k\cos2\lambda_1$$

From the friction criterion, $\tau_{OA} = \mu\sigma_{OA}$, the above relations can be written

$$\cos2\lambda_1 = \mu(\sin2\lambda_1 - 2\sin\phi' + 1)$$

or

$$\sin\phi' = \frac{1}{2}\left(\sin2\lambda_1 + 1 - \frac{\cos2\lambda_1}{\mu}\right)$$

ψ_x	β	μ_{max_1}	μ_{max_2}	μ	λ_1	λ_2'	α_1	α_2	γ_1	γ_2	$\frac{P}{b\delta_V k}$	$\frac{W}{b\delta_V k}$	$\frac{d_1}{\delta_V}$
0°	15°	0.344	0.344	0.169	31.77°	31.77°	21.24°	21.24°	6.994°	6.994°	2.716	0	1.467
	22.5°	0.320	0.320	0.169	30.49°	30.49°	28.53°	28.53°	8.475°	8.475°	4.156	0	1.637
	30°	0.297	0.297	0.169	28.99°	28.99°	36.94°	36.94°	9.068°	9.068°	6.044	0	1.843
	45°	0.257	0.257	0.169	25.42°	25.42°	56.19°	56.19°	8.395°	8.395°	11.87	0	2.453
15°	15°	0.422	0.290	0.169	35.11°	28.29°	1.760°	40.80°	8.130°	5.905°	2.777	1.801	1.336
	22.5°	0.389	0.272	0.169	34.00°	26.81°	8.291°	48.83°	10.21°	6.857°	4.315	2.185	1.445
	30°	0.358	0.254	0.169	32.68°	25.09°	15.99°	57.90°	11.33°	7.008°	6.399	2.649	1.571
	45°	0.303	0.223	0.169	29.49°	20.95°	34.16°	78.39°	11.35°	5.659°	13.41	3.986	1.906
30°	15°	0.545	0.250	0.169	38.35°	24.57°	-	60.58°	9.466°	4.846°	2.999	3.778	1.226
	22.5°	0.662	0.236	0.169	37.43°	22.81°	-	69.44°	12.19°	5.252°	4.902	4.767	1.289
	30°	0.448	0.222	0.169	36.29	20.75°	-	79.33°	13.95°	4.922°	7.785	6.106	1.361
	45°	0.370	0.196	0.169	33.42°	15.61°	11.68°	101.5°	14.90°	2.921°	21.64	11.81	1.543
45°	15°	0.771	0.220	0.169	41.19°	20.41°	-	80.91°	10.91°	3.682°	3.573	6.268	1.132
	22.5°	0.680	0.266	0.169	40.58°	18.21°	-	90.75°	14.56°	3.540°	6.582	8.806	1.162
	30°	0.601	0.196	0.169	39.75°	15.54°	-	101.7°	17.15°	2.717°	12.69	13.50	1.192
	45°	-	-	-	-	-	-	-	-	-	-	-	-
60°	15°	1.00	0.195	0.169	43.33°	15.38°	-	102.4°	12.44°	2.253°	5.379	11.10	1.059
	22.5°	1.00	0.185	0.169	43.03°	12.19°	-	113.9°	17.18°	1.385°	15.18	23.48	1.059
	30°	-	-	-	-	-	-	-	-	-	-	-	-
	45°	-	-	-	-	-	-	-	-	-	-	-	-

Table 1 Frictional/Lip Slip Line Field Solution for Infinite Wedge, $\epsilon = 0$

Substitution of (20) gives

$$\sin(\psi_x - \beta - \frac{\pi}{4} + \gamma_1 + \lambda) = \frac{1}{2}\left(\sin 2\lambda_1 + 1 - \frac{\cos 2\lambda_1}{\mu}\right) \tag{21}$$

The solution is obtained in the same manner as before if (21) is substituted for the first relationship of (13) above. The value of friction coefficient to be used in the analysis is in no case greater than the friction coefficient necessary for a rough wedge, as calculated from the results of the rough wedge analysis (Appendix A). Table 1 is the result of calculations made with a programmable desk top calculator for the case of $\mu = 0.169$ (experimentally determined) and $\varepsilon = 0$.

Plane Strain Solution for Actual Wedge

The actual wedge indentation solution assumes plane plastic flow on all sides of the wedge. This assumption may appear dubious for the ends of the wedge on first consideration. Deviation from plane plastic flow is due to shear forces of the surrounding medium during flow. Since no material is displaced by the vertical faces on the ends of the wedge, no plastic flow takes place and there are no forces causing a deviation from plane plastic flow. The assumption is a correct analysis for the ends of the wedge whereas for the plastic flow on the sides of the wedge it is only an approximation to actual behavior.

The geometry and nomenclature of the problem is shown in Figures 25 - 30. From the previous solution of the plane strain problem for the infinite wedge and $\psi_y = 0$, the following definitions will be made.

$$g_1(\beta, \psi_x) \equiv \frac{P}{b\delta_V k} \qquad g_2 = (\beta, \psi_x) \equiv \frac{W}{b\delta_V k}$$

$$\tau_o(\psi_y) \equiv \tau_{OE}(\psi_x)\Big|_{\substack{\beta = 0 \\ \psi_x = \psi_y}} \qquad \tau_b(\psi_y) \equiv \tau_{OA}(\psi_x)\Big|_{\substack{\beta = 0 \\ \psi_x = \psi_y}}$$

$$\sigma_o(\psi_y) \equiv \sigma_{OE}(\psi_x)\Big|_{\substack{\beta = 0 \\ \psi_x = \psi_y}} \qquad \sigma_b(\psi_y) \equiv \sigma_{OA}(\psi_x)\Big|_{\substack{\beta = 0 \\ \psi_x = \psi_y}}$$

Calculated values of τ_o, τ_b, σ_o, σ_b are given in Table 2. As is indicated in Figure 27 an integration of the plane strain functions g_1 and g_2 along the wedge is conducted to determine the forces F_z' and F_x.

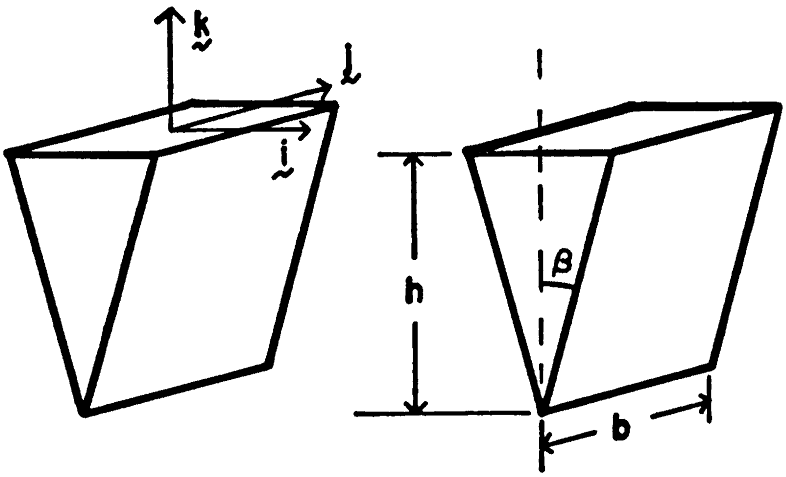

Figure 25 Wedge Nomenclature

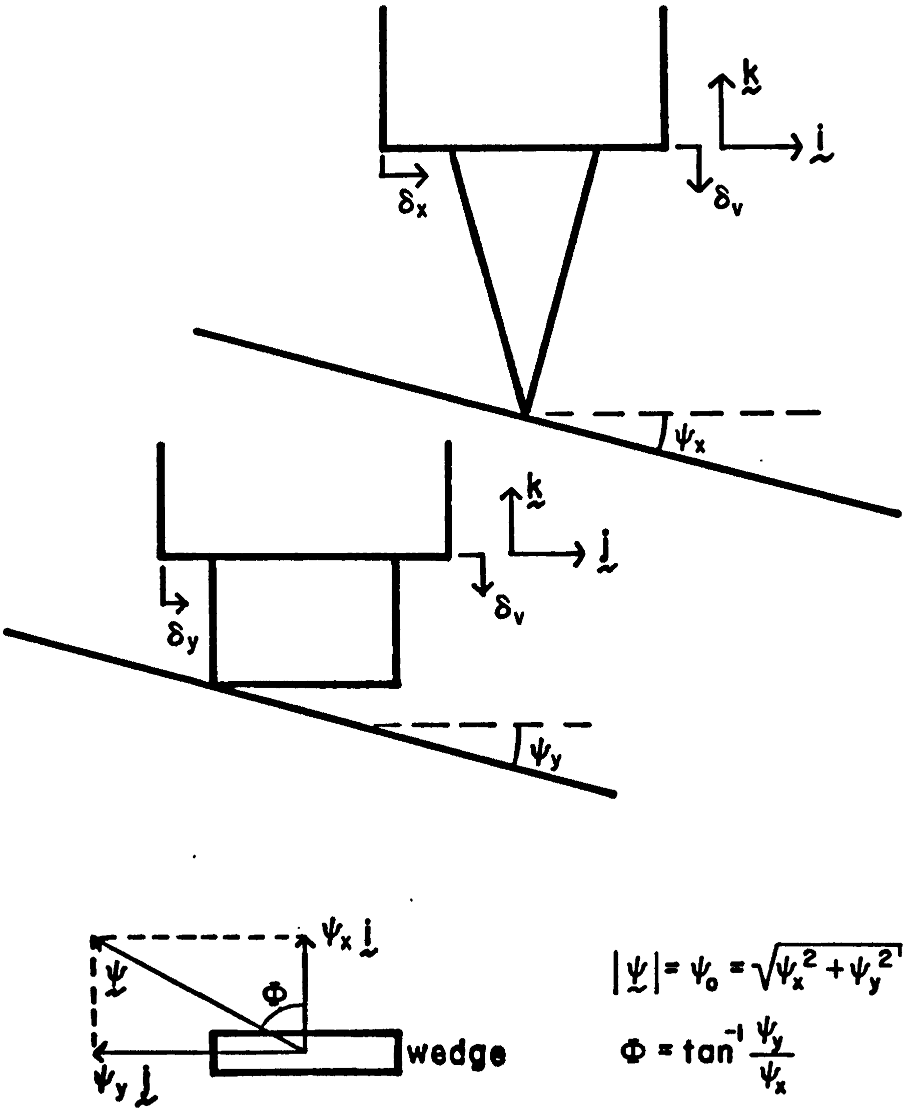

Figure 26 Inclination Nomenclature

ψ_y	λ_1	λ_2	$\frac{\tau_o}{k}$	$\frac{\tau_b}{k}$	$\frac{\sigma_o}{k}$	$\frac{\sigma_b}{k}$
0	33.44°	33.44°	0.3927	0.3927	2.323	2.323
5	34.47°	32.40°	0.4258	0.3593	2.519	2.126
10	35.49°	31.35°	0.4586	0.3259	2.714	1.928
15	36.50°	30.28°	0.4915	0.2924	2.908	1.730
20	37.49°	29.19°	0.5243	0.2592	3.102	1.533
25	38.45°	28.09°	0.5566	0.2267	3.293	1.341
30	39.37°	26.96°	0.5889	0.1953	3.485	1.155
35	40.24°	25.80°	0.6211	0.1654	3.675	0.9787
40	41.05°	24.61°	0.6532	0.1374	3.865	0.8133
45	41.79°	23.38°	0.6851	0.1118	4.054	0.6616
50	42.47°	22.10°	0.7169	0.08820	4.242	0.5219
55	43.07°	20.77°	0.7485	0.06732	4.429	0.3983

Table 2 Frictional/Lip Slip Line Field Solution for Wedge End Stresses

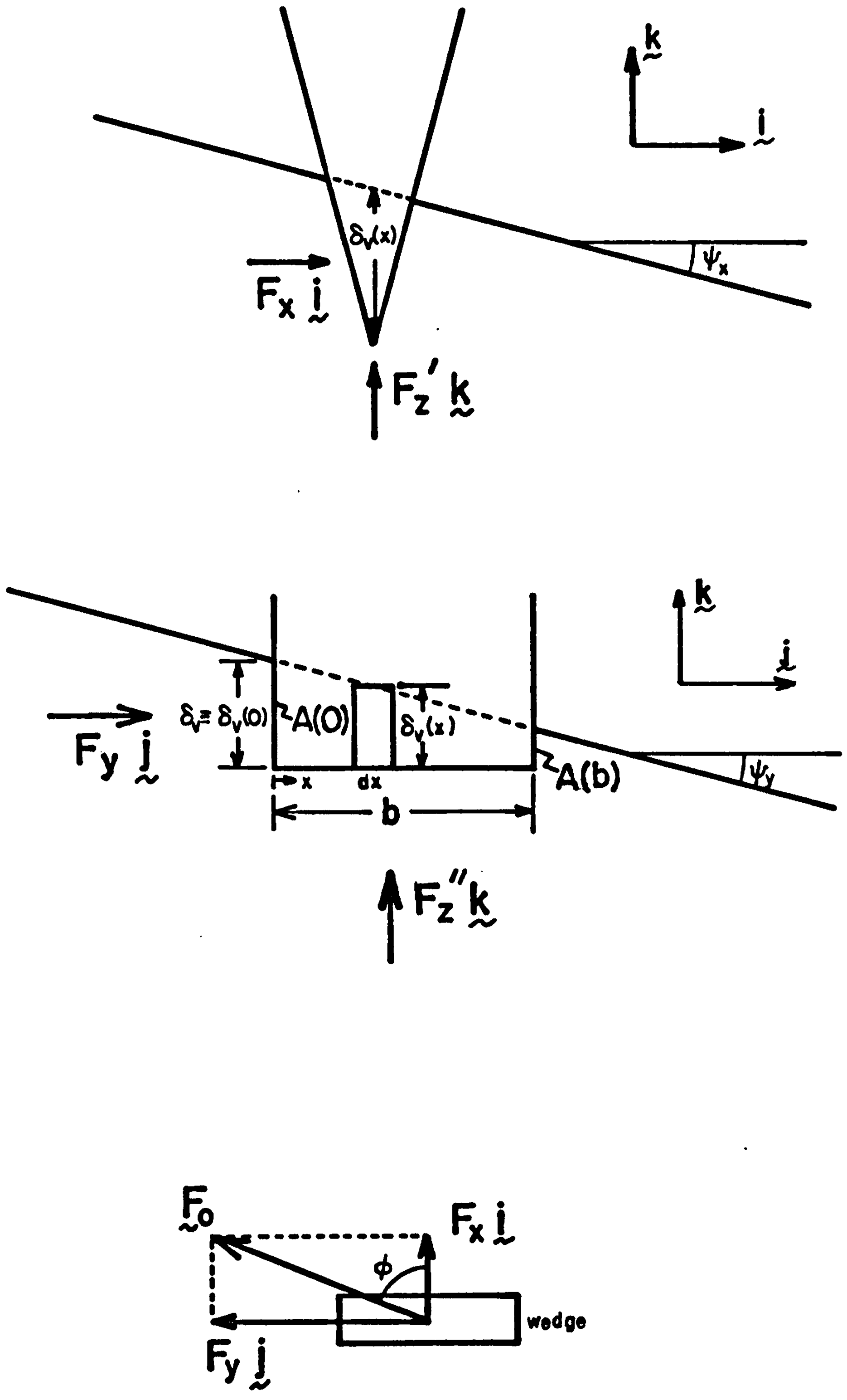

Figure 27 Nomenclature for Forces of Medium on Wedge

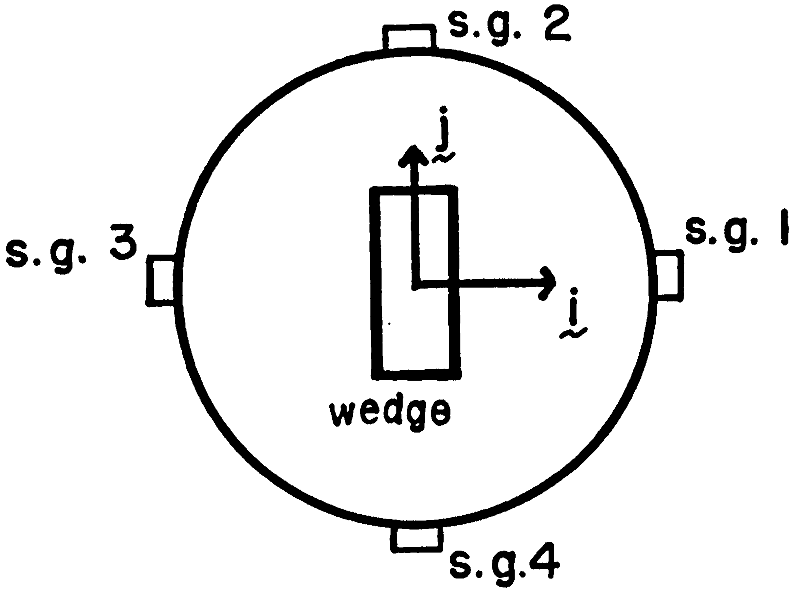

STRAIN READINGS

ϵ_{mn} caused by force in $m \rightarrow n$ direction as per numbering of strain gages

$\epsilon_{31} \Rightarrow \underset{\sim}{i}$

$\epsilon_{42} \Rightarrow \underset{\sim}{j}$

Figure 28 Load Cell Placement of Strain Gages, Readings

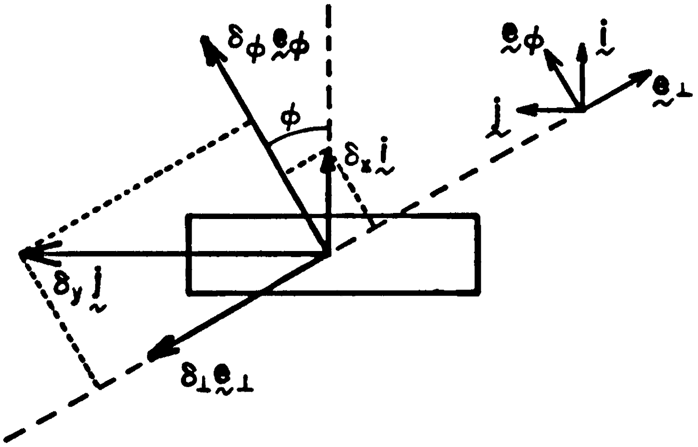

Figure 29 Horizontal Deflection Nomenclature

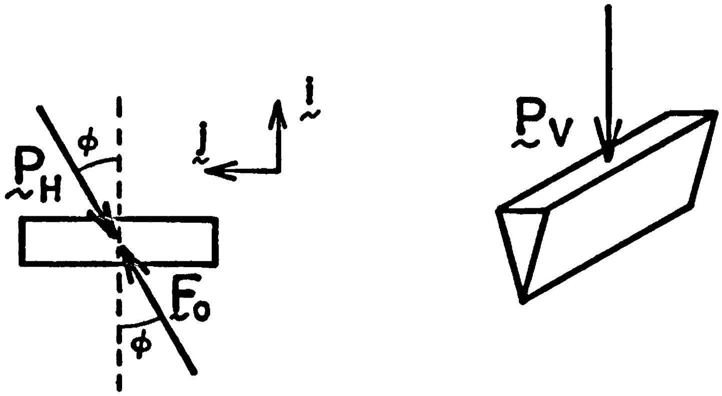

Figure 30 Applied Forces Nomenclature

$$dF_z' = kg_1(\beta,\ \psi_x)\delta_V(x)dx$$

$$F_z' = kg_1(\beta,\psi_x) \int_0^b \delta_V(x)dx$$

$$\delta_V(x) = \begin{bmatrix} \delta_V(0) - x\tan\psi_y & x \leq \delta_V(0)\cot\psi_y \\ 0 & x \geq \delta_V(0)\cot\psi_y \end{bmatrix}$$

The integration yields the following result for $\delta_V(0) \leq b\tan\psi_y$

$$\frac{F_z'}{\delta_V^2} = \tfrac{1}{2}\, kg_1(\beta,\ \psi_x)\cot\psi_y$$

$$\frac{F_x}{\delta_V^2} = \tfrac{1}{2}\, kg_2(\beta,\ \psi_x)\cot\psi_y \tag{22}$$

For $\delta_V(0) \geq b\tan\psi_y$,

$$F_z' = bkg_1(\beta,\psi_x)[\delta_V - \tfrac{1}{2}b\tan\psi_y]$$

$$F_x = bkg_2(\beta,\ \psi_x)[\delta_V - \tfrac{1}{2}b\tan\psi_y] \tag{23}$$

The cross-sectional indented areas of the ends of the wedge are calculated by inspection of the physical plane diagram for the plane plastic strain of the infinite wedge (Figure 18).

$$A(x) = \tfrac{1}{2}\cos^2\psi_x[\tan(\beta - \psi_x) + \tan(\beta + \psi_x)] \tag{24}$$

Knowing the state of stress on the ends of the wedge the forces F_z'' and F_y may readily be calculated.

$$F_z'' = \tau_o A(0) + \tau_b(b)$$

$$F_y = \sigma_o A(0) - \sigma_b A(b)$$

Substitution of (24) gives

$$F_z'' = \tfrac{1}{2}\cos^2\psi_x[\tan(\beta - \psi_x) + \tan(\beta + \psi_x)][\tau_o\delta_V(0)^2 + \tau_b\delta_V(b)^2]$$

$$F_y = \tfrac{1}{2}\cos^2\psi_x[\tan(\beta - \psi_x) + \tan(\beta + \psi_x)][\sigma_o\delta_V(0)^2 - \sigma_b\delta_V(b)^2]$$

For $\delta_V(0) \leq b\tan\psi_y$, $\delta_V(b) = 0$ and

$$\frac{F_z''}{\delta_V^{\,2}} = \tfrac{1}{2}\cos^2\psi_x[\tan(\beta - \psi_x) + \tan(\beta + \psi_x)]\; k\left(\frac{\tau_o}{k}\right)$$

$$\frac{F_y}{\delta_V^{\,2}} = \tfrac{1}{2}\cos^2\psi_x[\tan(\beta - \psi_x) + \tan(\beta + \psi_x)]\; k\left(\frac{\sigma_o}{k}\right) \tag{25}$$

For $\delta_V(0) \geq b\tan\psi_y$, $\delta_V(b) = \delta_V(0) - b\tan\psi_y$ and

$$F_z'' = \tfrac{1}{2}\cos^2\psi_x[\tan(\beta - \psi_x) + \tan(\beta + \psi_x)]\left[\left(\frac{\tau_o}{k} + \frac{\tau_b}{k}\right) k\,\delta_V^{\,2} - 2bk\left(\frac{\tau_b}{k}\right) \times \times\,(\tan\psi_y)\delta_V + b^2k\left(\frac{\tau_b}{k}\right)\tan^2\psi_y\right]$$

$$F_y = \tfrac{1}{2}\cos^2\psi_x[\tan(\beta - \psi_x) + \tan(\beta + \psi_x)]\left[\left(\frac{\sigma_o}{k} - \frac{\sigma_b}{k}\right) k\,\delta_V^{\,2} + 2bk\left(\frac{\sigma_b}{k}\right) \times \times\,(\tan\psi_y)\delta_V - b^2k\left(\frac{\sigma_b}{k}\right)\tan^2\psi_y\right] \tag{26}$$

The results of these calculations, (22), (23), (25), and (26) are then combined in the form necessary for correlation with experiment.

$$F_z = F_z' + F_z'' \qquad \phi = \tan^{-1}\left(\frac{F_y}{F_x}\right)$$

$$F_o = \sqrt{F_x^{\,2} + F_y^{\,2}}$$

These forces are the reaction of the medium on the wedge. The experiment measures forces which are applied to the wedge by external sources, such that $P_V = F_z$ and $P_H = F_o$ (Figure 30). It is necessary to know the angle ϕ so that the one horizontal force may correctly balance the forces $\underset{\sim}{F}_x$, and $\underset{\sim}{F}_y$.

Adjustments for True Upper Bound

It has been mentioned that these calculations constitute a true upper bound for P_H, but not for P_V (Figure 31). The power dissipation on the sides of the plane strain lip ($\overline{ABCDE}$) has not been included in the analysis. Since there is no wedge velocity in the horizontal direction in the model

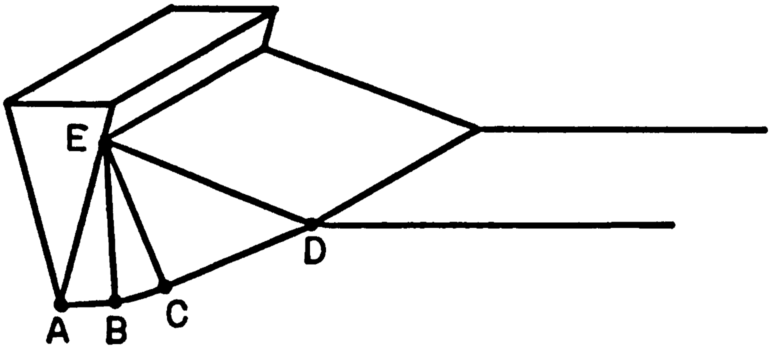

Figure 31 Plane Strain Indentation Geometry

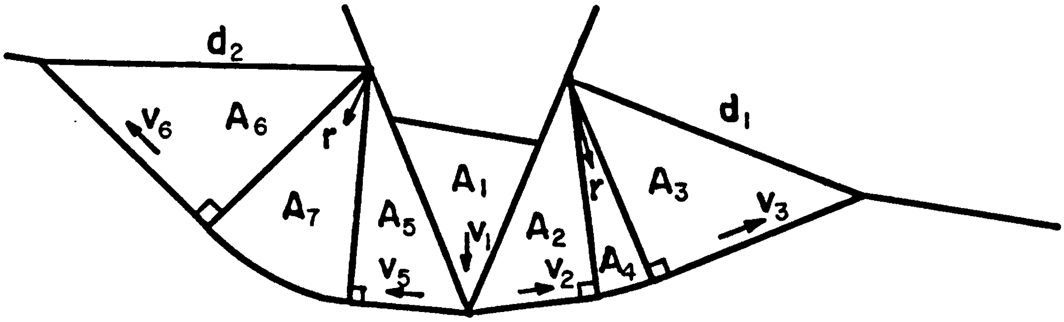

Figure 32 Plane Strain End Effect Geometry

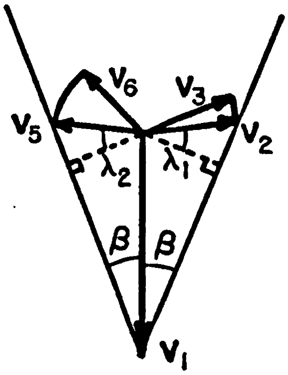

Figure 33 Hodograph for End Effects on Upper Bound

there can be no additional horizontal force due to the power dissipation across $(\overline{ABCDE})$. Therefore, the previous calculations do constitute a correct upper bound for the horizontal force. The additional power dissipation will cause a greater vertical force P_V for a correct upper bound to be obtained.

Consider the plane strain geometry previously determined (Figure 32). The added force is calculated by use of the upper bound principle discussed earlier. The rate of work done by the added force equals the rate of power dissipation by the shearing forces on the plastic flow in the vertical plane on each end of the wedge.

$$P_V{}'v_1 = n\left[eA_1v_1 + A_2v_2 + A_3v_3 + \int_{A_4} v_4 dA + A_5v_5 + A_6v_6 + \int_{A_7} v_7 dA\right]k \qquad (27)$$

$$n = \left[\begin{array}{ll} 2 & \psi_y = 0 \\ 1 & \psi_y \neq 0,\ \delta_V \leq b\tan\psi_y \\ 1 + (1 - \frac{b}{\delta_V}\tan\psi_y)^2 & \psi_y \neq 0,\ \delta_V \geq b\tan\psi_y \end{array}\right.$$

$$e = \left[\begin{array}{ll} 1 & \psi_y = 0 \\ 0 & \psi_y \neq 0 \end{array}\right.$$

n corrects for the differential indentation depth on each end due to ψ_y.

e corrects for the fact that in the actual calculations of P_V, the end effect slip line field was not considered for $\psi_y = 0$.

Normally, e = 0.

The hodograph (Figure 33) results in the following velocity relationships.

$$v_2 = v_3 = v_1 \frac{\sin\beta}{\cos\lambda_1} \qquad v_5 = v_6 = v_1 \frac{\sin\beta}{\cos\lambda_2}$$

In the centered fan regions,

$$v_4 = \frac{r}{d_1/\sqrt{2}}\, v_2 \quad \Rightarrow \quad \int_{A_4} v_4 dA = \frac{1}{6}\alpha_1 d_1{}^2 v_2 = \frac{1}{6}\alpha_1 d_1{}^2 v_1 \frac{\sin\beta}{\cos\lambda_1}$$

$$v_7 = \frac{r}{d_2/\sqrt{2}}\, v_5 \quad \Rightarrow \quad \int_{A_7} v_7 dA = \frac{1}{6}\alpha_2 d_2{}^2 v_5 = \frac{1}{6}\alpha_2 d_2{}^2 v_1 \frac{\sin\beta}{\cos\lambda_2}$$

The areas are determined geometrically,

$$A_1 = \tfrac{1}{2}\,\delta_V{}^2 \tan\beta$$

$$A_2 = \frac{1}{4}\, d_1{}^2 \tan\lambda_1 = \frac{1}{4}\left(\frac{d_1}{\delta_V}\right)^2 \delta_V{}^2 \tan\lambda_1$$

$$A_3 = \frac{1}{4}\, d_1{}^2 = \frac{1}{4}\left(\frac{d_1}{\delta_V}\right)^2 \delta_V{}^2$$

$$A_5 = \frac{1}{4}\left(\frac{d_2}{\delta_V}\right)^2 \delta_V{}^2 \tan\lambda_2$$

$$A_6 = \frac{1}{4}\left(\frac{d_2}{\delta_V}\right)^2 \delta_V{}^2$$

The substitutions are made into (27) to obtain

$$\frac{P_V'}{\delta_V{}^2} = n\left[e\,\frac{\tan\beta}{2} + \left(\frac{d_1}{\delta_V}\right)^2\left(\frac{\tan\lambda_1}{4} + \frac{1}{4} + \frac{\alpha_1}{6}\right)\frac{\sin\beta}{\cos\lambda_1} + \right.$$
$$\left. + \left(\frac{d_2}{\delta_V}\right)^2\left(\frac{\tan\lambda_2}{4} + \frac{1}{4} + \frac{\alpha_2}{6}\right)\frac{\sin\beta}{\cos\lambda_2}\right] k \qquad (28)$$

Several sample curves are shown in the discussion of the experimental results showing the effect of this upper bound adjustment.

The only remaining factor in the theoretical predictions is an error analysis to be discussed later in this report. The numerical results of the theoretical analysis are presented later in graphical form.

Experimental Solution of Isotropic Wedge Indentation

Historical Review of Experiment

The designs and procedures in conducting the experimental study were developed and continually revised over the entire course of the study. For this reason a brief chronological review of the entire study would help to see the experimental results in a true perspective.

An initial problem statement was first formulated and stated:

> Develop and experimentally verify an analysis of loading and deviation forces for wedge indentation into a transversely isotropic medium with arbitrary orientation of principal axes of anisotropy.

The initial phase of development towards the stated goals proceeded roughly as follows:

1. The design first required a loading source and a Riehle 60,000 lb. screw power testing machine was conveniently available.
2. Two general experimental methods were considered.
   a) direct measurement of horizontal forces with some sort of force transducer -- strain gage cell, hydraulic jack,...
   b) measurement of the bending of a load cell mounted in the vertical loading rod, due to horizontal forces

   The latter method (b) was selected for design flexibility and accuracy.
3. The load cell was designed and fabricated to maximize the strain being measured.
4. Plasticity theory was to be applied to predict experimental behavior. The transversely isotropic medium would be a rock substance, ductile only at high pressure.
5. A transversely isotropic sample was constructed by laminating thin slices of a weak and strong medium alternately.
6. Two basic pressure vessel methods were considered. It was undecided whether or not the pressure vessel would enclose the load cell. If so, electrical connections would be designed to preserve high pressure integrity. If the vessel would not en-

> close the load cell, a hydraulic sealing problem would be caused by horizontal flexibility.

It was considered imprudent to attempt high pressure testing until the wedge indentation problem was first studied at atmospheric pressure. The experimental goals were appropriately revised:

> Only atmospheric tests would be conducted. An isotropic, ductile substance will be utilized as the indentation medium, its flat surface inclined at various levels and orientations to model transverse isotropy.

The ensuing development of the project proved the merit of this revision:

7. The loading rod assembly was modified to minimize horizontal flexibility.
8. An attempt was made to assemble continuous output devices -- strain gage bridge networks, X Y recorders,...
9. Lead was chosen as the experimental medium.
10. Tests conducted revealed time dependent strength properties of lead. The lead exhibited rapid "relaxation" rates under load. When loaded the lead would not reach a state of equilibrium for an extended period of time, causing continuous, dynamic tests to be impractical. The data would of necessity simply be observed and recorded by the observer.
11. A 5% antimonial lead (Pb - Sb) was selected as the indentation medium to minimize "relaxation" effects.
12. Load cell calibration tests, Pb-Sb mechanical strength compression tests, and steel - lead friction tests were conducted.
13. Tests for which $\psi_x = \psi_y = 0$ were conducted successfully.
14. Tests for which $\psi_y = 0$, $\psi_x \neq 0$ failed because the horizontal flexibility of the loading rod assembly was too great.
15. Equipment was designed and fabricated to apply a horizontal force directly and force the wedge to travel vertically. (Note, both experimental methods above, 2a, 2b were eventually employed).
16. The remaining tests were conducted successfully.

The theoretical analysis was developed gradually throughout all stages of the experiment. Certain end effect revisions were made in the upper bound analysis after a detailed error analysis had been completed. Rather than completely rework the error analysis the effect of these revisions is simply demonstrated for a number of cases.

The basic indentation test design is shown in Figure 34 and the detailed design and stress analysis of components is presented in Appendix B. To facilitate discussion of the actual indentation test, the procedures and results of the load cell and hydraulic jack calibrations, and the lead-steel friction tests are presented in Appendix C. Before the actual wedge indentation tests may be discussed, the important preliminary study of Pb-Sb compressive strength properties is presented.

Compression Tests on 5% Antimonial Lead

A cylindrical specimen of about 1" diameter and 2" long was placed in the Riehle testing machine between two flat steel plates and loaded in compression (Figure 35). For each datum point the loading was stopped and readings taken of load (L), diameter of sample (D), and deflection (δ).

Antimonial lead is quite ductile, but also exhibits a marked time - dependent compressive strength. After the loading is ceased the deflection remains constant, but the load will decrease, rapidly at first and slowing with time. The possible effect of relaxation on the wedge indentation slip line field is depicted in Figure 36. It was desired for the purposes of the wedge indentation tests to eliminate or at least minimize this time dependency, so load readings were taken for various "relaxation" times, for example, at $t = 0, \frac{1}{4}, \frac{1}{2}, 1, 2, \ldots$ minutes. The strength value of interest was determined by the load after the most rapid relaxation had taken place.

The diameter changed for each increasing load, the frictional end conditions causing the sample to bulge. The change during relaxation was too small to be measured.

It was desired to characterize this material as rigid - perfectly plastic to be able to apply plasticity theory to the indentation problem, so the data was analyzed in the form of a stress - strain curve. Diameter readings were recorded for each load at the sample midpoint, where the diameter was a maximum and stress a minimum. The strain measurement was of minimal importance in determining the compressive strength, so the true stress at the sample midpoint (σ) was just plotted vs. the deflection (δ).

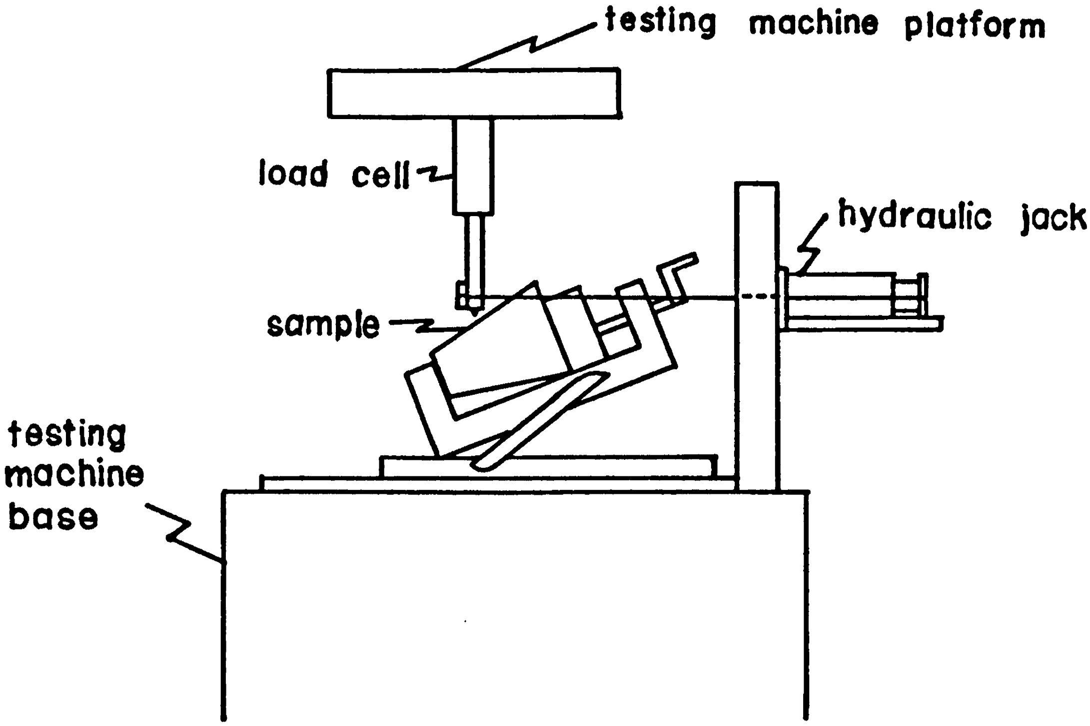

Figure 34 General Experimental Set-Up

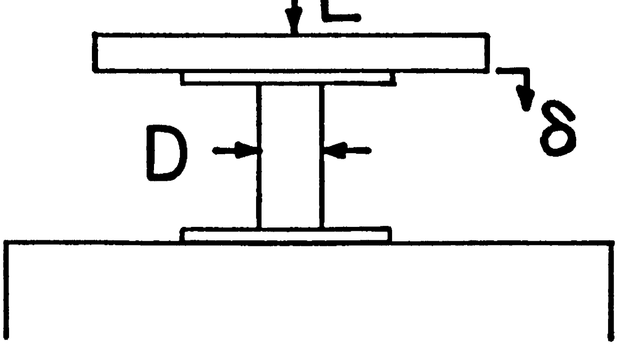

Figure 35 Compressive Strength Test Set-Up

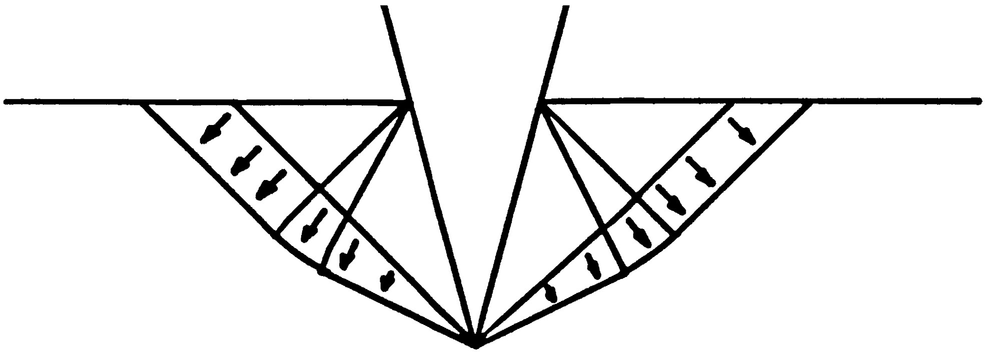

Figure 36 Hypothetical Plastic Flow During Relaxation

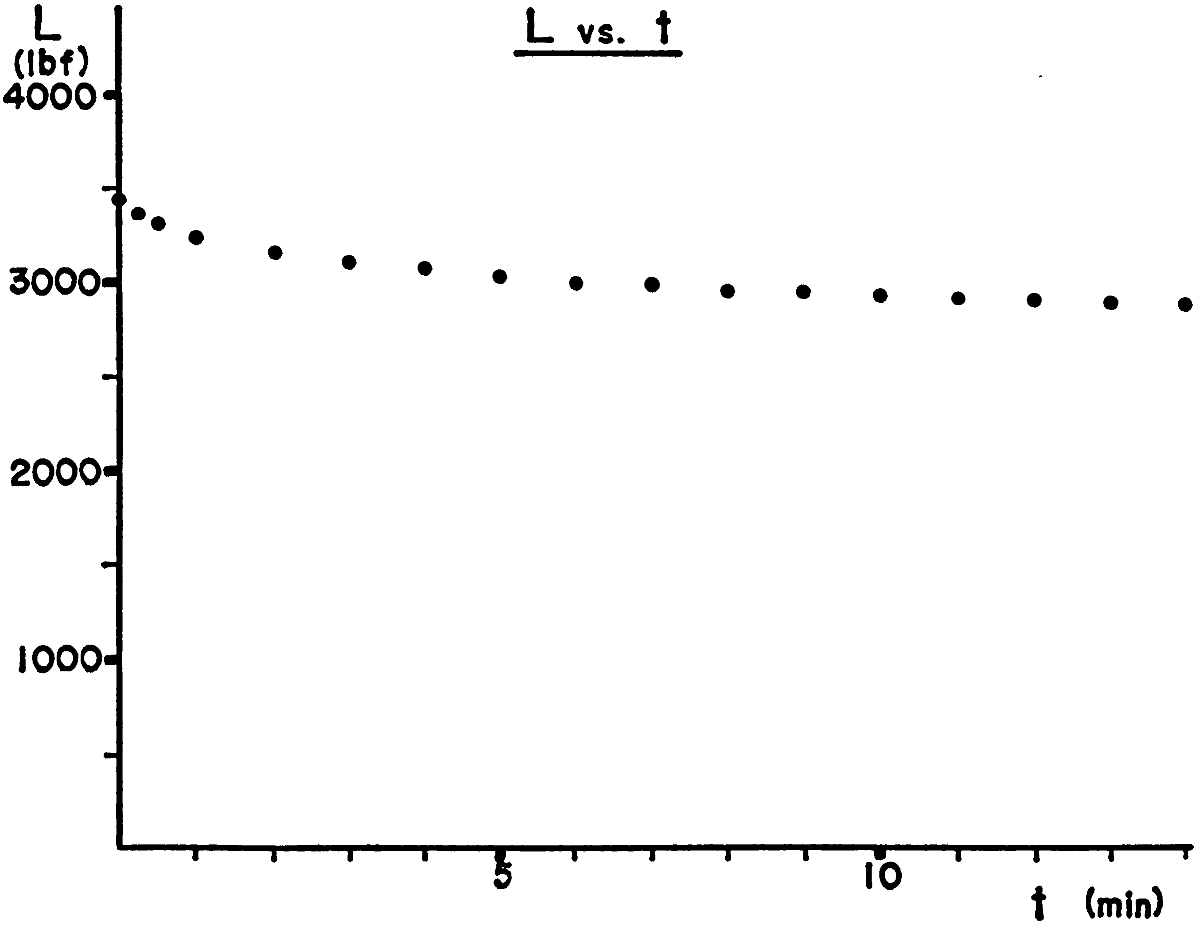

Figure 37 Sample Relaxation Curve for Compression Tests (Test 12,δ=0.5")

Three tests were recorded, over different ranges of deflection, and plotted on the same graph.

The test specimen was made by melting a portion of the indentation test ingot and pouring into a thin cylindrical aluminum mold. The samples were not perfectly circular in cross section, so the diameter measurements were actually averages. This inherent uncertainty, plus the uncertainty of correlating the time - dependent compression test with the time - dependent wedge indentation test required a rather liberal uncertainty to be assigned to the results of the compression test, ± 20%.

Preliminary compression tests with relaxation times up to ninety minutes revealed that there is still perceptible relaxation after ninety minutes, but that all of the most rapid relaxation takes place during the first two minutes (Figure 37). An effort was made mathematically to determine from a typical test such as this the load as $t \to \infty$, thus to eliminate all relaxation effects (Appendix C).

A satisfactory means of determining a compressive strength value independent of time-dependent "relaxation" effects was not found. For this reason and for the sake of convenience the compression test stress - strain curve is plotted for load readings $t = 3$ minutes, and is used to estimate a rigid - perfectly plastic compressive strength in wedge indentation tests for which loads are again recorded at $t = 3$ minutes. The results of three compression tests are plotted with stress values shown for both $t = 0$ and $t = 3$ minutes (Figure 38). A compressive strength (σ_y) with a tolerance of 20% is estimated to be $\sigma_y = 9500$ psi. Using the von Mises yield condition, $J_2 = k^2$, $k = \frac{\sigma_y}{\sqrt{3}}$. The result of the compression tests to be applied to the wedge indentation test is then,

$$k = 5500 \pm 1100 \text{psi}$$

Wedge Indentation Tests

The actual experimental wedge indentation tests were conducted, recorded, and analyzed according to the following procedure.

A steel wedge was forced vertically into an inclined, flat lead (Pb - Sb) surface, and vertical and horizontal forces measured at various depths of indentation. Three parameters were varied in conducting the tests -- wedge angle (2β), and two inclination angles (ψ_x, ψ_y) as shown in Figure 26 . Four wedge angles were available ($\beta = 15^\circ$, 22.5° , 30° ,

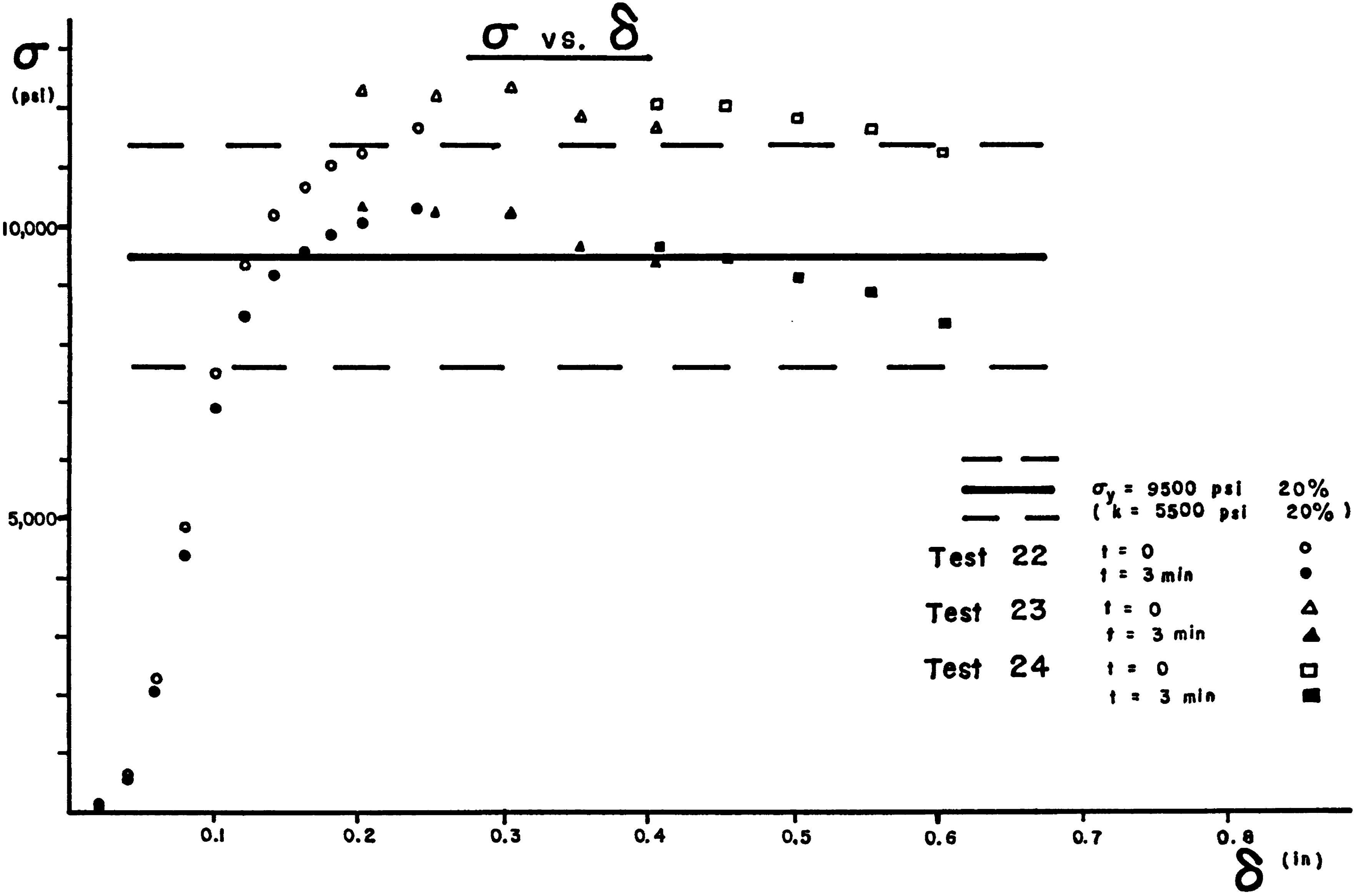

Figure 38 Compressive Strength Curve and Resultant Simplification of Perfectly Plastic Yield

45°) and the tests were run in basically three series. The first tests were for zero inclination ($\psi_x = \psi_y = 0$). The second series consisted of two dimensional inclination tests ($\psi_y = 0$) and the last series were for arbitrary inclinations with $\psi_y \neq 0$.

The hydraulic jack assembly was not used for the case of zero inclination of the lead surface. The jack assembly was deemed necessary for non-zero inclination tests as a means of directly applying a horizontal load to force the wedge to follow a vertical path. Although the design of the loading rod assembly minimized horizontal flexibility, the flexibility was great enough to allow the wedge to slip down slope such that no plastic flow took place on the uphill side of the wedge, thus rendering plasticity theory inapplicable.

To conduct a typical zero inclination test the wedge was first lowered by the loading mechanism until the wedge just touched the lead surface. A dial indicator measuring vertical deflection (δ_V) was then set at zero before beginning the test. The wedge was loaded until a certain deflection was reached (0.02", for example), and the testing machine was then stopped. Vertical force readings (P_V) were made from the loading machine gauge and recorded for "relaxation" times of t = 0, ¼, ½, 1, 2, and 3 minutes. For maximum reliability of the compressive strength measured earlier, the loading speed was the same as in the previous compression tests and the force reading for t = 3 minutes was the only reading considered of further interest. Data was recorded for several different indentation depths, not exceeding 0.1", limiting depth for maximum reliability of the two dimensional plasticity theory.

In a typical test for which $\psi_y = 0$ and $\psi_x \neq 0$ the hydraulic jack assembly was used and additional readings recorded for jack pressure (p) and horizontal deflection in the direction opposite to the force of the jack (δ_ϕ). The pressure was adjusted during loading such that there was no horizontal deflection.

To conduct a test for which $\psi_y \neq 0$, a theoretical prediction of the horizontal force direction was first calculated and the sample oriented such that the force of the jack would just balance this horizontal force. An additional horizontal deflection was measured in the direction perpendicular to the jack force direction ($\delta_\perp$).

P_H was determined primarily from pressure readings and the results of the hydraulic jack calibration test, and the load cell was used in all tests to provide an additional indication of horizontal forces. Since the load cell was not the primary means of force measurement, accuracy was of marginal importance. From the calibration tests previously conducted, the approximate relationship between horizontal force and strain reading was, $P_H \cong 0.11\varepsilon$.

The most complex series of tests ($\psi_x \neq 0$, $\psi_y \neq 0$) involved the recording of nine observed quantities (t, P_V, p, x_o, δ_V, δ_ϕ, $\delta_\perp$, ε_{31}, ε_{24}) from which experimental values of P_V, P_H and $\frac{P_H}{P_V}$ were determined and plotted as functions of δ_V. The other tests were just simplifications of this procedure.

The following adjustments to the indentation data were necessary due to experimental errors.

$\delta_V \rightarrow \delta_V + 0.002''$ error in zero setting of gauge

$p \rightarrow 0.95p$ (Tests 49-83) relaxation effect error

$P_H \rightarrow P_H + 0.11\varepsilon$ adjustment due to ε_{24}, ε_{31} readings

$x_o \rightarrow 0.75x_o$ (Tests 25 - 72) estimated average from final reading

Each test conducted in the course of this study (less the load cell and hydraulic jack calibrations) was numbered in chronological order. The results presented in Appendix F are complete, except for the data deletions listed in Appendix E.

For tests where $\psi_y = 0$, an additional data reduction was made. A linear regression analysis on P_V vs. δ_V (and P_H vs. δ_V) gave an average slope $m_V(m_H)$. The non - dimensional quantity $\frac{m_v}{bk}$ $\frac{m_H}{bk}$ was plotted. β or ψ_x and compared with theoretical results for $\frac{P_V}{b\delta_V k} \left(\frac{P_H}{b\delta_V k}\right)$.

A complete listing of the sources of error in this study is given in Appendix D. In general, the greatest portion of experimental error was the 20% uncertainty in the compressive strength of the lead medium. This uncertainty was quite difficult to estimate and the result of 20% arguable. The complete error analysis resulted in toleration limits for both theoretical and experimental values. These error limits should be interpreted in light of the above difficulties.

The analysis of test results consists of a graphical comparison of experimental data points with theoretical prediction curves. The complete series of force -deflection results is presented in Appendix F.

Discussion of Experimental and Theoretical Results

The initial zero inclination test results are first presented as a plot of $\frac{P_V}{b\delta_V k}$ vs. β without an error analysis shown (Figure 39). Each solid line corresponds to a theoretical prediction based on a particular set of assumptions and resulting plane strain slip line field. The actual details of the theoretical analyses in addition to the friction/lip analysis presented earlier are found in Appendix A. Although these curves are not valid upper bounds for the corresponding assumptions used in the analyses, for the present purpose the curves may be considered upper bound predictions. It is estimated on inspection that the smooth wedge analyses will not yield a satisfactory upper bound. The two frictional wedge predictions are experimental (not analytically true) upper bounds and give closer predictions than the rough wedge analyses. The frictional wedge with lip formation assumption was selected over the assumption of no lip formation for the remaining predictions, simply because it is a more correct analysis of actual behavior and it gives a kinematically admissible velocity field for determination of a true upper bound.

The results to follow and those presented in Appendix F demonstrate that the frictional analysis without lip formation is perhaps a closer prediction of actual behavior. This may be explained as reflecting two offsetting tendencies for error. It is readily noticed that the difference between the two frictional analyses increases with greater wedge angle. The two analyses will also have diverging predictions on the force - deflection curves due to the differing predictions of $\frac{P_V}{b\delta_V k}$. The "F/L" prediction will always be greater than the "F" prediction. From a perspective directly above the indentation the geometry for both the plane strain plastic flow and the actual observed plastic flow is depicted in Figure 53. The deviation from the plane strain prediction of the horizontal and vertical forces due to the actual non - plane strain plastic flow around the wedge increases with indentation depth and with wedge angle. The plane strain analysis will always predict larger loads than are actually observed. If a frictional, no lip analysis is conducted the discrepancies due to the actual lip formation and the actual non - plane strain plastic flow tend to

KEY FOR ALL GRAPHS

UNITS δ_V — in

P_V, P_H — lbf

THEORETICAL CURVE	———
LIMIT TO THEORETICAL PREDICTION UNCERTAINTY	— —
EXPERIMENTAL DATA	• ×
EXPERIMENTAL ERROR LIMITS	□
TRUE UPPER BOUND CORRECTION	· · · · · ·

Chart 1 Interpretation Key for Experimental Graphs

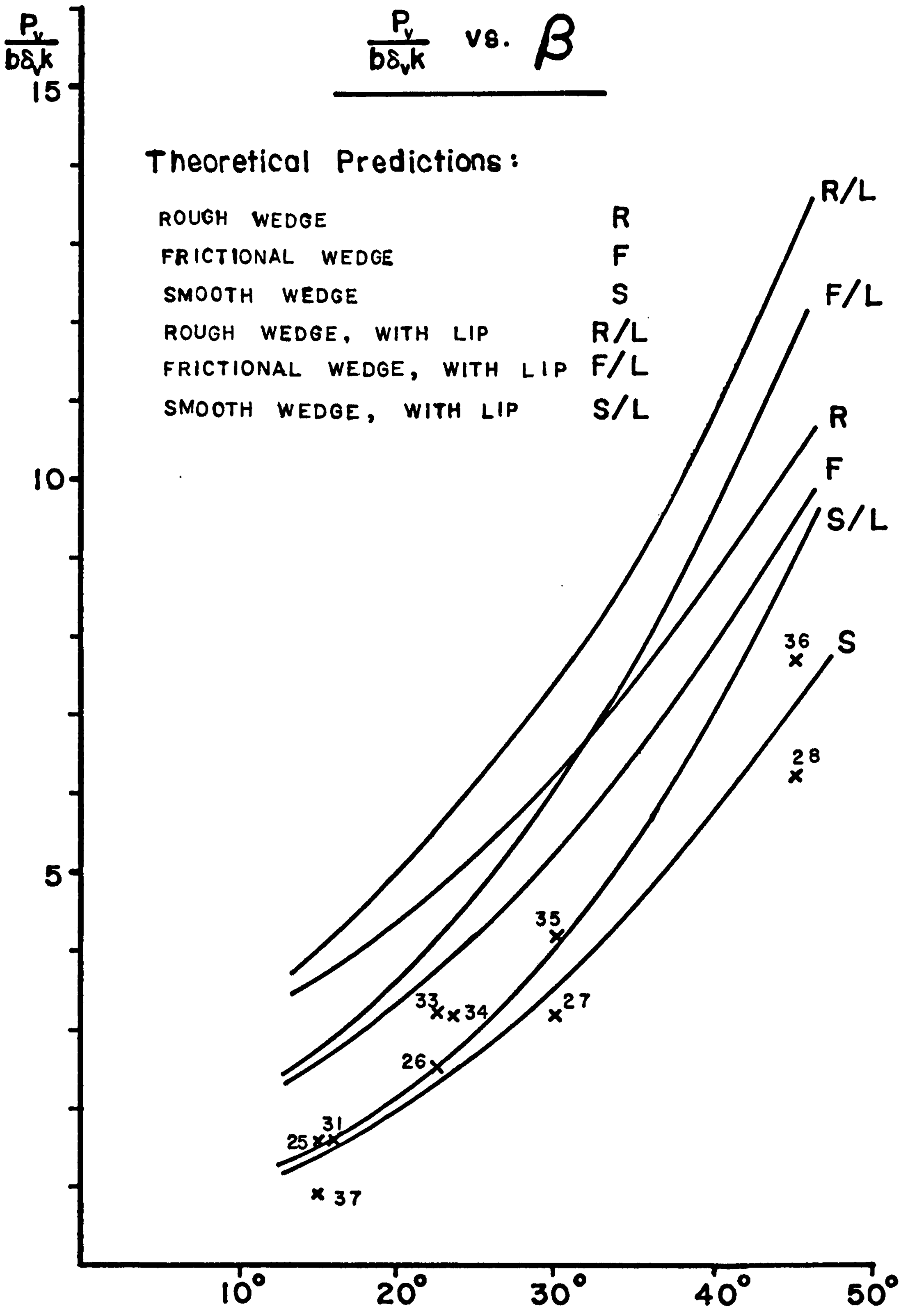

Figure 39 Experimental and Theoretical Results for $\psi_x = \psi_y = 0$ (Tests 25-37)

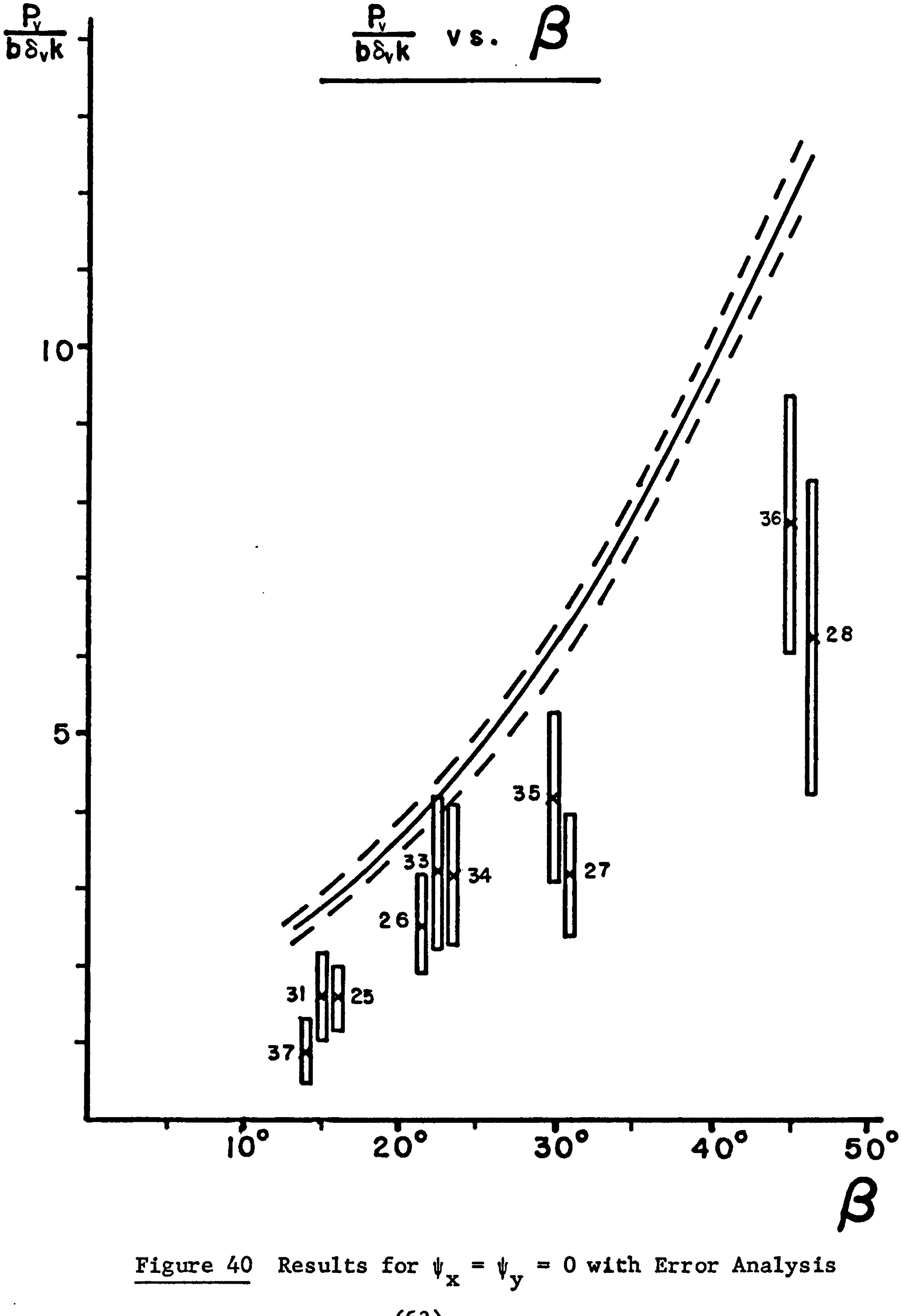

Figure 40 Results for $\psi_x = \psi_y = 0$ with Error Analysis

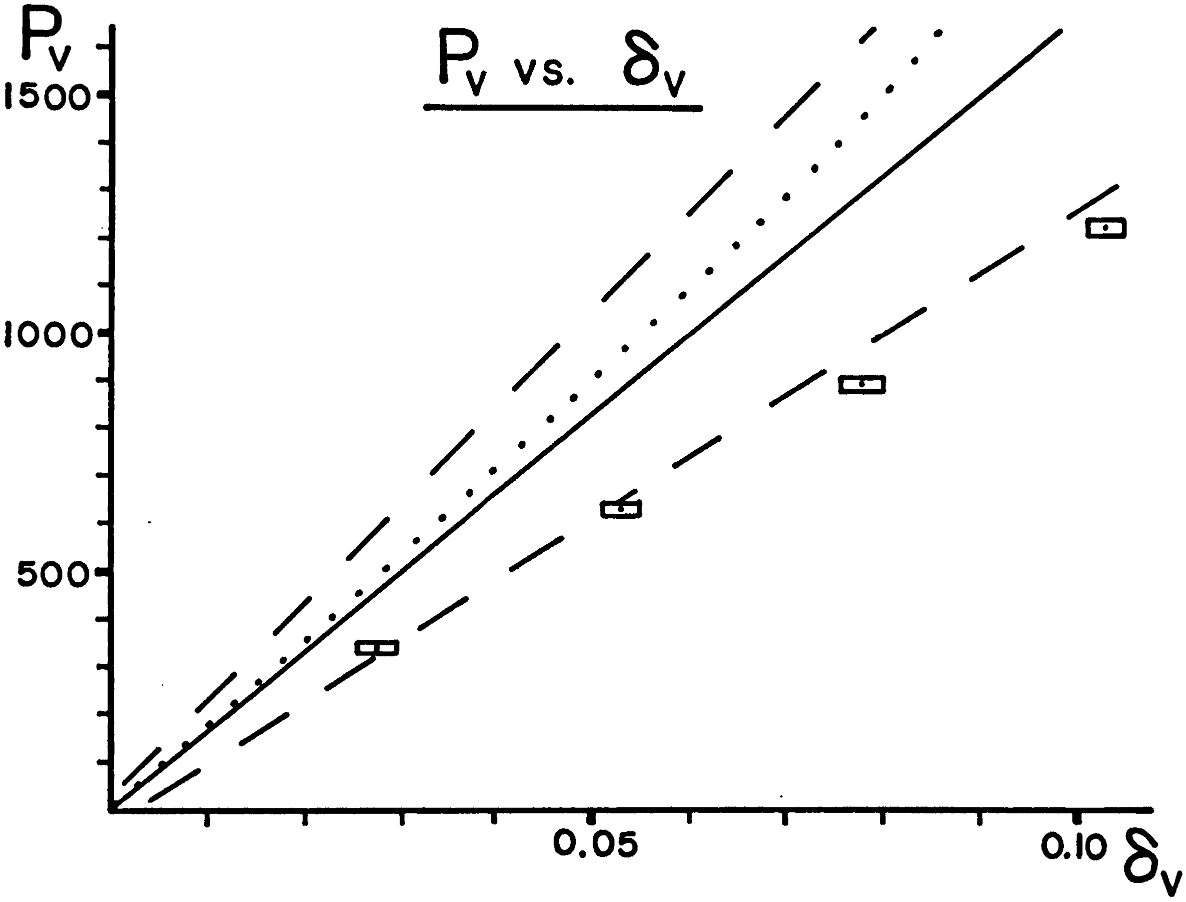

Figure 41 Force Deflection Results, $\beta = 30^{\circ}$, $\psi_x = \psi_5 = 0$ (Test 35)

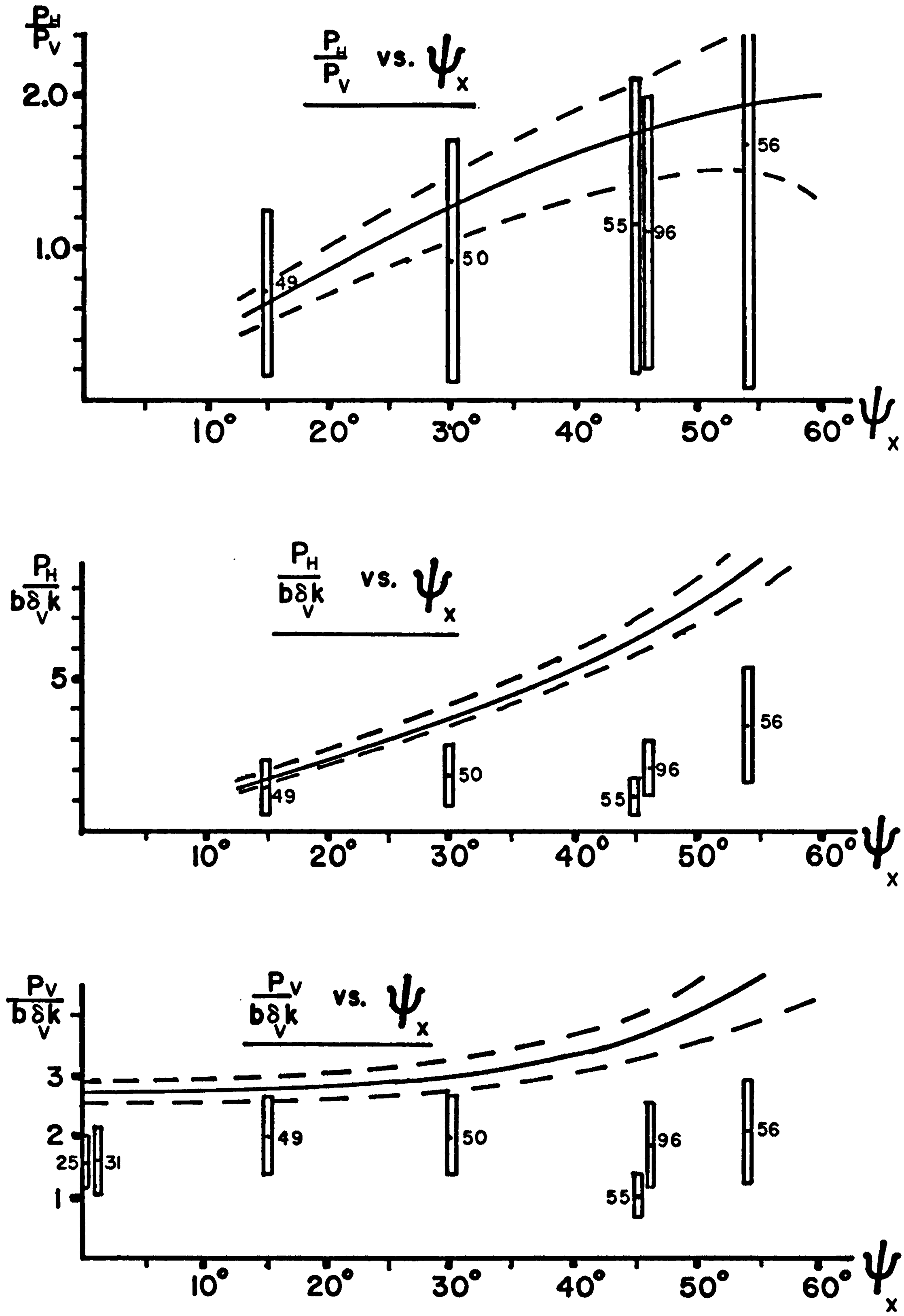

Figure 42 Experimental Results, $\beta = 15^\circ$, $\psi_y = 0$ (Tests 25,31,49,50,55, 56,95)

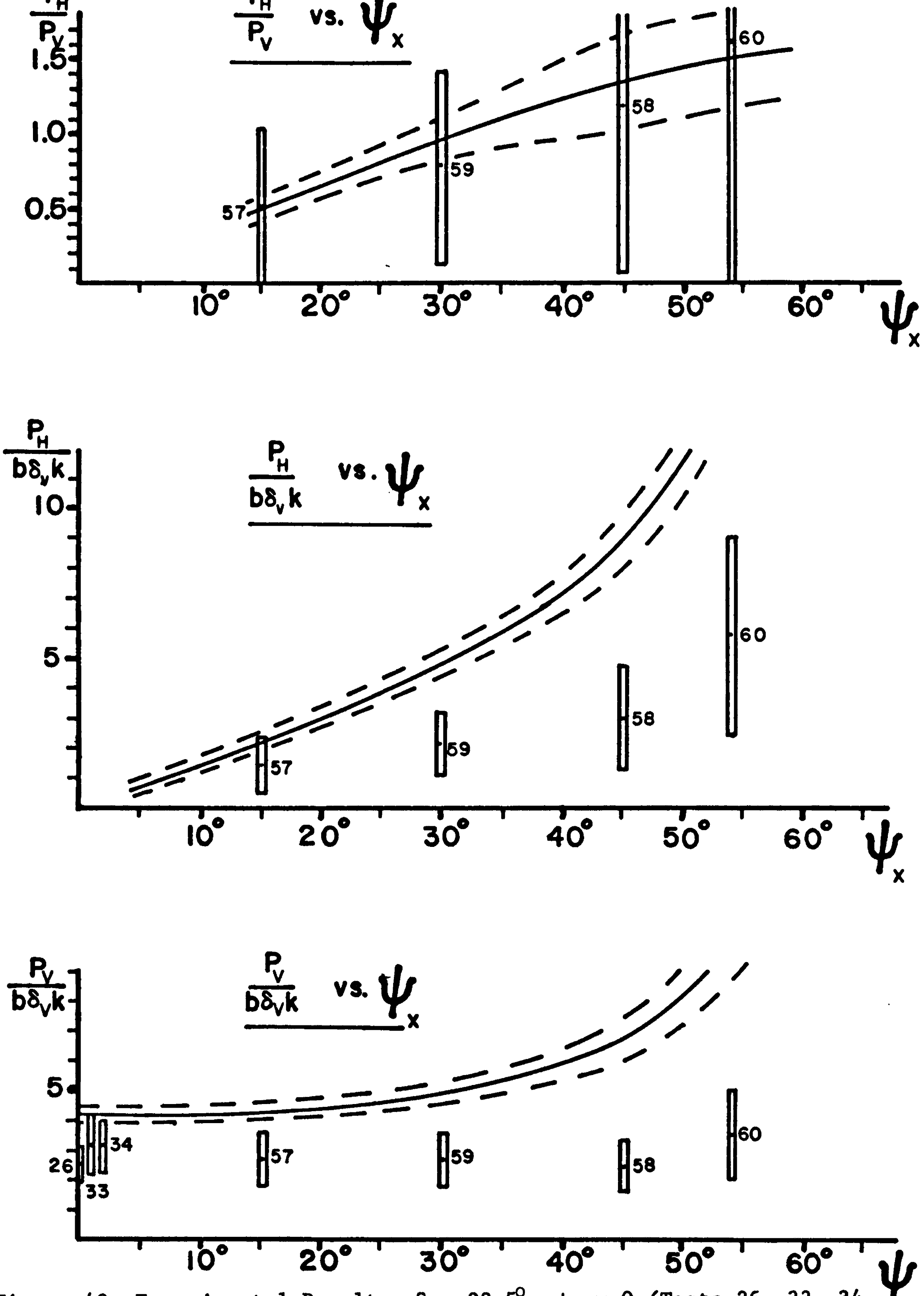

Figure 43 Experimental Results, $\beta = 22.5^\circ$, $\psi_y = 0$ (Tests 26, 33, 34, 57, 58, 59, 60)

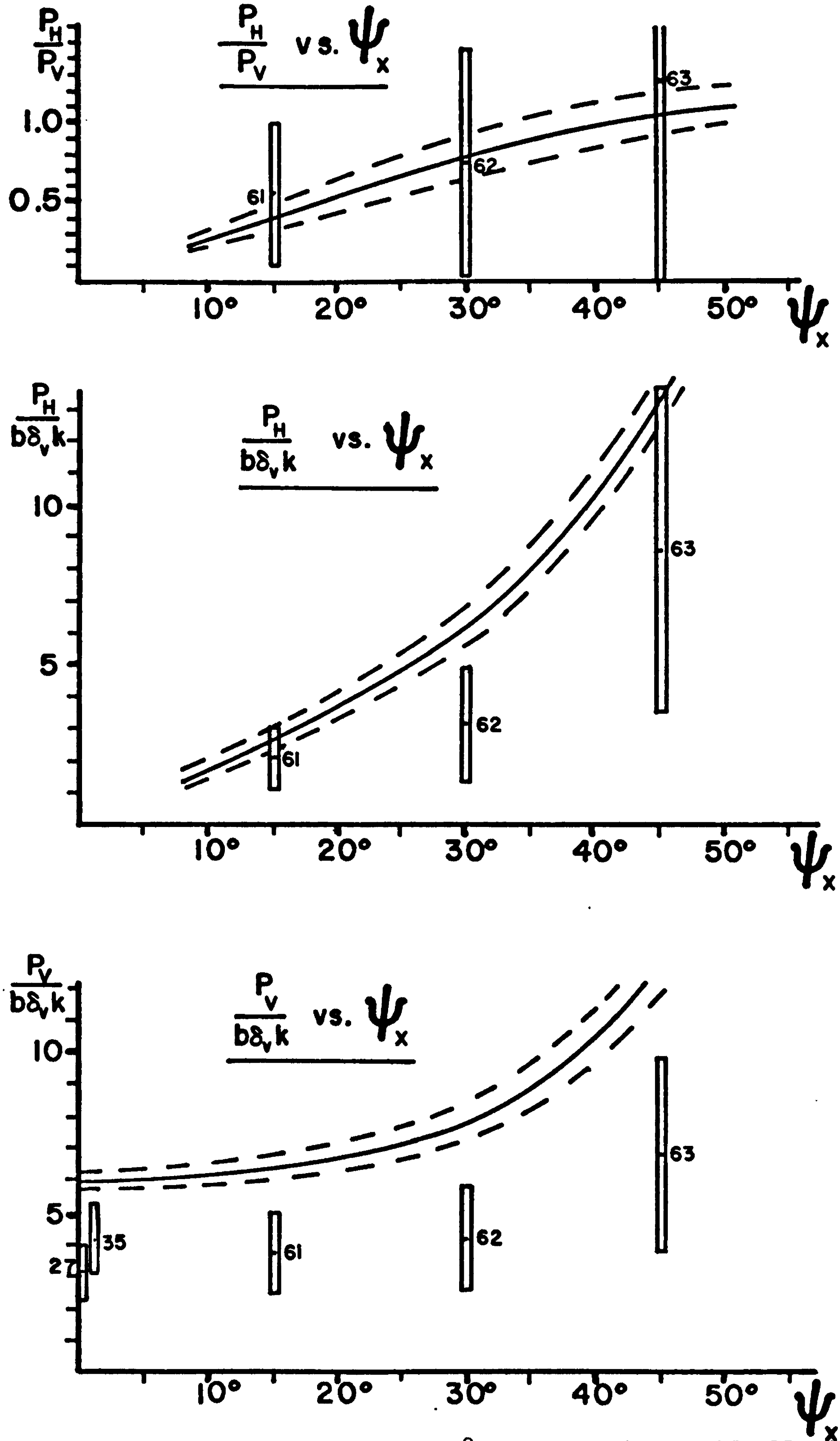

Figure 44 Experimental Results, $\beta = 30^0$, $\psi_y = 0$, (Tests 27, 35, 61, 62, 63)

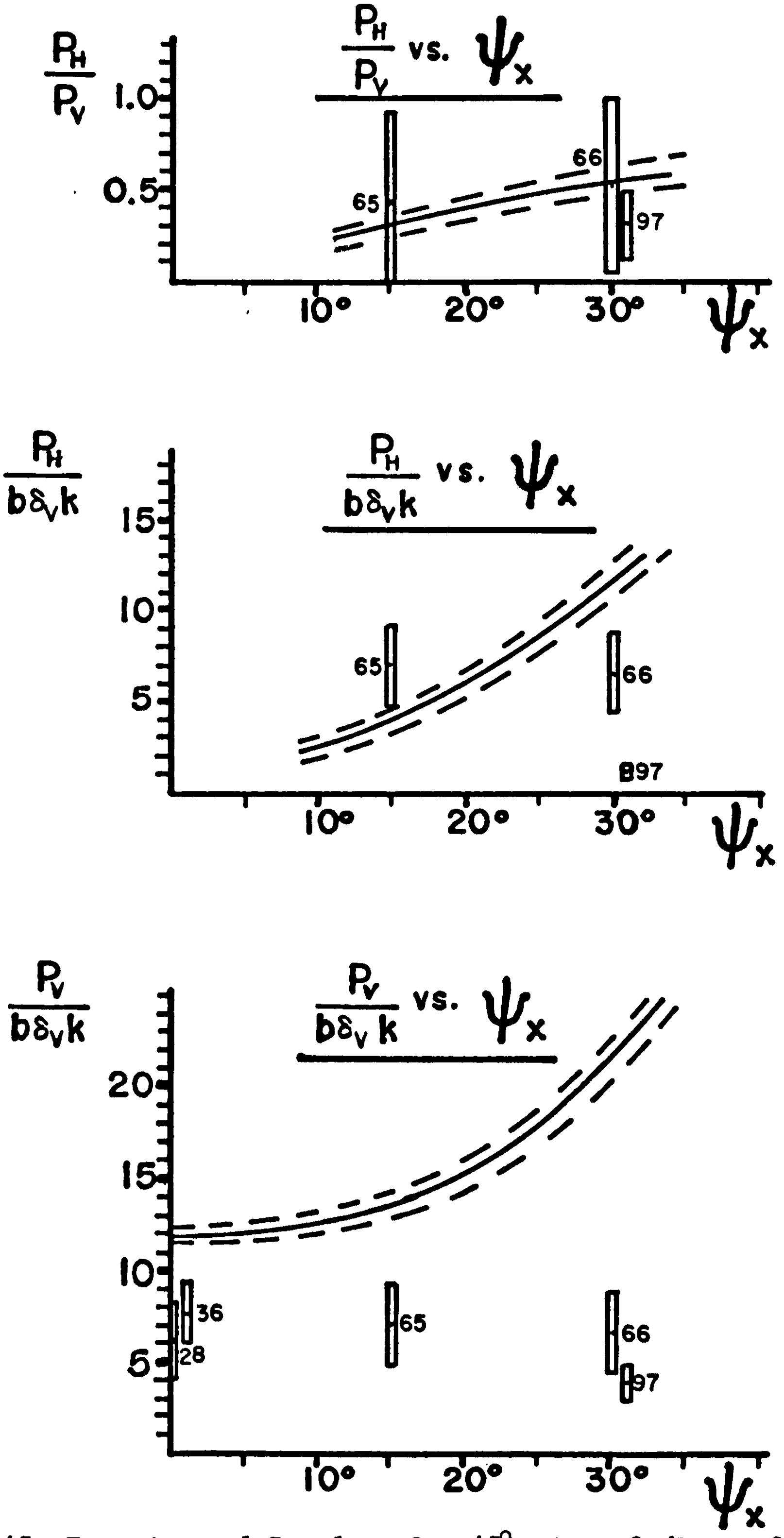

Figure 45 Experimental Results, $\beta = 45^\circ$, $\psi_y = 0$ (Tests 28,36,65,66,97)

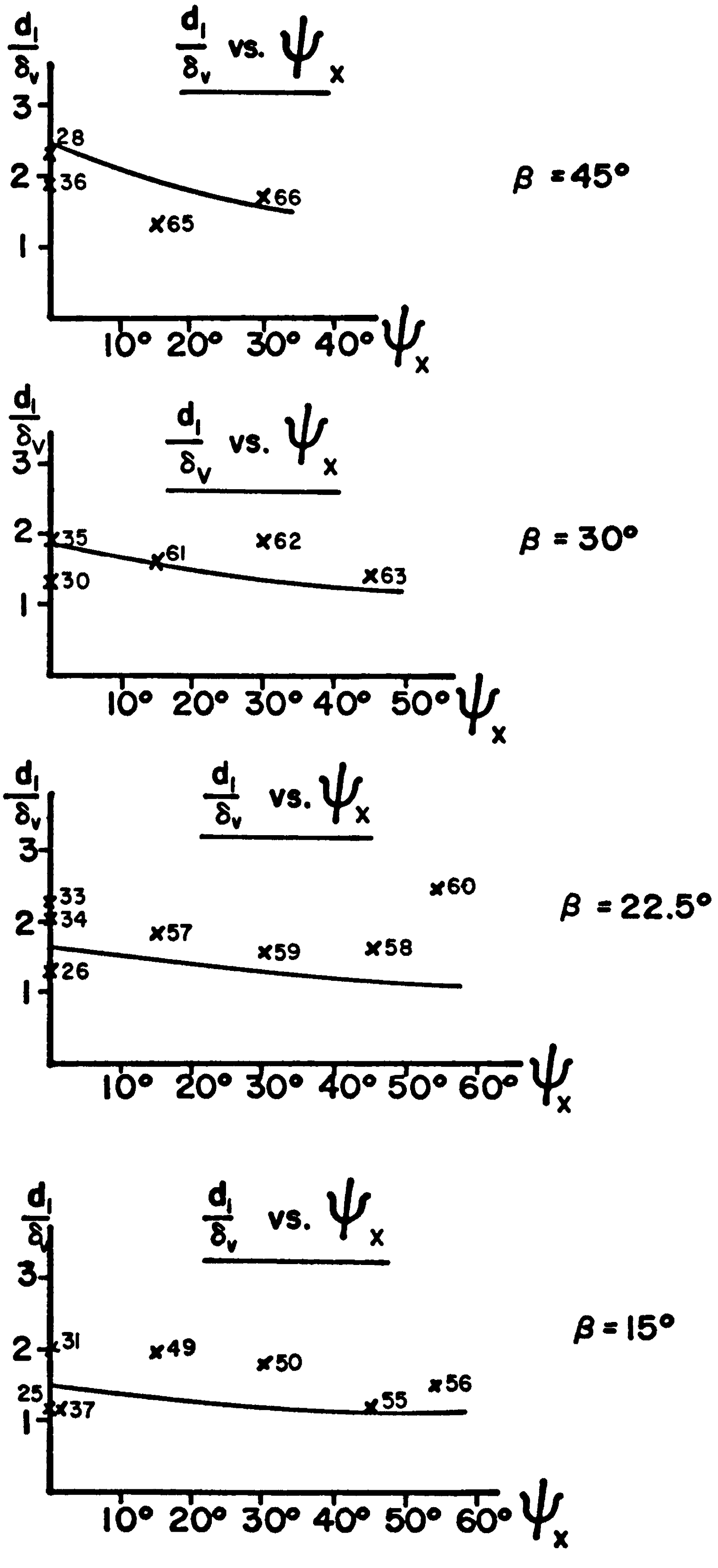

Figure 46 Downslope Lip Formation Results, $\psi_y = 0$

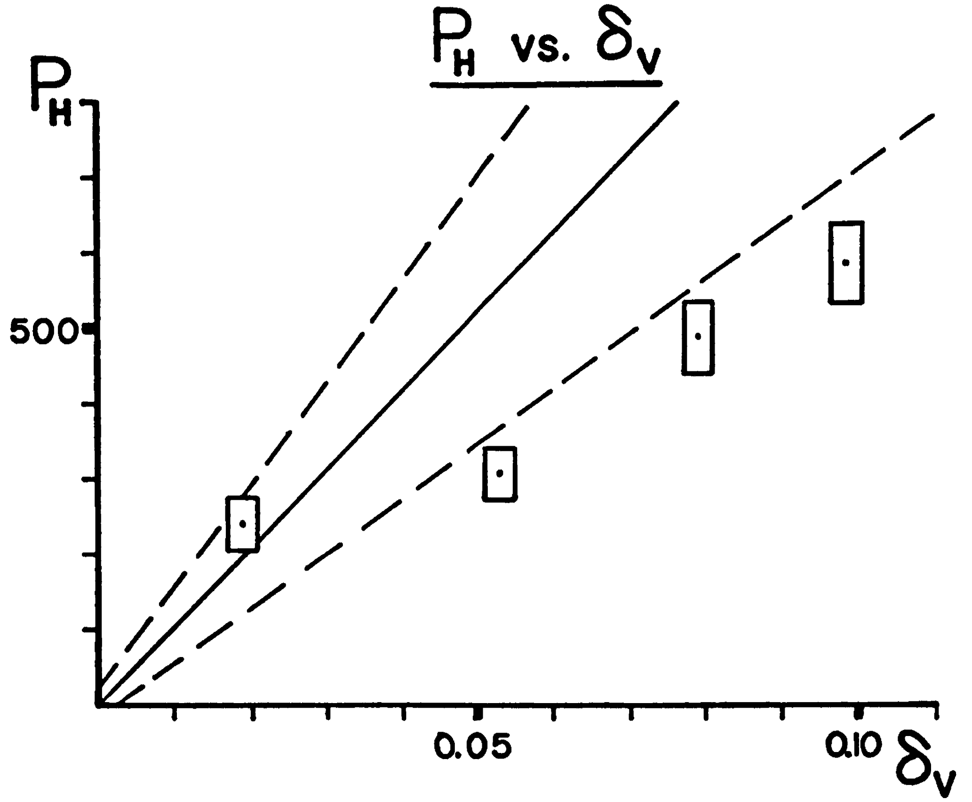

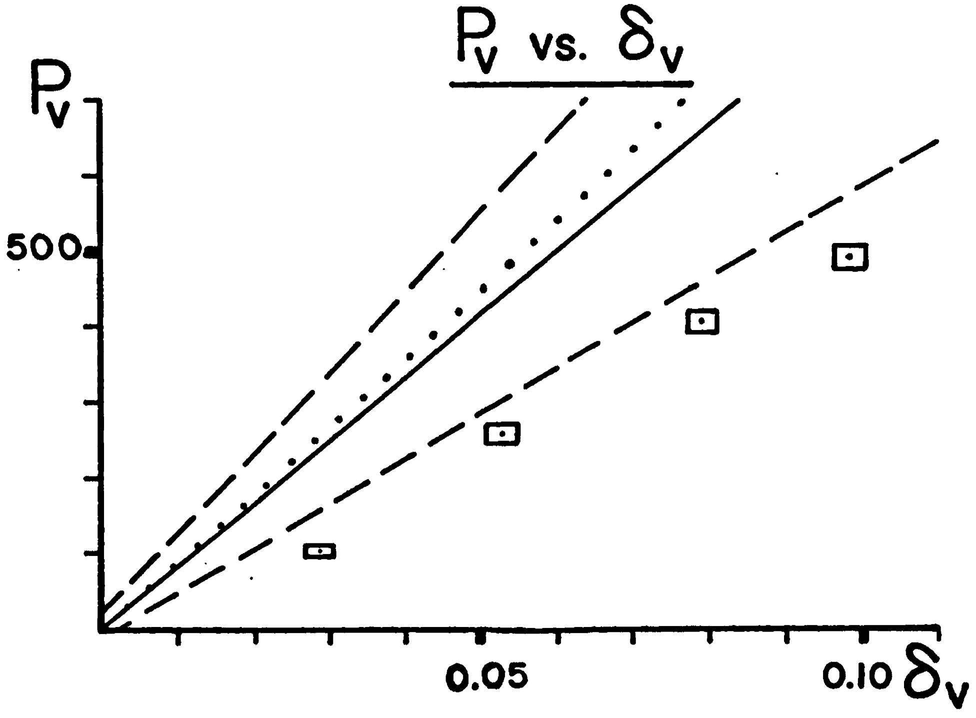

Figure 47 Force-Deflection Results, $\beta = 15^\circ$, $\psi_x = 30^\circ$, $\psi_y = 0$ (Test 50)

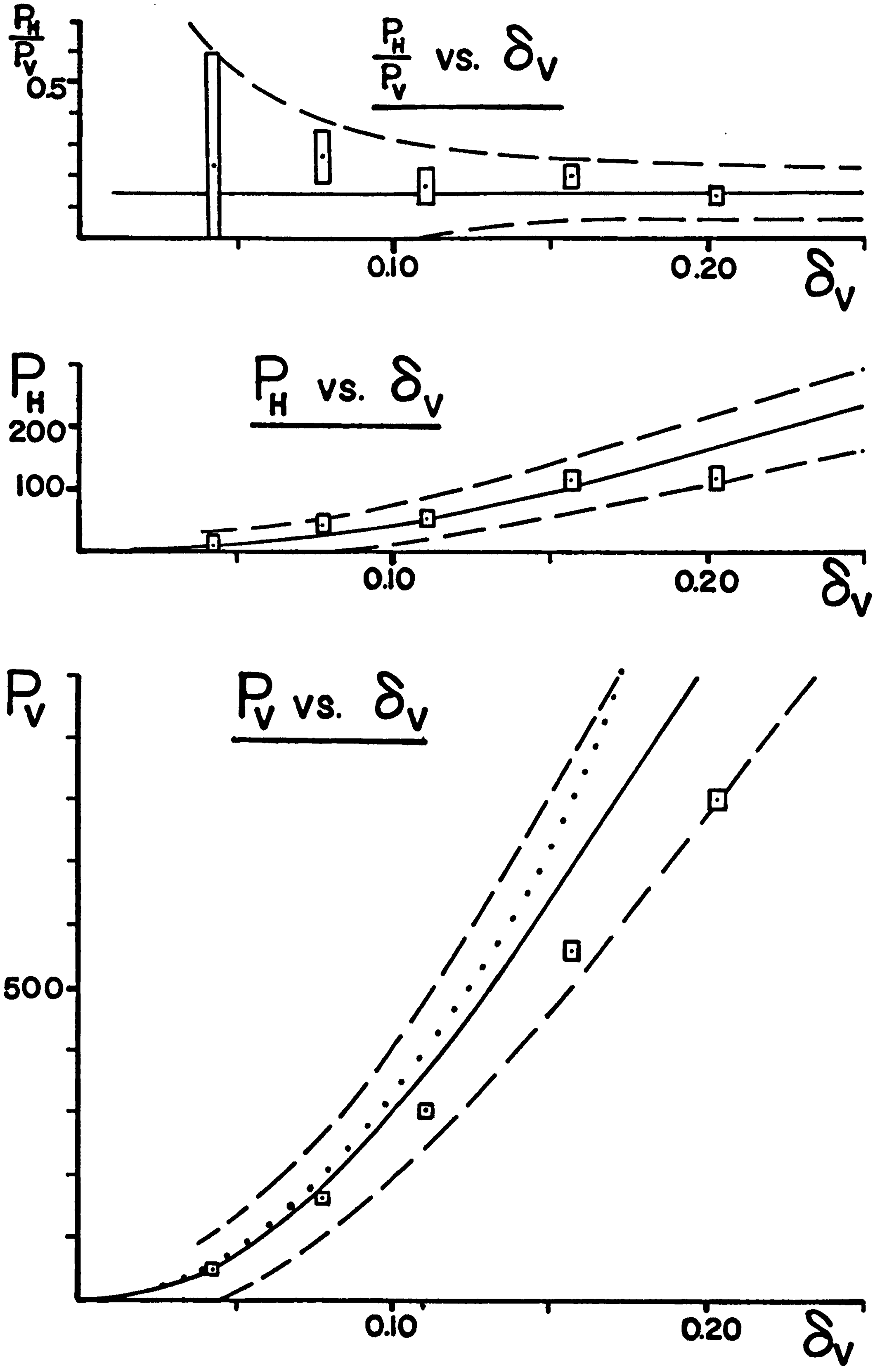

Figure 48 Force-Deflection Results, $\beta = 15^\circ$, $\psi_x = 0$, $\psi_y = 15^\circ$ (Test 95)

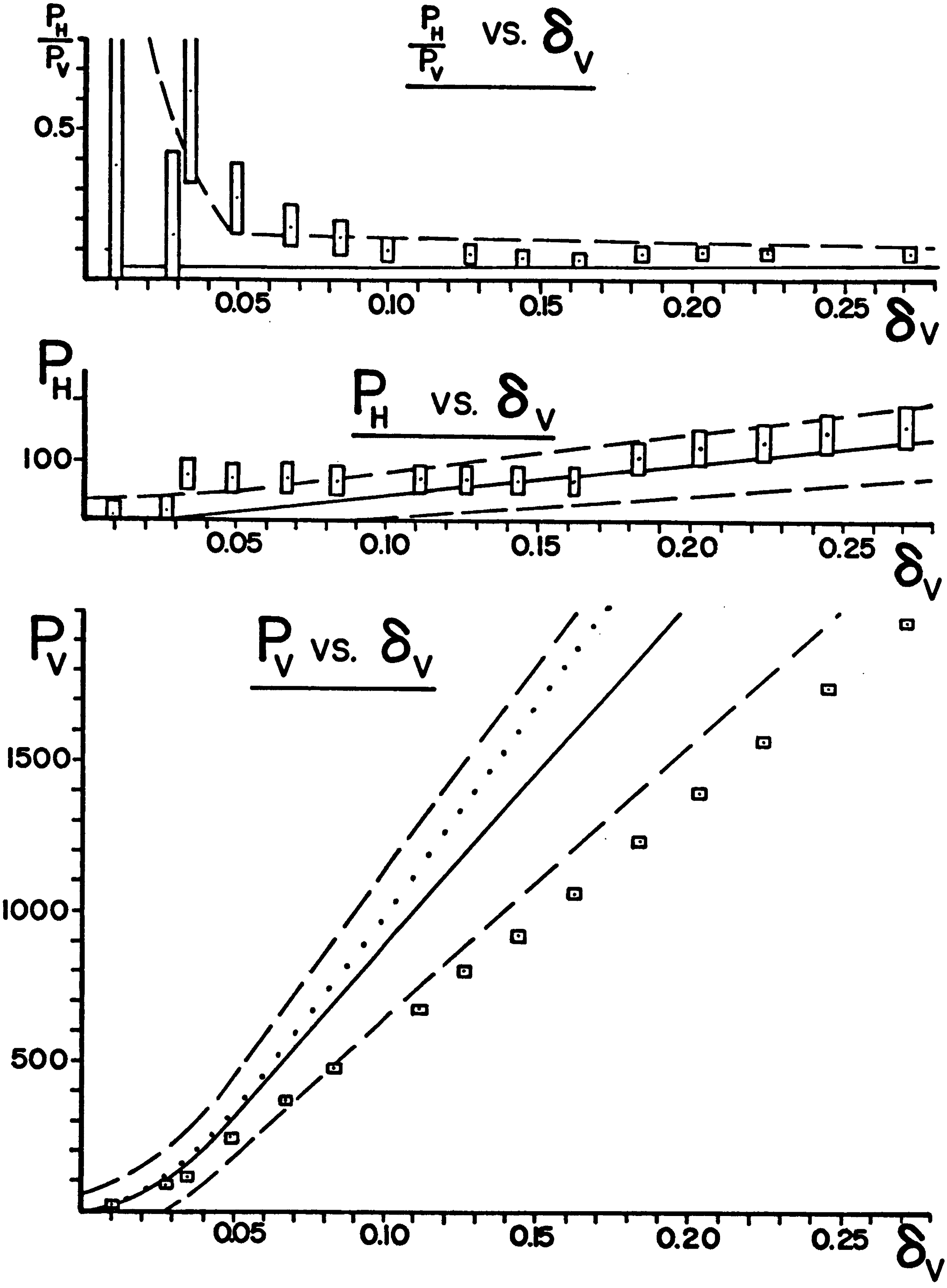

Figure 49 Force-Deflection Results, $\beta = 22.5^\circ$, $\psi_x = 0$, $\psi_y = 5^\circ$ (Test 75)

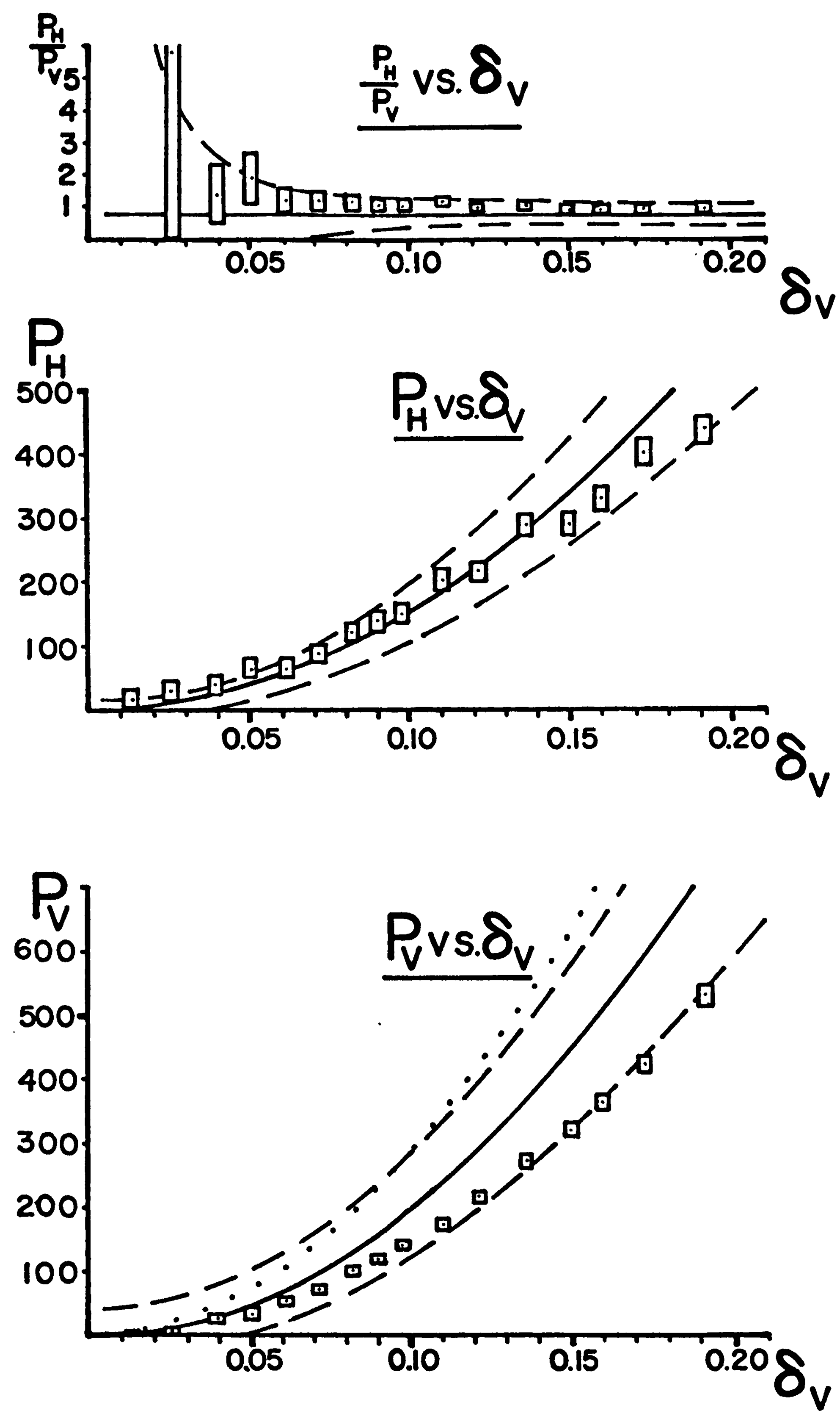

Figure 50 Force-Deflection Results, $\beta = 30^\circ$, $\psi_x = 15^\circ$, $\psi_y = 45^\circ$ (Test 87)

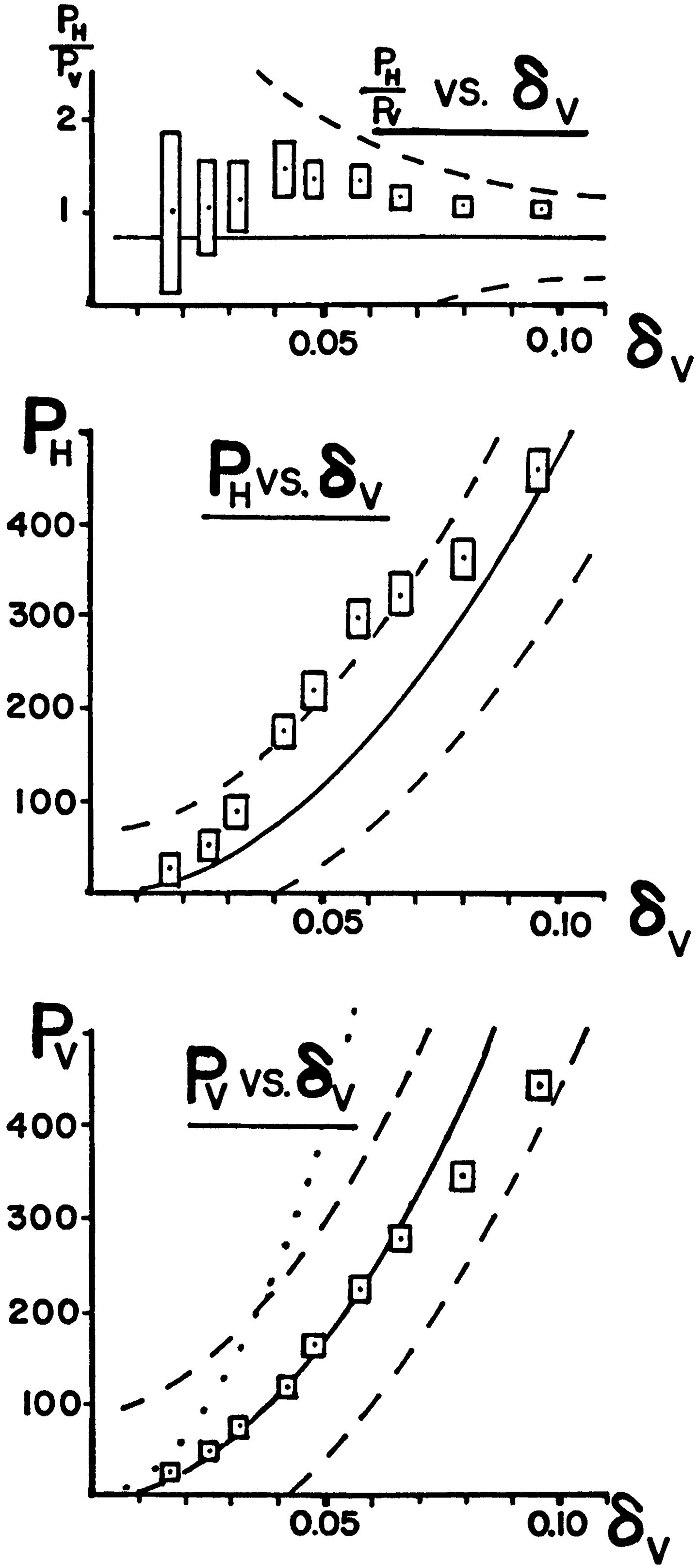

Figure 51 Force-Deflection Results, $\beta = 45^\circ$, $\psi_x = 30^\circ$, $\psi_y = 45^\circ$, (Test 93)

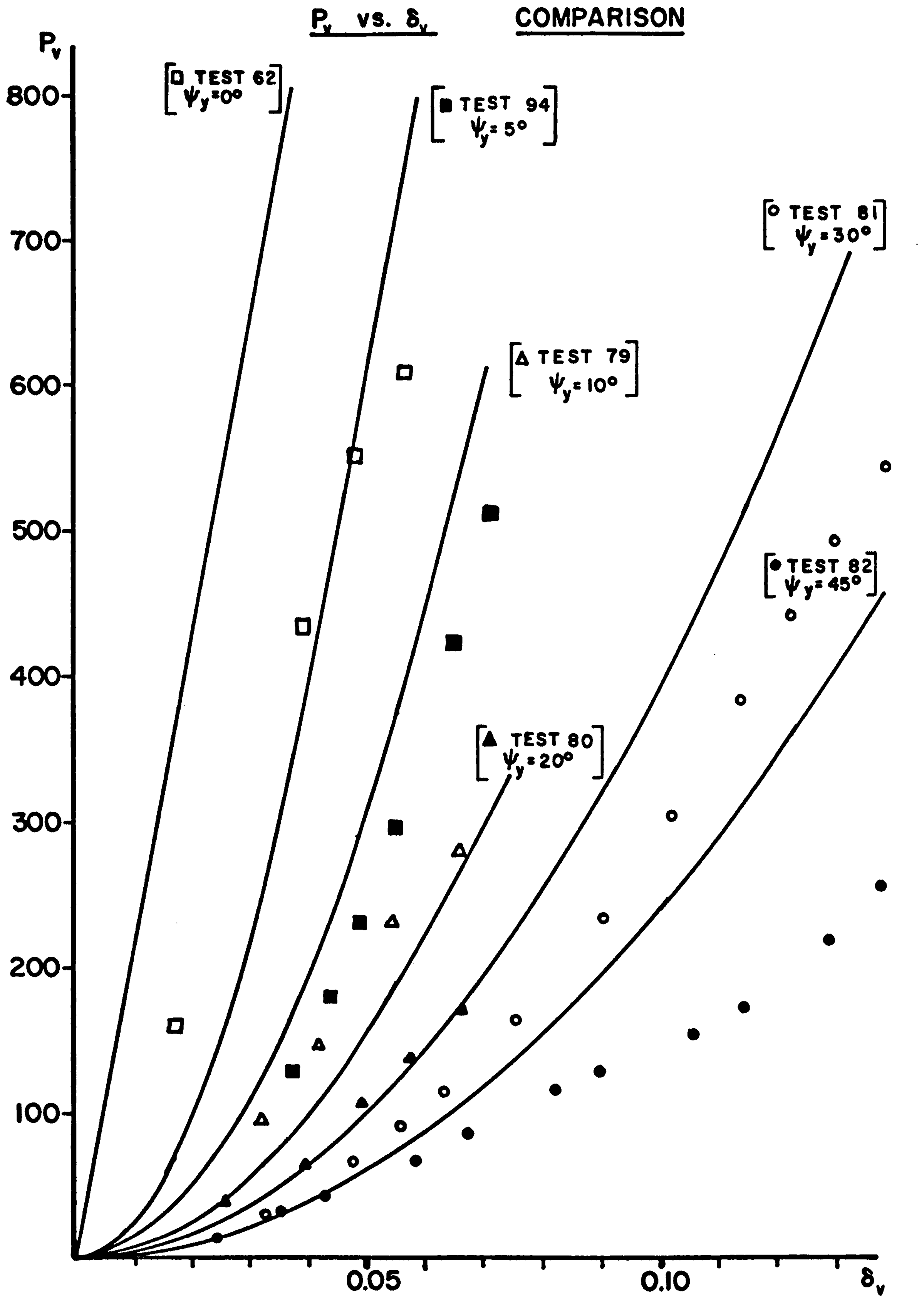

Figure 52 Comparison of Force-Deflection Tests, $\beta = 30^\circ$, $\psi_x = 30^\circ$

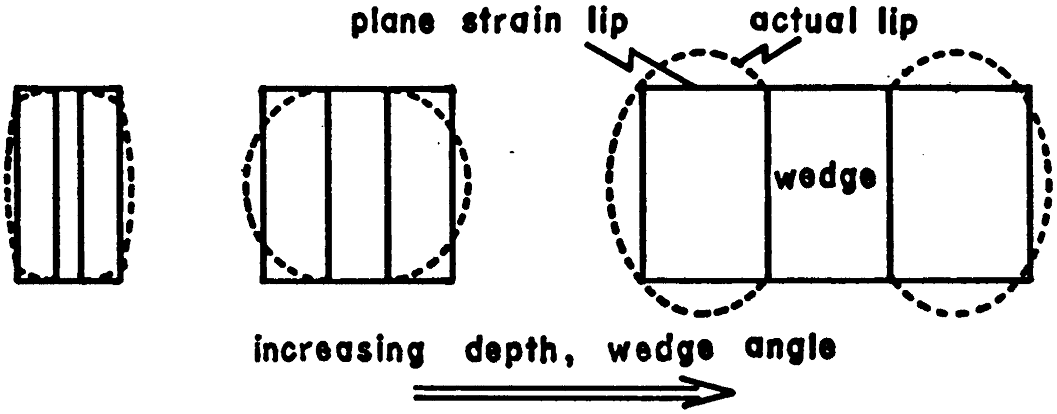

Figure 53 Deviation from Plane Strain Lip Formation

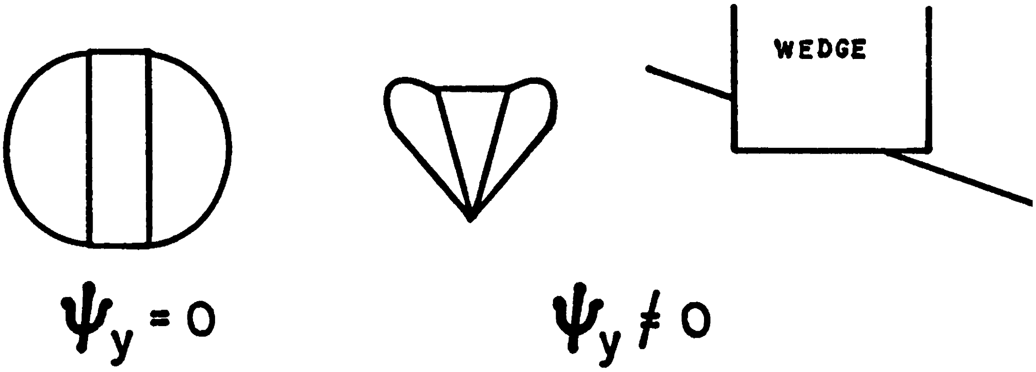

Figure 54 Effect of Inclination ψ_y on End Effects

offset one another. The analysis without lip formation is a closer prediction of experimental behavior, but the more complex lip formation slip line field must be considered if a true upper bound analysis is desired.

The same plot of experimental data is shown with only the frictional/lip formation prediction (Figure 40). The error analysis results are presented here and in all plots to follow in the form of dashed lines to show theoretical tolerances and boxes to show the experimental errors for each coordinate, abscissa and ordinate. The validity of the theoretical prediction as an experimental upper bound is verified by inspection.

The force - deflection curve for Test 35 ($\beta = 30^\circ$) shown in Figure 41 for two purposes. A true upper bound has been calculated and is shown by the dotted line curve. On the previous plot of $\frac{P_V}{b\delta_V k}$ vs. β, the Test 35 result was well below the prediction whereas in the force - deflection plot it is observed that one half of the test falls within the toleration limits. The force - deflection curve is a somewhat less efficient method of presenting results, but it gives a more honest portrayal of the experiment. It is wholly possible that a test might fall completely within tolerance on a force - deflection curve, but the non-dimensional plot $\frac{P_V}{b\delta_V k}$ vs. β may indicate discrepancies beyond projected errors.

The next four graphs depict the entire series of tests for which $\psi_y = 0$ by plotting $\frac{P_V}{b\delta_V k}$, $\frac{P_H}{b\delta_V k}$, and $\frac{P_H}{P_V}$ as functions of ψ_x for each wedge angle (Figures 42 - 45). Several observations may readily be made.

1. The experimental upper bound characteristic of the theoretical predictions is verified.
2. The deviation from predictions tends to increase with inclination angle. This is partially explained by an experimental observation of no lip formation on the up slope side of the wedge for very steep inclinations.
3. Even though the range of possible error is quite large for the $\frac{P_H}{P_V}$ results the actual experimental points are in near agreement with predictions.

A very crude experimental measurement was made of the lip on the down slope side of the wedge. The errors were large and difficult to estimate, so the results are presented without error analysis (Figure 46). Although no real conclusions can be made from these measurements, the plot does suggest reasonable agreement with predictions.

Curves for a sample test in this series are shown with the corresponding adjustment to the P_V plot to obtain a true upper bound prediction for both P_V and P_H (Figure 47). Verification of the upper bound is readily observed.

A number of representative curves for the more general tests where $\psi_y \neq 0$ are presented showing the true upper bound correction to P_V (Figures 48 - 51). The necessary upper bound adjustment is a rapidly increasing function of wedge angle. The experimental results seem to be in consistently close agreement with the unadjusted predictions. The experimental upper bound criterion for the theoretical analysis holds true for the entire experimental study except for one datum point -- Test 93, P_H, $\delta_V = 0.0575''$ (Figure 51). These observations may be verified by inspection of the complete series of graphical results in Appendix F.

The series of tests for which $\beta = 30^\circ$, $\psi_x = 30^\circ$, and ψ_y was varied is plotted on a composite P_V vs. δ_V graph without an error analysis indicated (Figure 52). The purpose of this plot is to show that the experimental data exhibit the same relationships between tests as the relationships between theoretical predictions. If the theoretical prediction for one test is greater than for another, then likewise are the corresponding experimental data.

It may be observed that the tests for which $\psi_y \neq 0$ seemed to be in closer agreement with theoretical predictions than the simpler tests for which $\psi_y = 0$. A possible explanation is deduced from experimental observation of the lip formation. The indentation obtained in each type of test is diagrammed in Figure 54. The deviation from plane strain plastic flow is caused by the end effects of a finite wedge. For the case where $\psi_y = 0$, these end effects occur on both ends of the wedge. Generally, the wedge was not fully indented when $\psi_y \neq 0$ so that the effects occurred on only one end of the wedge. The assumption of plane strain plastic flow seems very nearly correct on the down slope end of the indentation. Therefore, the experimental deviation from theoretical predictions for $\psi_y \neq 0$ should have been nearly half as great as when $\psi_y \neq 0$. The graphical results seem to verify this type of behavior.

To summarize the discussion of experimental results, the plotted data seem to verify the validity of the theoretical upper bound analysis. The experimental deviation from theoretical prediction varies from 0 - 50% of the theoretical value. Possible causes for the variation in error are known from experimental observations. The prediction curves with associated errors constitute an experimental upper bound approximation to the actual behavior. The necessary adjustments to obtain analytically true upper bounds must increase the predictions. The true upper bounds are, therefore, also experimentally valid upper bounds. A closer prediction of results can be obtained by using the non - lip forming slip line field in the plane strain analysis. The inherent discrepancies in this case tend to offset one another. This analysis cannot, however, be called a true upper bound even if the end effects are considered, because the slip line field is not a kinematically admissible velocity field for indentation into an initially flat surface. It would appear from these results that a meaningful solution has been obtained for the isotropic wedge indentation problem considered herein.

Methods of Analysis for Transversely Isotropic Wedge Indentation

The purpose of investigating isotropic wedge indentation was to gain some understanding of the problem of indentation into the flat, level surface of a transversely isotropic medium. It has been demonstrated how a rigorous true upper bound prediction of horizontal and vertical forces can be formulated and verified by experimental evidence. In principle the same sort of analysis can be developed for a transversely isotropic medium with arbitrary orientation of the axis of symmetry using an isotropic von Mises yield condition.

The isotropic analysis developed above is an attempt to find the best possible upper bound approximation to experimental behavior. An upper bound (probably less accurate) could have been found by equating the rate of work done by the external loads to the power dissipation associated with any kinematically admissible velocity field. A similarly possible upper bound analysis method is presented for the transversely isotropic wedge indentation problem.

Consider the plane strain velocity field for an upper bound analysis shown in Figure 55. It is recognized as the outset that this is not a kinematically admissible velocity field for indentation into an initially flat smooth surface. It is sufficient, however, to illustrate the method. The wedge is assumed rough. If the primed coordinate system refers to the principal axes of anisotropy, then their arbitrary orientation in the medium is described by the matrix multiplication

$$\{\underset{\sim}{e}_i'\} = [a_{ij}]\{\underset{\sim}{e}_j\}$$

where a_{ij} is the directional cosine between the $\underset{\sim}{e}_i'$ and $\underset{\sim}{e}_j$ coordinates. The shearing force at yield varies throughout the field and is a function of $[a_{ij}]$, $[(\sigma_{ij}')_y]$, and ϕ_T where $[(\sigma_{ij}')_y]$ is the matrix of yield strengths in the direction of the principal axes of anisotropy, and ϕ_T describes the orientation of the shearing plane in the zx plane of strain

$$\tau = \tau([a_{ij}],[(\sigma_{ij}')_y],\ \phi_T)$$

In general a horizontal force P_H is necessary to force the wedge vertically. Assume for an instant that $P_H = 0$ (Figure 56) and the wedge is allowed to travel in a non-vertical direction (dashed line). The angles

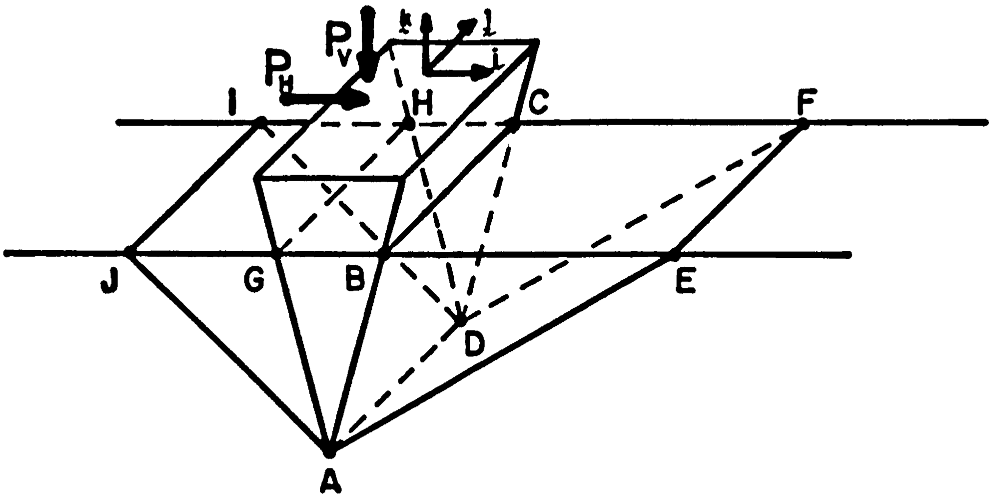

Figure 55 Transversely Isotropic Indentation Model

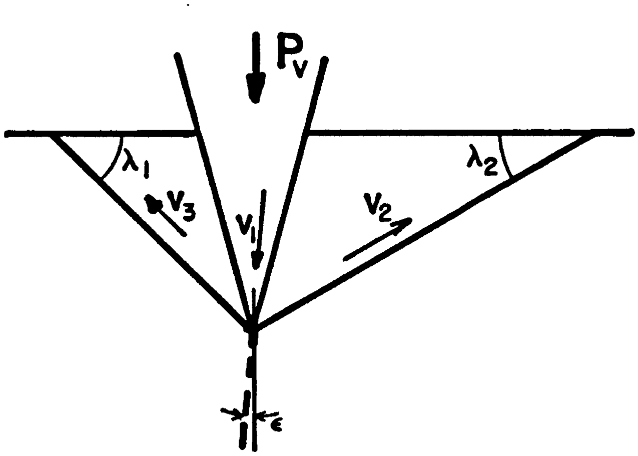

Figure 56 Assumed Velocity Field for $P_H = 0$

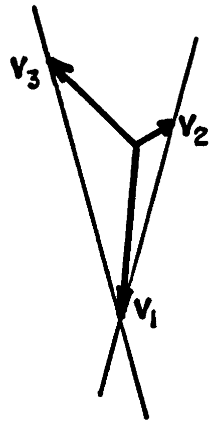

Figure 57 Hodograph for $P_H=0$

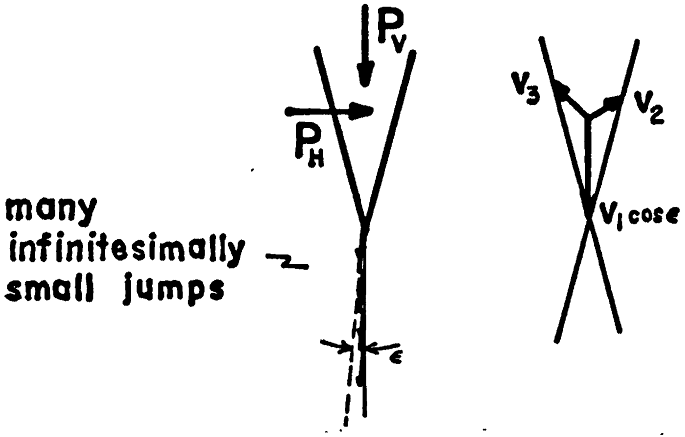

Figure 58 Assumed Behavior for Vertical Indentation Upper Bound

λ_1, and λ_2 are arbitrarily assumed. The velocity hodograph (Figure 57) is determined from the velocity field (Figure 56).

$$v_2 = v_1 \frac{\cos(\beta - \epsilon)}{\sin(\pi/2 - \beta - \lambda_2)}$$

$$v_3 = v_1 \frac{\cos(\beta - \epsilon)}{\sin(\pi/2 - \beta - \lambda_1)}$$

An upper bound analysis is further developed as follows.

$$\begin{aligned} P_V v_1 \cos\epsilon = {} & (\overline{ABCD})[v_1\cos(\beta - \epsilon) + v_2\cos(\pi/2 - \beta - \lambda_2)]\tau_{ABCD} + \\ & + (\overline{AGHD})[v_1\cos(\beta + \epsilon) + v_3\cos(\pi/2 - \beta - \lambda_1)]\tau_{AGHD} + \\ & + (\overline{ADEF})\, v_2\tau_{ADEF} + (\overline{AJID})\, v_3\tau_{AJID} + \\ & + 2\,(\overline{ABG})\, v_1\tau_{ABG} + 2\,(\overline{ABE})\, v_2\tau_{ABG} + 2\,(\overline{AGJ})\, v_3\tau_{AGJ} \end{aligned}$$

or $P_V \cos\epsilon = F_1(\beta,\ b,\ \delta_V, \lambda_1, \lambda_2, \epsilon, [a_{ij}], [(\sigma_{ij}')_y])$ (29)

The angle ϵ is determined numerically by requiring P_V to be a minimum. Assume now a horizontal force is applied to force the wedge vertically and the wedge travels as shown in Figure 58.

$$v_2 = \frac{v_1 \cos\beta\cos\epsilon}{\sin(\pi/2 - \beta - \lambda_2)}$$

$$v_3 = \frac{v_1 \cos\beta\cos\epsilon}{\sin(\pi/2 - \beta - \lambda_1)}$$

The upper bound principle is then formulated by including the work done by the horizontal force.

$$P_V v_1 \cos\epsilon + P_H v_1 \sin\epsilon = v_1 F_2(\beta,\ b,\ \delta_V,\ \lambda_1,\ \lambda_2,\ \epsilon, [a_{ij}], [(\sigma_{ij}')_y]) \qquad (30)$$

Combining (29) and (30) the upper bounds for the vertical and horizontal forces are determined.

$$P_V = F_1 \sec\epsilon$$

$$P_H = (F_2 - F_1)\sec\epsilon$$

The entire procedure is repeated assuming different angles λ_1, λ_2 until least upper bound approximations to the forces P_V and P_H are obtained.

This type of analysis cannot predict an upper bound for the horizontal force in the $\underset{\sim}{j}$ direction (along the wedge), because there is no plastic flow on the end of the wedge. A slip line field analysis must be developed to estimate this force. In any case it is possible to estimate horizontal and vertical forces for transversely isotropic wedge indentation similar in form to the forces predicted and measured in the above investigation of isotropic wedge indentation.

Once an analysis has been completed for the anisotropic von Mises type yield condition it may be deemed appropriate to generalize the analysis to include anisotropic Coulomb - type yield behavior [21] or even the anisotropic parabolic yield criterion of Smith [32].

Summary, Conclusions, and Recommendations for Further Work

An isotropic model has been constructed for transversely isotropic wedge indentation into a flat surface of a medium with arbitrary orientation of the principal axes of anisotropy. The aim of the theoretical analysis of the isotropic model is an upper bound approximation to experimental brhavior. Examination of the experimental evidence shows that the theoretical prediction is indeed an upper bound approximation with experimental verification to within 0 - 50% of the theoretical prediction. Deviation from theoretical predictions is greatest for large wedge angles, large inclinations on the face of the wedge (ψ_x) and zero inclination on the end of the wedge ($\psi_y = 0$).

It is found that a closer prediction to experimental behavior could be obtained by using a non - lip formation slip line field for the frictional wedge, although a true upper bound would not be obtainable. Since the difficulty of calculation is greatly increased when considering a lip - formation slip line field, it is suggested that further work with the transversely isotropic model could consider only the non - lip formation analysis.

Previous work on the wedge indentation problem has been focused on the infinite width wedge (two dimensional) simplification of the finite wedge. The analysis above has taken into consideration three dimensional aspects of the finite width wedge problem and produced a rigorous upper bound approximation to the external loads. The techniques of analysis for the horizontal and vertical loads necessary to force a wedge vertically into the smooth, flat, inclined surface of an isotropic medium may be applied to estimate analogous external loads for wedge indentation into the level surface of a transversely isotropic medium.

Due to the largely unknown implications of the relaxation characteristics of the ductile medium, the uncertainties in the above experimental study are undesirably large. Further work needs to be done investigating the time dependent non - equilibrium behavior of a material which exhibits relaxation effects.

The logical extension to the study above is a theoretical and experimental study of transversely isotropic wedge indentation. It may be expected that the experimental techniques developed for the isotropic problem will be of value in the design of a transversely isotropic wedge indentation experiment. Successful completion of this sort of study will lead to a fuller understanding of the causes and methods of control for the hole deviation problem in drilling mechanics.

Appendix A

Additional Theoretical Wedge Indentation Solutions

For purposes of brevity, the analyses herein do not contain a detailed explanatory text as is presented in the theoretical solution above. The procedure used is basically the same as is described above, with certain obvious simplifications.

Additional Theoretical Wedge Indentation Solutions

Rough Wedge (Figures A-1, A-2)

$\beta > \psi - \frac{\pi}{4}$:

$$\boxed{\begin{aligned} \alpha_1 &= \frac{\pi}{4} + \beta - \psi \\ \alpha_2 &= \frac{\pi}{4} + \beta + \psi \end{aligned}} \qquad \begin{aligned} \sigma_{OA} &= k(2\alpha_1 + 1) \qquad & \tau_{OA} &= k \\ \sigma_{OD} &= k(2\alpha_2 + 1) \qquad & \tau_{OD} &= k \end{aligned}$$

$$P = b(\overline{OA})[\sigma_{OA}\sin\beta + \tau_{OA}\cos\beta] + b(\overline{OD})[\sigma_{OD}\sin\beta + \tau_{OD}\cos\beta]$$

$$(\overline{OA}) = \delta_V\cos\psi\sec(\beta - \psi)$$

$$(\overline{OD}) = \delta_V\cos\psi\sec(\beta + \psi)$$

$$\begin{aligned} P = {} & b\delta_V\cos\psi\sec(\beta - \psi)[k(2\alpha_1 + 1)\sin\beta + k\cos\beta] + \\ & + b\delta_V\cos\psi\sec(\beta + \psi)[k(2\alpha_2 + 1)\sin\beta + k\cos\beta] \end{aligned}$$

$$\boxed{\frac{P}{b\delta_V k} = \left[\frac{(2\alpha_1 + 1)\sin\beta + \cos\beta}{\cos(\beta - \psi)} + \frac{(2\alpha_2 + 1)\sin\beta + \cos\beta}{\cos(\beta + \psi)}\right]\cos\psi}$$

$$W = b(\overline{OA})[-\sigma_{OA}\cos\beta + \tau_{OA}\sin\beta)] + b(\overline{OD})[\sigma_{OD}\cos\beta - \tau_{OD}\sin\beta]$$

$$\begin{aligned} W = {} & b\delta_V\cos\psi\sec(\beta - \psi)[-k(2\alpha_1 + 1)\cos\beta + k\sin\beta] + \\ & + b\delta_V\cos\psi\sec(\beta + \psi)[k(2\alpha_2 + 1)\cos\beta - k\sin\beta] \end{aligned}$$

$$\boxed{\frac{W}{b\delta_V k} = \left[\frac{(2\alpha_2 + 1)\cos\beta - \sin\beta}{\cos(\beta + \psi)} - \frac{(2\alpha_1 + 1)\cos\beta - \sin\beta}{\cos(\beta - \psi)}\right]\cos\psi}$$

$\beta < \psi - \frac{\pi}{4}$:

As before, $\boxed{\alpha_2 = \frac{\pi}{4} + \beta + \psi}$, $\sigma_{OD} = k(2\alpha_2 + 1) \quad \tau_{OD} = k$

∴Assume, $\boxed{\alpha_1 = 0}$, $\sigma_{OA} = \tau_{OA} = k$

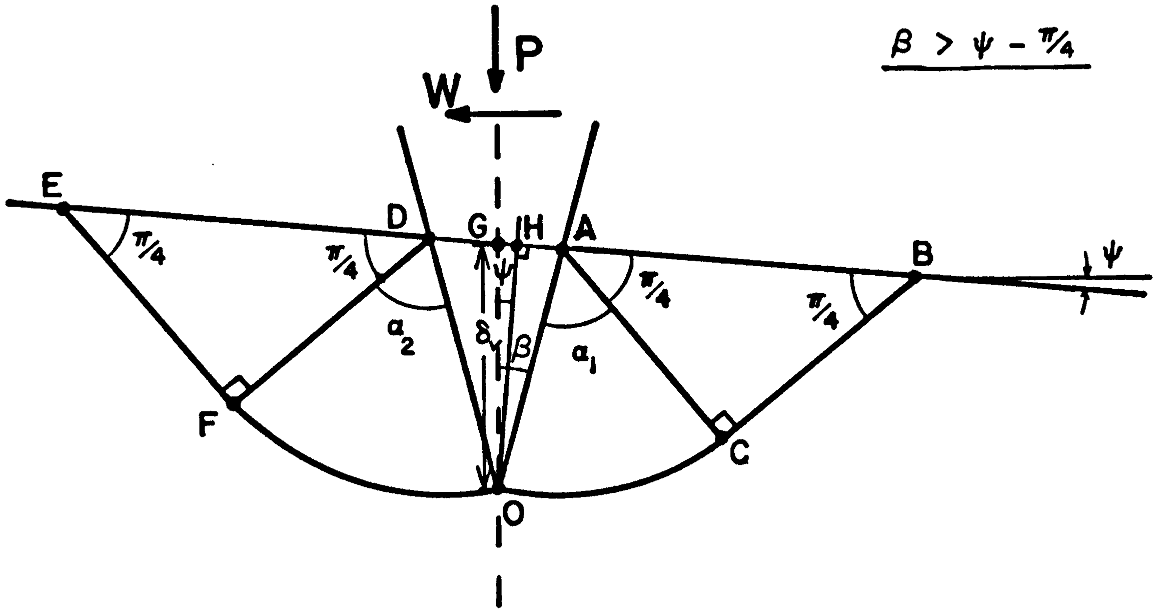

<u>Figure A-1</u> Rough Wedge Slip Line Field

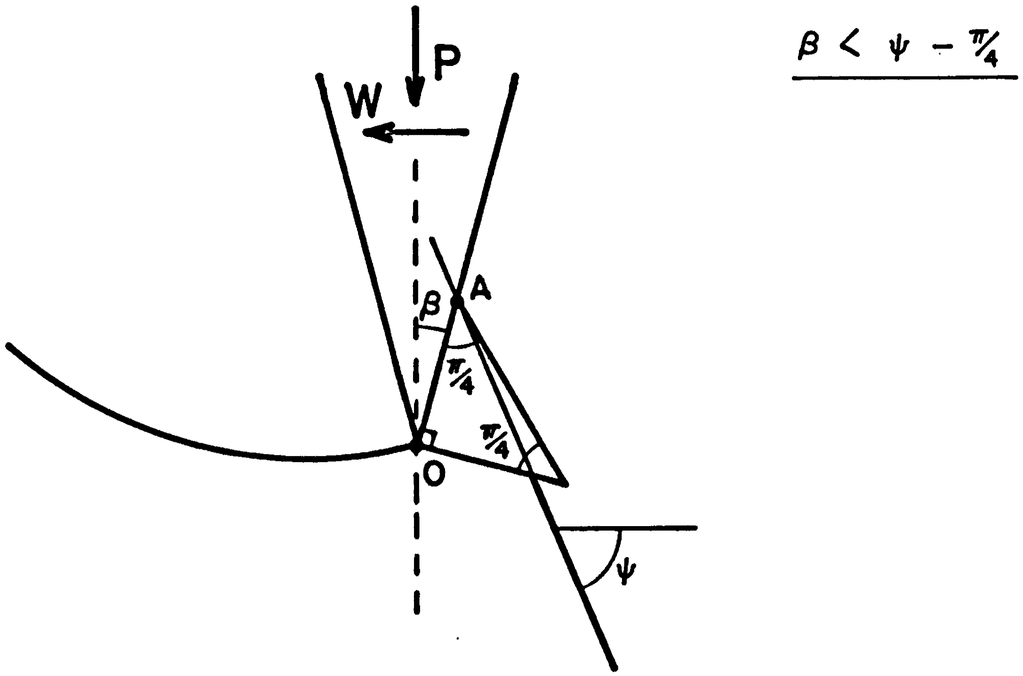

<u>Figure A-2</u> Extreme Inclination Rough Wedge Slip Line Field

ψ	β	α_1	α_2	$\frac{P}{b\delta_V k}$	$\frac{W}{b\delta_V k}$
0°	15°	60°	60°	3.658	0
	22.5°	67.5°	67.5°	4.780	0
	30°	75°	75°	6.178	0
	45°	90°	90°	10.283	0
15°	15°	45°	75°	3.697	1.461
	22.5°	52.5°	82.5°	4.889	1.721
	30°	60°	90°	6.425	2.038
	45°	75°	105°	11.381	2.942
30°	15°	30°	90°	3.837	3.042
	22.5°	37.5°	97.5°	5.290	3.714
	30°	45°	105°	7.403	4.637
	45°	60°	120°	17.239	8.583
45°	15°	15°	105°	4.184	5.016
	22.5°	22.5°	112.5°	6.421	6.734
	30°	30°	120°	10.837	9.979
	45°	45°	135°	∞	∞
60°	15°	0°	120°	5.326	8.682
	22.5°	7.5°	127.5°	12.416	17.331
	30°	15°	135°	∞	∞
	45°	30°	150°	-	-

Table A-1 Rough Wedge Slip Line Field Solution for Infinite Wedge

Smooth Wedge (Figures A-3 to A-5)

$\beta > \psi$:

$$\boxed{\begin{array}{l}\alpha_1 = \beta - \psi \\ \alpha_2 = \beta + \psi\end{array}} \qquad \begin{array}{ll}\sigma_{OA} = 2k(\alpha_1 + 1) & \tau_{OA} = 0 \\ \sigma_{OD} = 2k(\alpha_2 + 1) & \tau_{OD} = 0\end{array}$$

$$P = b(\overline{OA})[\sigma_{OA}\sin\beta + \tau_{OA}\cos\beta] + b(\overline{OD})[\sigma_{OD}\sin\beta + \tau_{OD}\cos\beta]$$

$$(\overline{OA}) = \delta_V\cos\psi\sec(\beta - \psi)$$

$$(\overline{OD}) = \delta_V\cos\psi\sec(\beta + \psi)$$

$$P = b\delta_V\cos\psi\sec(\beta - \psi)[2k(\alpha_1 + 1)\sin\beta] +$$

$$+ b\delta_V\cos\psi\sec(\beta + \psi)[2k(\alpha_2 + 1)\sin\beta]$$

$$\boxed{\frac{P}{b\delta_V k} = 2\cos\psi\sin\beta\left[\frac{(\alpha_1 + 1)}{\cos(\beta - \psi)} + \frac{(\alpha_2 + 1)}{\cos(\beta + \psi)}\right]}$$

$$W = b(\overline{OA})[-\sigma_{OA}\cos\beta + \tau_{OA}\sin\beta] + b(\overline{OD})[\sigma_{OD}\cos\beta - \tau_{OD}\sin\beta]$$

$$W = b\delta_V\cos\psi\sec(\beta - \psi)[-2k(\alpha_1 + 1)\cos\beta] +$$

$$+ b\delta_V\cos\psi\sec(\beta + \psi)[2k(\alpha_2 + 1)\cos\beta]$$

$$\boxed{\frac{W}{b\delta_V k} = 2\cos\psi\cos\beta\left[\frac{(\alpha_2 + 1)}{\cos(\beta + \psi)} - \frac{(\alpha_1 + 1)}{\cos(\beta - \psi)}\right]}$$

$\beta < \psi$:

$$\angle TBO = \angle BOS$$

$$\frac{\pi}{4} - \psi + \frac{\phi}{2} = \frac{\pi}{2} - \beta - \frac{\pi}{4} - \frac{\phi}{2}$$

$$\boxed{\phi = \psi - \beta}$$

$$\sigma_{OA} = k + (k - \Delta p) \qquad \Delta p = 2k\sin\phi$$

$$\sigma_{OA} = 2k(1 - \sin\phi) \qquad \Rightarrow \sigma_{OA} = 2k(1 - \sin(\psi - \beta))$$

$$\tau_{OA} = 0$$

$$P = b\delta_V\cos\psi\sec(\beta - \psi)[2k(1 - \sin(\psi - \beta))\sin\beta] +$$

$$+ b\delta_V\cos\psi\sec(\beta + \psi)[2k(\alpha_2 + 1)\sin\beta]$$

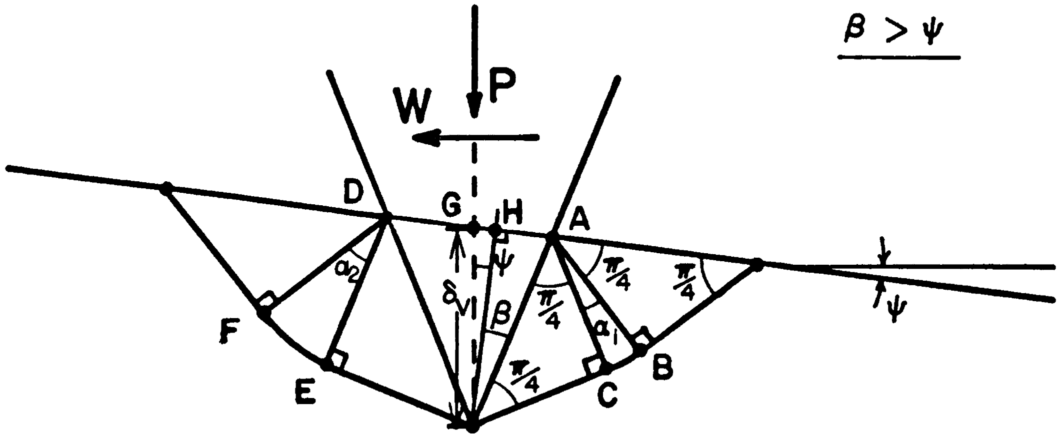

Figure A-3 Smooth Wedge Slip Line Field

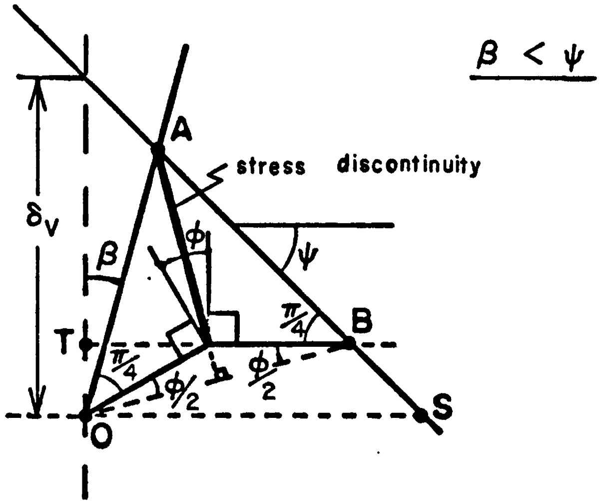

Figure A-4 Extreme Inclination Smooth Wedge Slip Line Field

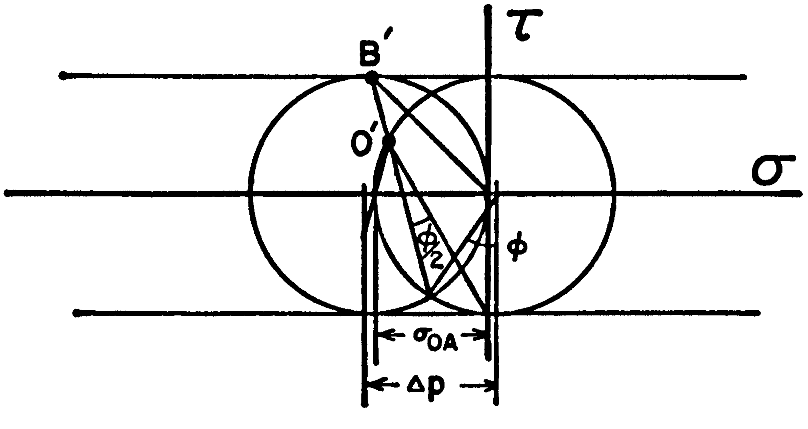

Figure A-5 Extreme Inclination Smooth Wedge Stress Plane

$$\boxed{\frac{P}{b\delta_V k} = 2\cos\psi\sin\beta\left[\frac{1 - \sin(\psi - \beta)}{\cos(\beta - \psi)} + \frac{(\alpha_2 + 1)}{\cos(\beta + \psi)}\right]}$$

$$\boxed{\frac{W}{b\delta_V k} = 2\cos\psi\cos\beta\left[\frac{\alpha_2 + 1}{\cos(\beta + \psi)} - (\frac{1 - \sin(\psi - \beta))}{\cos(\beta - \psi)}\right]}$$

ψ	β	α_1	α_2	$\frac{P}{b\delta_V k}$	$\frac{W}{b\delta_V k}$
0°	15°	15°	15°	1.352	0
	22.5°	22.5°	22.5°	2.307	0
	30°	30°	30°	3.519	0
	45°	45°	45°	7.142	0
15°	15°	0°	30°	1.352	1.047
	22.5°	7.5°	37.5°	2.385	1.686
	30°	15°	45°	3.701	2.039
	45°	30°	60°	7.996	3.190
30°	15°	-	45°	1.476	2.941
	22.5°	-	52.5°	2.668	3.634
	30°	0°	60°	4.412	4.642
	45°	15°	75°	12.526	9.326
45°	15°	-	60°	1.710	4.804
	22.5°	-	67.5°	3.442	6.563
	30°	-	75°	6.851	9.987
	45°	0°	90°	∞	∞
60°	15°	-	75°	2.416	8.217
	22.5°	-	82.5°	7.342	16.814
	30°	-	90°	∞	∞
	45°	-	105°	-	-

Table A-2 Smooth Wedge Slip Line Field Solution for Infinite Wedge

Frictional Wedge (Figures A-6 to A-8)

$\beta > \psi + \lambda_1 - \frac{\pi}{4}$:

$$\boxed{\begin{aligned} \alpha_1 + \lambda_1 &= \frac{\pi}{4} + \beta - \psi \\ \alpha_2 + \lambda_2 &= \frac{\pi}{4} + \beta + \psi \end{aligned}} \qquad (1)$$

$$\sigma_{OA} = k(2\alpha_1 + 1 + \sin 2\lambda_1)$$

$$\tau_{OA} = k\cos 2\lambda_1 = \mu\sigma_{OA} = \mu k(2\alpha_1 + 1 + \sin 2\lambda_1)$$

$$\sigma_{OD} = k(2\alpha_2 + 1 + \sin 2\lambda_2)$$

$$\tau_{OD} = k\cos 2\lambda_2 = \mu\sigma_{OD} = \mu k(2\alpha_2 + 1 + \sin 2\lambda_2)$$

$$\boxed{\begin{aligned} \cos 2\lambda_1 &= \mu(2\alpha_1 + 1 + \sin 2\lambda_1) \\ \cos 2\lambda_2 &= \mu(2\alpha_2 + 1 + \sin\lambda_2) \end{aligned}} \qquad (2)$$

Combine (1), (2):

$$\boxed{\begin{aligned} \cos 2\lambda_1 &= \mu[\tfrac{\pi}{2} + 1 + 2\beta - 2\psi - 2\lambda_1 + \sin 2\lambda_1] \\ \cos 2\lambda_2 &= \mu[\tfrac{\pi}{2} + 1 + 2\beta + 2\psi - 2\lambda_2 + \sin 2\lambda_2] \end{aligned}}$$

$$P = b(\overline{OA})[\sigma_{OA}\sin\beta + \tau_{OA}\cos\beta] + b(\overline{OD})[\sigma_{OD}\sin\beta + \tau_{OD}\cos\beta]$$

$$(\overline{OA}) = \delta_V\cos\psi\sec(\beta - \psi)$$

$$(\overline{OD}) = \delta_V\cos\psi\sec(\beta + \psi)$$

$$P = b\delta_V\cos\psi\sec(\beta - \psi)[k\cos 2\lambda_1(\frac{1}{\mu}\sin\beta + \cos\beta)] +$$

$$+ b\delta_V\cos\psi\sec(\beta + \psi)[k\cos 2\lambda_2(\frac{1}{\mu}\sin\beta + \cos\beta)]$$

$$\boxed{\frac{P}{b\delta_V k} = \left(\frac{\sin\beta}{\mu} + \cos\beta\right)\cos\psi\left[\frac{\cos 2\lambda_1}{\cos(\beta - \psi)} + \frac{\cos 2\lambda_2}{\cos(\beta + \psi)}\right]}$$

$$W = b(\overline{OA})[-\sigma_{OA}\cos\beta + \tau_{OA}\sin\beta] + b(\overline{OD})[\sigma_{OD}\cos\beta - \tau_{OD}\sin\beta]$$

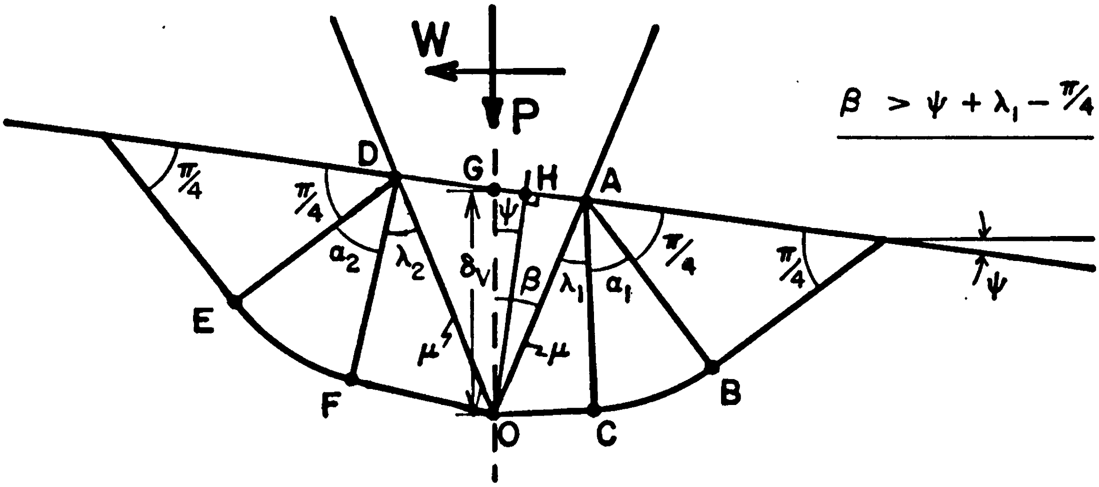

Figure A-6 Frictional Wedge Slip Line Field

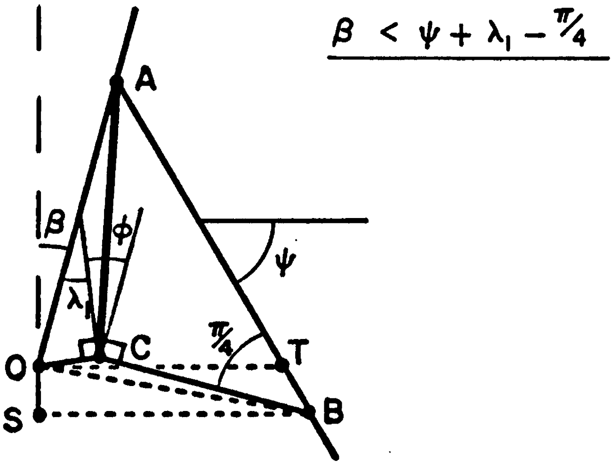

Figure A-7 Extreme Inclination Frictional Wedge Slip Line Field

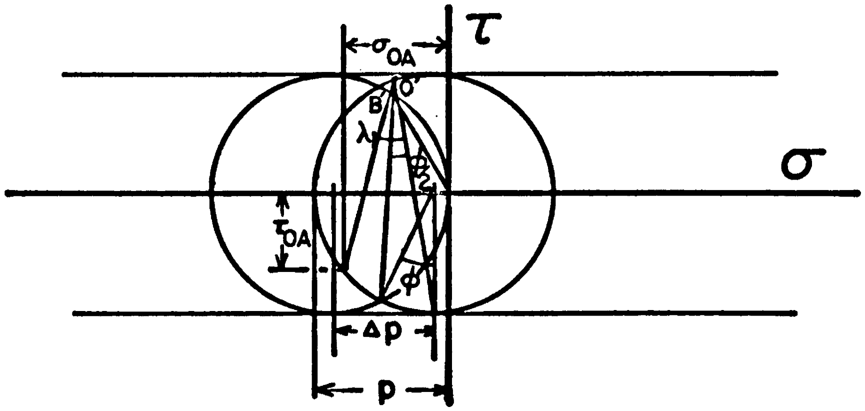

Figure A-8 Extreme Inclination Frictional Wedge Stress Plane

$$W = b\delta_V \cos\psi \sec(\beta - \psi)[k\cos 2\lambda_1(-\frac{1}{\mu}\cos\beta + \sin\beta)] +$$

$$+ b\delta_V \cos\psi \sec(\beta + \psi)[k\cos 2\lambda_2(\frac{1}{\mu}\cos\beta - \sin\beta)]$$

$$\boxed{\frac{W}{b\delta_V k} = \left(\sin\beta - \frac{\cos\beta}{\mu}\right) \cos\psi \left[\frac{\cos 2\lambda_1}{\cos(\beta - \psi)} - \frac{\cos 2\lambda_2}{\cos(\beta + \psi)}\right]}$$

$\underline{\underline{\beta < \psi + \lambda_1 - \pi/4}}$:

Sum angles about C: $\angle OCB + \frac{\pi}{2} + \phi + \frac{\pi}{2} = 2\pi$

$$\angle OCB + \phi = \pi$$

$$\phi = \angle COB + \angle CBO \tag{3}$$

Sum angles about B: $\frac{\pi}{4} + \angle CBS = \psi$

$$\frac{\pi}{4} + \angle CBO + \angle OBS = \psi \tag{4}$$

Sum angles about O: $\beta + (\frac{\pi}{2} - \lambda_1) + \angle COT = \frac{\pi}{2}$

$$\angle COB - \angle TOB = \lambda_1 - \beta \tag{5}$$

(4), (5): Using $\angle TOB = \angle OBS$,

(5): $\angle TOB = \angle COB + \beta - \lambda_1$

$$(4): \quad \frac{\pi}{4} + \angle CBO + \angle COB + \beta - \lambda_1 = \psi \tag{6}$$

(3), (6): $\frac{\pi}{4} + \phi + \beta - \lambda_1 = \psi$

$$\boxed{\phi = \psi - \beta + \lambda_1 = \frac{\pi}{4}} \tag{7}$$

$\Delta p = 2k\sin\phi$

$p = 2k(1 - \sin\phi)$

$\sigma_{OA} = k\sin 2\lambda_1 - (k-p) = k(\sin 2\lambda_1 - 1 + 2(1 - \sin\phi))$

$\sigma_{OA} = k(1 + \sin 2\lambda_1 - 2\sin\phi)$

$\tau_{OA} = k\cos 2\lambda_1 = \mu\sigma_{OA}$

$$\boxed{\cos 2\lambda_1 = \mu\ (1 + \sin 2\lambda_1 - 2\sin\phi)} \tag{8}$$

Combine (7), (8):

$$\boxed{\cos 2\lambda_1 = \mu\ [1 + \sin 2\lambda_1 - 2\sin(\psi - \beta + \lambda_1 - \frac{\pi}{4})]}$$

ROUGH: $$\left.\begin{aligned} \lambda_1 &= 0 \\ \lambda_2 &= 0 \end{aligned}\right] \Rightarrow \begin{aligned} \alpha_1 &= \frac{\pi}{4} + \beta - \psi \\ \alpha_2 &= \frac{\pi}{4} + \beta + \psi \end{aligned}$$

$$\left.\begin{aligned} 1 &= \mu_{max}[2(\tfrac{\pi}{4} + \beta - \psi) + 1] \\ 1 &= \mu_{max}[2(\tfrac{\pi}{4} + \beta + \psi) + 1] \end{aligned}\right] \Longrightarrow \boxed{\begin{aligned} \mu_{max_1} &= (\tfrac{\pi}{2} + 1 + 2\beta - 2\psi)^{-1} \\ \mu_{max_2} &= (\tfrac{\pi}{2} + 1 + 2\beta + 2\psi)^{-1} \end{aligned}}$$

ψ	β	μ_{max_1}	μ_{max_2}	μ	λ_1	λ_2	$\frac{P}{b\delta_V k}$	$\frac{W}{b\delta_V k}$
0°	15°	0.323	0.323	0.169	30.28°	30.28°	2.542	0
	22.5°	0.298	0.298	0.169	28.64°	28.64°	3.731	0
	30°	0.276	0.276	0.169	26.96°	26.96°	5.202	0
	45°	0.241	0.241	0.169	23.38°	23.38°	9.477	0
15°	15°	0.389	0.276	0.169	33.44°	26.96°	2.588	1.515
	22.5°	0.353	0.258	0.169	31.88°	25.21°	3.847	1.754
	30°	0.323	0.241	0.169	30.28°	23.38°	5.459	2.055
	45°	0.276	0.214	0.169	26.96°	19.37°	10.583	2.955
30°	15°	0.488	0.241	0.169	36.50°	23.38°	2.750	3.148
	22.5°	0.433	0.227	0.169	34.98°	21.44°	4.278	3.778
	30°	0.389	0.214	0.169	33.44°	19.37°	6.468	4.675
	45°	0.323	0.193	0.169	30.28°	14.58°	16.447	8.627
45°	15°	0.656	0.214	0.169	39.52°	19.37°	3.143	5.172
	22.5°	0.459	0.203	0.169	38.01°	17.12°	5.460	6.826
	30°	0.488	0.193	0.169	36.50°	14.58°	9.943	10.043
	45°	0.389	0.175	0.169	33.44°	7.616°	-	-
60°	15°	1.000	0.193	0.169	42.52°	14.58°	4.366	8.872
	22.5°	0.793	0.183	0.169	41.01°	11.59°	11.506	17.458
	30°	0.656	0.175	0.169	39.52°	7.616°	-	-
	45°	0.488	0.160	0.169	37.03°	1.922°	-	-

Table A-3 Frictional Wedge Slip Line Field for Infinite Wedge

Rough Wedge with Lip Formation (Figures A-9 to A-12)

$\beta > \psi - \frac{\pi}{4}$:

$$(\overline{OI}) = \delta_V\cos\psi + d_1\sin\gamma_1 \qquad (\overline{OI}) = (\overline{OA})\cos(\beta - \psi) = \frac{1}{\sqrt{2}}d_1\cos(\beta - \psi)$$

$$(\overline{OJ}) = \delta_V\cos\psi + d_2\sin\gamma_2 \qquad (\overline{OJ}) = (\overline{OD})\cos(\beta + \psi) = \frac{1}{\sqrt{2}}d_2\cos(\beta + \psi)$$

$$\frac{1}{\sqrt{2}}d_1\cos(\beta - \psi) = \delta_V\cos\psi + d_1\sin\gamma_1$$

$$\frac{1}{\sqrt{2}}d_2\cos(\beta + \psi) = \delta_V\cos\psi + d_2\sin\gamma_2$$

$$\boxed{\begin{aligned} \frac{d_1}{\delta_V} &= \frac{\sqrt{2}\cos\psi}{\cos(\beta - \psi) - \sqrt{2}\sin\gamma_1} \\ \frac{d_2}{\delta_V} &= \frac{\sqrt{2}\cos\psi}{\cos(\beta + \psi) - \sqrt{2}\sin\gamma_2} \end{aligned}} \qquad (1)$$

$$b_1 = (\overline{BG})\sin\gamma_1 \qquad (\overline{BG}) = d_1\cos\gamma_1 + (\overline{OA})\sin(\beta - \psi) + \delta_V\cos\psi\tan(\varepsilon + \psi)$$

$$b_2 = (\overline{EG})\sin\gamma_2 \qquad (\overline{EG}) = d_2\cos\gamma_2 + (\overline{OD})\sin(\beta + \psi) - \delta_V\cos\psi\tan(\varepsilon + \psi)$$

$$b_1 = [d_1\cos\gamma_1 + \frac{1}{\sqrt{2}}d_1\sin(\beta - \psi) + \delta_V\cos\psi\tan(\varepsilon + \psi]\sin\gamma_1$$

$$b_2 = [d_2\cos\gamma_2 + \frac{1}{\sqrt{2}}d_2\sin(\beta + \psi) - \delta_V\cos\psi\tan(\varepsilon + \psi]\sin\gamma_2$$

$$\boxed{\begin{aligned} \frac{b_1}{\delta_V} &= \left[(\cos\gamma_1 + \frac{1}{\sqrt{2}}\sin(\beta - \psi))\frac{d_1}{\delta_V} + \cos\psi\tan(\varepsilon + \psi)\right]\sin\gamma_1 \\ \frac{b_2}{\delta_V} &= \left[(\cos\gamma_2 + \frac{1}{\sqrt{2}}\sin(\beta + \psi))\frac{d_2}{\delta_V} - \cos\psi\tan(\varepsilon + \psi)\right]\sin\gamma_2 \end{aligned}} \qquad (2)$$

$$v_1 = v\sin(\beta + \varepsilon)$$

$$v_2 = v\sin(\beta - \varepsilon)$$

let $t \equiv \frac{\kappa}{v}$

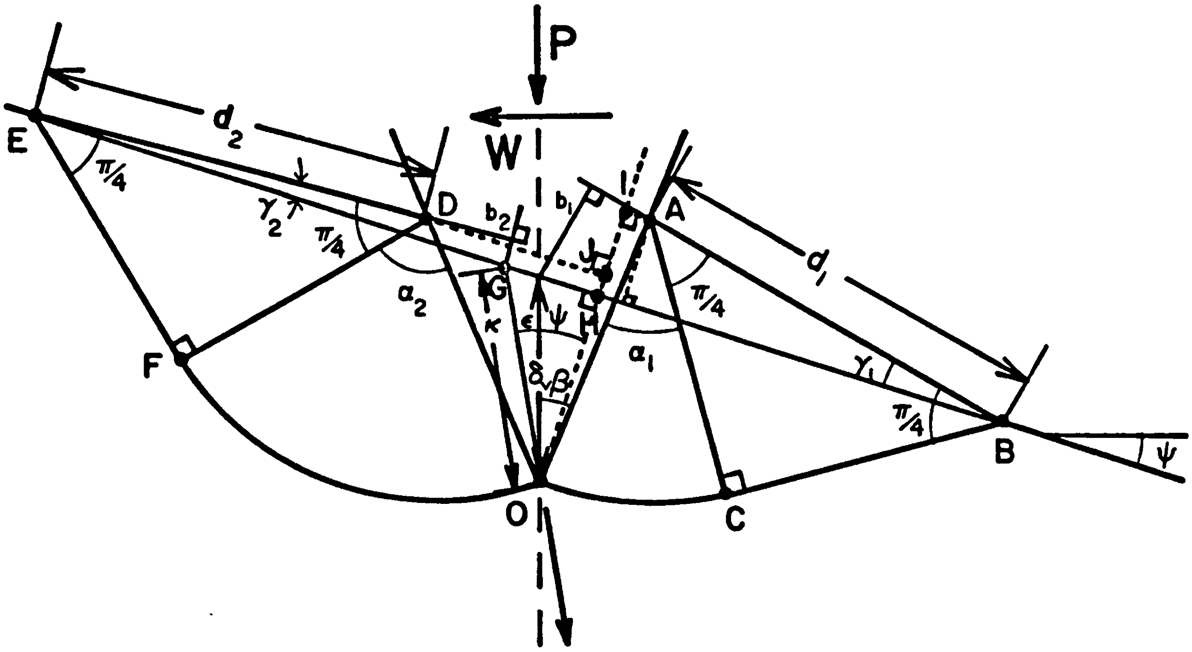

Figure A-9 Rough/Lip Slip Line Field

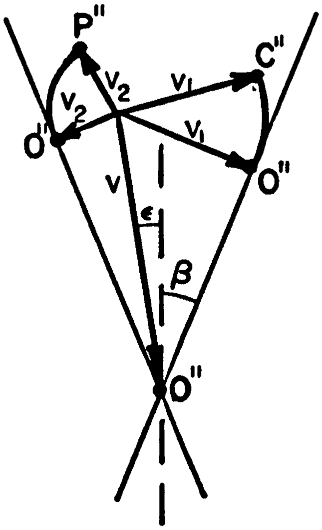

Figure A-10 Rough/Lip Hodograph

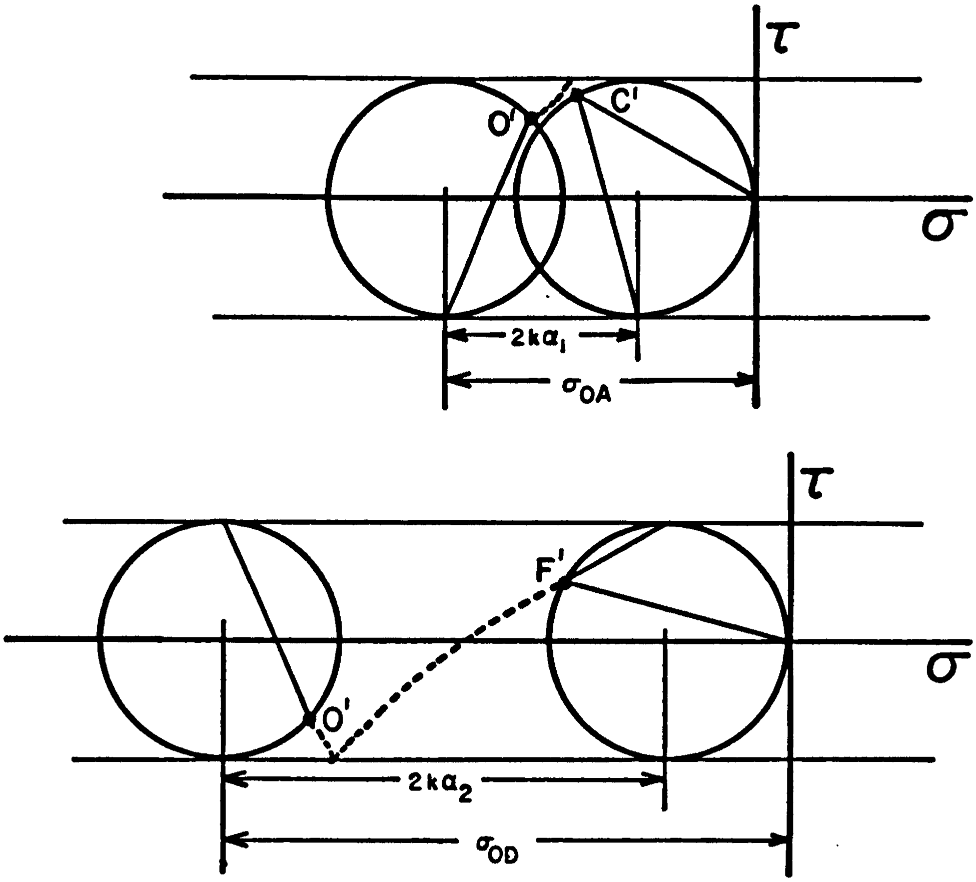

Figure A-11 Rough/Lip Stress Plane

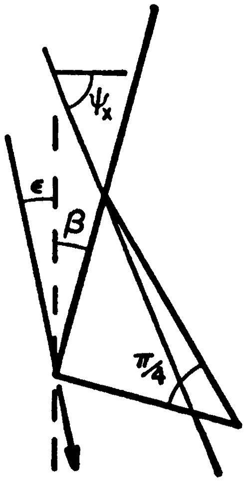

Figure A-12 Extreme Inclination Rough/Lip Slip Line Field

$$b_1 = \frac{v_1 t}{\sqrt{2}} \qquad b_2 = \frac{v_2 t}{\sqrt{2}}$$

$$b_1 = \frac{vt}{\sqrt{2}} \sin(\beta + \epsilon) \quad b_2 = \frac{vt}{\sqrt{2}} \sin(\beta - \epsilon)$$

$$b_1 = \frac{1}{\sqrt{2}} \varkappa \sin(\beta + \epsilon) \quad b_2 = \frac{1}{\sqrt{2}} \varkappa \sin(\beta - \epsilon)$$

$$\varkappa = \delta_V \cos\psi \sec(\psi + \epsilon)$$

$$\boxed{\begin{aligned} \frac{b_1}{\delta_V} &= \frac{\cos\psi \sin(\beta + \epsilon)}{\sqrt{2}\cos(\psi + \epsilon)} \\ \frac{b_2}{\delta_V} &= \frac{\cos\psi \sin(\beta - \epsilon)}{\sqrt{2}\cos(\psi + \epsilon)} \end{aligned}} \qquad (3)$$

Combine (1),(2), (3) to find γ

Summing angles about A, D:

$$\frac{\pi}{4} + \alpha_1 + (\frac{\pi}{2} - \beta) + \psi + \gamma_1 = \pi$$

$$\frac{\pi}{4} + \alpha_2 + (\frac{\pi}{2} - \beta) - \psi + \gamma_2 = \pi$$

$$\boxed{\begin{aligned} \alpha_1 &= \frac{\pi}{4} + \beta - \psi - \gamma_1 \\ \alpha_2 &= \frac{\pi}{4} + \beta + \psi - \gamma_2 \end{aligned}}$$

$$\sigma_{OA} = k(2\alpha_1 + 1) \text{ , } \tau_{OA} = k$$

$$\sigma_{OD} = k(2\alpha_2 + 1) \text{ , } \tau_{OD} = k$$

$$P = b(\overline{OA})[\sigma_{OA}\sin\beta + \tau_{OA}\cos\beta] + b(\overline{OD})[\sigma_{OD}\sin\beta + \tau_{OD}\cos\beta]$$

$$W = b(\overline{OA})[-\sigma_{OA}\cos\beta + \tau_{OA}\sin\beta] + b(\overline{OD})[\sigma_{OD}\cos\beta - \tau_{OD}\sin\beta]$$

$$(\overline{OA}) = \frac{d_1}{\sqrt{2}} = \frac{\delta_V}{\sqrt{2}}\left(\frac{d_1}{\delta_V}\right)$$

$$(\overline{OD}) = \frac{d_2}{\sqrt{2}} = \frac{\delta_V}{\sqrt{2}}\left(\frac{d_2}{\delta_V}\right)$$

$$P = \frac{b\delta_V}{\sqrt{2}}\left(\frac{d_1}{\delta_V}\right)\left[k(2\alpha_1 + 1)\sin\beta + k\cos\beta\right] + \frac{b\delta_V}{\sqrt{2}}\left(\frac{d_2}{\delta_V}\right)\left[k(2\alpha_2 + 1)\sin\beta + k\cos\beta\right]$$

$$\boxed{\frac{P}{b\delta_V k} = \left[\frac{(2\alpha_1 + 1)\sin\beta + \cos\beta}{\cos(\beta - \psi) - \sqrt{2}\sin\gamma_1} + \frac{(2\alpha_2 + 1)\sin\beta + \cos\beta}{\cos(\beta + \psi) - \sqrt{2}\sin\gamma_2}\right]\cos\psi}$$

$$W = \frac{b\delta_V}{\sqrt{2}}\left(\frac{d_1}{\delta_V}\right)\left[k\sin\beta - k(2\alpha_1 + 1)\cos\beta\right] - \frac{b\delta_V}{\sqrt{2}}\left(\frac{d_2}{\delta_V}\right)\left[k\sin\beta - k(2\alpha_2 + 1)\cos\beta\right]$$

$$\boxed{\frac{W}{b\delta_V k} = \left[\frac{\sin\beta - (2\alpha\ + 1)\cos\beta}{\cos(\beta - \psi) - \sqrt{2}\sin\gamma_1} - \frac{\sin\beta - (2\alpha_2 + 1)\cos\beta}{\cos(\beta + \psi) - \sqrt{2}\sin\gamma_2}\right]\cos\psi}$$

$\underline{\underline{\beta < \psi - \frac{\pi}{4}}}$:

$$\sigma_{OA} = \tau_{OA} = k$$

$$\alpha_1 = \gamma_1 = 0$$

ψ	β	ϵ	γ_1	γ_2	α_1	α_2	$\frac{P}{b\delta_V k}$	$\frac{W}{b\delta_V k}$	$\frac{d_1}{\delta_V}$
0°	15°	0°	5.267°	5.267°	54.73°	54.73°	4.112	0	1.691
	22.5°	0°	6.615°	6.615°	60.89°	60.89°	5.572	0	1.858
	30°	0°	7.321°	7.321°	67.68°	67.68°	7.428	0	2.062
	45°	0°	7.209°	7.209°	82.79°	82.79°	13.06	0	2.670
15°	15°	6.65°	7.603°	3.125°	37.40°	71.88°	4.151	1.494	1.680
	22.5°	13.35°	10.40°	3.200°	42.10°	79.30°	5.651	1.698	1.856
	30°	16.85°	11.56°	3.829°	48.44°	86.17°	7.654	2.094	2.001
	45°	29.55°	12.66°	3.380°	62.34°	101.6°	14.22	3.141	2.457
15°	15°	0	5.707°	4.762°	39.29°	70.24°	4.175	1.684	1.590
	22.5°	0	7.438°	5.701°	45.06°	76.80°	5.731	2.082	1.690
	30°	0	8.552°	5.987°	51.45°	84.01°	7.783	2.559	1.808
	45°	0	9.215°	5.109°	65.79°	99.89°	14.61	3.914	2.136
30°	15°	0	6.113°	4.145°	23.89°	85.86°	4.394	3.550	1.502
	22.5°	0	8.220°	4.625°	29.28°	92.88°	6.322	4.561	1.552
	30°	0	9.752°	4.455°	35.25°	100.5°	9.182	5.926	1.611
	45°	0	11.24°	2.776°	48.76°	117.2°	22.88	11.65	1.774
45°	15°	0	6.511°	3.333°	8.49°	101.7°	4.932	6.005	1.417
	22.5°	0	9.010°	3.261°	13.49°	79.24°	7.030	6.262	1.424
	30°	0	10.99°	2.566°	19.01°	117.4°	14.08	13.205	1.436
	45°	-	-	-	-	-	-	-	-
60°	15°	0	6.936°	2.138°	0°	117.9°	6.698	4.472	1.318
	22.5°	0	9.873°	1.348°	0°	126.2°	16.57	23.21	1.284
	30°	-	-	-	-	-	-	-	-
	45°	-	-	-	-	-	-	-	-

Table A-4 Rough/Lip Slip Line Field Solution for Infinite Wedge

Smooth Wedge with Lip Formation (Figures A-13 to A-17)

$\beta > \psi + \gamma_1$:

$$(\overline{OM}) = \delta_V\cos\psi + d_1\sin\gamma_1 \qquad (\overline{OM}) = (\overline{OA})\cos(\beta - \psi) = d_1\cos(\beta - \psi)$$

$$(\overline{OL}) = \delta_V\cos\psi + d_2\sin\gamma_2 \qquad (\overline{OL}) = (\overline{OE})\cos(\beta + \psi) = d_2\cos(\beta + \psi)$$

$$d_1\cos(\beta - \psi) = \delta_V\cos\psi + d_1\sin\gamma_1$$

$$d_2\cos(\beta + \psi) = \delta_V\cos\psi + d_2\sin\gamma_2$$

$$\boxed{\begin{aligned} \frac{d_1}{\delta_V} &= \frac{\cos\psi}{\cos(\beta - \psi) - \sin\gamma_1} \\ \frac{d_2}{\delta_V} &= \frac{\cos\psi}{\cos(\beta + \psi) - \sin\gamma_2} \end{aligned}} \qquad (1)$$

$$b_1 = (\overline{BI})\sin\gamma_1 \qquad (\overline{BI}) = d_1\cos\gamma_1 + (\overline{OA})\sin(\beta - \psi) + \delta_V\cos\psi\tan(\varepsilon + \psi)$$

$$b_2 = (\overline{FI})\sin\gamma_2 \qquad (\overline{FI}) = d_2\cos\gamma_2 + (\overline{OE})\sin(\beta + \psi) - \delta_V\cos\psi\tan(\varepsilon + \psi)$$

$$b_1 = [d_1\cos\gamma_1 + d_1\sin(\beta - \psi) + \delta_V\cos\psi\tan(\varepsilon + \psi)]\sin\gamma_1$$

$$b_2 = [d_2\cos\lambda_2 + d_2\sin(\beta + \psi) - \delta_V\cos\psi\tan(\varepsilon + \psi)]\sin\gamma_2$$

$$\boxed{\begin{aligned} \frac{b_1}{\delta_V} &= \left[(\cos\gamma_1 + \sin(\beta - \psi))\frac{d_1}{\delta_V} + \cos\psi\tan(\varepsilon + \psi)\right]\sin\gamma_1 \\ \frac{b_2}{\delta_V} &= \left[(\cos\gamma_2 + \sin(\beta + \psi))\frac{d_2}{\delta_V} - \cos\psi\tan(\varepsilon + \psi)\right]\sin\gamma_2 \end{aligned}} \qquad (2)$$

$$v_1 = [v\sin(\beta + \varepsilon)]\sqrt{2}$$

$$v_2 = [v\sin(\beta - \varepsilon)]\sqrt{2}$$

let $t = \frac{\kappa}{v}$

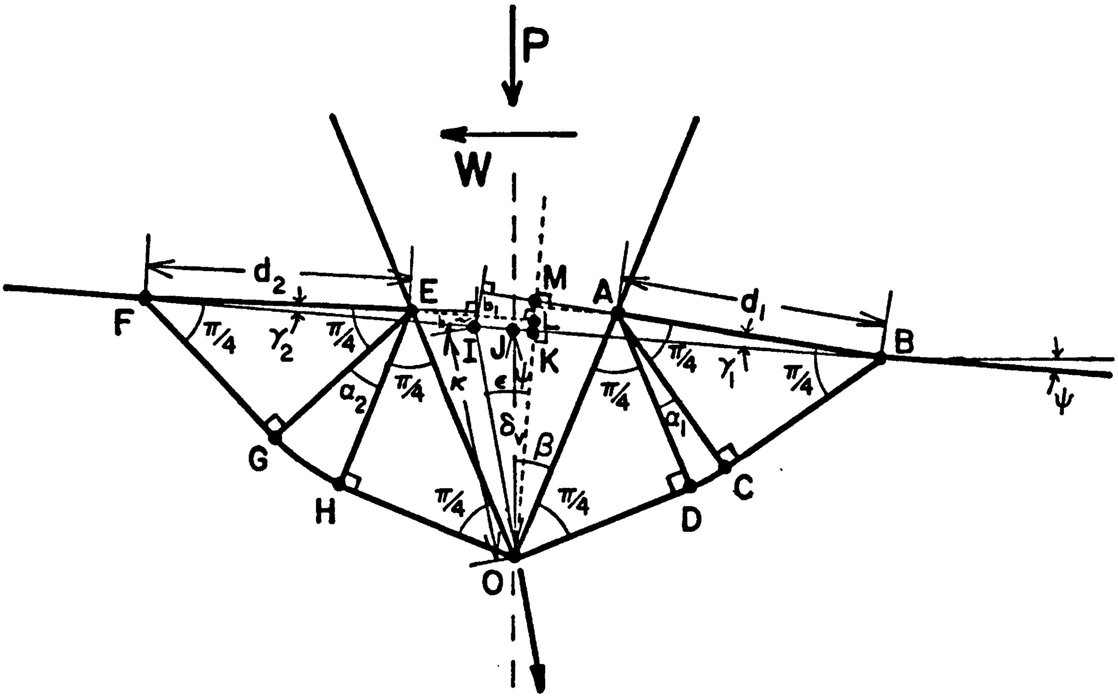

Figure A-13 Smooth/Lip Slip Line Field

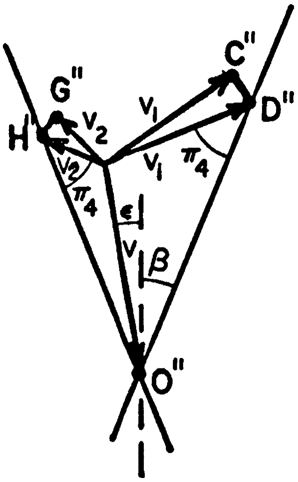

Figure A-14 Smooth/Lip Hodograph

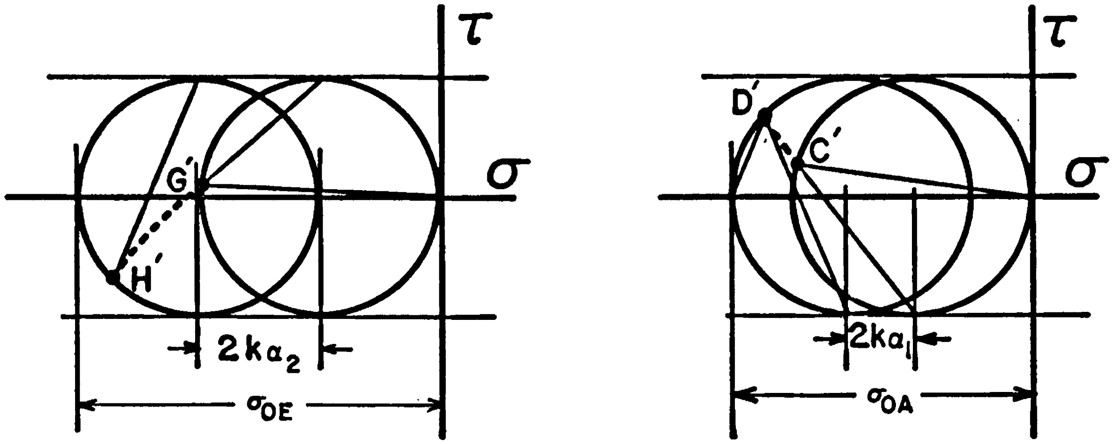

Figure A-15 Smooth/Lip Stress Plane

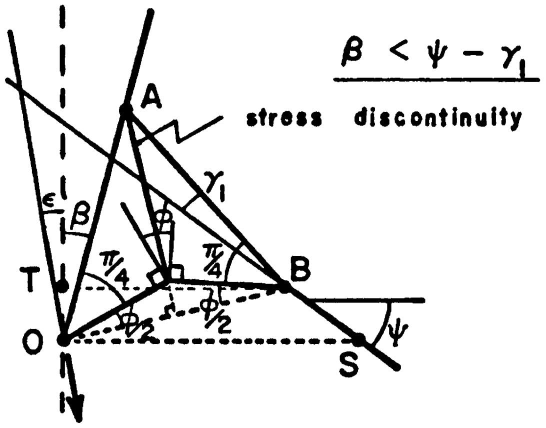

Figure A-16 Extreme Inclination Smooth/Lip Slip Line Field

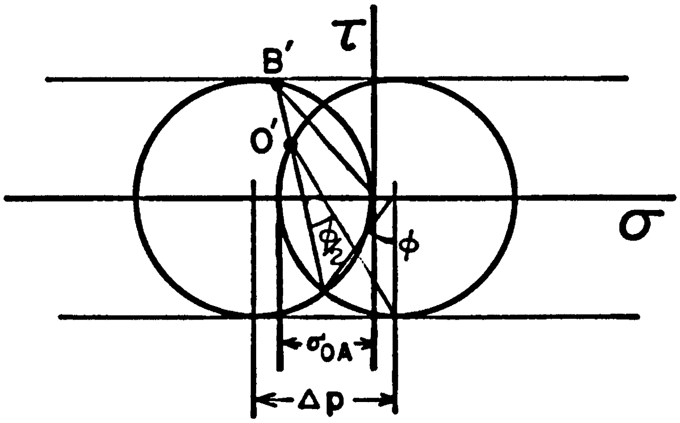

Figure A-17 Extreme Inclination Smooth/Lip Stress Plane

$$b_1 = \frac{v_1 t}{\sqrt{2}} \qquad b_2 = \frac{v_2 t}{\sqrt{2}}$$

$$b_1 = vt\sin(\beta + \epsilon) \quad b_2 = vt\sin(\beta - \epsilon)$$

$$b_1 = \kappa\sin(\beta + \epsilon) \quad b_2 = \kappa\sin(\beta - \epsilon)$$

$$\kappa = \delta_V \cos\psi \sec(\psi + \epsilon)$$

$$\boxed{\begin{aligned} \frac{b_1}{\delta_V} &= \frac{\cos\psi\sin(\beta + \epsilon)}{\cos(\psi + \epsilon)} \\ \frac{b_2}{\delta_V} &= \frac{\cos\psi\sin(\beta - \epsilon)}{\cos(\psi + \epsilon)} \end{aligned}} \tag{3}$$

Combine (1), (2), (3) to find γ

Summing angles about A, E:

$$\frac{\pi}{4} + \alpha_1 + \frac{\pi}{4} + (\frac{\pi}{2} - \beta) + \psi + \gamma_1 = \pi$$

$$\frac{\pi}{4} + \alpha_2 + \frac{\pi}{4} + (\frac{\pi}{2} - \beta) - \psi + \gamma_2 = \pi$$

$$\boxed{\begin{aligned} \alpha_1 &= \beta - \psi - \gamma_1 \\ \alpha_2 &= \beta + \psi - \gamma_2 \end{aligned}}$$

$$\sigma_{OA} = 2k(\alpha_1 + 1) \quad , \tau_{OA} = 0$$

$$\sigma_{OE} = 2k(\sigma_2 + 1) \quad , \tau_{OE} = 0$$

$$P = b(\overline{OA})[\sigma_{OA}\sin\beta + \tau_{OA}\cos\beta] + b(\overline{OE})[\sigma_{OE}\sin\beta + \tau_{OE}\cos\beta]$$

$$W = b(\overline{OA})[-\sigma_{OA}\cos\beta + \tau_{OA}\sin\beta] + b(\overline{OE})[\sigma_{OE}\cos\beta - \tau_{OE}\sin\beta]$$

$$(\overline{OA}) = d_1 = \delta_V\left(\frac{d_1}{\delta_V}\right) \qquad (\overline{OE}) = d_2 = \delta_V\left(\frac{d_2}{\delta_V}\right)$$

$$P = b\delta_V\left(\frac{d_1}{\delta_V}\right)[2k(\alpha_1 + 1)\sin\beta] + b\delta_V\left(\frac{d_2}{\delta_V}\right)[2k(\alpha_2 + 1)\sin\beta]$$

$$\boxed{\frac{P}{b\delta_V k} = 2\cos\psi\sin\beta\left[\frac{\alpha_1 + 1}{\cos(\beta - \psi) - \sin\gamma_1} + \frac{\alpha_2 + 1}{\cos(\beta + \psi) - \sin\gamma_2}\right]}$$

$$W = b\delta_V\left(\frac{d_1}{\delta_V}\right)[-2k(\alpha_1 + 1)\cos\beta] + b\delta_V\left(\frac{d_2}{\delta_V}\right)[2k(\alpha_2 + 1)\cos\beta]$$

$$\boxed{\frac{W}{b\delta_V k} = 2\cos\psi\cos\beta\left[\frac{\alpha_2 + 1}{\cos(\beta + \psi) - \sin\gamma_2} - \frac{\alpha_1 + 1}{\cos(\beta - \psi) - \sin\gamma_1}\right]}$$

$\underline{\underline{\beta < \psi - \gamma_1}}$:

$$\angle TBO = \angle BOS$$

$$\frac{\phi}{2} - \left[\psi - \left(\frac{\pi}{4} - \gamma_1\right)\right] = \frac{\pi}{2} - \beta - \frac{\pi}{4} - \frac{\phi}{2}$$

$$\boxed{\phi = \psi - \beta + \gamma_1}$$

$$\Delta p = 2k\sin\phi$$

$$\Delta p - k = k - \sigma_{OA}$$

$$\sigma_{OA} = 2k(1 - \sin\phi)\ ,\ \tau_{OA} = 0$$

$$\boxed{\begin{aligned} \frac{P}{b\delta_V k} &= 2\cos\psi\sin\beta\left[\frac{1 - \sin(\psi - \beta + \gamma_1)}{\cos(\beta - \psi) - \sin\gamma_1} + \frac{\alpha_2 + 1}{\cos(\beta + \psi) - \sin\gamma_2}\right] \\ \frac{W}{b\delta_V k} &= 2\cos\psi\cos\beta\left[\frac{\alpha_2 + 1}{\cos(\beta + \psi) - \sin\gamma_2} - \frac{(1 - \sin(\psi - \beta + \gamma_1))}{\cos(\beta - \psi) - \sin\gamma_1}\right] \end{aligned}}$$

$\varepsilon = 0$

ψ	β	γ_1	γ_2	α_1	α_2	$\frac{P}{b\delta_V k}$	$\frac{W}{b\delta_V K}$	$\frac{d_1}{\delta_V}$
0°	15°	9.570°	9.570°	5.430°	5.430°	1.417	0	1.251
	22.5°	11.69°	11.69°	10.81°	10.81°	2.523	0	1.368
	30°	12.66°	12.66°	17.34°	17.34°	4.028	0	1.546
	45°	12.06°	12.06°	32.94°	32.94°	8.942	0	2.007
15°	15°	10.50°	8.529°	-	21.47°	1.458	1.708	1.181
	22.5°	13.33°	9.925°	-	27.58°	2.636	2.150	1.269
	30°	15.00°	10.20°	0°	34.80°	4.295	2.708	1.366
	45°	15.62°	8.444°	14.38°	51.56°	10.212	4.485	1.619
30°	15°	11.37°	7.300°	-	37.70°	1.605	3.573	1.126
	22.5°	14.92°	7.914°	-	44.59°	3.061	4.692	1.180
	30°	17.34°	7.467°	-	52.53°	5.352	6.270	1.234
	45°	19.30°	4.530°	-	70.47°	16.97	13.40	1.363
45°	15°	12.22°	5.748°	-	54.25°	1.966	5.966	1.081
	22.5°	16.54°	5.469°	-	62.03°	4.235	8.712	1.106
	30°	19.80°	4.223°	-	70.78°	9.020	13.95	1.127
	45°	-	-	-	-	-	-	-
60°	15°	13.08°	3.587°	-	71.41°	3.044	10.75	1.040
	22.5°	18.26°	2.205°	-	80.30°	10.12	23.77	1.042
	30°	-	-	-	-	-	-	-
	45°	-	-	-	-	-	-	-

Table A-5 Smooth/Lip Slip Line Field Solution for Infinite Wedge

Appendix B

Design and Stress Analysis of Experimental Equipment

The loading rod assembly was designed to maximize the strain reading from the load cell while minimizing the horizontal flexibility. The load cell was designed for a factor of safety of two. To calculate the load cell stresses a combination of pure bending and uniaxial compression was assumed. The only stress, then, is the axial normal stress. Energy methods are used to estimate the horizontal flexibilities of the loading rod assembly as a whole. The most important conclusion from the flexibility calculations is the estimate of errors in horizontal deflection measurements (δ_ϕ, $\delta_\perp$) due to the location of measurement at a distance x_δ above the wedge.

$$\text{error } (e_\delta) = 9.6x_\delta\%, \quad x_\delta \text{ in inches}$$

The flexibility estimation is below the actual flexibility of the assembly due to simplifications which had to be made to obtain an estimate using available methods.

The jack rack assembly was designed to be able to apply a horizontal load to the wedge in order to force vertical wedge travel. A stress analysis is conducted for a maximum jack force of 1000 lbf to show that all stresses are below yield.

The remaining components of experimental equipment are listed at the end of this appendix.

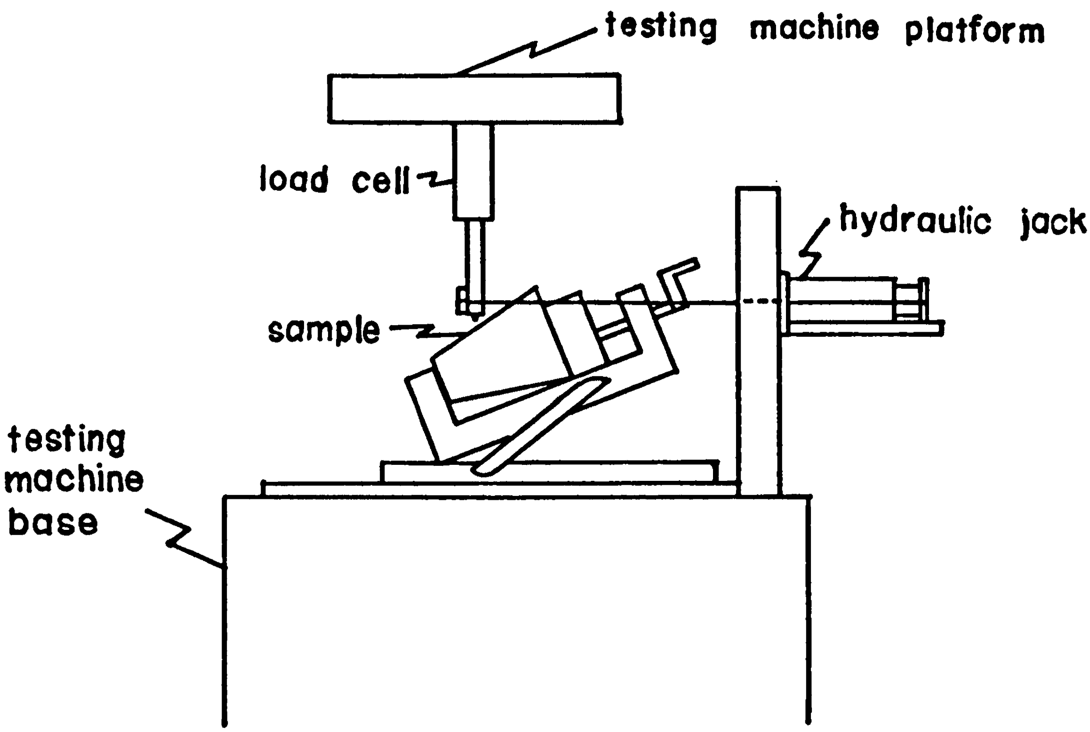

Figure B-1 General Experimental Set-Up

Design and Stress Analysis of Experimental Equipment

<u>Loading Rod Assembly (Figures B-2, B-3)</u>

Stress Analysis of Load Cell (Figure B-4)

bending

$$\sigma_{max} = \frac{P_H L_0 R_2}{I} \qquad I = \frac{\pi}{4}(R_2^4 - R_1^4)$$

$$\sigma_{max} = \frac{4}{\pi} P_H L_0 \frac{R_2}{R_2^4 - R_1^4}$$

compression

$$\sigma_{max} = \frac{P_V}{\pi(R_2^2 - R_1^2)}$$

combined

$$\sigma_{max} = \frac{4}{\pi} \frac{L_0 R_2}{(R_2^4 - R_1^4)} P_H + \frac{1}{\pi(R_2^2 - R_1^2)} P_V$$

$L_0 = 10.9"$

$R_1 = 1.108"$

$R_2 = 1.171"$

$$\boxed{\sigma_{max} = 43.6P_H + 2.22P_V}$$

$\sigma_{yp} = 40{,}000$psi

F.S. = 2

$\sigma_{max} < 20{,}000$psi

Table B-1 shows the maximum allowable P_H for a given P_V such that $\sigma_{max} < 20{,}000$psi

Horizontal Flexibility of Loading Rod Assembly (Figure B-5)

δ_1 due to bending of 3 and 5:

$U \equiv$ strain energy

$$\delta_1 = \frac{\partial U}{\partial P_H} = \int_0^L \frac{M}{EI} \frac{\partial M}{\partial P_H} dx = \int_{10}^{L_1} \frac{M}{E_1 I_1} \frac{\partial M}{\partial P_H} dx + \int_{L_1}^{L_1 + L_2} \frac{M}{E_2 I_2} \frac{\partial M}{\partial P_H} dx$$

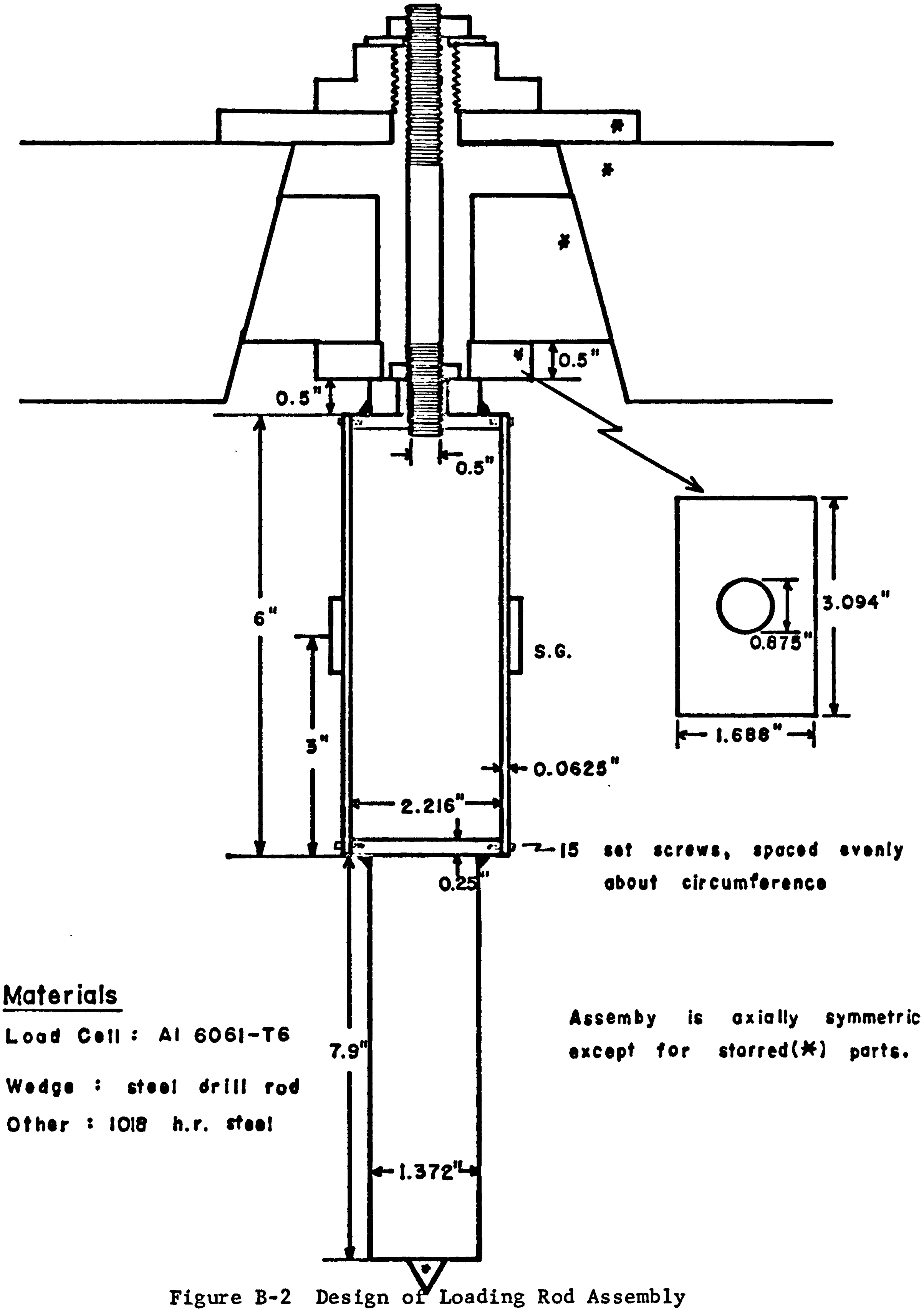

Materials

Load Cell : Al 6061-T6

Wedge : steel drill rod

Other : 1018 h.r. steel

Assemby is axially symmetric except for starred(*) parts.

Figure B-2 Design of Loading Rod Assembly

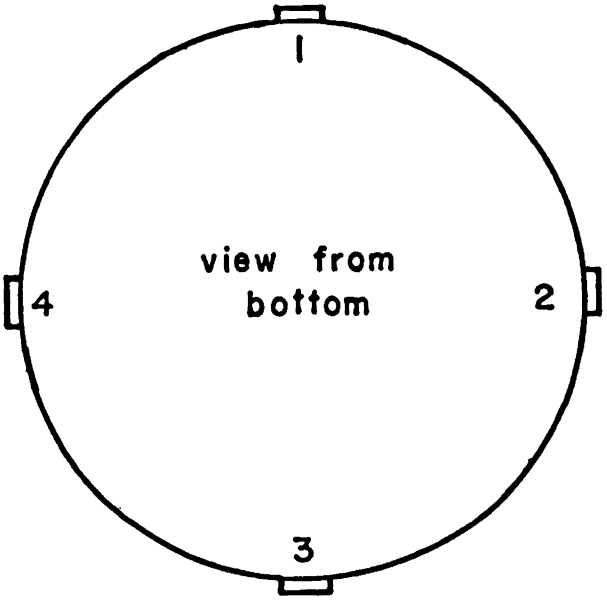

Gages 1, 3 : M-M CEA-06-250UW-120

R = 120 ± 0.3 %

F = 2.065 ± 0.5 % (@ 75°F)

Gages 2, 4 : M-M CEA-06-250UW-120

R = 120 ± 0.3 %

F = 2.105 ± 0.5 % (@ 75°F)

Figure B-3 Load Cell Strain Gages

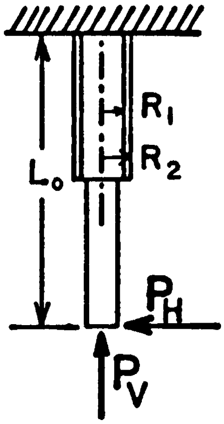

Figure B-4 Stress Analysis of Load Cell

P_V(lbf)	max. allow. P_H(lbf)
100	454
500	433
1000	408
1500	382

Table B-1 Maximum Allowable Horizontal Loads on Load Cell

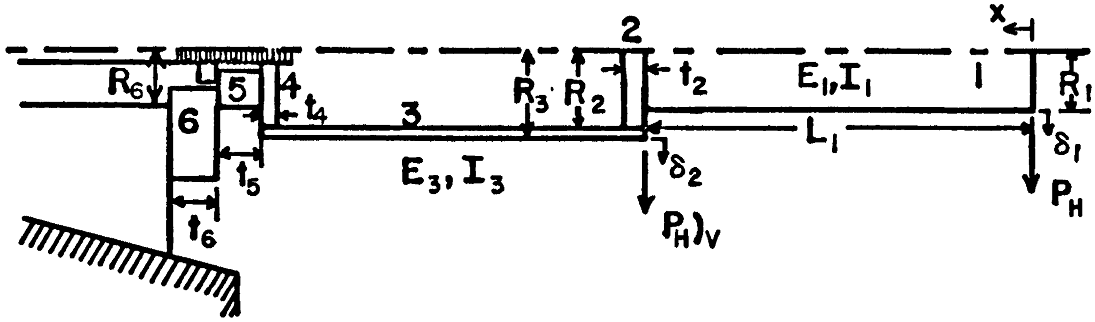

Figure B-5 Maximum Deflection Analysis of Loading Rod Assembly

$L_1 = 7.9''$ $\qquad$ $R_1 = 0.686''$

$L_2 = 6''$ $\qquad$ $R_2 = 1.108''$

$E_1 = 30 \times 10^6\text{psi}$ $\qquad$ $R_3 = 1.171''$

$E_2 = 20 \times 10^6\text{psi}$

$$I_1 = \frac{\pi R_1^{\;4}}{4} = 0.174 \text{ inches}^4$$

$$I_2 = \tfrac{1}{4}\pi(R_3^{\;4} - R_2^{\;4}) = 0.293 \text{ inches}^4$$

$M = P_H x$ for $x \leq L_1$

$M = P_H x + [P_H)_v](x - L_1)$ for $x \geq L_1$ (but $P_H)_v = 0$)

$\delta_1 = 0.000156P_H$

Calculation of error in δ_ϕ, $\delta_\perp$ measurements due to location of measurement at x_δ above wedge:

$$\delta_2 = \frac{\partial U}{\partial P_H)_v} = \int_{L_1}^{L_1 + L_2} \left[\frac{P_H x(x - L_1)}{E_2 I_2} \right] dx$$

$P_H)$ is a virtual load

$$\delta_2 = \frac{P_H}{E_2 I_2} \left[\tfrac{1}{3} x^3 - \tfrac{1}{2} x^2 L_1 \right] \Bigg|_{L_1}^{L_1 + L_2} = 0.000037P_H$$

$$\text{error } (e_\delta) = \frac{x_\delta}{L_1} \left(\frac{\delta_1 - \delta_2}{\delta_1} \right) = \underline{\underline{9.6x_\delta\%}}$$

δ_V due to deformation of 2([28], p. 368, #21)

$$\theta = \frac{\alpha M}{Et^3}$$

$\alpha = 0.031$

$E = 30 \times 10^6\text{psi}$

$t = t_2 = 0.25''$

$\delta_1 \sim L_1 \theta$

$M = P_H L_1$

$$\delta_1 = P_H \frac{L_1^{\;2}\alpha}{ET^3} = 4.13 \times 10^{-6} P_H$$

δ_V due to deformation of 4, 5, 6 ([28], p. 368, #21):

For purposes of calculation, model plate 6 as circular with outer radius $R_7 = 0.844''$ ($R_6 \equiv 0.438''$)

(A gross misapplication of the solution is understood, but a more accurate method was unavailable).

plates 4, 5 : $\theta_{4-5} = \frac{\alpha M}{ET^3}$ $\qquad \alpha = 0.373$

$$\frac{P_H}{\theta_{4-5}} = 2.10 \times 10^5 \equiv k_{4-5} \quad \text{a "spring constant"}$$

plate 6 : $\theta_6 = \frac{\alpha M}{ET^3}$ $\qquad \alpha = 0.05$

$$\frac{P_H}{\theta_6} = 5 \times 10^6 \equiv k_6$$

$$k_T = [k_{4-5}{}^{-1} + k_6{}^{-1}] = 2 \times 10^5 \quad \text{a total "spring" constant}$$

$$\delta_1 = 14\theta = 14\frac{P_H}{k_T} = 0.00007P_H$$

Summation of contributions to δ_1 calculated above gives:

$$\delta_1 = 0.00023P_H$$

Check with the results of the calibration test (Table C-1):

$P_H = 10$ lb, $\qquad \delta_1 = 0.0023$ calculated

$\qquad\qquad\qquad \delta_1 = 0.0040$ actual

Jack Rack Assembly (Figures B-6 to B-14)

The system was designed to be safe for horizontal jack loads in excess of 1000 lb, it was tested at 750 lb, and use was restricted to loads less than 500 lb. The entire assembly was fabricated from 1018 H.R. steel with $\sigma_{yp} = 40{,}000$ psi. The vise holding the indentation sample was designed to be bolted to the base.

(1) Base (Figure B-8)

Assume a maximum wedge load of $P_V = 2000$ lbf. The area of the vise is approximately 240 in.^{2} Then $P_2 \cong \frac{2000 \text{ lbf}}{240 \text{ in.}^2} = 8.3$psi. For a maximum

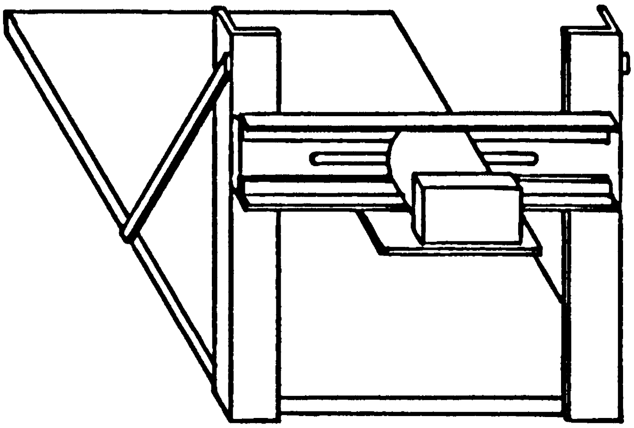

Figure B-6 Hydraulic Jack Rack Assembly

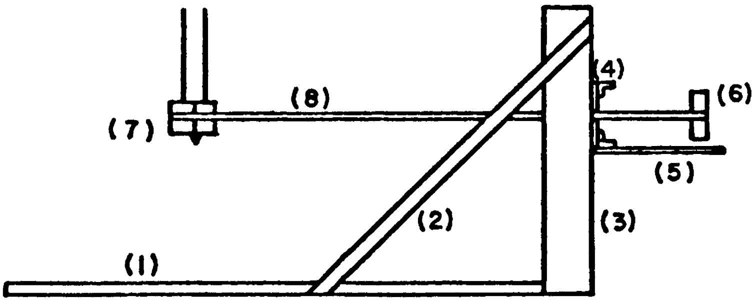

Figure B-7 Jack Rack Assembly Components

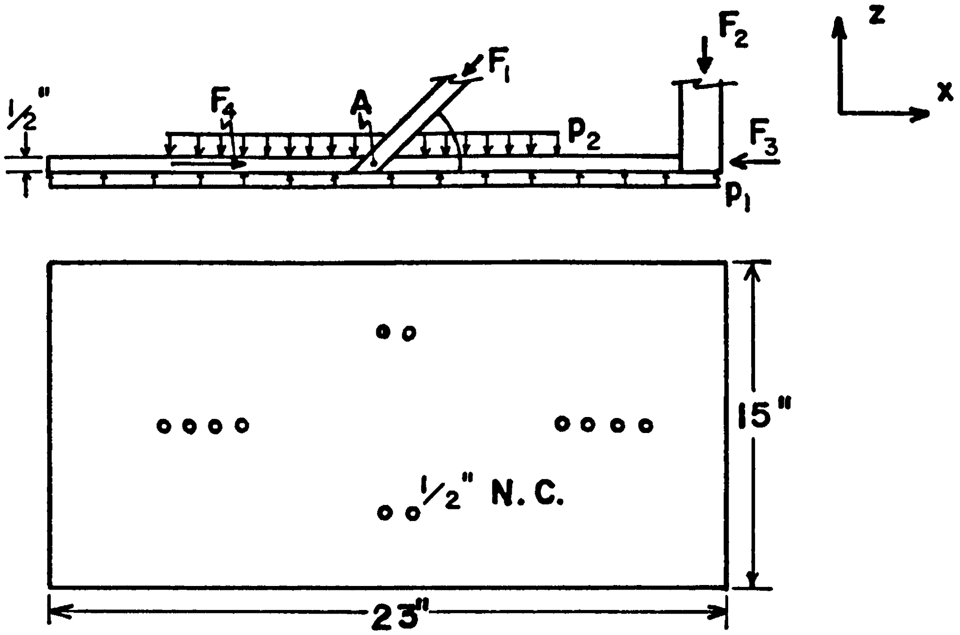

Figure B-8 Design and Stress Analysis of Base (1)

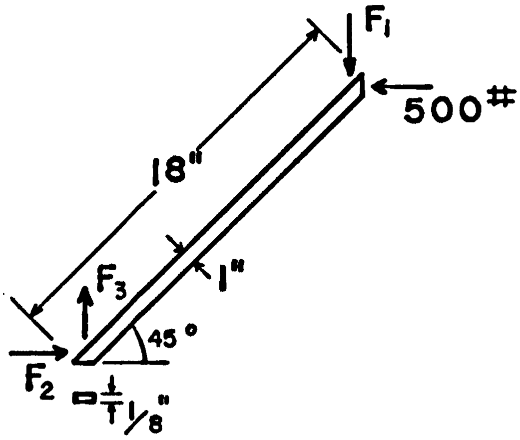

Figure B-9 Design and Stress Analysis of Brace (2)

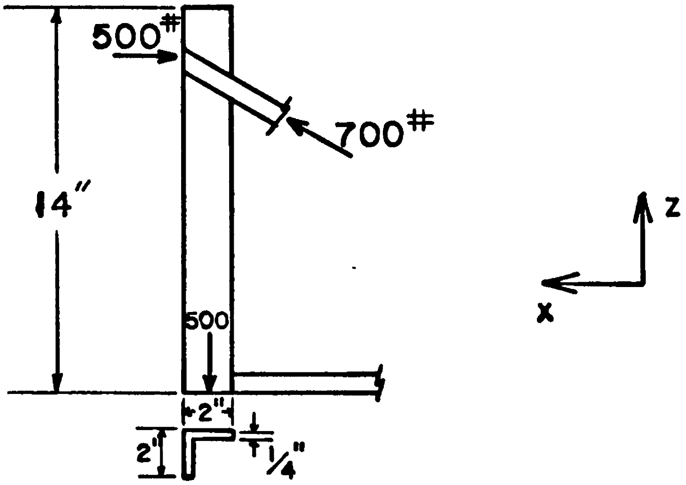

Figure B-10 Design and Stress Analysis of Stanchion (3)

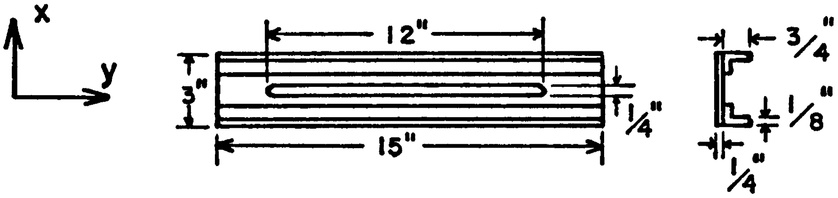

Figure B-11 Design and Stress Analysis of Jack Stand (4)

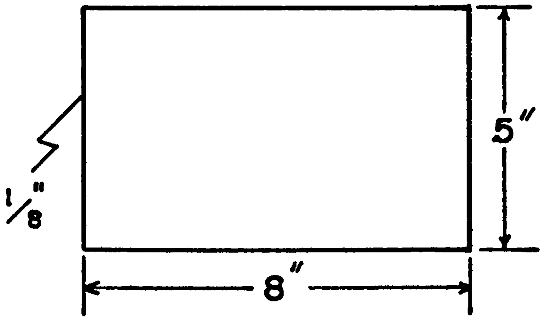

Figure B-12 Design of Jack Support (5)

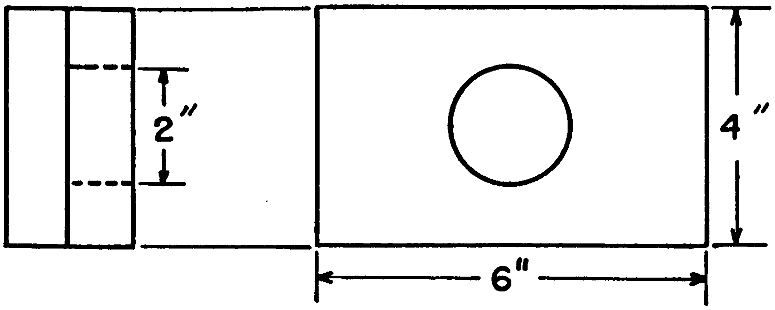

Figure B-13 Design of Jack Cap (6)

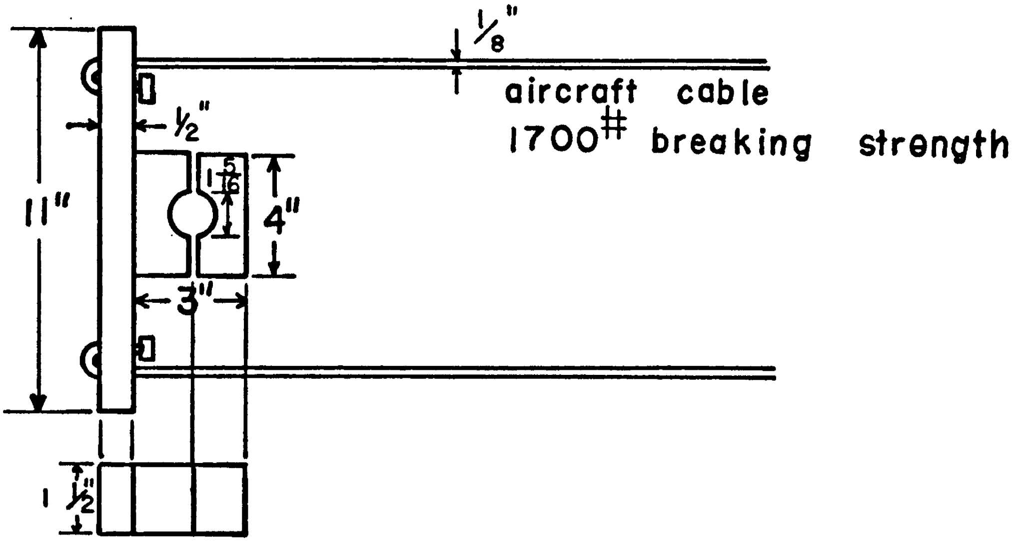

Figure B-14 Design of Wedge Collar (7) and Cable (8)

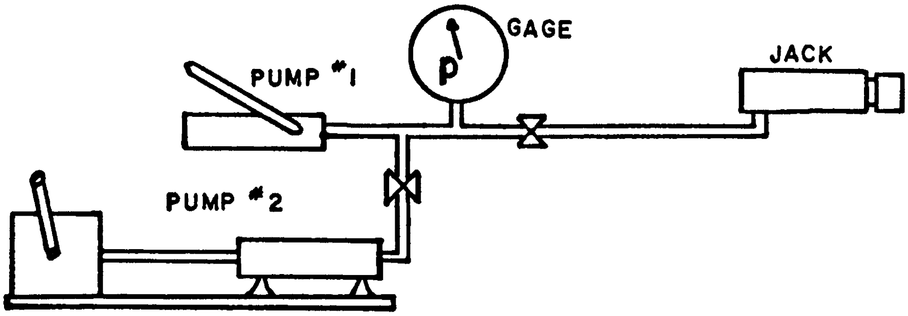

Figure B-15 Design of Hydraulic Pressure System jack load of 1000 lbf applied to the top of the rack, $F_1 \cong$ 700 lbf, $F_2 \cong$ -500 lbf, $F_3 \cong$ 0 lbf, and F_4 (horizontal load on bolts) $\cong$ 500 lbf. The maximum stress in the base will be at point A. At this point,

$$\sigma_x = \frac{F_1 \cos 45^\circ}{(\text{area})_x} \cong \frac{500 \text{ lbf}}{3.75 \text{in}^2} = 133 \text{ psi}$$

and $$\sigma_y = \frac{F_1 \cos 45^\circ}{(\text{area})_y} + p_2 = \frac{500 \text{ lbf}}{7.5 \text{ in}^2} + 8.3\text{psi.} = 75\text{psi.}$$

These stresses are well below yield.

(2) Brace (Figure B-9)

The worst stress situation will occur when a horizontal load of 500 lbf is supported at the top of the brace. For this case, $F_1 = F_2 = F_3 = 500$ lbf and the maximum normal axial stress can be calculated,

$$\sigma_{max} = \frac{(F_2 + F_3)\cos 45^\circ}{\text{area}} = \frac{700 \text{ lbf}}{1/8 \text{ in}} = 5600\text{psi}$$

This stress is well below yield.

(3) Stanchion (Figure B-10)

The worst stress situation occurs at the base for a horizontal load of 500 lbf applied at the brace. The stresses are,

$$\sigma_z = \frac{500 \text{ lbf}}{(\text{area})_z} \cong \frac{500 \text{ lbf}}{1 \text{ in.}^2} = 500 \text{ psi}$$

$$\sigma_x = \frac{700 \text{ lbfcos}45^\circ}{(\text{area})_x} \cong \frac{500 \text{ lbf}}{1/2 \text{ in}^2} = 1000\text{psi.}$$

These stresses are well below yield.

(4) Jack Stand (Figure B-11)

Pure bending is considered for the beam consisting of one angle plus 1/2 of the plate.

$$\sigma_{max} = \frac{M_{max} C}{I}$$

The slot is 12" long and the jack is 2" in diameter which gives a maximum moment arm of 1/2(12" - 2") = 5" when jack is in the center of the stand. For P_H = 1000 lbf, the maximum moment in the beam (1/4 of the jack stand) is $M_{max} = \frac{1000 \text{ lbf}}{4}$ (5 in.) = 1250 in.-lbf.

The position of the centroid (and neutral axis) for the beam cross section can be calculated to be 0.244" from the back of the plate. The moment of inertia (I) and C can then be calculated as

$$I = 0.0251 \text{ in.}^4$$

$$C = 0.756"$$

The maximum stress then is readily found.

$$\sigma_{max} = \frac{(1250)(0.756)}{(0.0251)} = 37{,}600\text{psi.}$$

This stress is below yield with a factor of safety of,

$$\text{F.S.} = \frac{\sigma_{yp}}{\sigma_{max}} = \frac{40{,}000}{37{,}600} = 1.06$$

Welds

The most critical weld joins the brace to the base. The area of the weld is estimated as $A = 0.75 \text{ in}^2$. For an axial force in the brace of $F = 700$ lbf, the maximum shear stress in the weld can be estimated.

$$\tau = \frac{F}{A} = \frac{700 \text{ lbf}}{0.75 \text{ in}^2} = 930\text{psi.}$$

This stress is well below yield.

Jack Pressure System (Figure B-15)

Pump 1: Enerpac, Model #F39, 10000 psi capacity

Pump 2: Ruska, Model #2260, 25000 psi capacity

Gauge: Ashcraft, 30 psi, 5psi per division, can be read to ± 0.5psi.

Jack: Enerpac, 2" displacement

Pressure fittings all high pressure capacity

Strain Gage Instrumentation

BLH Digital Strain Indicator, Model #1200, can be read to ± 1μ inches/inches

BLH Switching and Balancing Unit, Model #1225

Displacement Instrumentation

Lufkin Dial Indicators -- Model #J380-1, 1" displacement
-- Model #J380-2, 2" displacement

Testing Machine

Riehle FS-60 60,000 lb universal screw power testing machine

Variable Inclination Vise

Palmgren, Model #3, Type H-D

Appendix C

Preliminary Studies for the Wedge Indentation Tests

Load Cell Calibration

The loading rod assembly was fitted into the testing machine (as shown in Appendix B) and a dead weight - pulley apparatus assembled as in (Figure C-1). The horizontal deflection was measured with a dial indicator mounted as close as possible to the wedge.

$\varepsilon \propto M = P_H \ell$ ℓ = distance from strain gages to point of applied force

$P_H = C\frac{\varepsilon}{\ell}$ C = strain - moment proportionality constant

$$P_x = C_{13}\frac{\varepsilon_{13}}{\ell}$$

$$P_y = C_{24}\frac{\varepsilon_{24}}{\ell}$$

It was assumed that applied forces P_x and P_y would not be perfectly aligned with $\underset{\sim}{i}$ and $\underset{\sim}{j}$, so the following correction scheme was devised (Figure C-2).

P_x', P_y' are the actual applied forces

$$e_{13} = \tan^{-1}\frac{\varepsilon_{42}}{\varepsilon_{13}} \qquad e_{24} = \tan^{-1}\frac{\varepsilon_{13}}{\varepsilon_{24}}$$

$$P_x = P_x' \cos e_{13} \qquad P_y = P_y' \cos e_{24}$$

In every calibration test, $e_{13} \cong e_{24} \cong 0$, and $P_x = P_x'$, $P_y = P_y'$.

To conduct a test a load was hung across the pulley in 5 lb. increments to 50 lb and readings recorded for δ_x (or δ_y), ε_{24}, and ε_{31}. Table C-1 shows a sample set of calibration data. Readings for δ_x (or δ_y) are taken to directly measure the flexibility of the loading rod assembly and are used later in the experiment to adjust data and evaluate errors. x_δ is significant because the deflection measured is less than the deflection at the wedge by 9.6 x_δ% (Appendix B). Note $C_{31} = C_{13}$, $\varepsilon_{24} = \varepsilon_{42}, \ldots$

To be as accurate as possible, a calibration would have to be conducted immediately preceding each session of testing. However, strain gage readings were not of primary importance in the wedge indentation tests and calibrations were conducted only at the beginning of the experimental study.

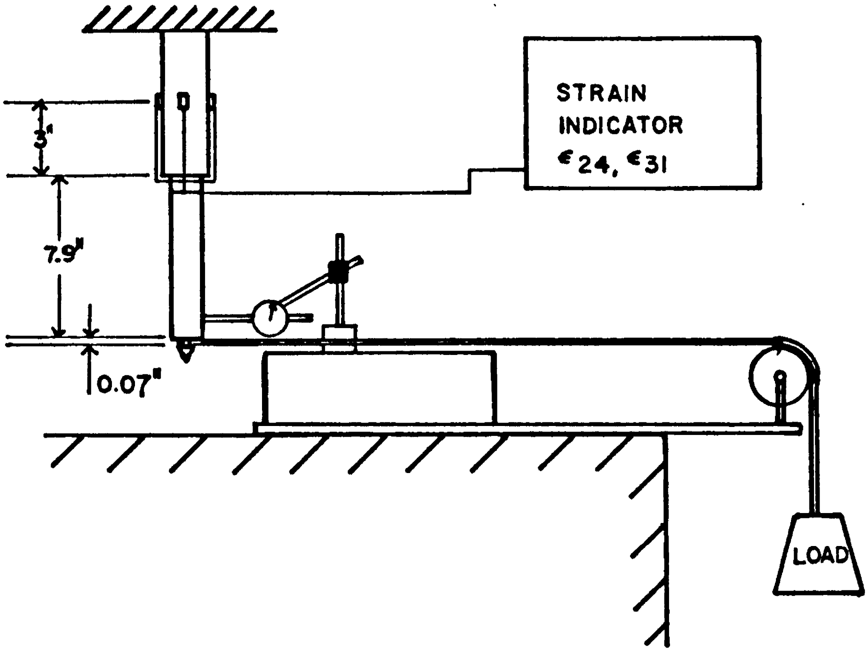

Figure C-1 Load Cell Calibration Set

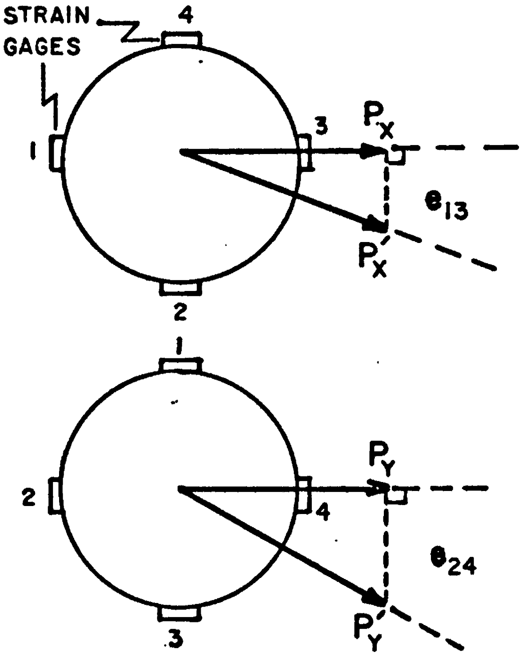

Figure C-2 Inaccuracies in Load Cell Calibration Set-Up

P_x'(lbf)	$-\delta_x$(in)	ϵ_{24}	ϵ_{31}	e_{13}	P_x(lbs)	C_{31}
0	0	0	0	-	0	-
5	0.0020	1	42	0.0238	5	1.306
10	0.0040	1	85	negligible	10	1.291
15	0.0063	1	128	-	15	1.286
20	0.0090	1	171	-	20	1.283
25	0.0120	2	214	-	25	1.282
30	0.0150	2	257	-	30	1.281
35	0.0180	3	301	-	35	1.276
40	0.0210	4	340	-	40	1.291
45	0.0243	4	382	-	45	1.292
50	0.0285	5	426	-	50	1.288
0	0.0017	3	1	-	0	

$\ell = 10.97''$ $X_\delta = 1.34''$ $C_{31} = 1.288 \pm 0.008$

Table C-1 Sample Load Cell Calibration

Hydraulic Jack Calibration

The jack with pressure connections in place was set upright in the testing machine as shown on the calibration graph (Figure C-3).

F_c = calibration force
p = jack pressure
x_o = jack displacement

Each test was conducted by adjusting the jack pressure with the testing machine off (constant displacement). The pressure was always increasing during the first half of the test and solely decreasing throughout the latter portion of the test. Four tests were run, for $x_o \cong 0.01''$, $0.5''$, $1.0''$, and $1.5''$. Actually, x_o changed $\pm \sim \frac{1}{2}\%$ during each test due to system flexibilities. For a given pressure, the force was always greater upon unloading than when loading. It was assumed the difference was due to frictional effects in the jack. Since only increasing loads were of concern in the wedge indentation tests, the data for increasing pressure was used exclusively. Each test yielded a linear relationship of p to F_c and the results are presented in the form of a calibration graph (Figure C-3).

Coefficient of Friction Test

The coefficient of friction (μ) for the interface of two materials can be determined, in principle, by placing a block of one material on a plate made from the second material and inclining the plate either until slippage initiates (static test) or until a constant velocity of the block is observed (kinetic). The coefficient of friction is just the tangent of the inclination angle.

For this test a steel plate, oiled and wiped clean, was selected to model the oiled steel wedge (oiled to prevent corrosion) and the block was an antimonial lead indentation test specimen (50 lb ingot). The inclination was gradually adjusted by a vise as shown (Figure C-4), and a machinist's level - protractor was used to measure the slope. Only the kinetic friction coefficient was required for the plasticity analysis. As the result of four tests,

$$\mu = 0.169 \pm 0.009$$

Methods of Determining Equilibrium Compressive Strength of Lead

The first method is to find the best fit curve of the following form, to satisfy the boundary conditions:

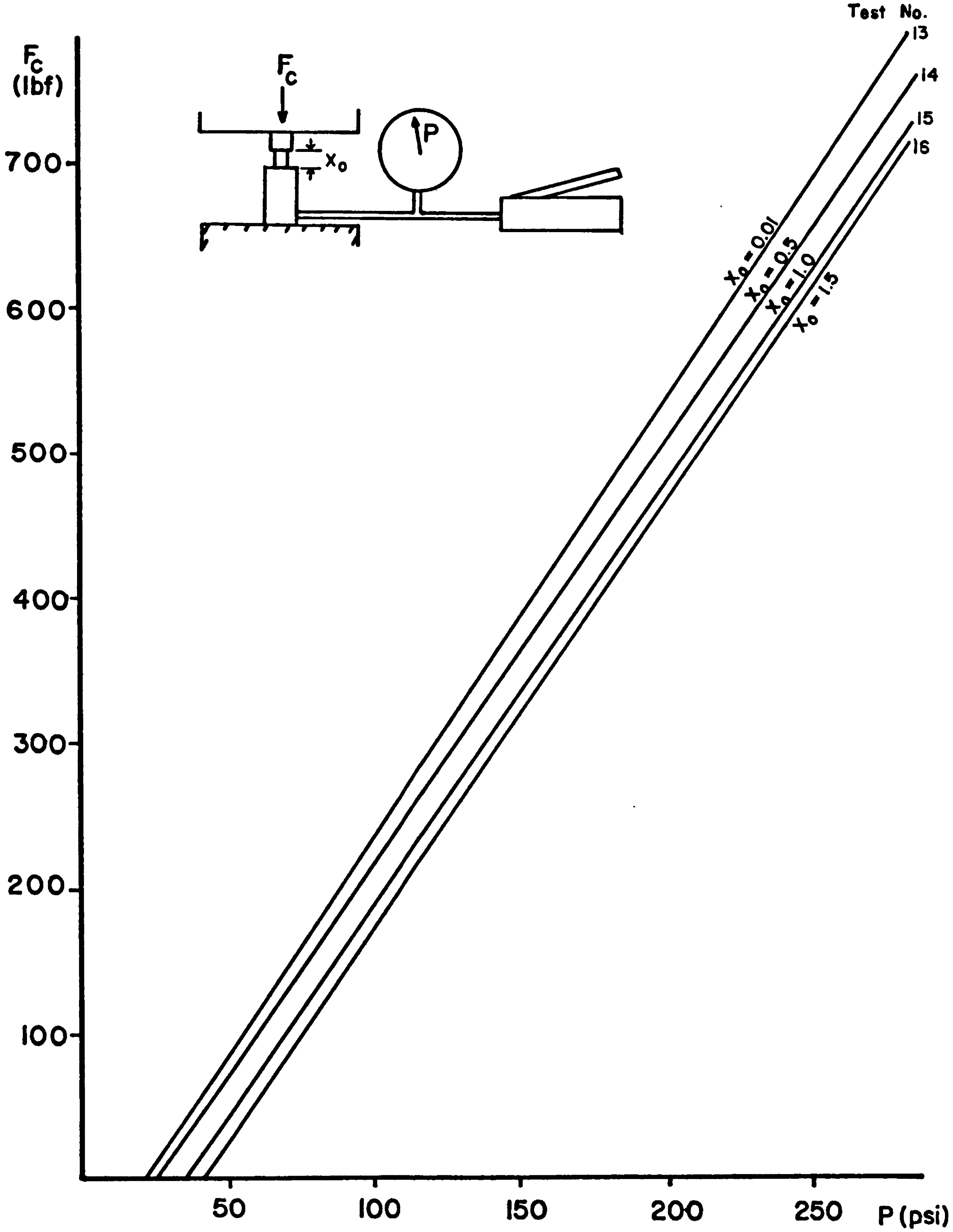

Figure C-3 Hydraulic Jack Calibration

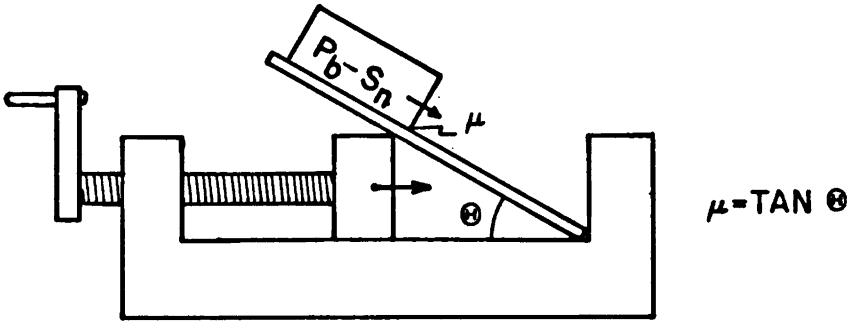

Figure C-4 Coefficient of Friction Test

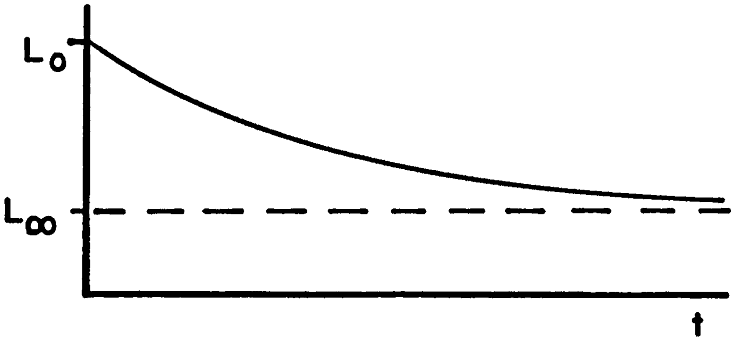

Figure C-5 Assumed Relaxation Curve, Method 1

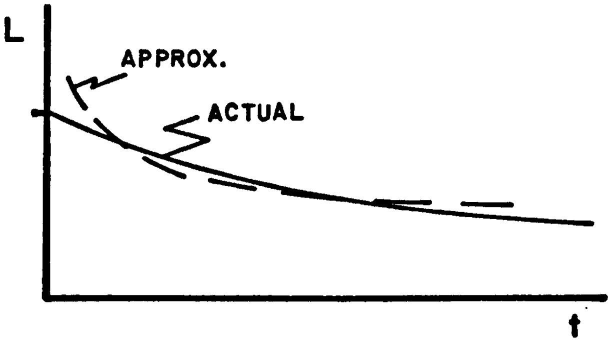

Figure C-6 Approximation to Relaxation Curve, Method 2

DATA: Test #23, $\delta = 0.3017$

t(min)	L(lbf)
0	13880
¼	12770
½	12470
1	12130
2	11730
3	11490

Table C-2 Sample Compression Test Data

Assumed L_∞ (lbf)	n	L_∞ from graph (lbf)
11500	0.95	10480
9000	0.29	6880
7000	0.22	3880
5000	0.19	3380
3000	0.17	2580
1000	0.15	0
0	0.146	0

Table C-3 Determination of L_∞, Method 1

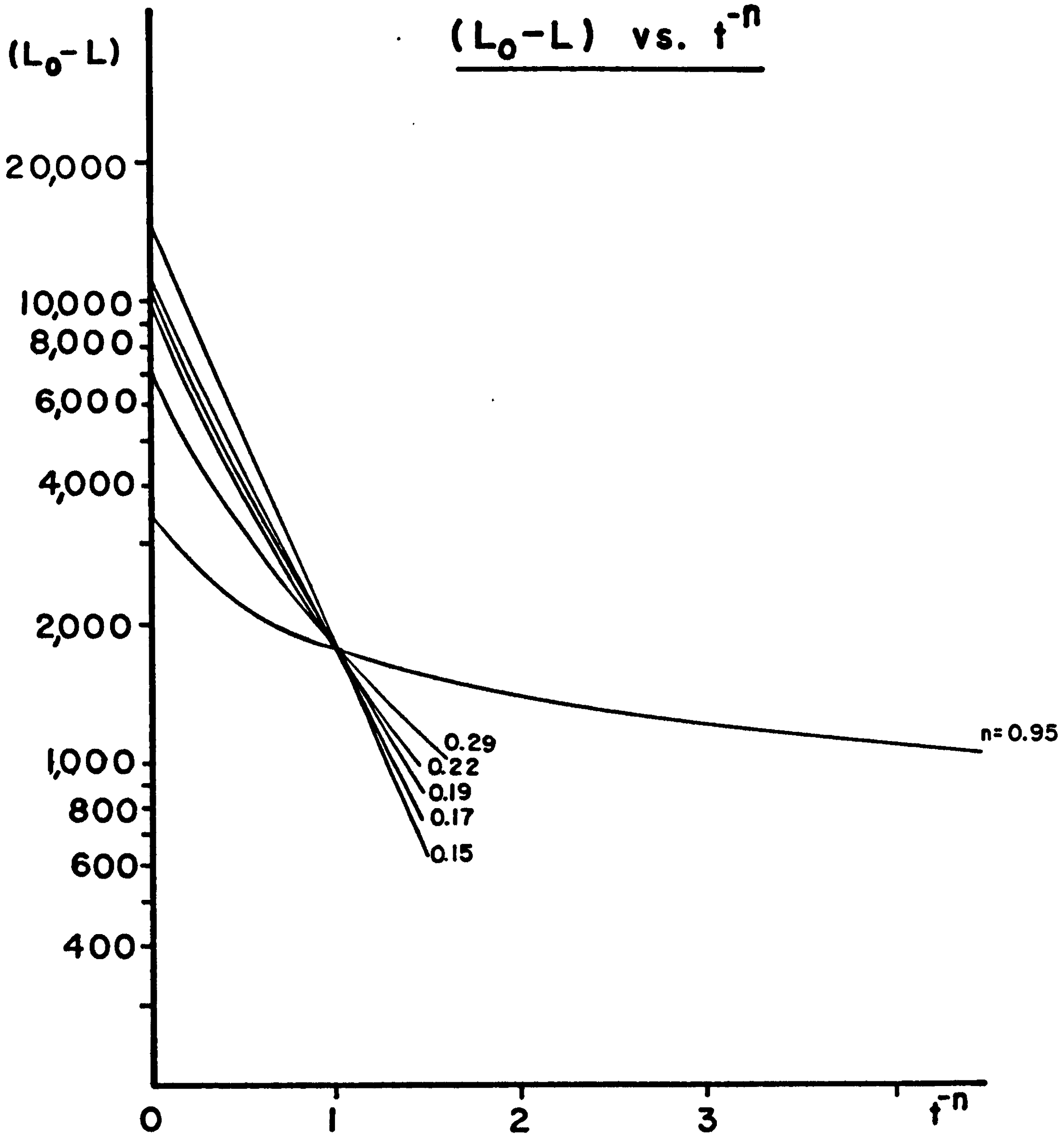

Figure C-7 Graphical Determination of L_∞ , Method 1

DATA: Test #12, δ = 0.500" (Presented in graphical form, Figure 37)

L(lbf)	t (min)	t^{-1}	t^{-2}
3430	0	-	-
3370	¼	4.00	16.0
3310	½	2.00	4.00
3240	1	1.00	1.00
3160	2	0.500	0.250
3110	3	0.333	0.111
3070	4	0.250	0.0625
3040	5	0.200	0.0400
3010	6	0.167	0.0278
2990	7	0.143	0.0204
2970	8	0.125	0.0156
2955	9	0.111	0.0123
2940	10	0.100	0.0100
2925	11	0.0909	0.00826
2910	12	0.0833	0.00694
2895	13	0.0769	0.00592
2890	14	0.0714	0.00510

Results of linear regression:

	L_∞	2978	3014

Table C-4 Determination of L_∞, Method 2

$L = L_o$ at $t = o$, $L \rightarrow L_\infty$ as $t \rightarrow \infty$ (Figure C-5).

$$\frac{L_o - L}{L_o - L_\infty} = 10^{-ct^{-n}} \qquad n > o, \; c = \text{constant}$$

Take logarythms twice.

$$\mathrm{Log}\left[\mathrm{Log}\left(\frac{L_o - L_\infty}{L_o - L}\right)\right] = \mathrm{Log}c - n\mathrm{Log}t$$

n is determined by a linear regression analysis of

$$\mathrm{Log}\left[\mathrm{Log}\left(\frac{L_o - L_\infty}{L_o - L}\right)\right] \text{ vs. } \mathrm{Log}t$$

using an assumed value of L_∞. Then a plot is made of $\mathrm{Log}(L_o - L)$ vs. t^{-n}. $L_o - L_\infty$ is read off the graph at $t^{-n} = o$ and compared with the assumed value. Tables C-2, C-3 and the resulting curves in Figure C-7 illustrate the procedure for sample data. The only conclusions which can be made are either that the material can support no significant load in compression for an indefinite period of time, or that the method is unsuccessful.

The second attempt at finding the load is to use an inverse relationship curve to approximate the relaxation curve (Figure C-6). A linear regression analysis of L vs. t^{-n} is conducted to determine L_∞ for a sample set of data, the results presented in Table C-4. This method is obviously unsuccessful, for the predicted L_∞ is greater than the load at $t = 14$ min.

Appendix D
Error Analysis

Significant Errors

$k \pm 1100$ psi

$\delta_V \pm 0.002''$, $\pm 0.005''$ on Test #83

$P_V \pm (6 + 0.05(|\epsilon_{24}| + |\epsilon_{31}|))$ lbf

$b \pm 0.001$

$P_H \pm (14 + 0.05|\epsilon_\perp| + 100(|\delta_\phi| + |\delta_\perp|) + e_1 + e_2)$ lbf

e_1 = change due to $x_o \rightarrow 0.75\ x_o$ (Tests 25 - 72)

e_2 = change due to $p \rightarrow 0.95p$ (Tests 49 - 83)

$\epsilon_\perp$ = component of ϵ_{24}, ϵ_{31} in $\underset{\sim}{e}_\perp$ direction

$\beta \pm 0.05^\circ$

$\psi_x \pm 1.0^\circ$

$\psi_y \pm 1.0^\circ$

$\mu \pm 0.01^\circ$

Insignificant Errors

$C_{mn} \pm 0.02$

$t \pm$ (up to 5 sec for several tests)

$\delta_\phi \pm (0.004$ in $+ 10\%\ \delta_\phi)$ ditto for $\delta_\perp$

$h \pm 0.01''$

Sources of Errors

$k \pm 1100$ psi : errors in compression tests, relaxation properties, and rigid - plastic model

$\delta_V \pm 0.0002$: : reading accuracy

± 0.002 : zero adjustment (wedge partially indented at $\delta_V = 0$)

± 0.005 : zero adjustment (Test 83)

$P_V \pm 1$ lbf : reading accuracy

± 5 lbf : final "zero" readings in error (machine error)

$\pm 0.05(|\epsilon_{24}| + |\epsilon_{31}|)$: estimate of behavior for non-vertical indentation

$P_H \pm 2.5$ lbf : error in jack calibration

± 4 lbf : due to $x_o \pm 0.1''$

± 5 lbf : due to relaxation, control difficulties for p

$P_H \pm e_1$: change due to $x_o \rightarrow 0.75\ x_o$ (Tests 25 - 72)

$\pm e_2$: change due to $p \rightarrow 0.95p$ (Tests (49 - 83)

± 2 lbf : due to $\varepsilon_{mn} \pm 15\mu$ in/in

$\pm 0.05|\varepsilon_\perp|$
$\pm 100(|\delta_\phi| + |\delta_\perp|)$: estimate of behavior for non-vertical indentation

$b \pm 0.001$: measurement

$\beta \pm 0.5^\circ$: measurement

$\psi_x \pm 1.0^\circ$
$\psi_y \pm 1.0^\circ$: measurement, sample surface not exactly level

$\mu \pm 0.01$: standard deviation of friction test data

$C_{mn} \pm 0.02$:deviation in calibration tests

$h \pm 0.01''$: measurement

$\delta_\phi \pm 0.0002''$: measurement

± 0.0040 : final "zero" readings in error

$\pm 10\%\delta_\phi$: due to $x_\delta \neq 0$

$\delta_\perp \pm 0.0002''$: measurement

± 0.0040 : final "zero" readings in error

$\pm 10\%\delta_\perp$: due to $x_\delta \neq 0$

$t \pm 1$ sec : measurement

$\pm < 5$ sec : measurement (various tests)

$x_o \pm 0.1$: measurement

$\varepsilon_{mn} \pm 15\mu$ in/in : final "zero" readings in error

$P_V \pm 20$ lbf : measurement (Test 36, $\delta_V = 0.10$)

Basic Calculation Method:

$$F = F(x_1, x_2, \ldots x_n)$$

$$|\Delta F| \leq \sum_{i=1}^{n} \left|\frac{\partial F}{\partial x_i}\right| \, |\Delta x_i|$$

Appendix E

Data Deletions

Tests 1-7	(faulty procedure - max. forces recorded)
Tests 8-12, 14, 16-18	(compression tests on lead)
Test 13	(friction test, lead - steel)
Test 15	(test on rock samples)
Test 19	(indentation w/pure lead - good test)
Test 20	(compressor test, another testing machine
Test 21	(friction test, PbSn - steel)
Test 28: $\delta_V = 0.0275$	(sample non-uniformity)
Tests 29-30	(indentation tests w/comp. test samples - to obtain strain-haedening props.)
Test 31: $\delta_V = 0.1017$	(sample non-uniformity)
Test 32	(chip formation, possible variations in sample props.)
Tests 39-48	(faulty procedure, must force wedge vertically, redesign exp.)
Tests 51-54	(vise slipping, bolt to base)
Test 57: $\delta_V = 0.0951$	(abrupt drop in P_V while loading)
Test 64	(high speed loading)
Test 68: $\delta_V = 0.1391$	(collar touching sample)
Test 71	(faulty dial indicator)
Test 74	(initial indentation depth too great for valid test)
Test 76: $\delta_V > 0.09$	(wedge slipped in machine jaws)
Test 77	(collar touching sample)
Test 78: $\delta_V > 0.05$	(sample slipped in vise)
Test 79: $\delta_V > 0.07$	(sample slipped in vise)
Test 80: $\delta_V > 0.07$	(collar touching sample)
Test 83: $\delta_V > 0.145$	(collar touching sample)
Test 84: $\delta_V = 0.1868$	(collar touching sample)
Test 85: $\delta_V > 0.05$	(sample slipped in vise)
Test 86: $\delta_V > 0.06$	(sample slipped in vise)

Test 87: $\delta_V > 0.196$ (collar touching sample)
Test 88: $\delta_V > 0.17$ (collar touching sample)
Test 91: $\delta_V > 0.14$ (collar touching sample)

Appendix F

Complete Force - Deflection Wedge Indentation Results

Wedge Indentation Tests

Test	β	ψ_x	ψ_y
25	15°	0	0
31	15°	0	0
37	15°	0	0
26	22.5°	0	0
33	22.5°	0	0
34	22.5°	0	0
27	30°	0	0
35	30°	0	0
28	45°	0	0
36	45°	0	0
49	15°	15°	0
50	15°	30°	0
96	15°	30°	0
55	15°	45°	0
56	15°	54°	0
57	22.5°	15°	0
59	22.5°	30°	0
58	22.5°	45°	0
60	22.5°	54°	0
61	30°	15°	0
62	30°	30°	0
63	30°	45°	0
65	45°	15°	0
66	45°	30°	0
97	45°	30°	0
67	15°	0	15°
95	15°	0	15°
68	15°	0	30°
69	15°	0	45°
70	15°	0	54°
75	22.5°	0	5°

Test	β	ψ_x	ψ_y
72	22.5°	0	15°
73	22.5°	0	15°
76	15°	30°	5°
88	15°	30°	20°
89	15°	45°	20°
90	22.5°	30°	20°
91	22.5°	30°	45°
84	30°	15°	20°
87	30°	15°	45°
78	30°	30°	5°
94	30°	30°	5°
79	30°	30°	10°
80	30°	30°	20°
81	30°	30°	30°
82	30°	30°	45°
83	30°	30°	55°
86	30°	45°	20°
85	30°	45°	45°
92	45°	30°	20°
93	45°	30°	45°

KEY FOR ALL GRAPHS

UNITS

δ_V — in

P_V, P_H — lbf

THEORETICAL CURVE	———
LIMIT TO THEORETICAL PREDICTION UNCERTAINTY	— —
EXPERIMENTAL DATA	•
EXPERIMENTAL ERROR LIMITS	☐

Chart F-1 Interpretation Key for Force-Deflection Plots

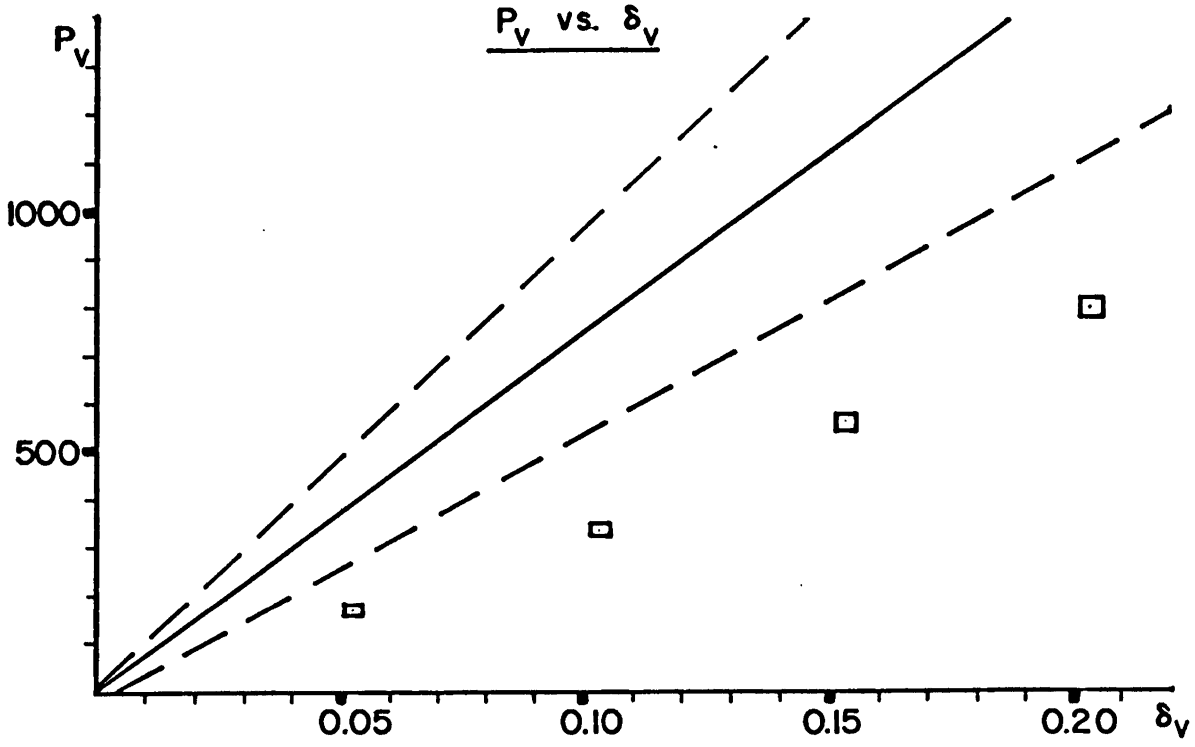

Figure F-1 Force-Deflection, Test 25, $\beta = 15^\circ$, $\psi_x = 0$, $\psi_y = 0$

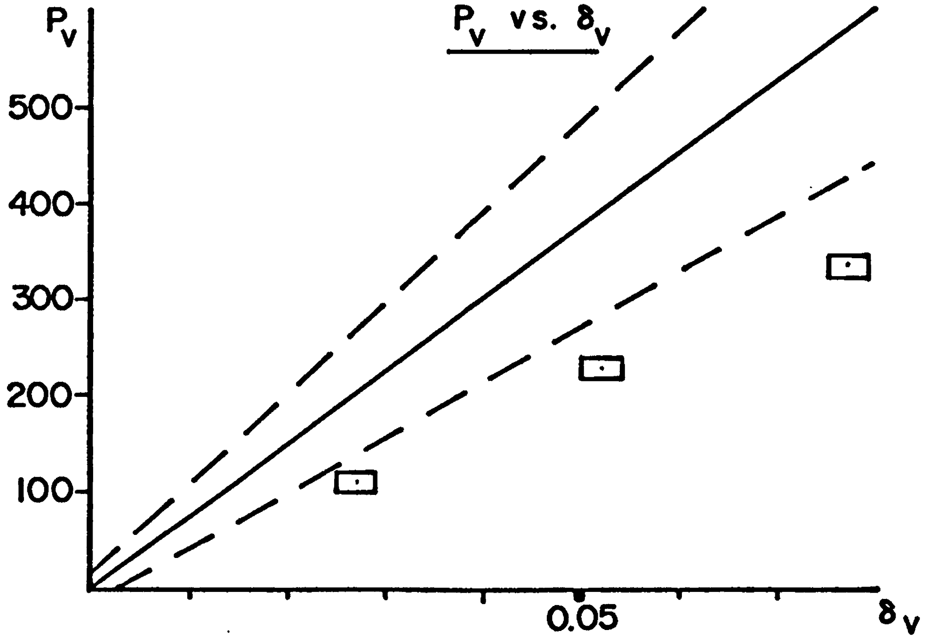

Figure F-2 Force Deflection, Test 31, $\beta = 15^\circ$, $\psi_x = \psi_y = 0$

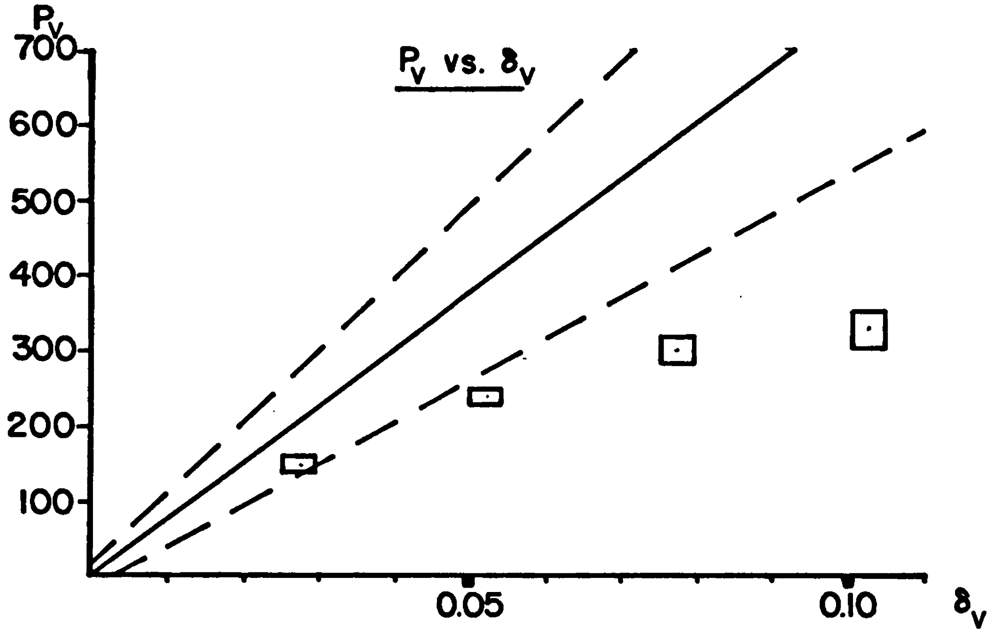

Figure F-3 Force-Deflection, Test 37 , $\beta = 15^\circ$, $\psi_x = 0$, $\psi_y = 0$

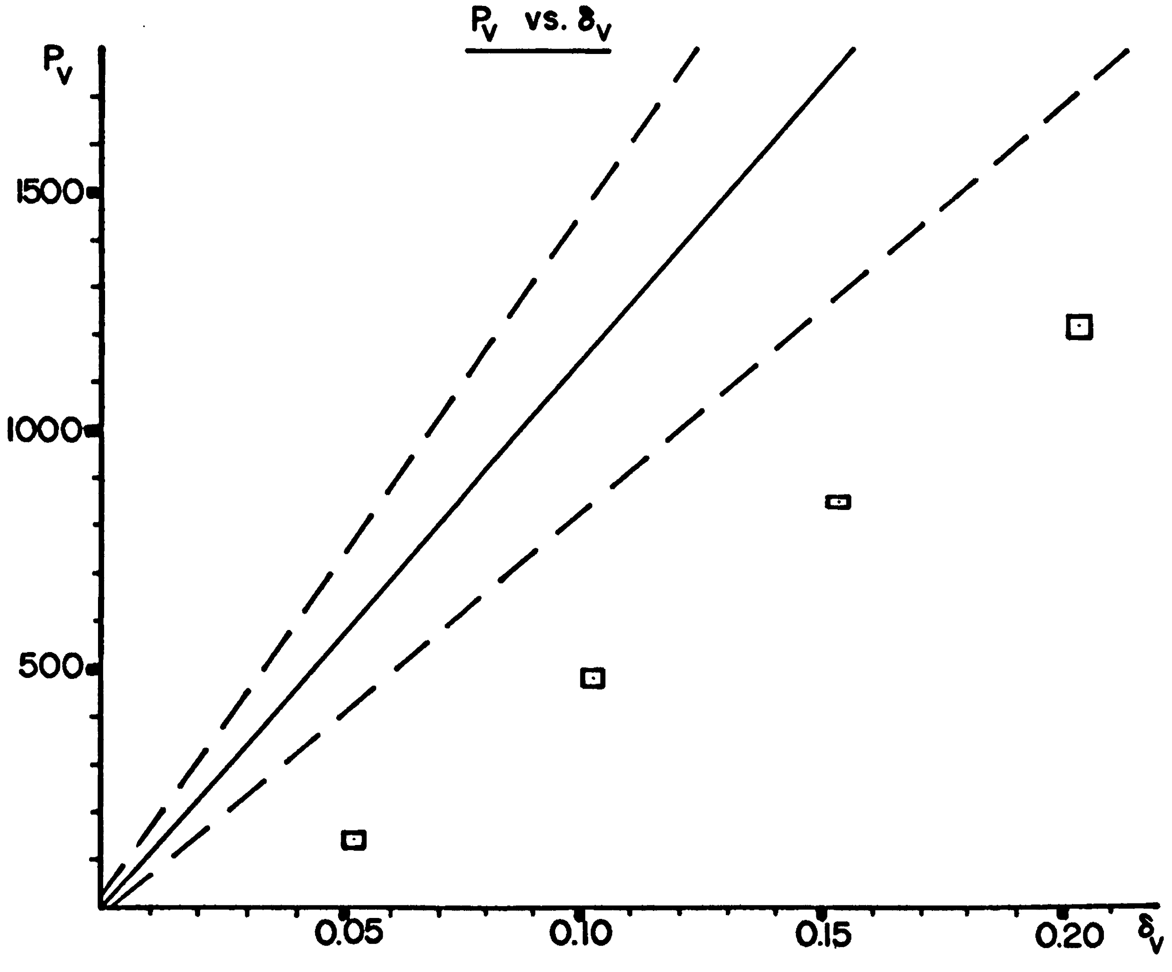

Figure F-4 Force-Deflection , Test 26 , $\beta = 22.5^\circ$, $\psi_x = 0$, $\psi_y = 0$

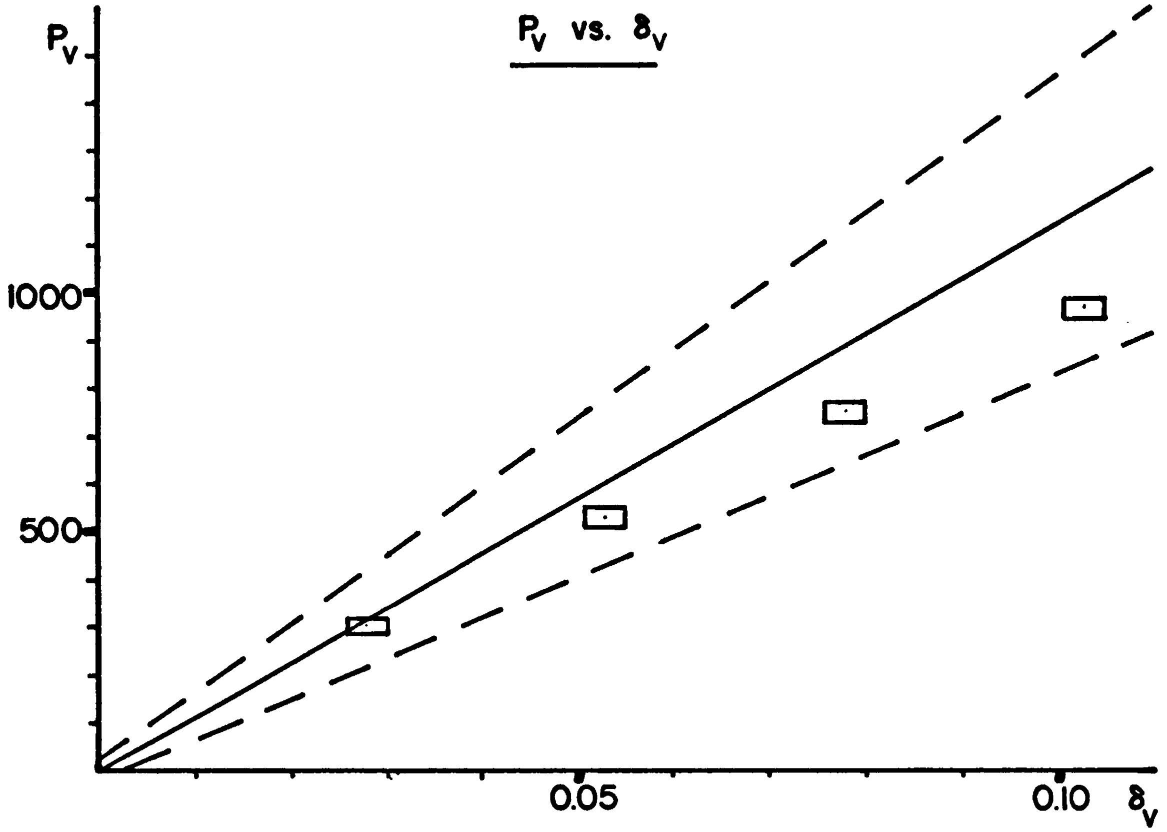

Figure F-5 Force-Deflection, Test 33 , β = 22.5° , ψ_x = 0 , ψ_y = 0

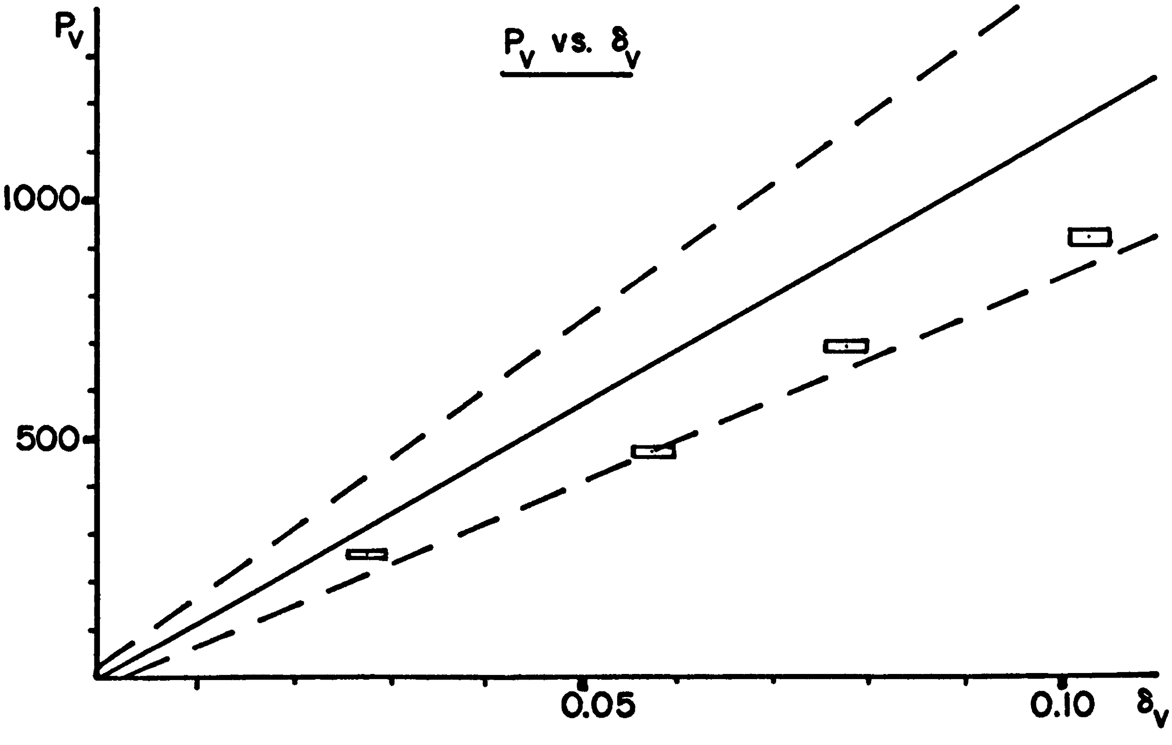

Figure F-6 Force-Deflection, Test 34 , β = 22.5° , ψ_x = 0 , ψ_y = 0

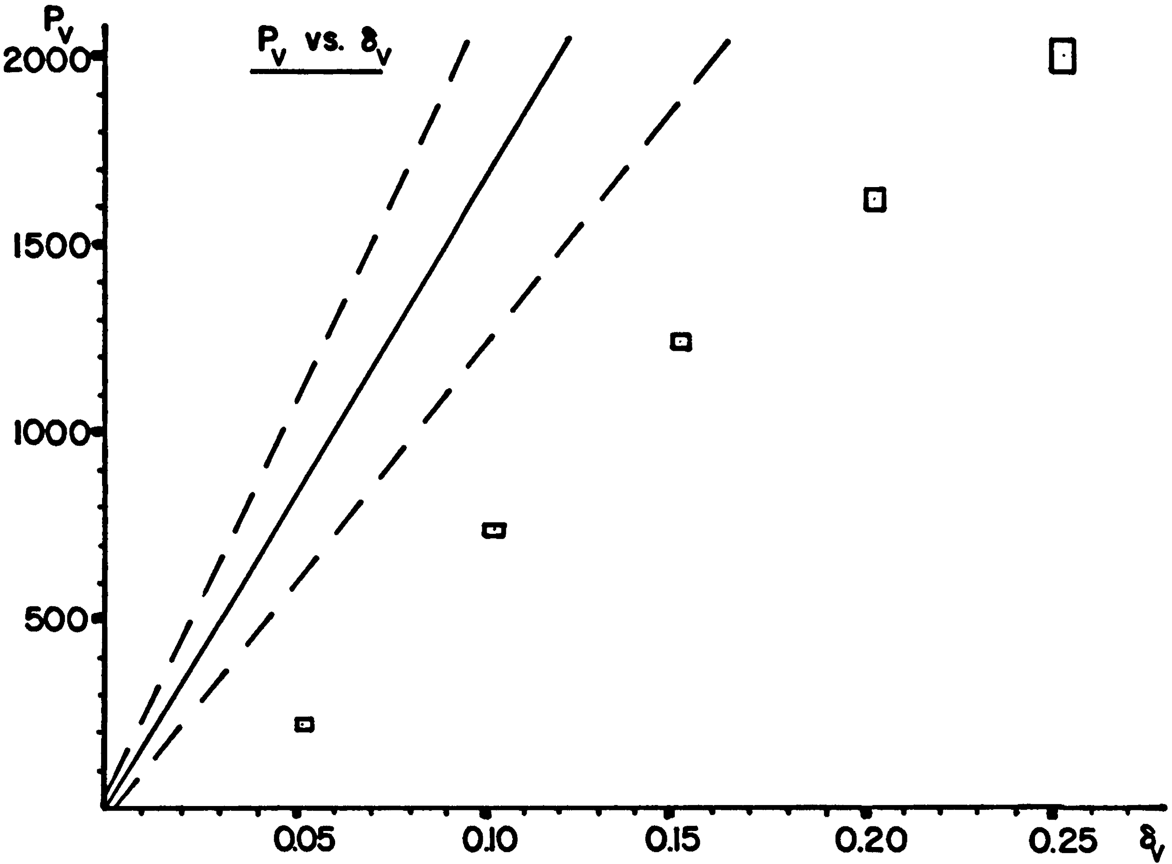

Figure F-7 Force-Deflection, Test 27 , $\beta = 30^\circ$, $\psi_x = 0$, $\psi_y = 0$

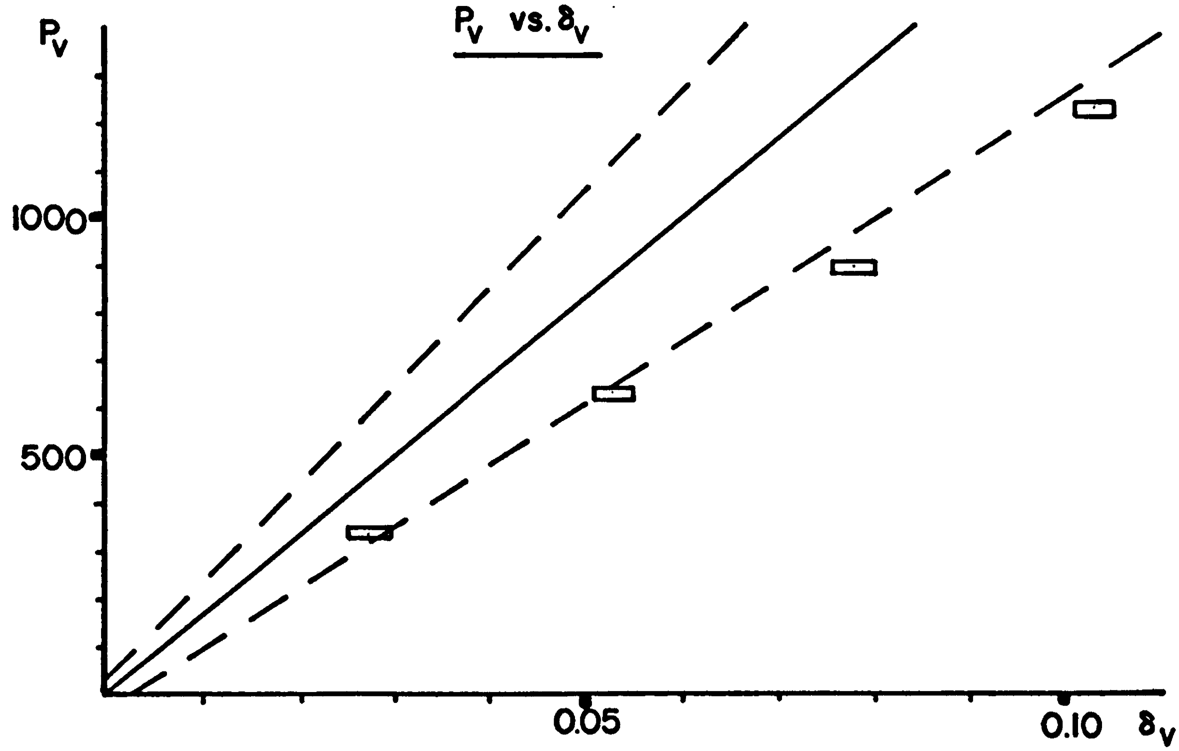

Figure F-8 Force-Deflection, Test 35 , $\beta = 30^\circ$, $\psi_x = 0$, $\psi_y = 0$

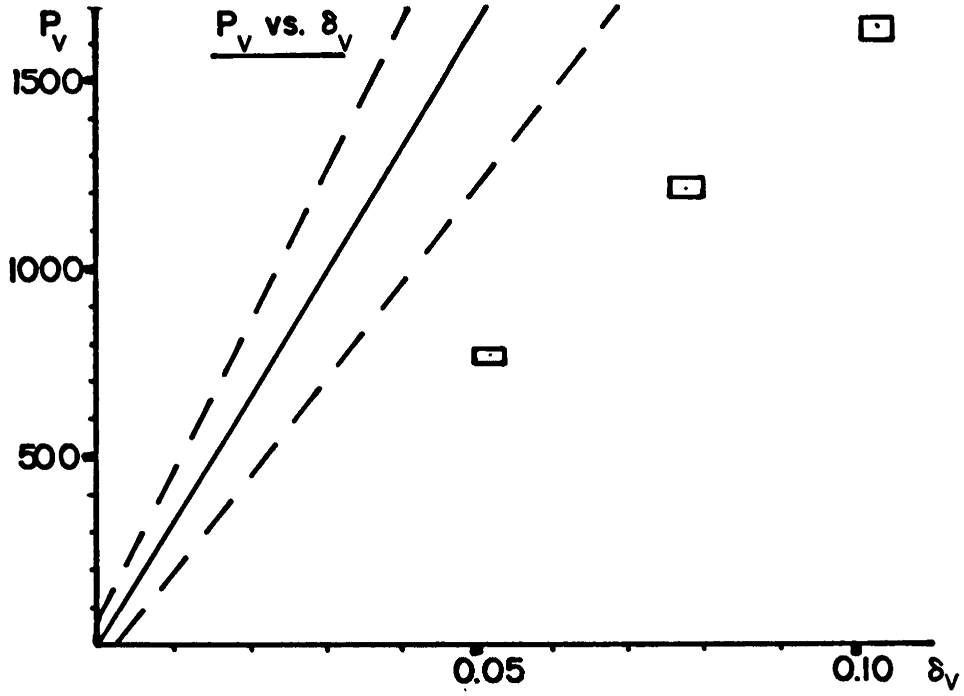

Figure F-9 Force-Deflection, Test 28 , $\beta = 45^\circ$, $\psi_x = 0$, $\psi_y = 0$

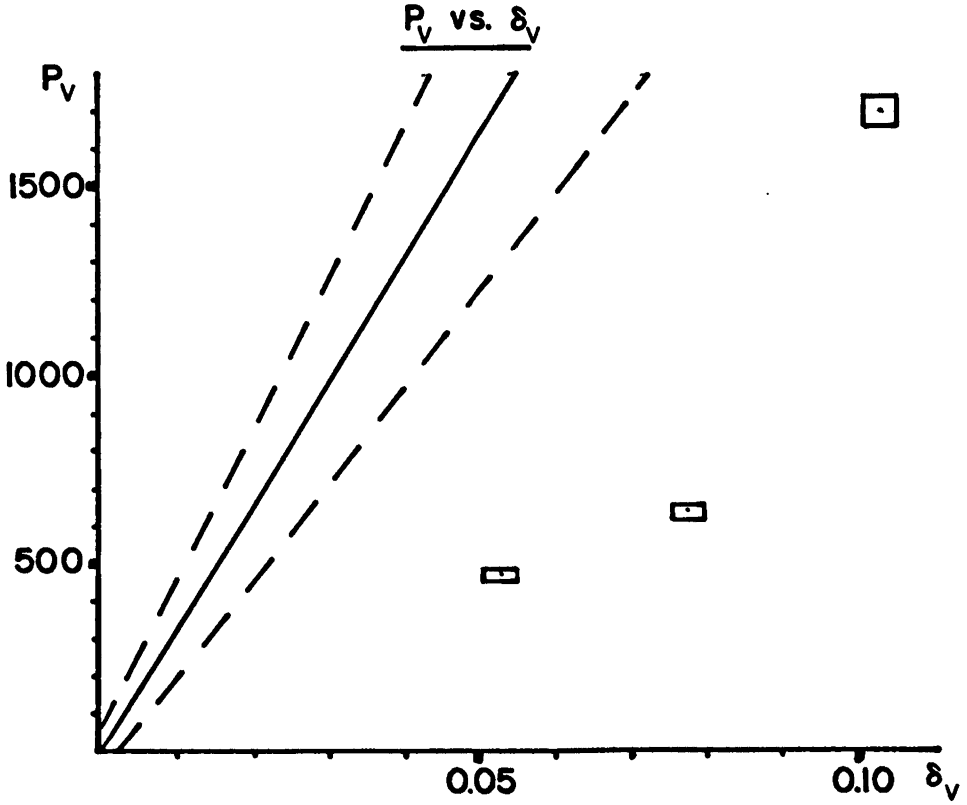

Figure F-10 Force-Deflection, Test 36 , $\beta = 45^\circ$, $\psi_x = 0$, $\psi_y = 0$

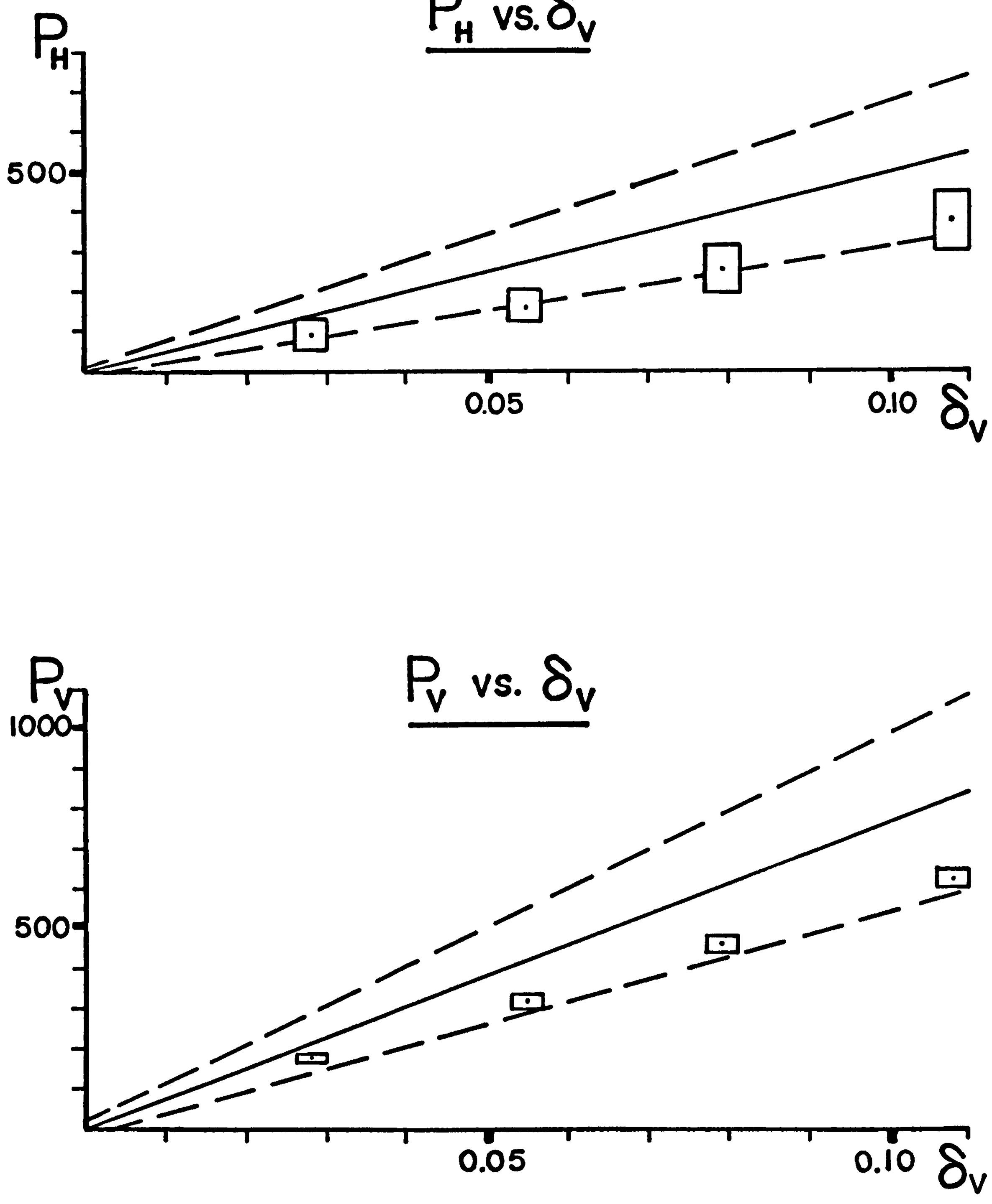

Figure F-11 Force-Deflection, Test 49, $\beta = 15^\circ$, $\psi_x = 15^\circ$, $\psi_y = 0$

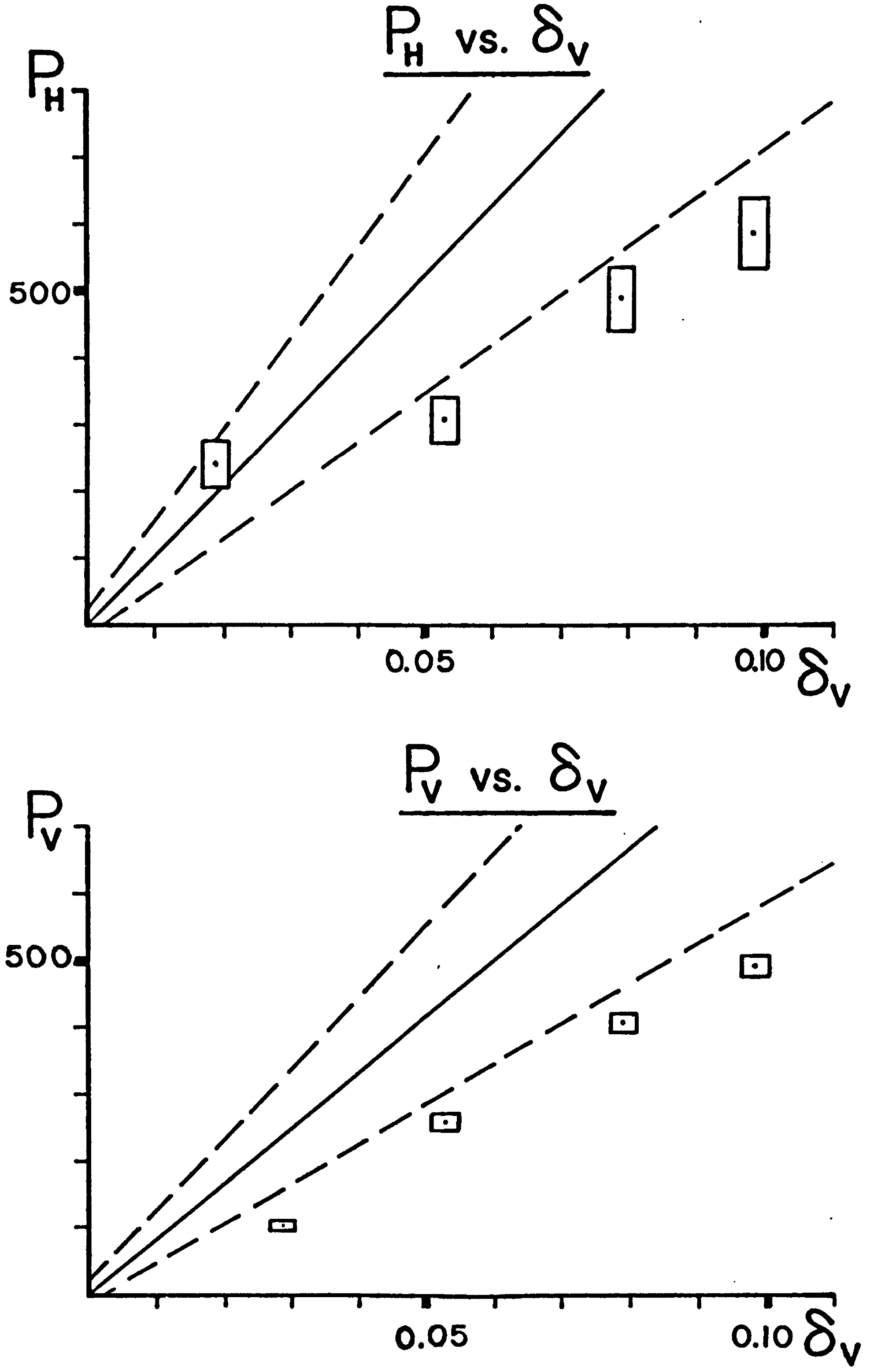

Underlined Figure F-12 Force-Deflection, Test 50 , $\beta = 15^{\circ}$, $\psi_x = 30^{\circ}$, $\psi_y = 0$

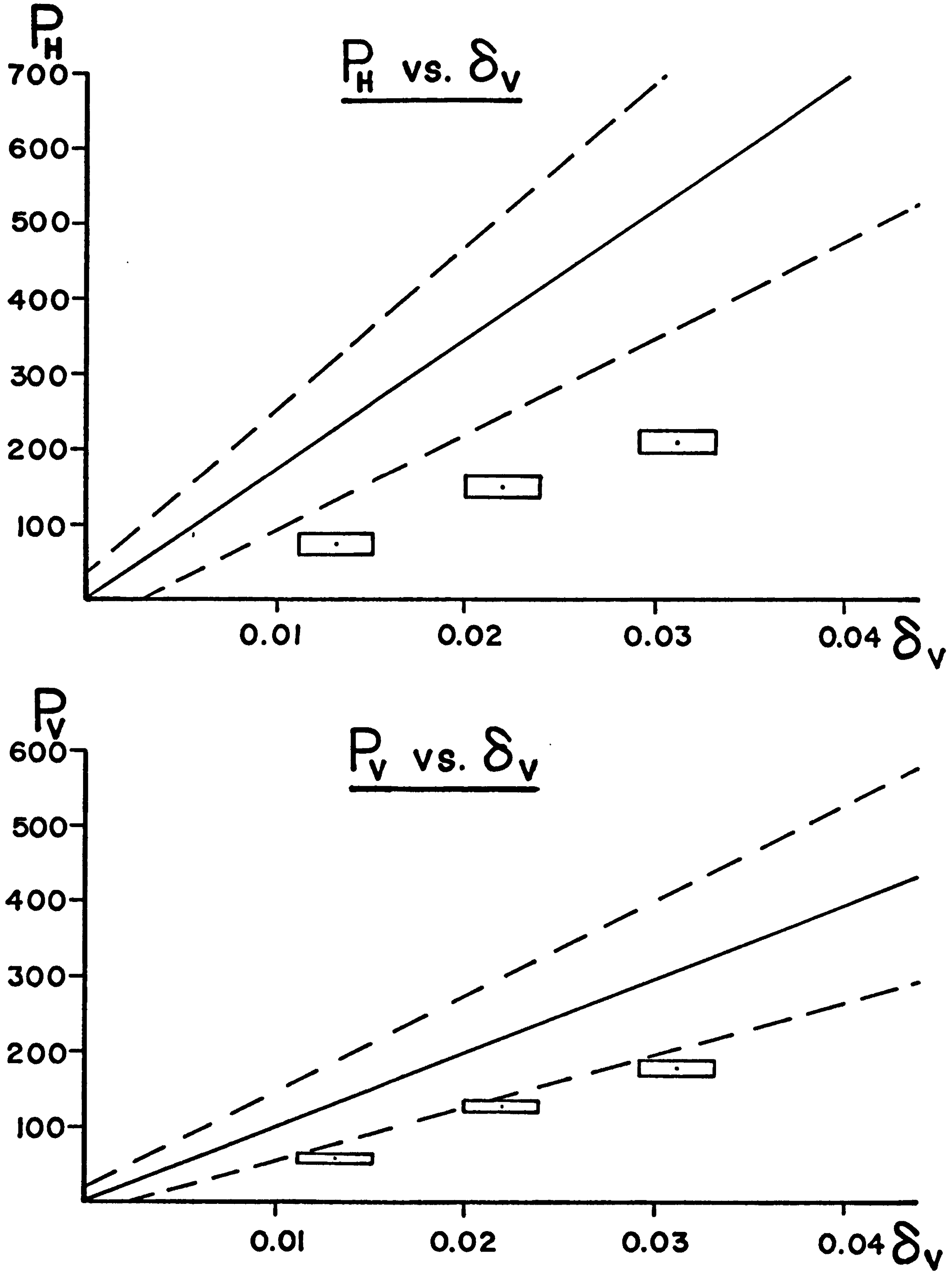

Figure F-13 Force-Deflection, Test 96 , $\beta = 15^\circ$, $\psi_x = 30^\circ$, $\psi_y = 0$

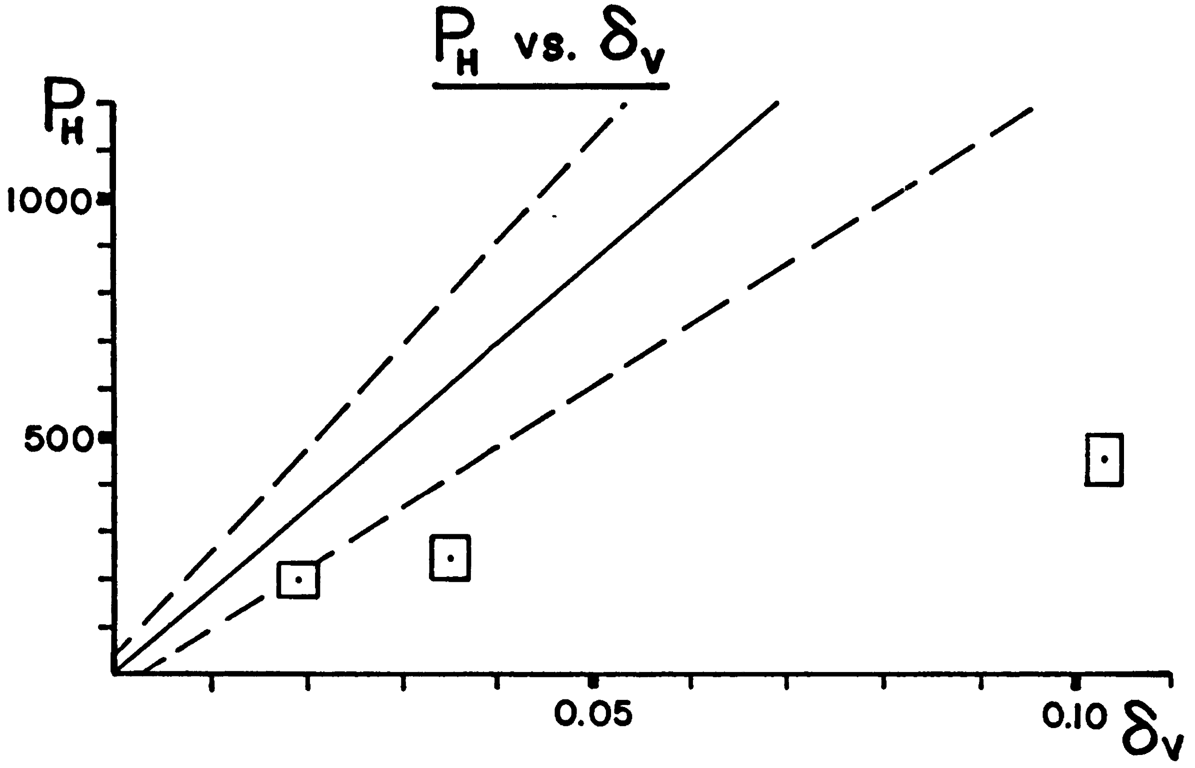

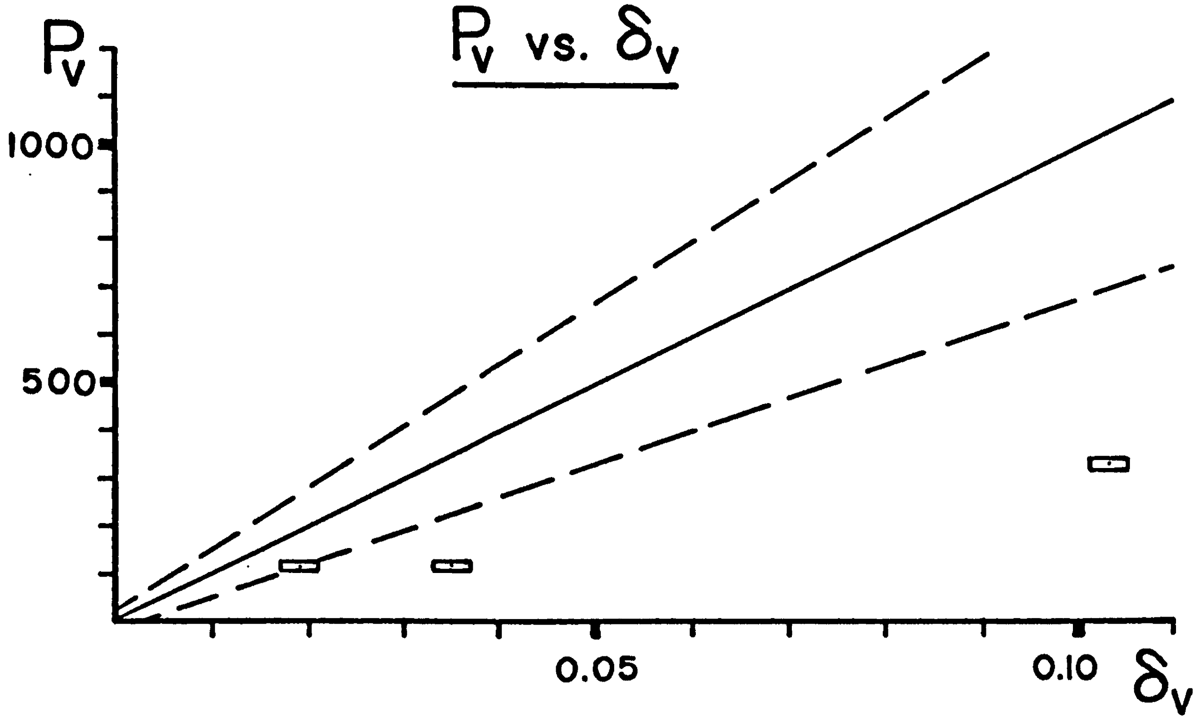

Figure F-14 Force-Deflection, Test 55 , $\beta = 15^\circ$, $\psi_x = 45^\circ$, $\psi_y = 0$

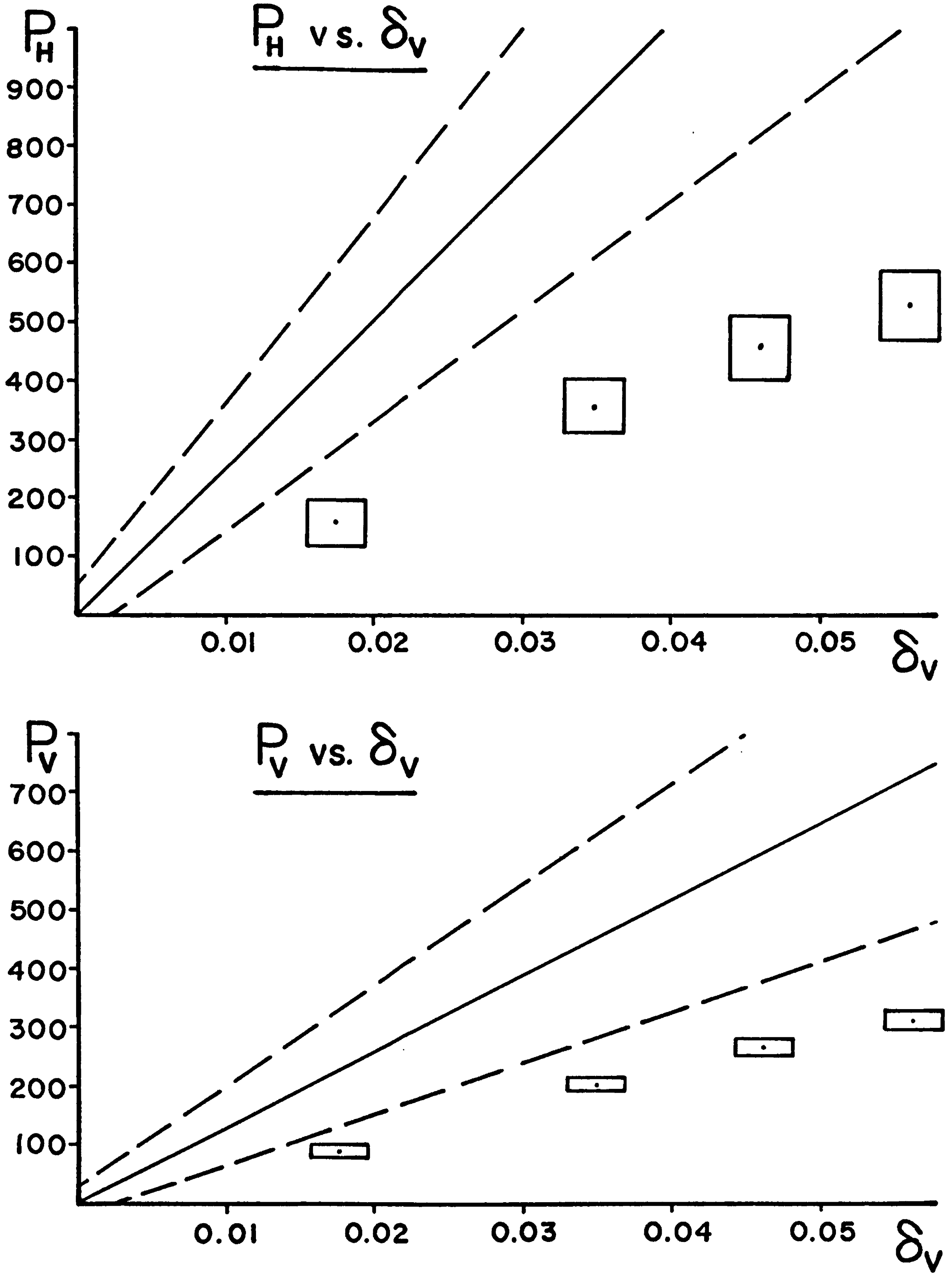

Figure F-15 Force-Deflection, Test 56 , $\beta = 15^\circ$, $\psi_x = 54^\circ$, $\psi_y = 0$

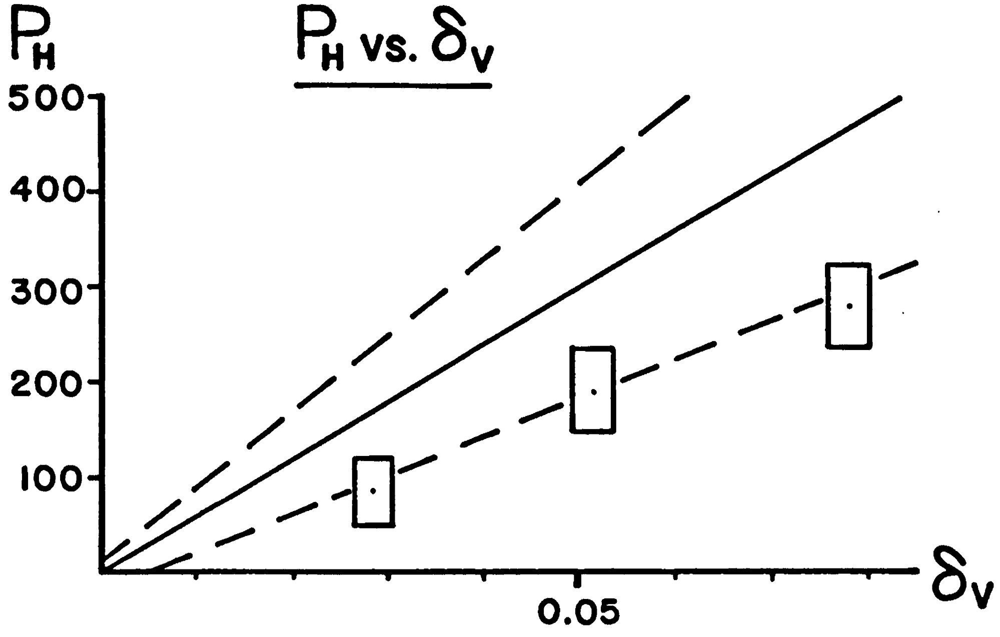

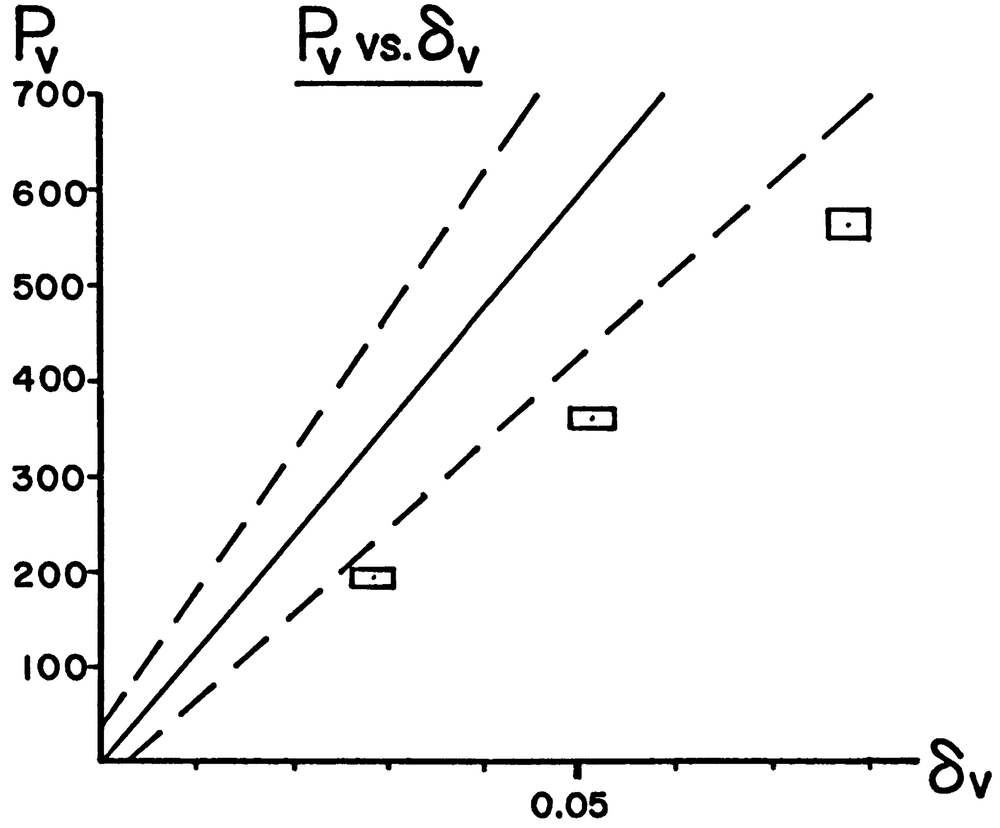

Figure F-16 Force-Deflection, Test 57, β = 22.5°, ψ_x = 15°, ψ_y = 0

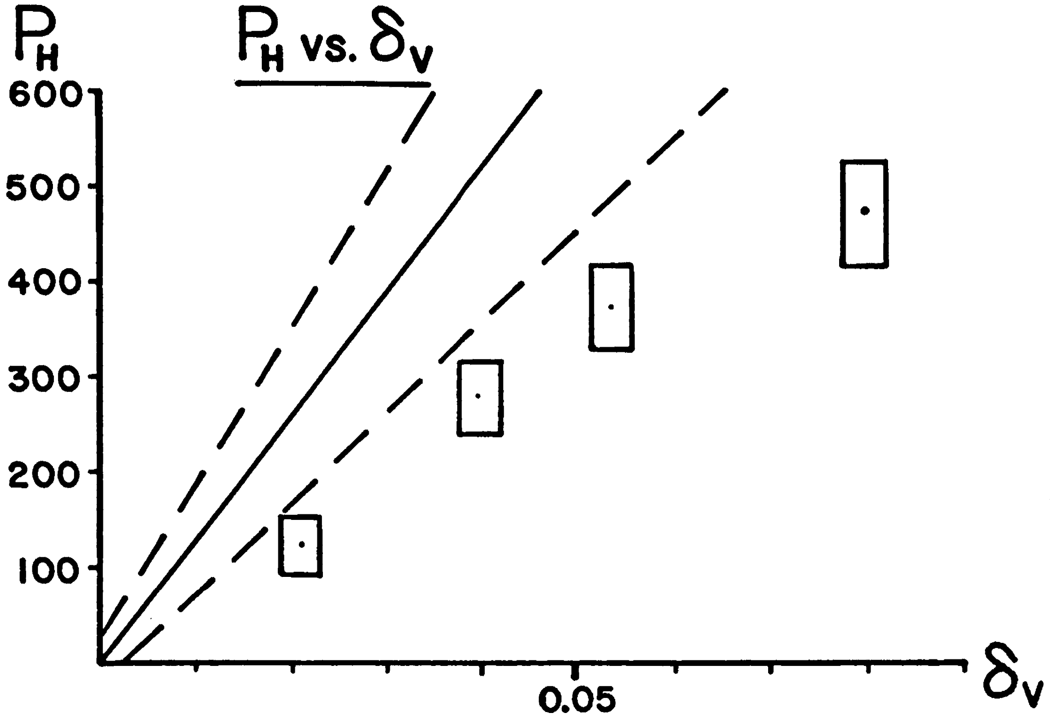

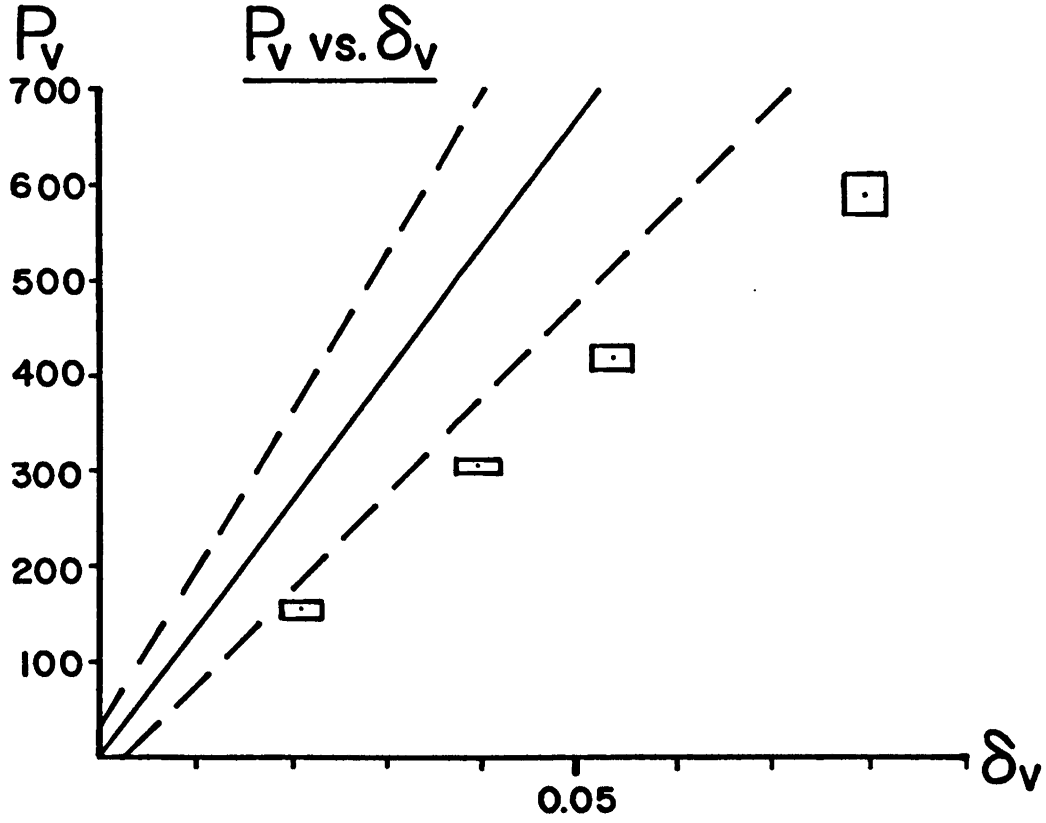

Figure F-17 Force-Deflection, Test 59, $\beta = 22.5^\circ$, $\psi_x = 30^\circ$, $\psi_y = 0$.

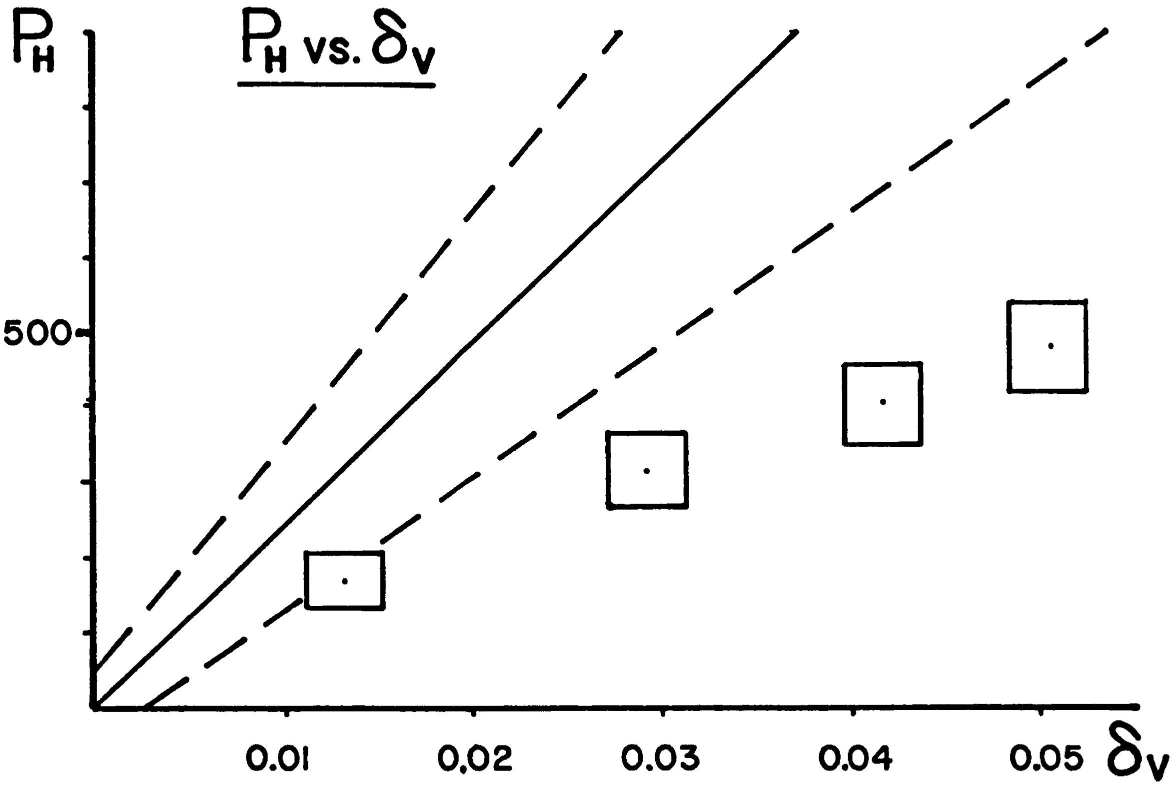

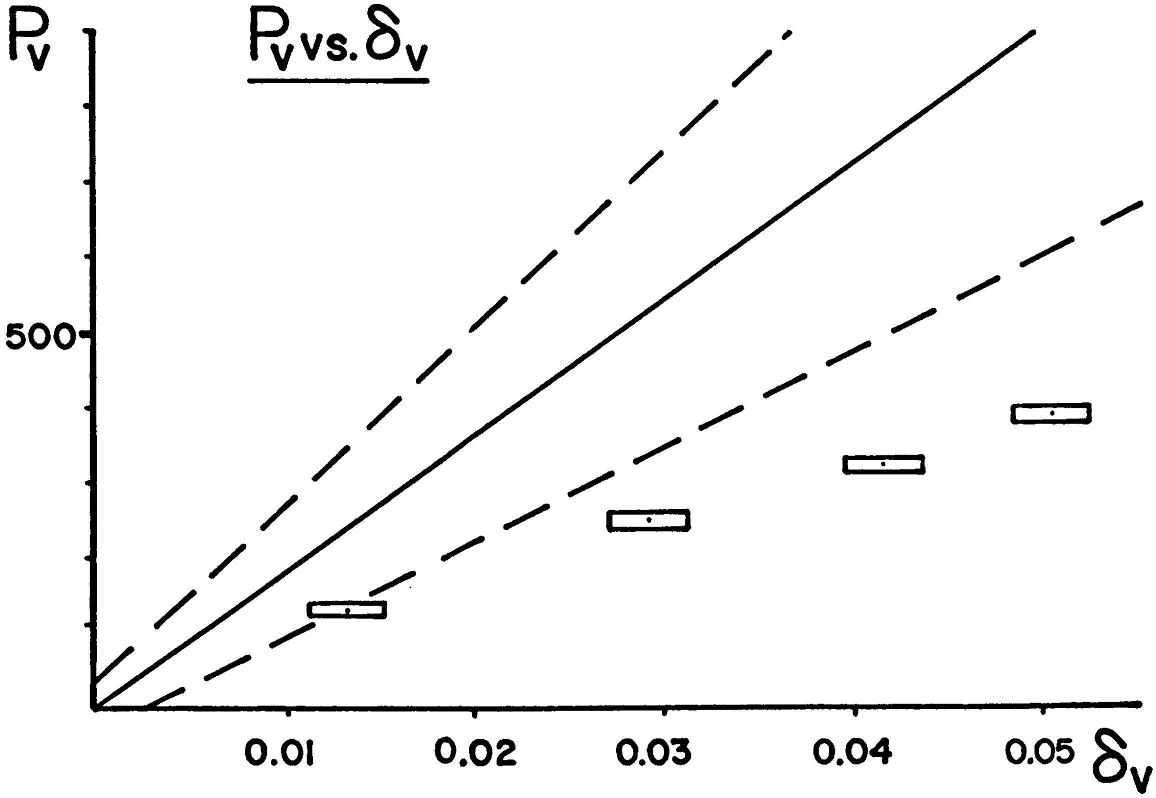

Figure F-18 Force-Deflection, Test 58, $\beta = 22.5^\circ$, $\psi_x = 45^\circ$, $\psi_y = 0$

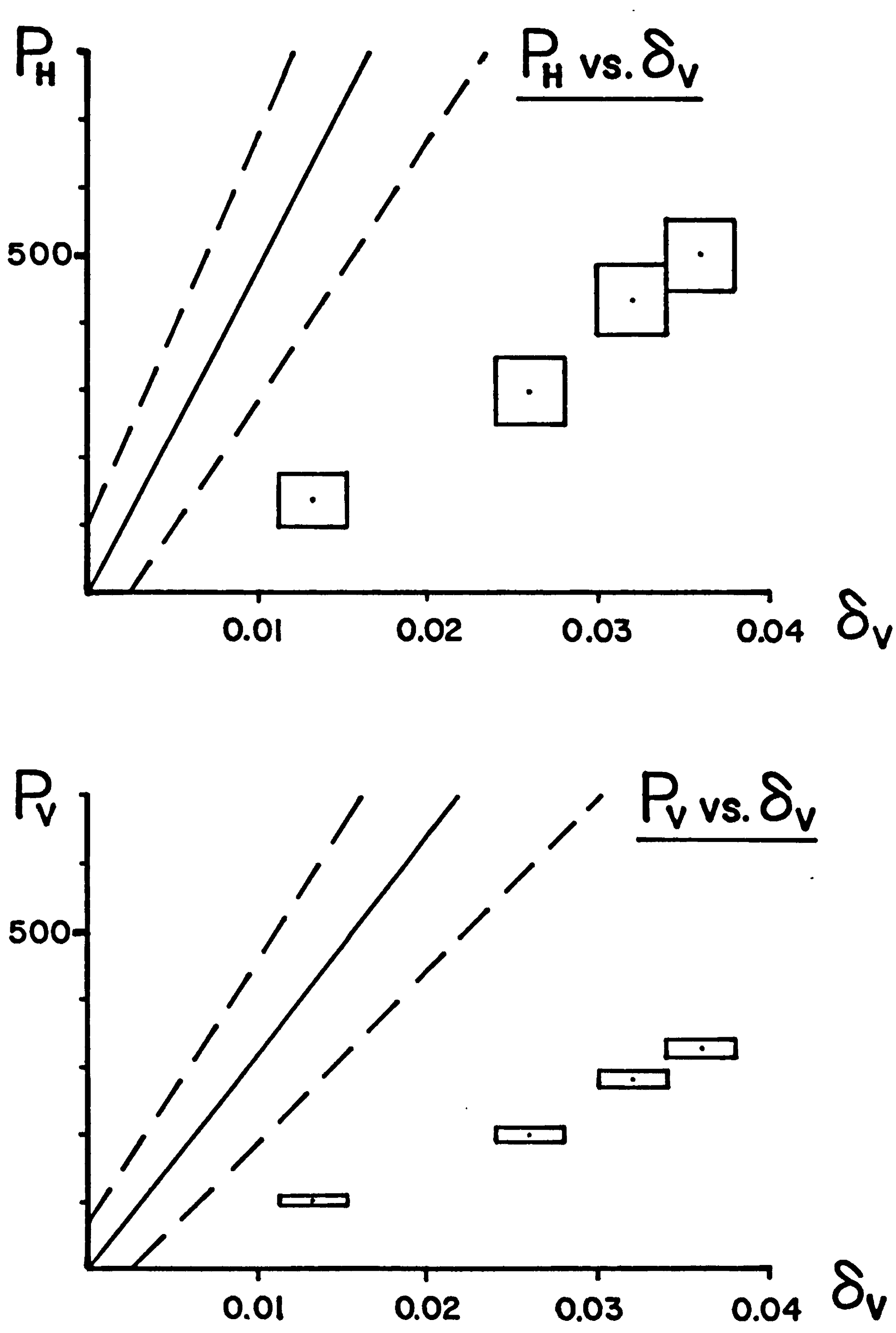

Figure F-19 Force-Deflection, Test 60 , $\beta = 22.5^\circ$, $\psi_x = 54^\circ$, $\psi_y = 0$

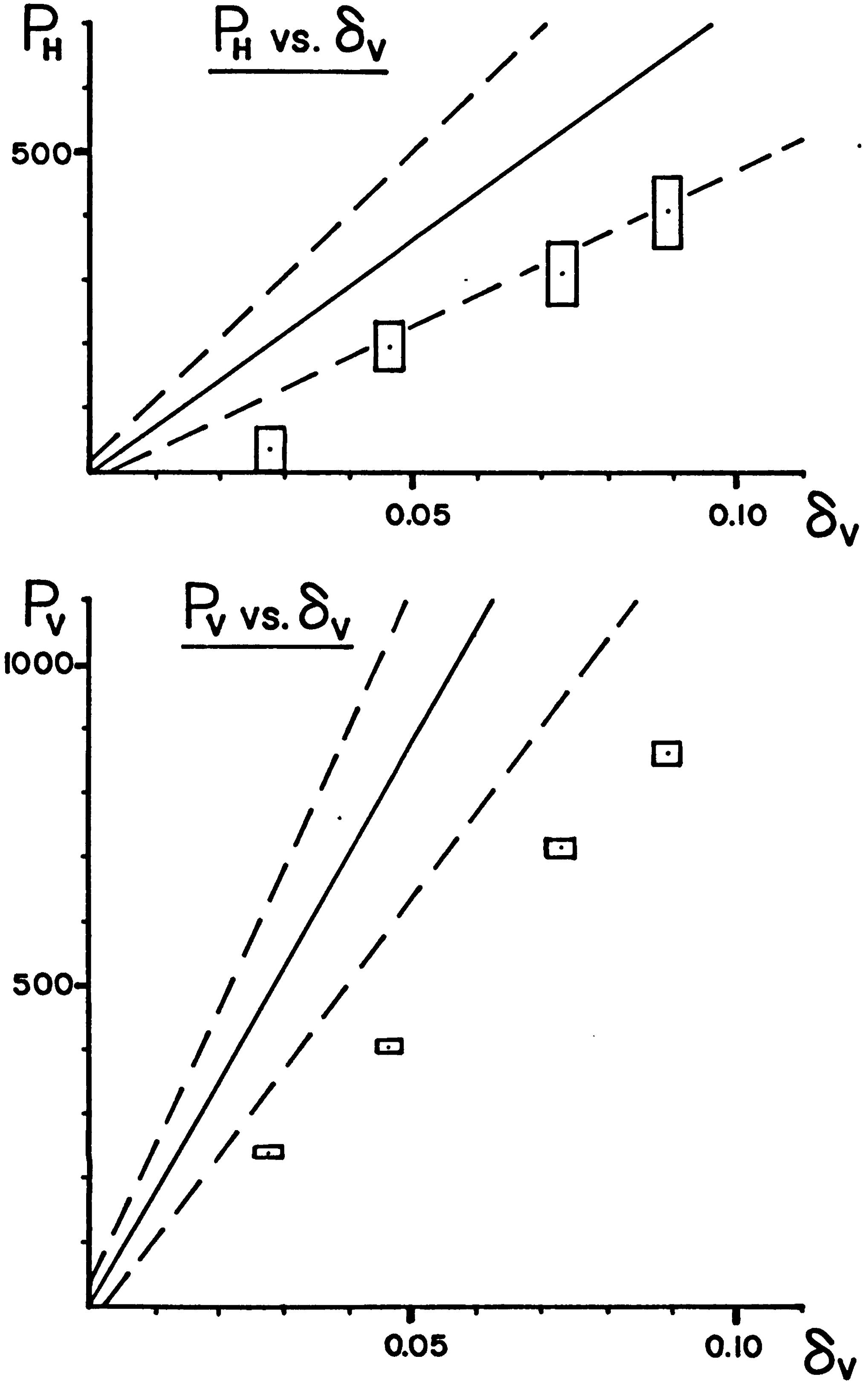

Figure F-20 Force-Deflection, Test 61, $\beta = 30^\circ$, $\psi_x = 15^\circ$, $\psi_y = 0$

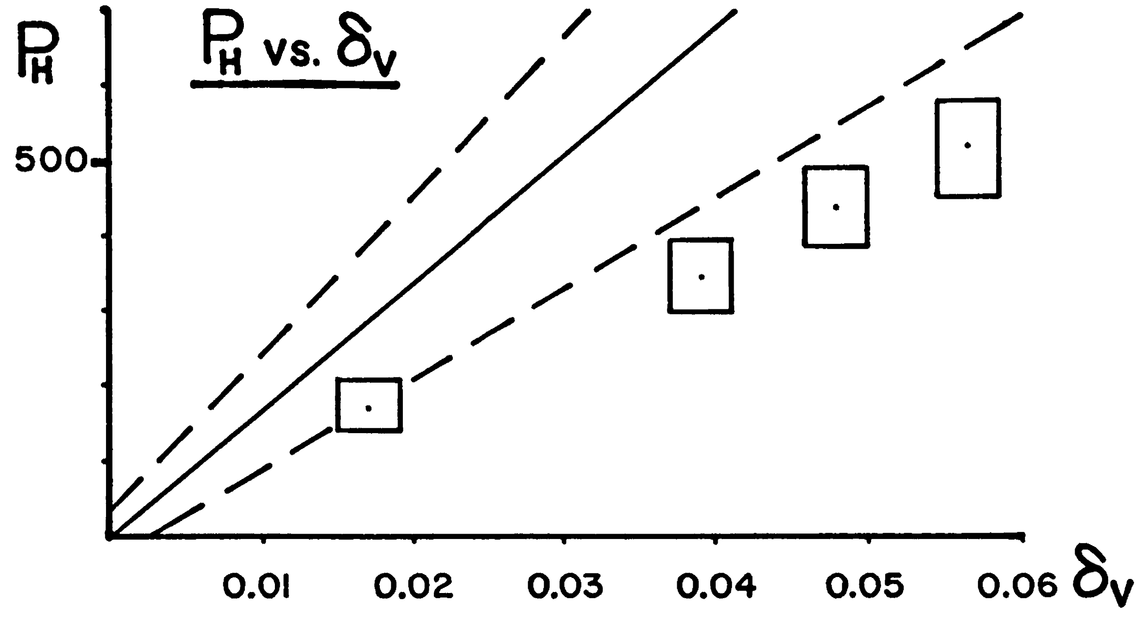

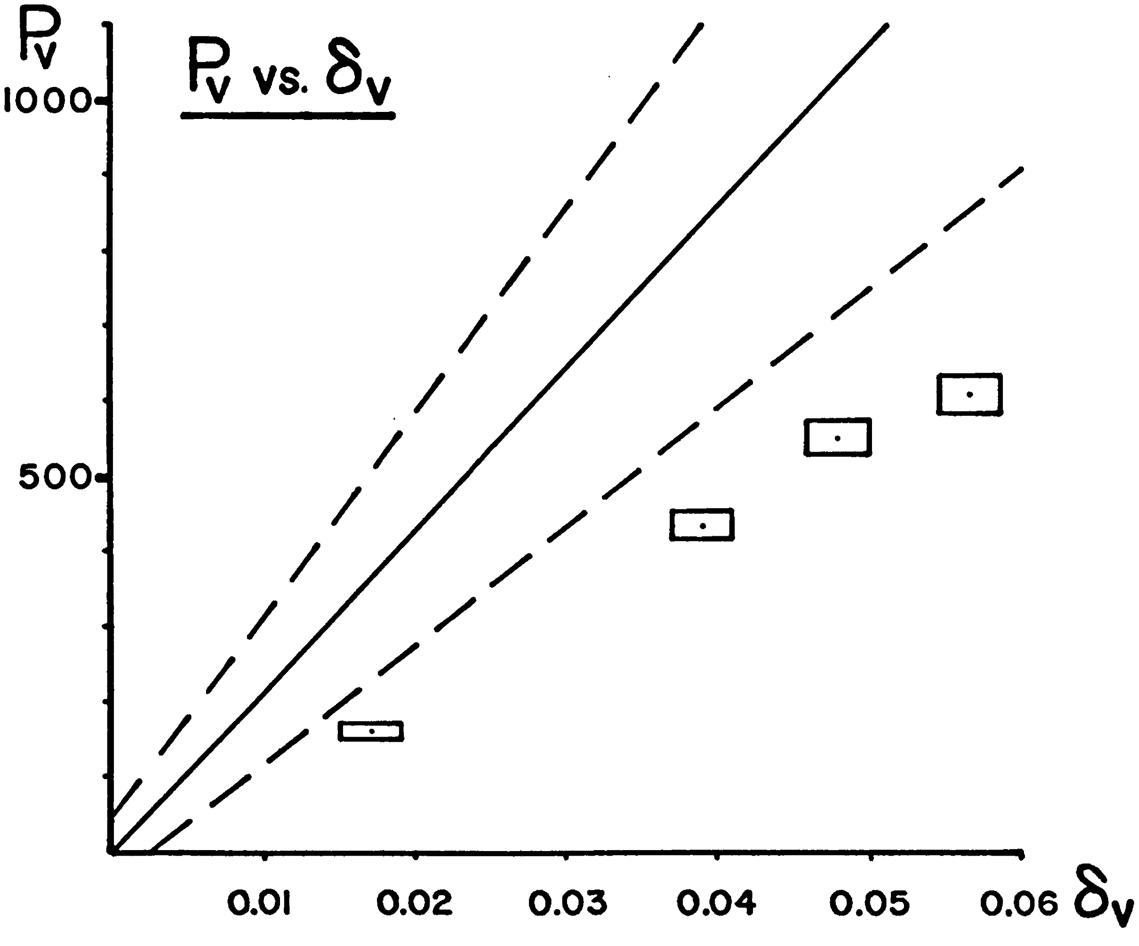

Figure F-21 Force-Deflection, Test 62 , $\beta = 30^\circ$, $\psi_x = 30^\circ$, $\psi_y = 0$

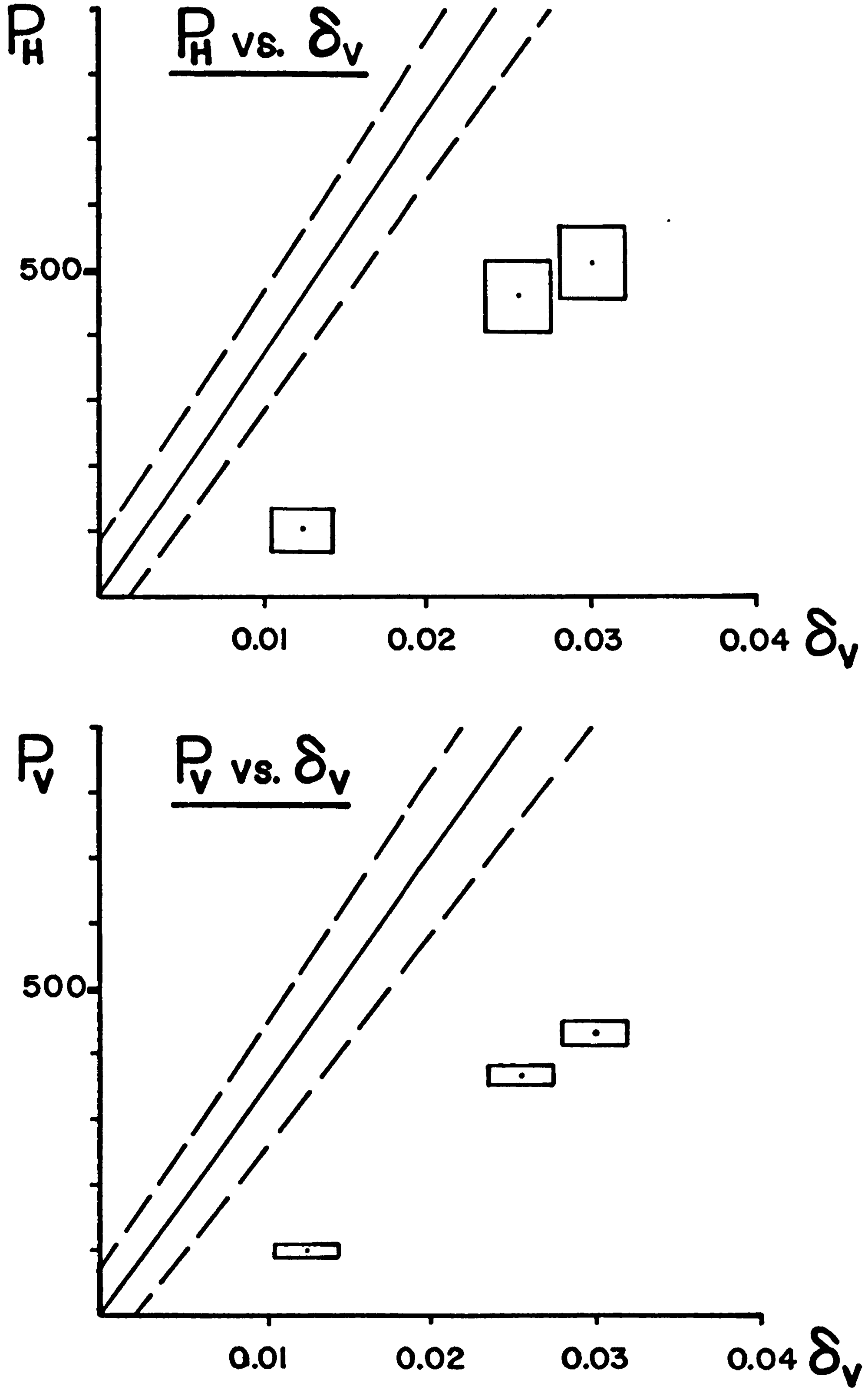

Figure F-22 Force-Deflection, Test 63, $\beta = 30^\circ$, $\psi_x = 45^\circ$, $\psi_y = 0$

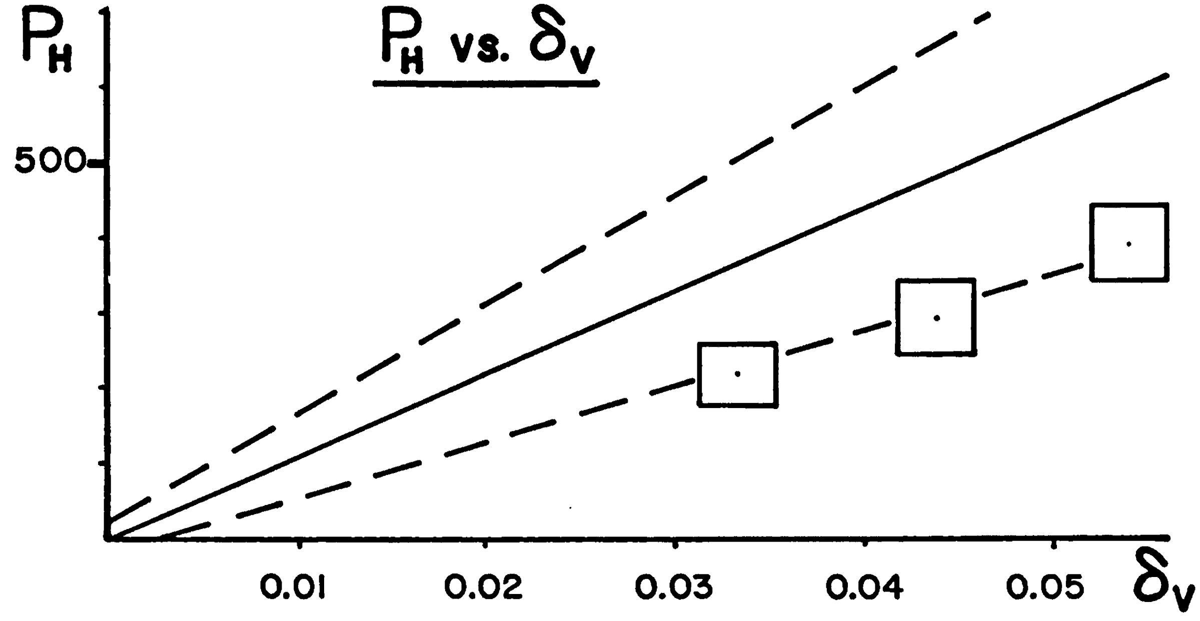

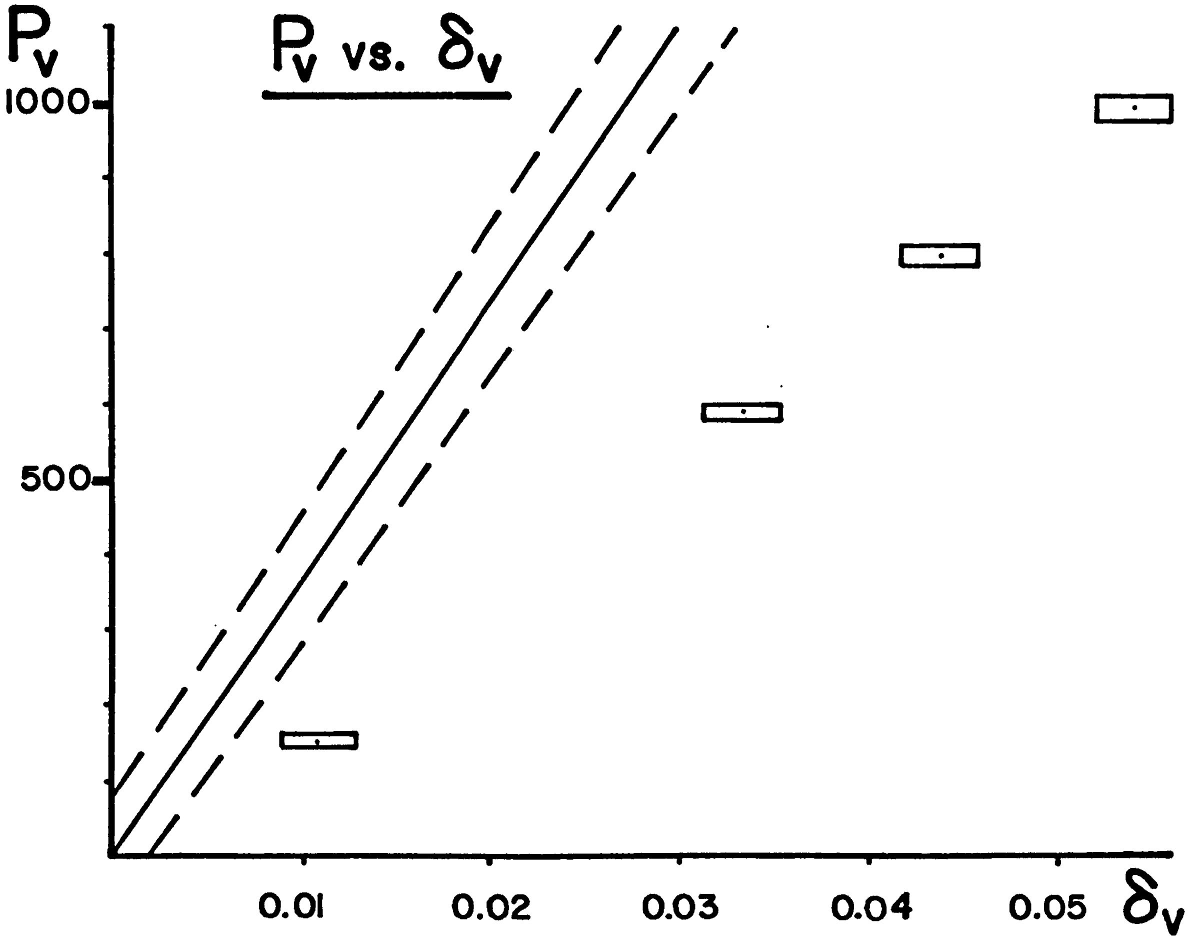

Figure F-23 Force-Deflection, Test 65 , $\beta = 45^{\circ}$, $\psi_x = 15^{\circ}$, $\psi_y = 0$

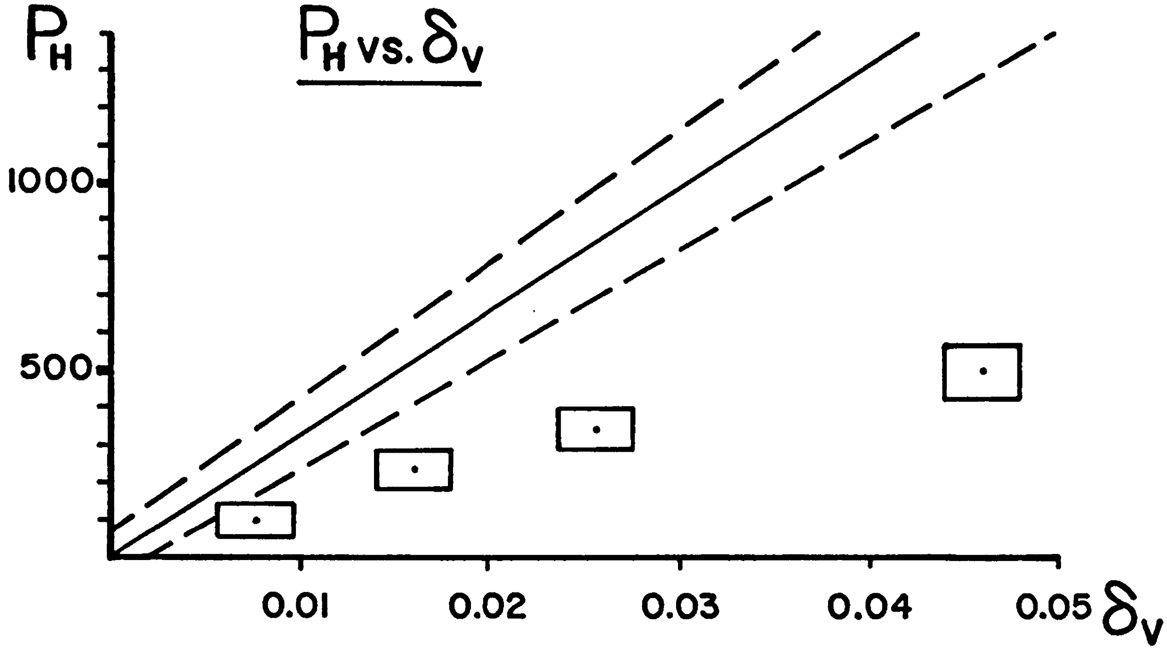

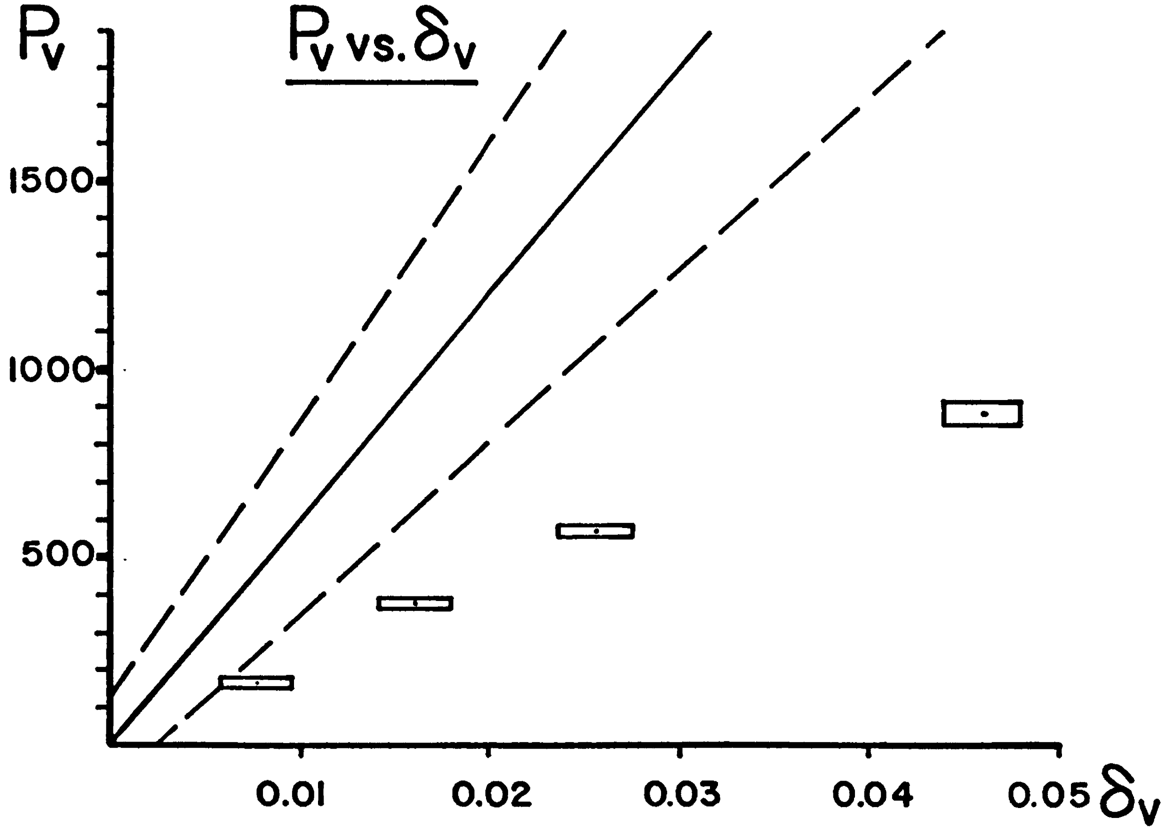

Figure F-24 Force-Deflection, Test 66, $\beta = 45^\circ$, $\psi_x = 30^\circ$, $\psi_y = 0$

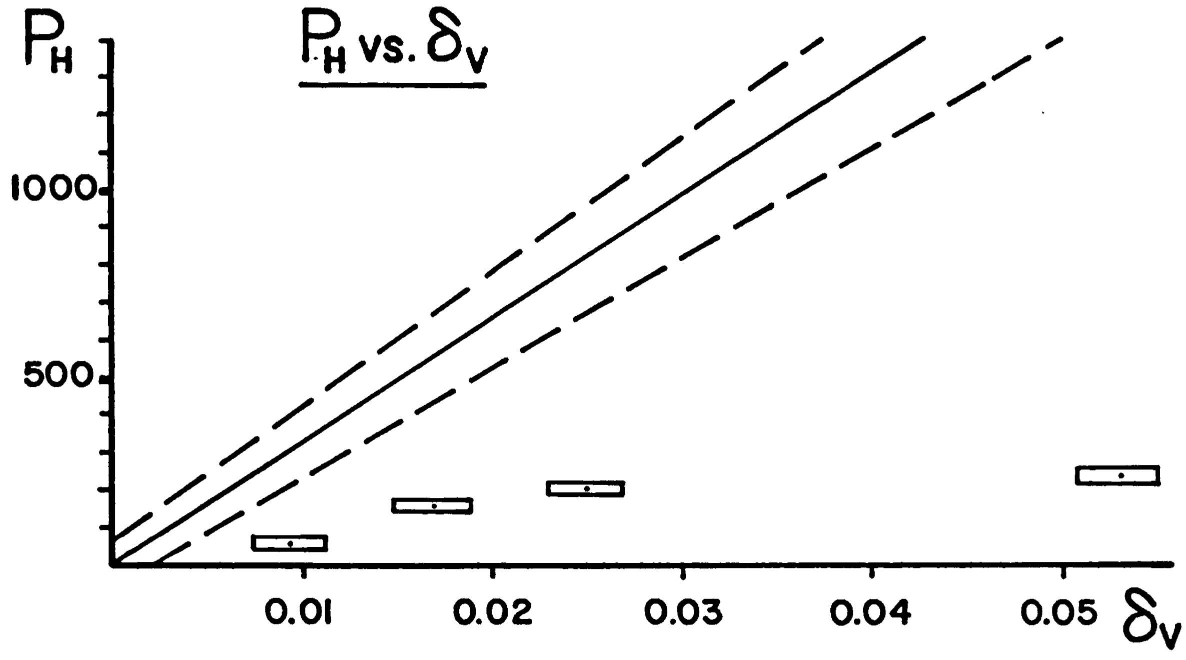

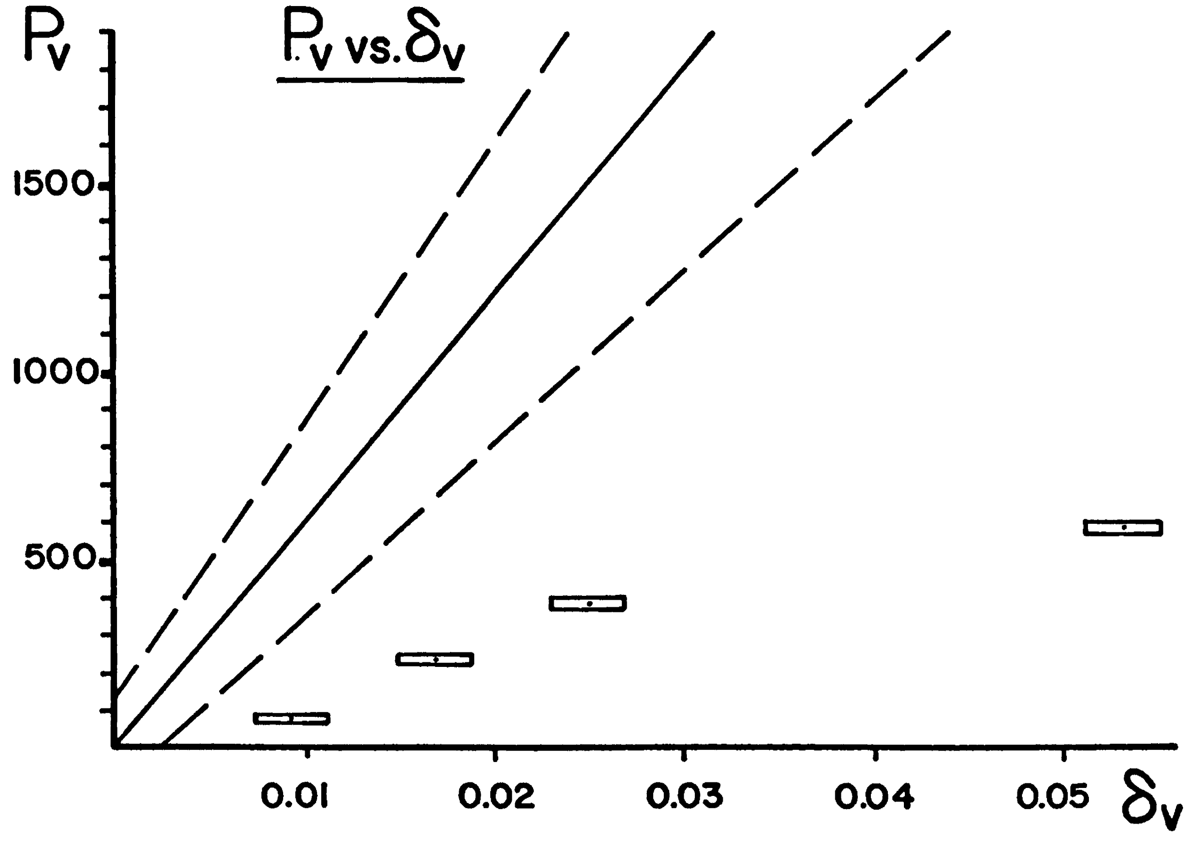

Figure F-25 Force-Deflection, Test 97 , $\beta = 45^\circ$, $\psi_x = 30^\circ$, $\psi_y = 0$

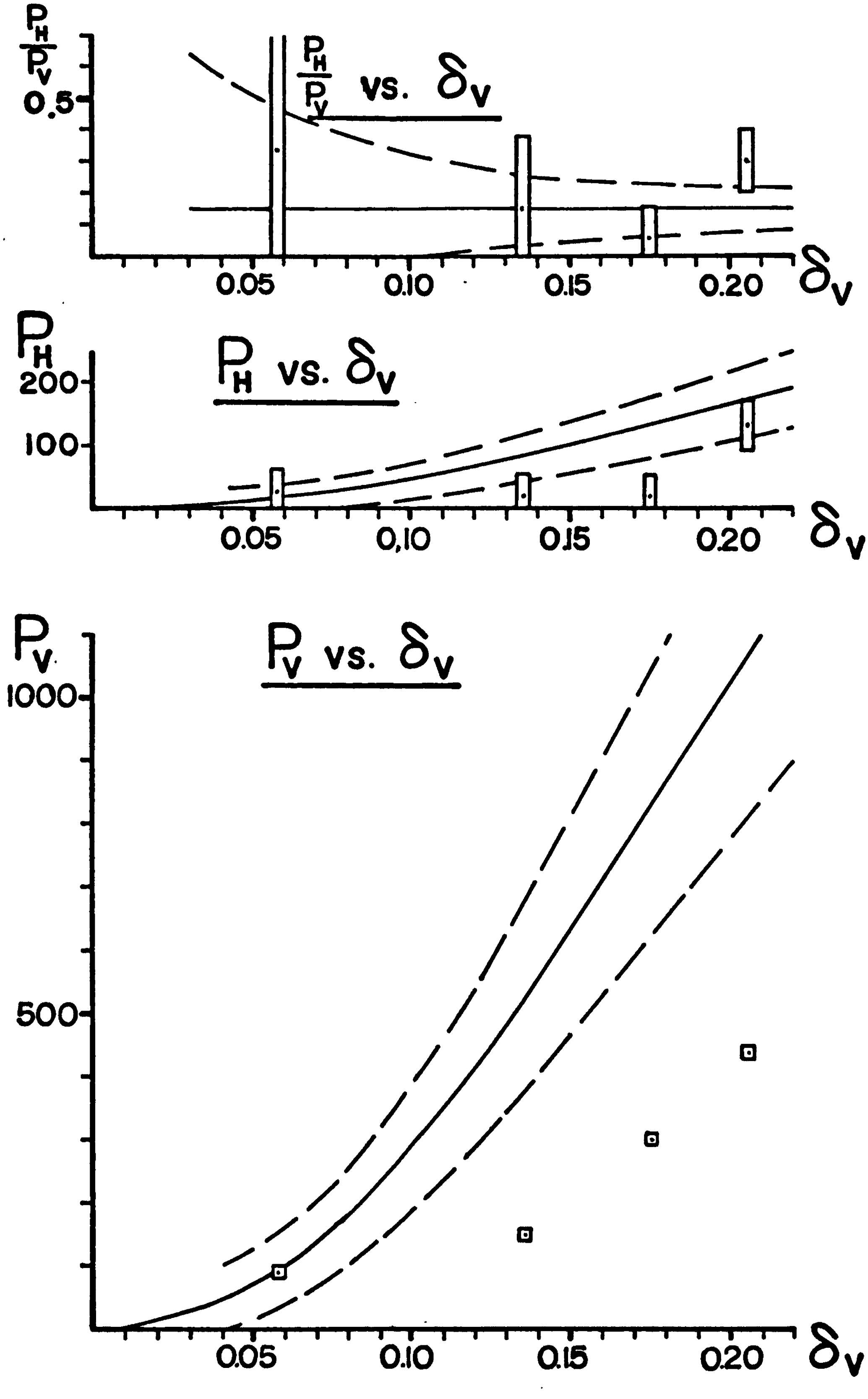

Figure F-26 Force-Deflection, Test 67 , $\beta = 15^\circ$, $\psi_x = 0$, $\psi_y = 15^\circ$

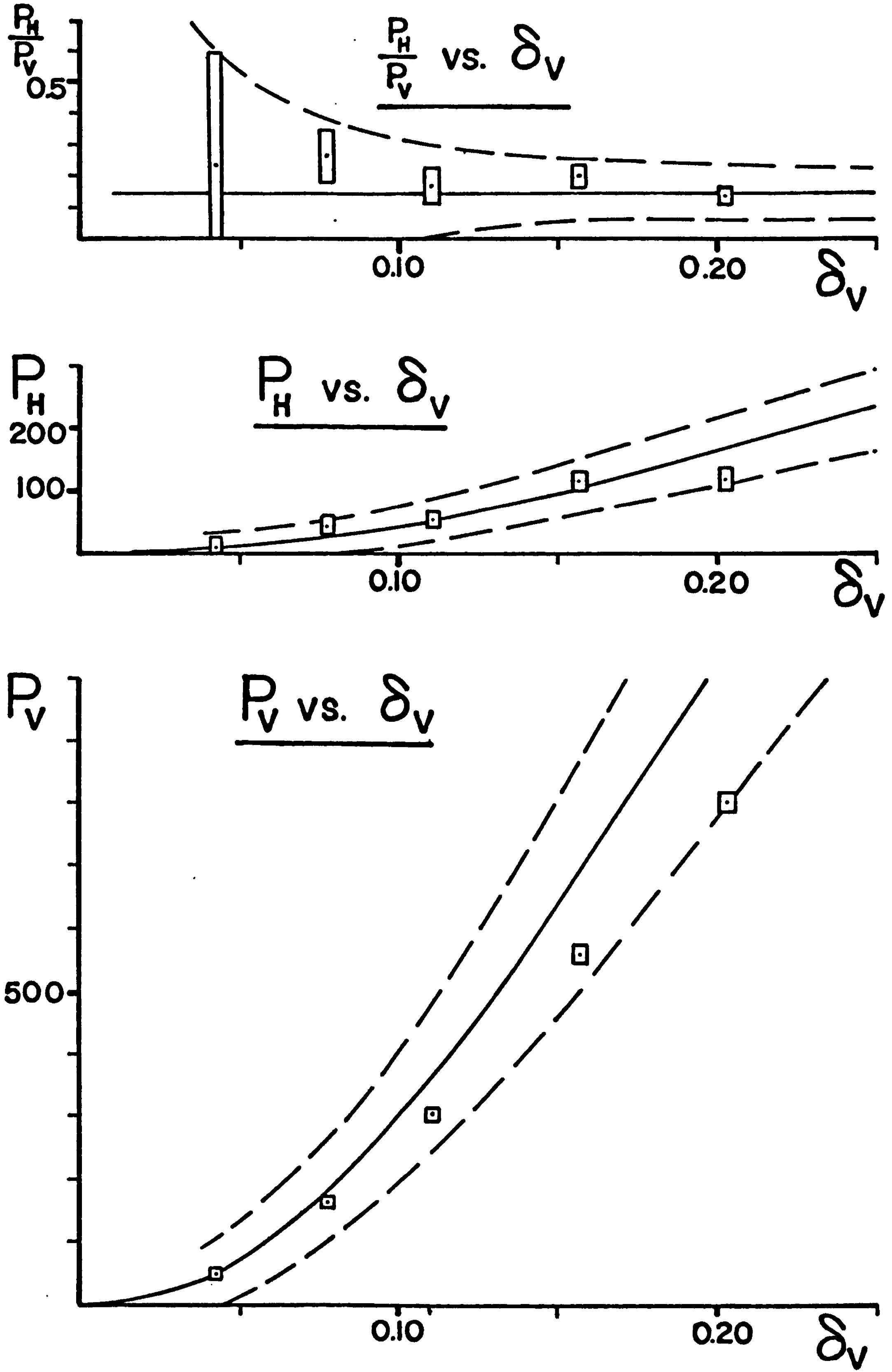

Figure F-27 Force-Deflection, Test 95, $\beta = 15^\circ$, $\psi_x = 0$, $\psi_y = 15^\circ$

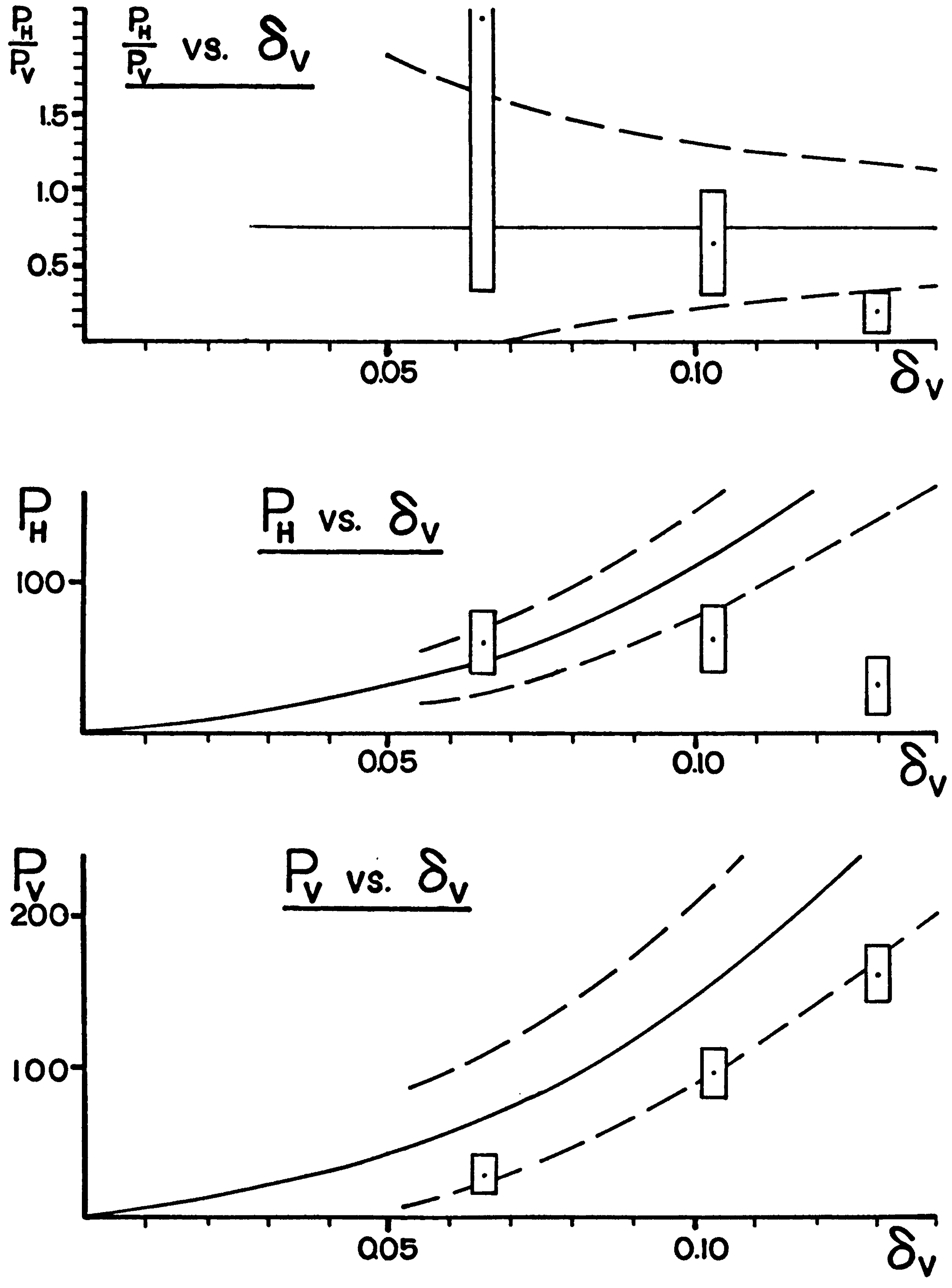

Figure F-28 Force-Deflection, Test 68, $\beta = 15^\circ$, $\psi_x = 0$, $\psi_y = 30^\circ$

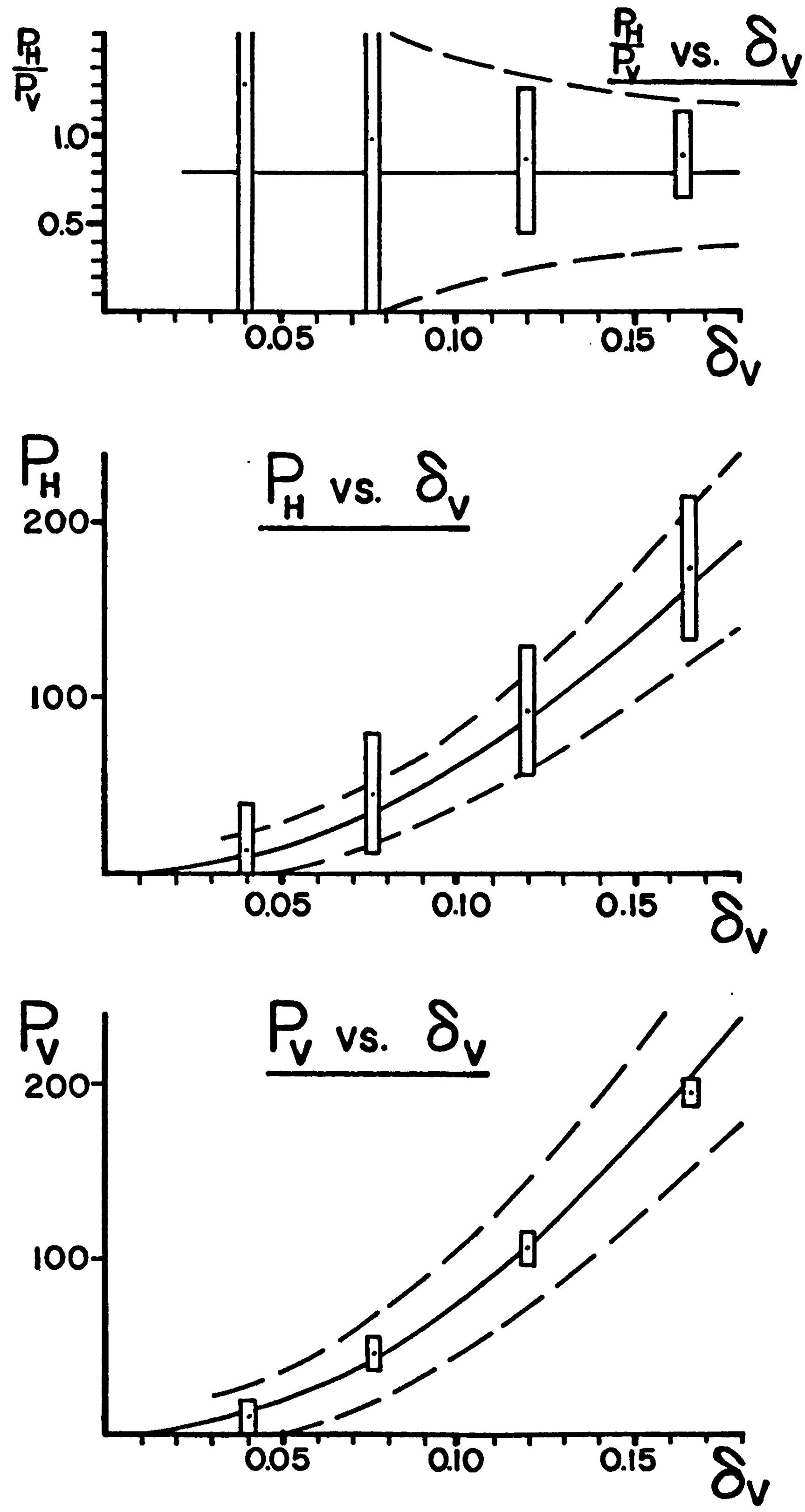

Figure F-29 Force-Deflection, Test 69 , β = 15° , ψ_x = 0 , ψ_y = 45°

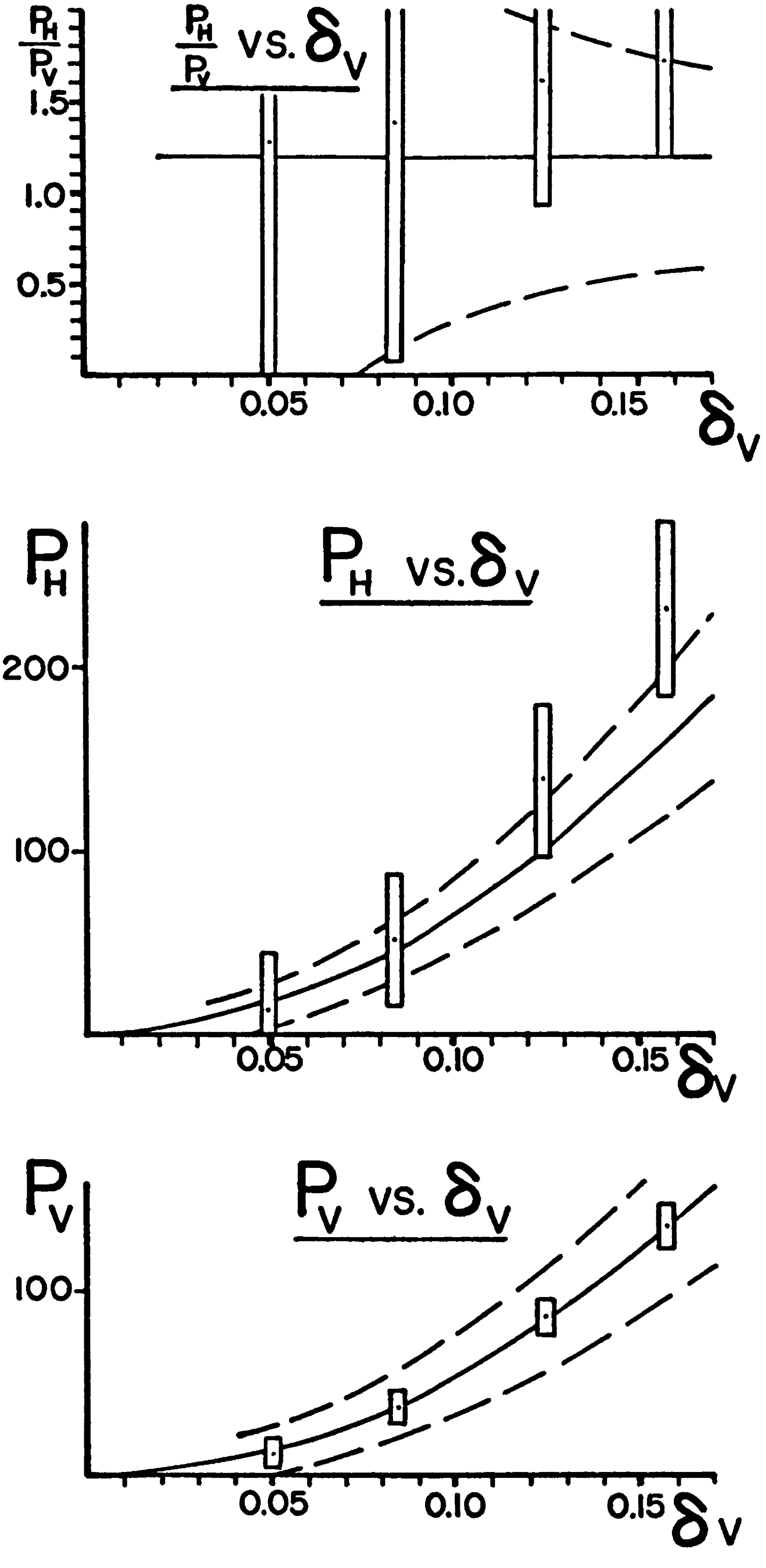

Figure F-30 Force-Deflection, Test 70 , β = 15° , ψ_x = 0 , ψ_y = 54°

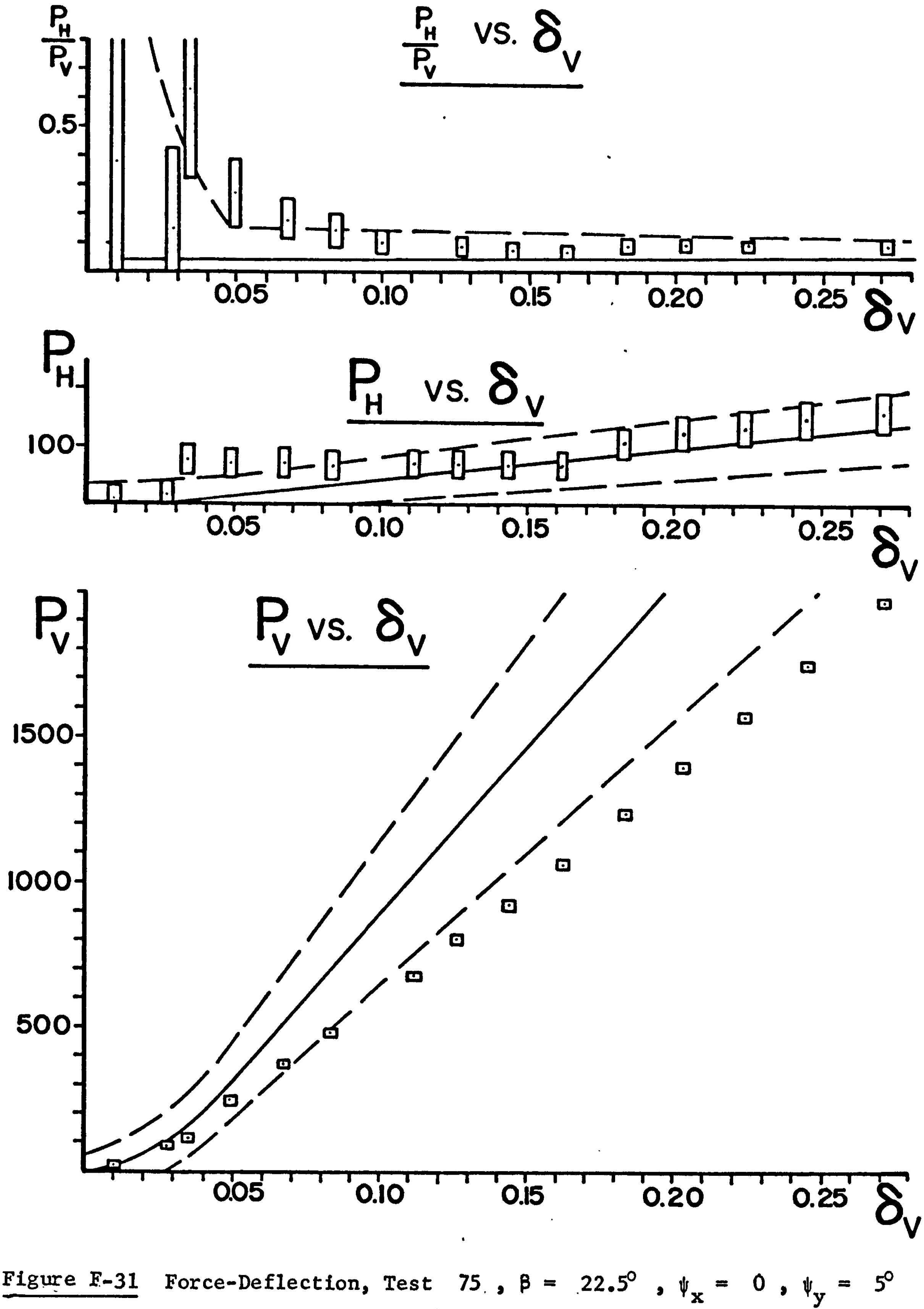

Figure F-31 Force-Deflection, Test 75 , β = 22.5° , ψ_x = 0 , ψ_y = 5°

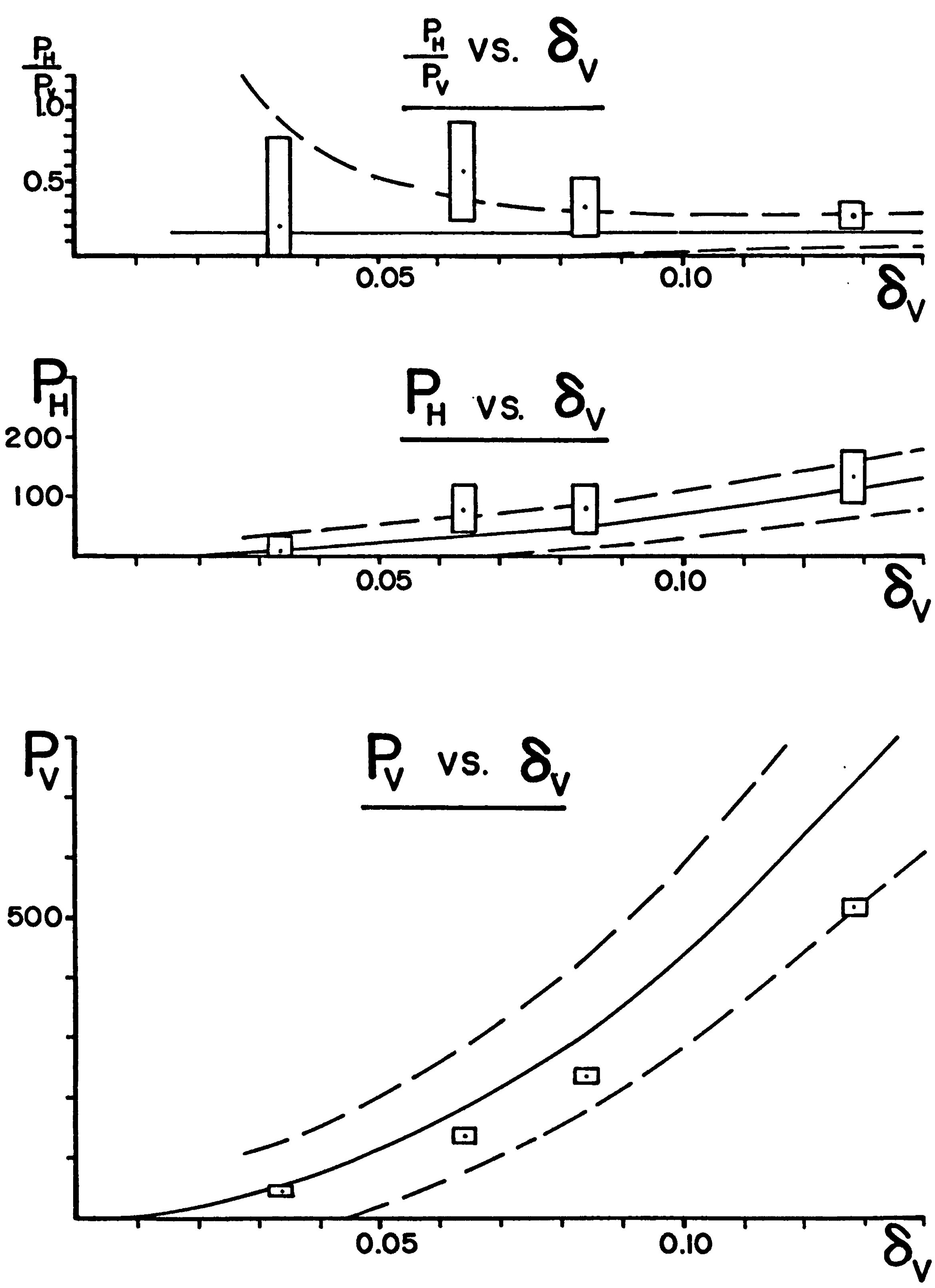

Figure F-32 Force-Deflection, Test 72 , β = 22.5° , ψ_x = 0 , ψ_y = 15°

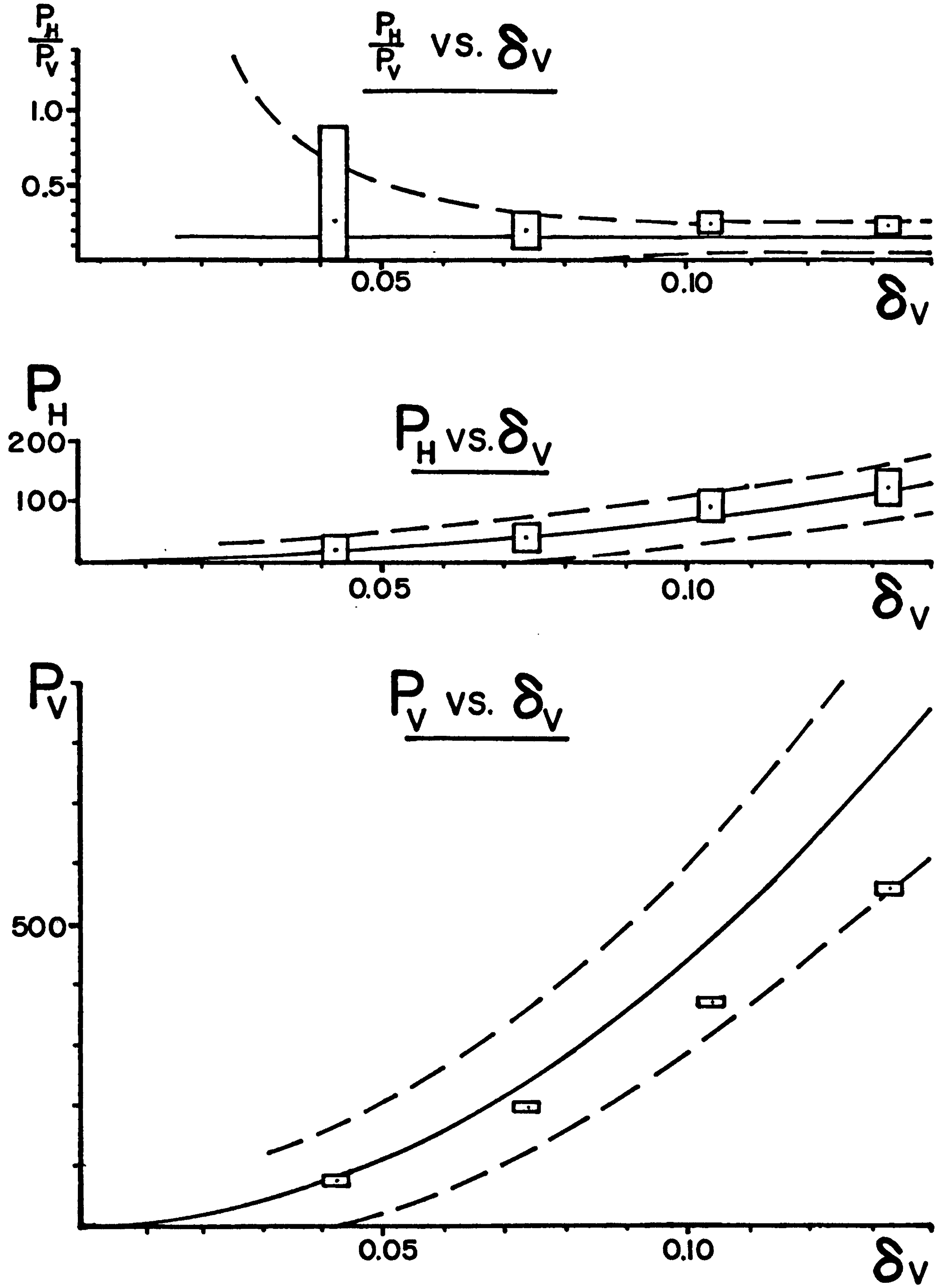

Figure F-33 Force-Deflection, Test 73 , β = 22.5° , ψ_x = 0 , ψ_y = 15°

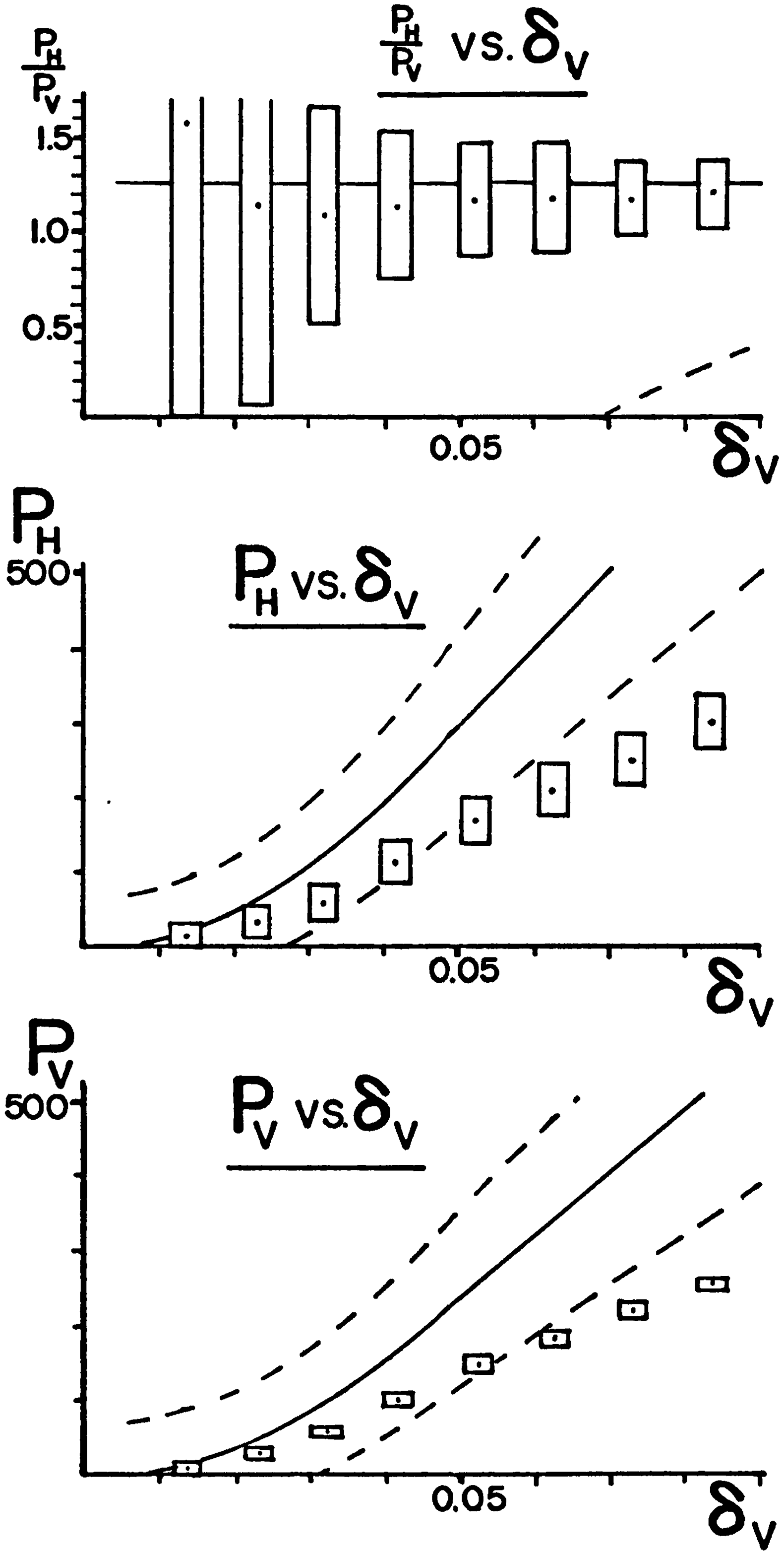

Figure F-34 Force-Deflection, Test 76, β = 15°, ψ_x = 30°, ψ_y = 5°

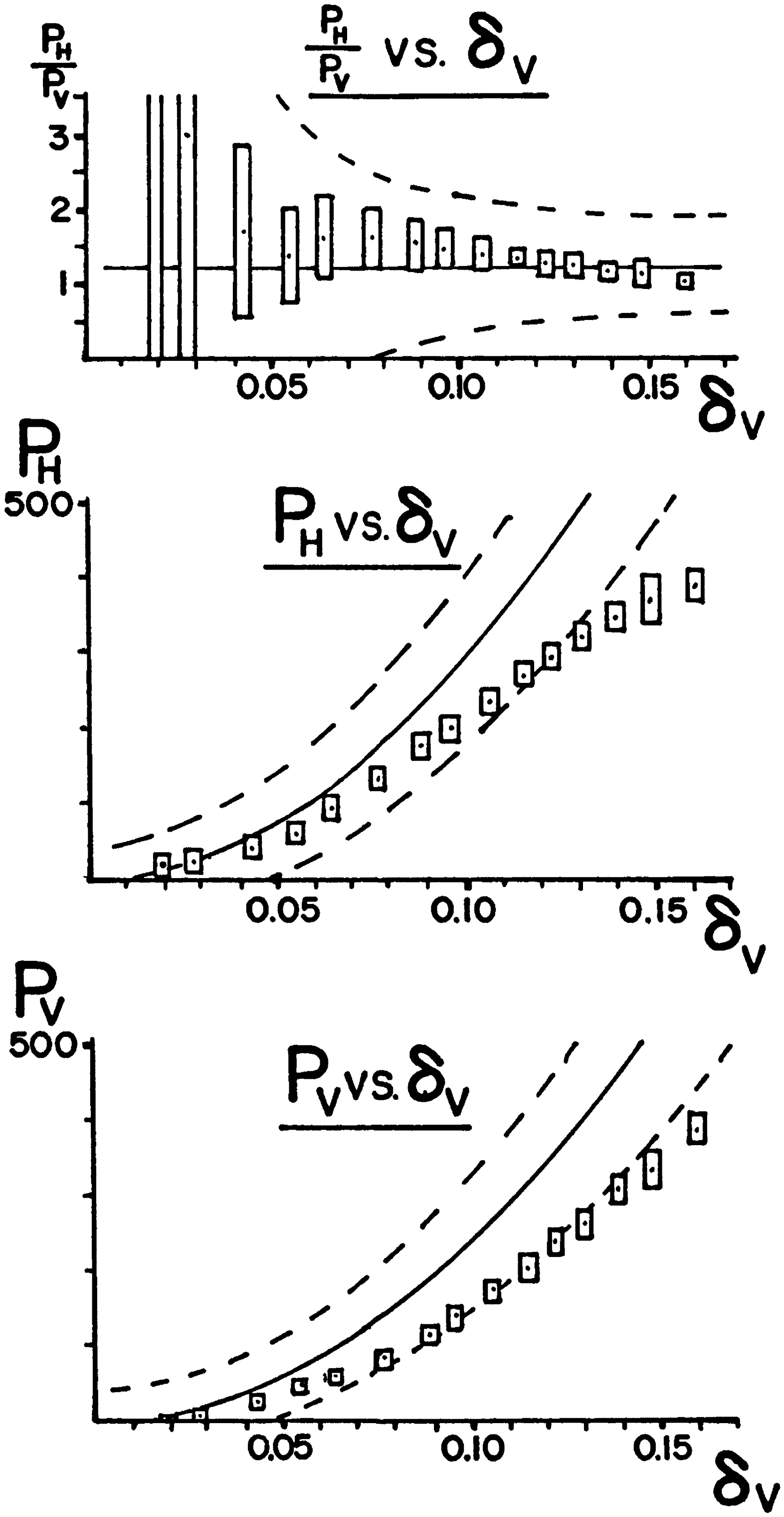

Figure F-35 Force-Deflection, Test 88 , β = 15° , ψ_x = 30° , ψ_y = 20°

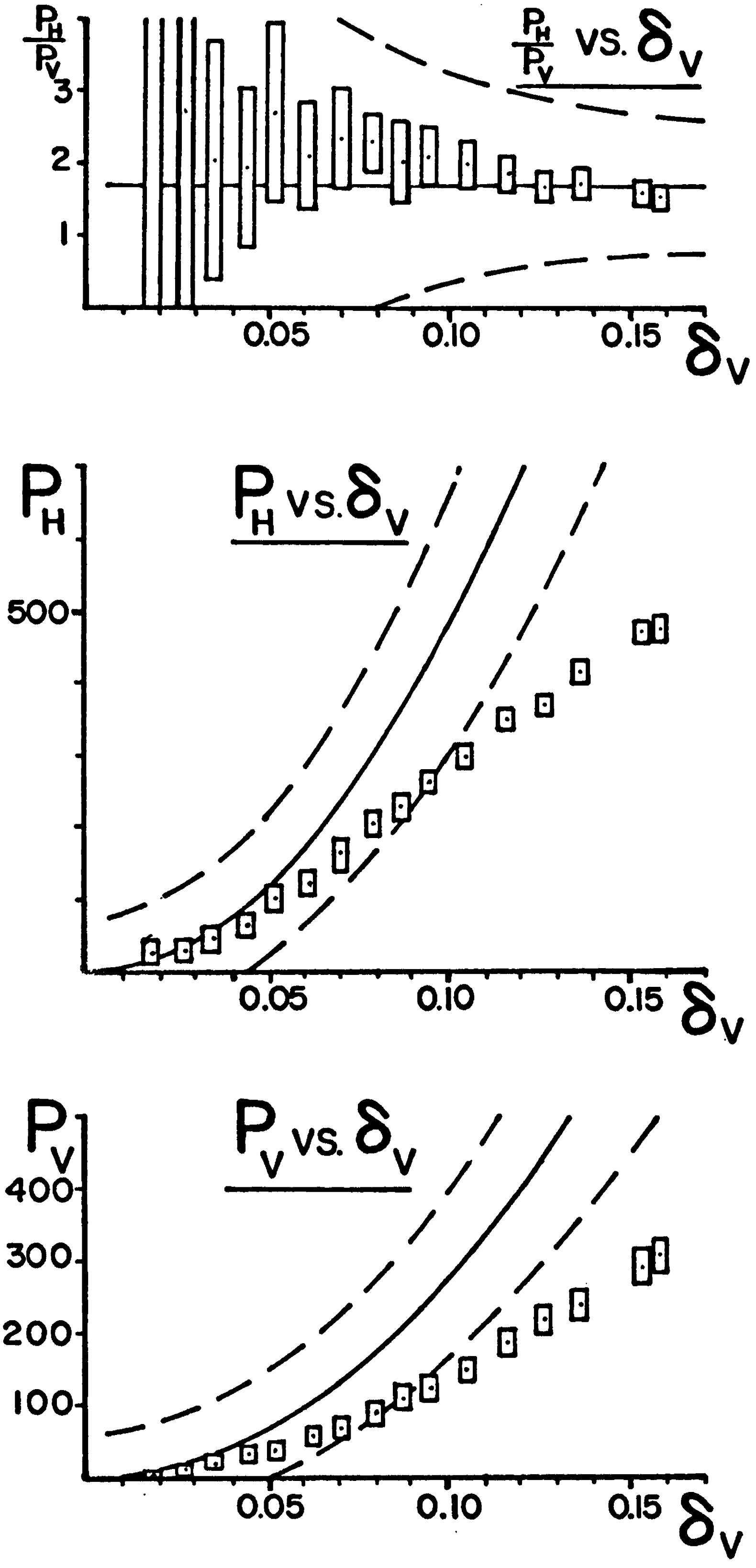

Figure F-36 Force-Deflection, Test 89 , $\beta = 15^\circ$, $\psi_x = 45^\circ$, $\psi_y = 20^\circ$

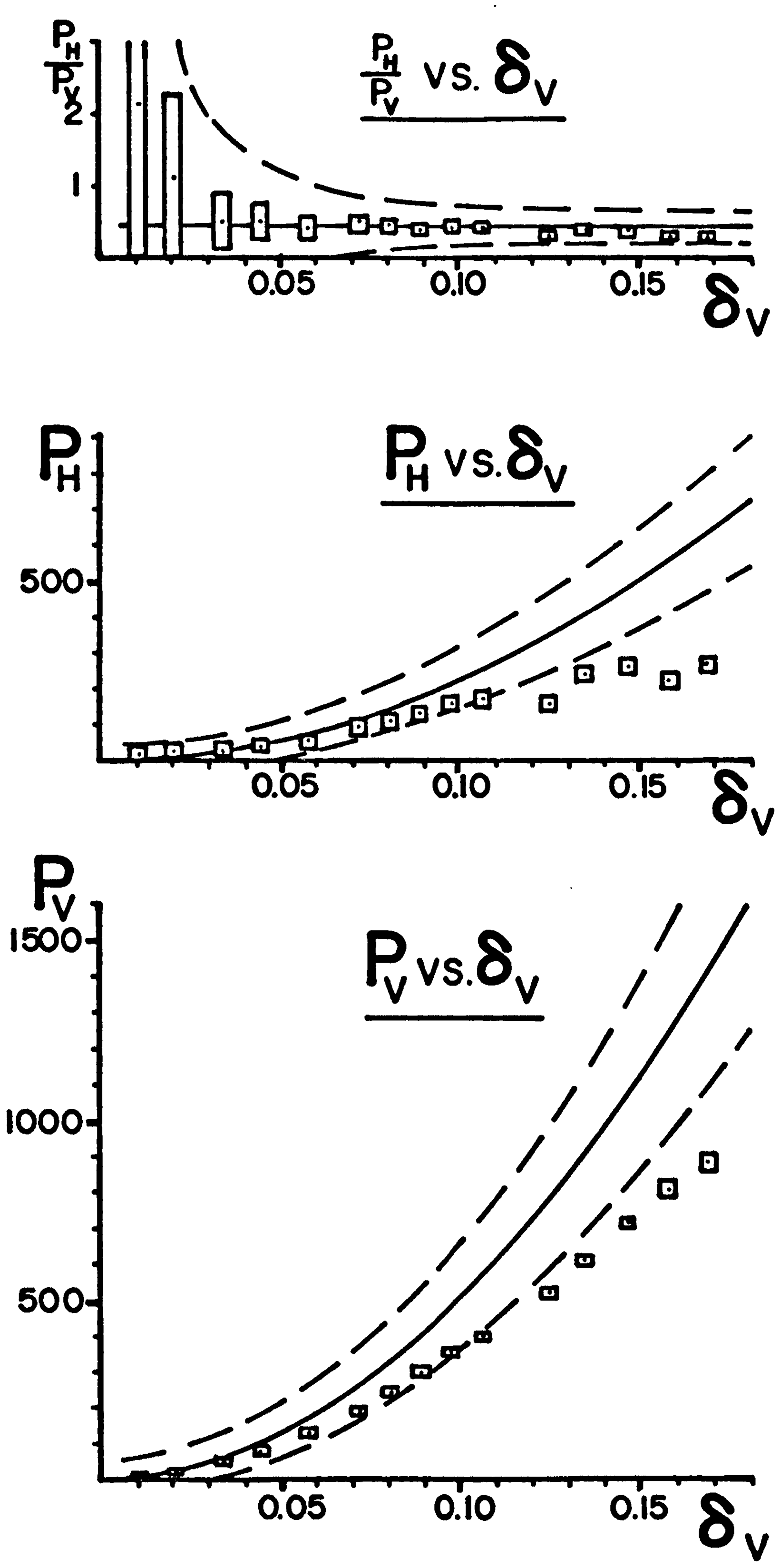

Figure F-37 Force-Deflection, Test 90 , β = 22.5° , ψ_x = 30° , ψ_y = 20°

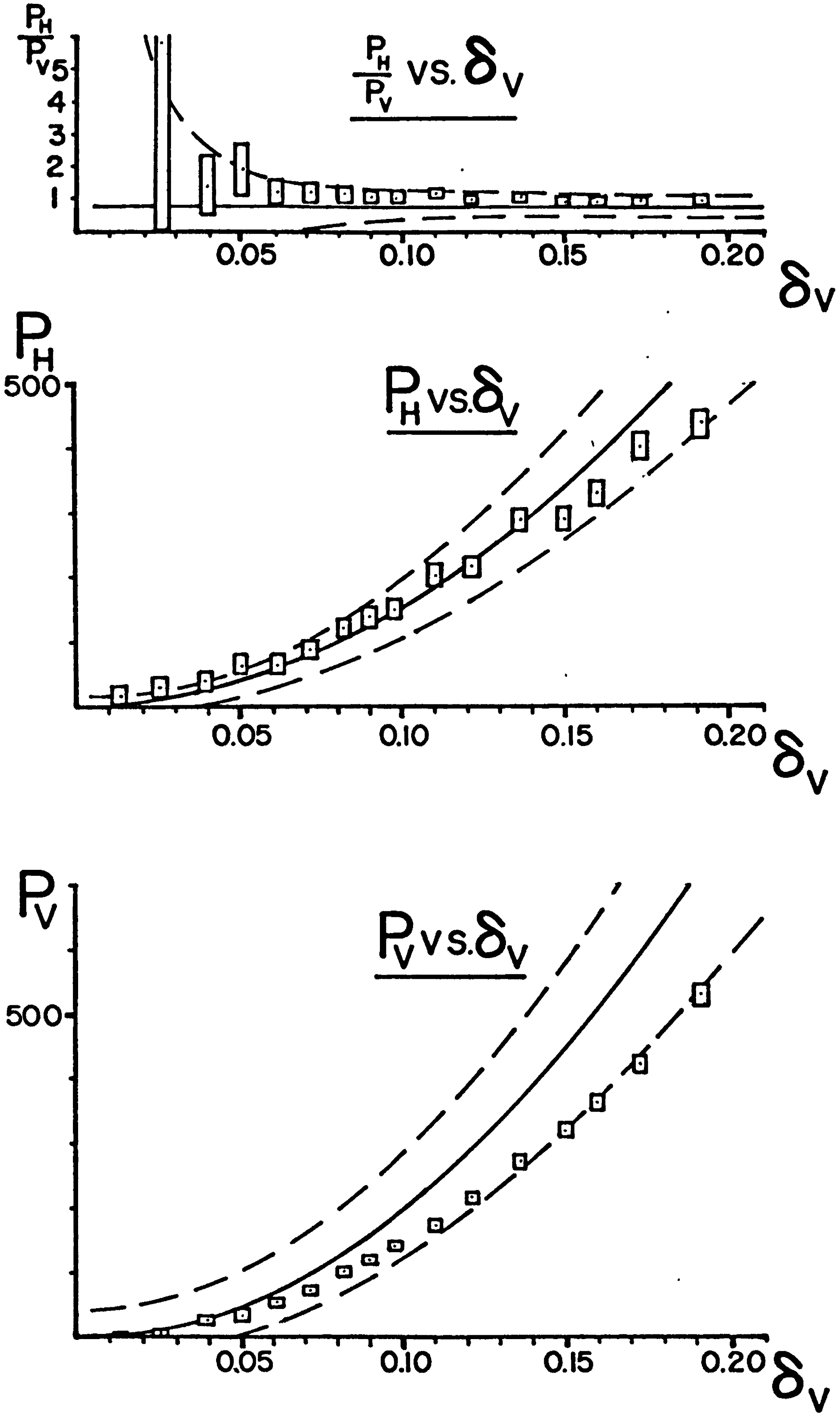

Figure F-38 Force-Deflection, Test 91, β = 22.5°, ψ_x = 30°, ψ_y = 45°

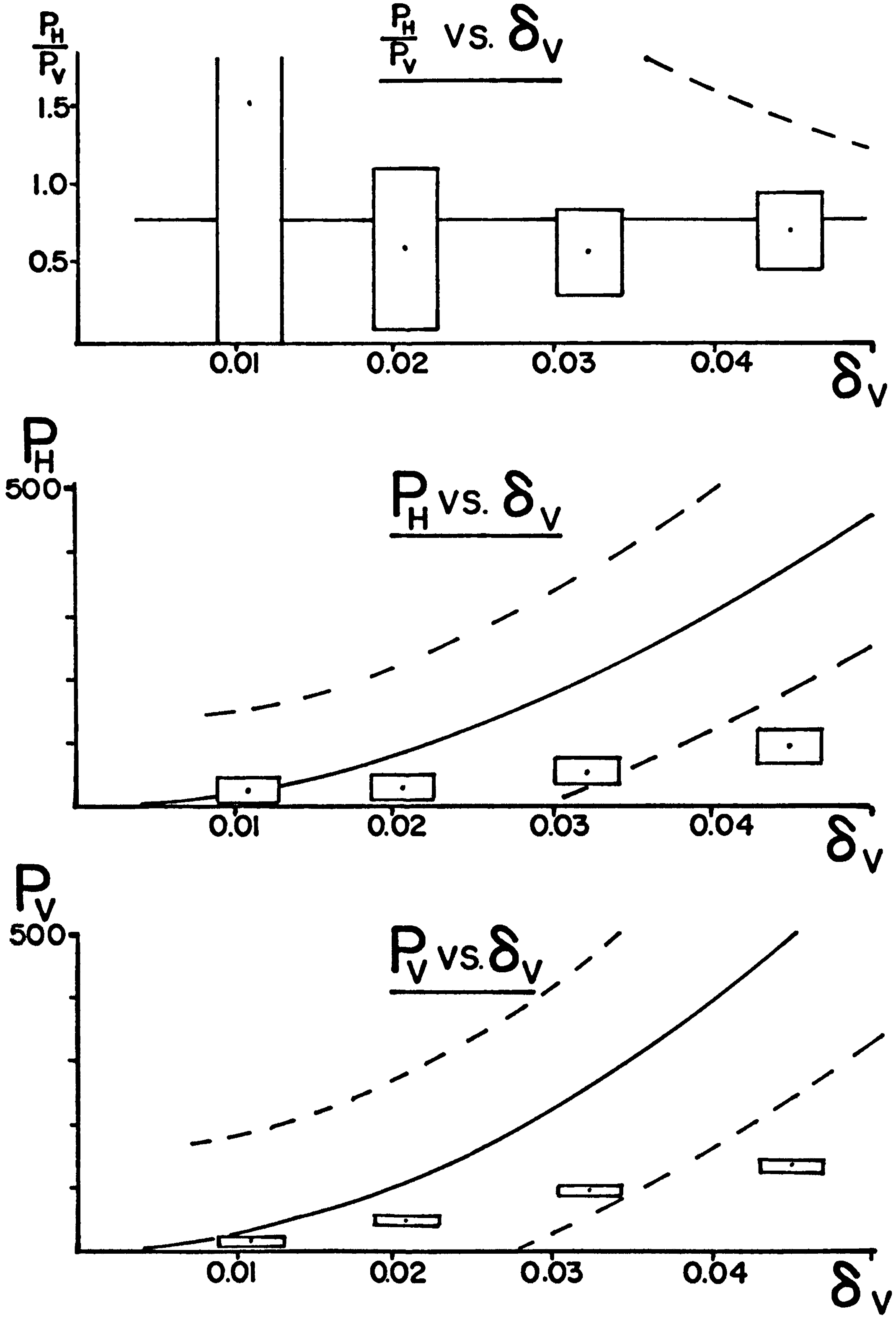

Figure F-39 Force-Deflection, Test 84, $\beta = 30^\circ$, $\psi_x = 15^\circ$, $\psi_y = 20^\circ$

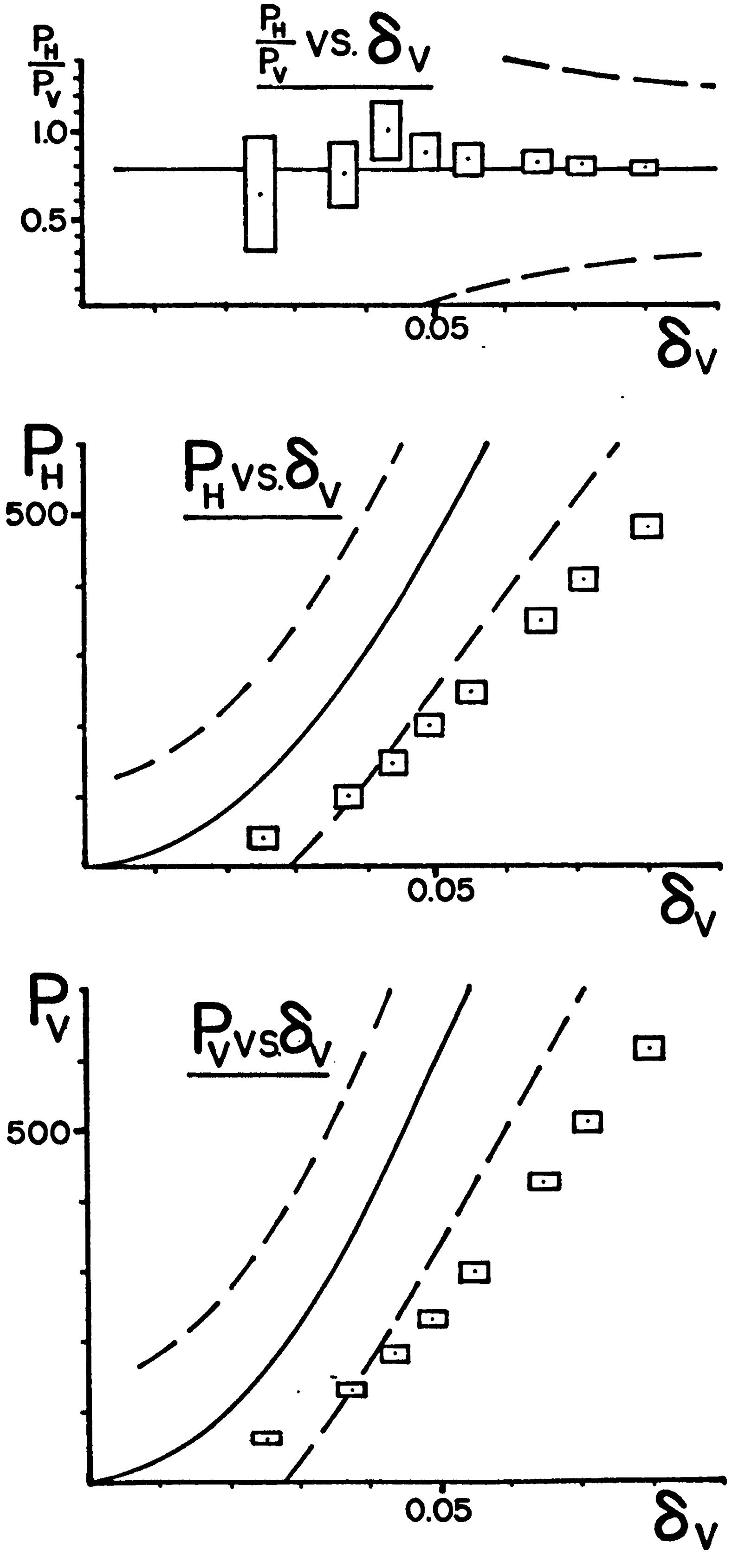

Figure F-40 Force-Deflection, Test 87, $\beta = 30^\circ$, $\psi_x = 15^\circ$, $\psi_y = 45^\circ$

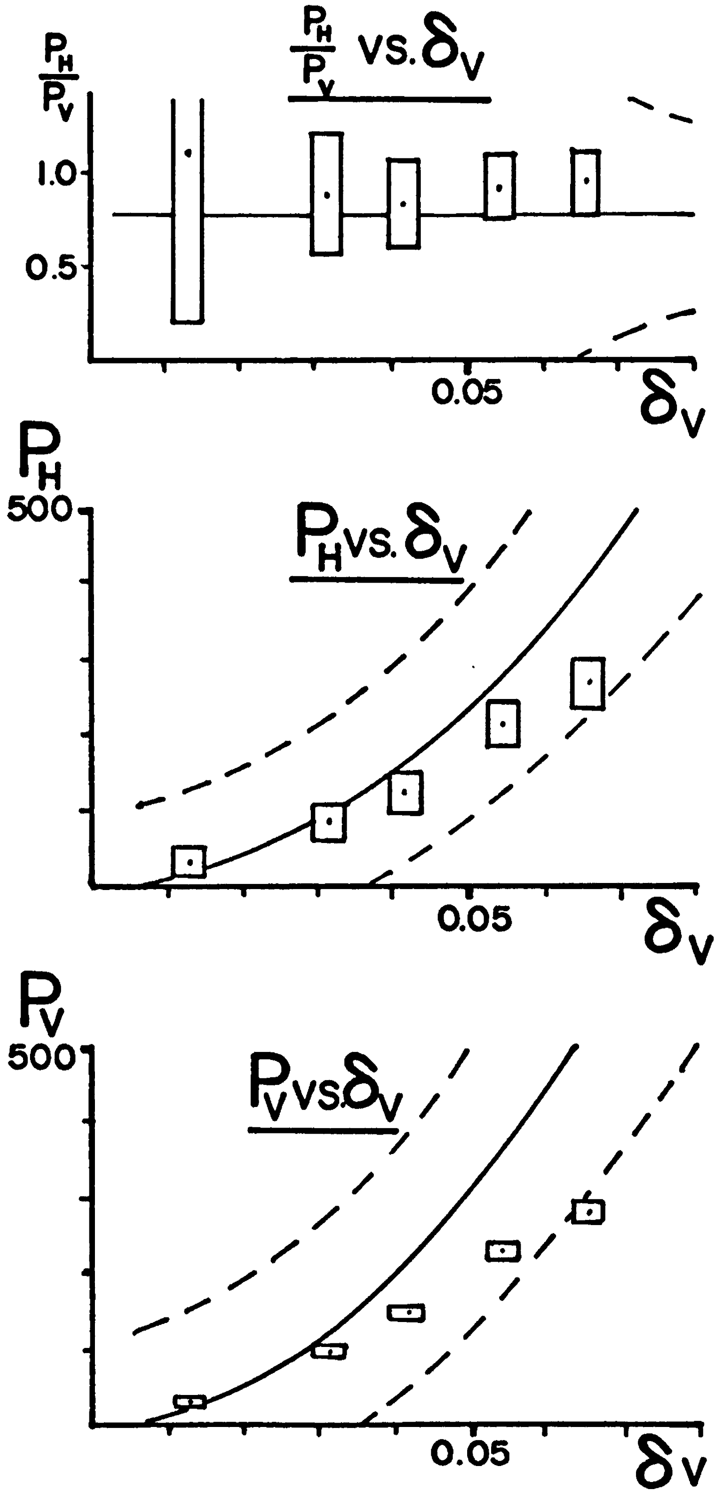

Figure F-41 Force-Deflection, Test 78, β = 30°, ψ_x = 30°, ψ_y = 5°

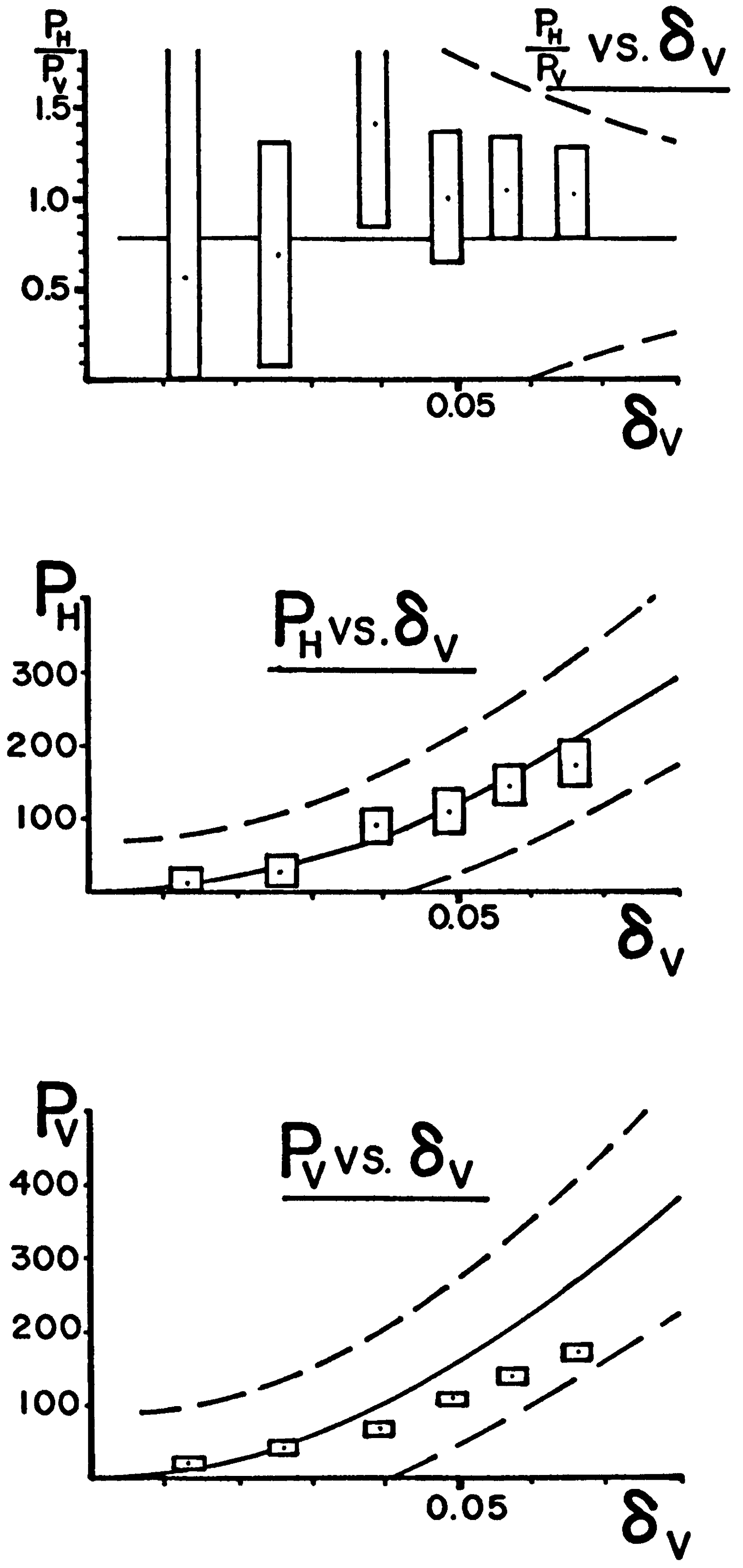

Figure F-42 Force-Deflection, Test 94 , $\beta = 30^\circ$, $\psi_x = 30^\circ$, $\psi_y = 5^\circ$

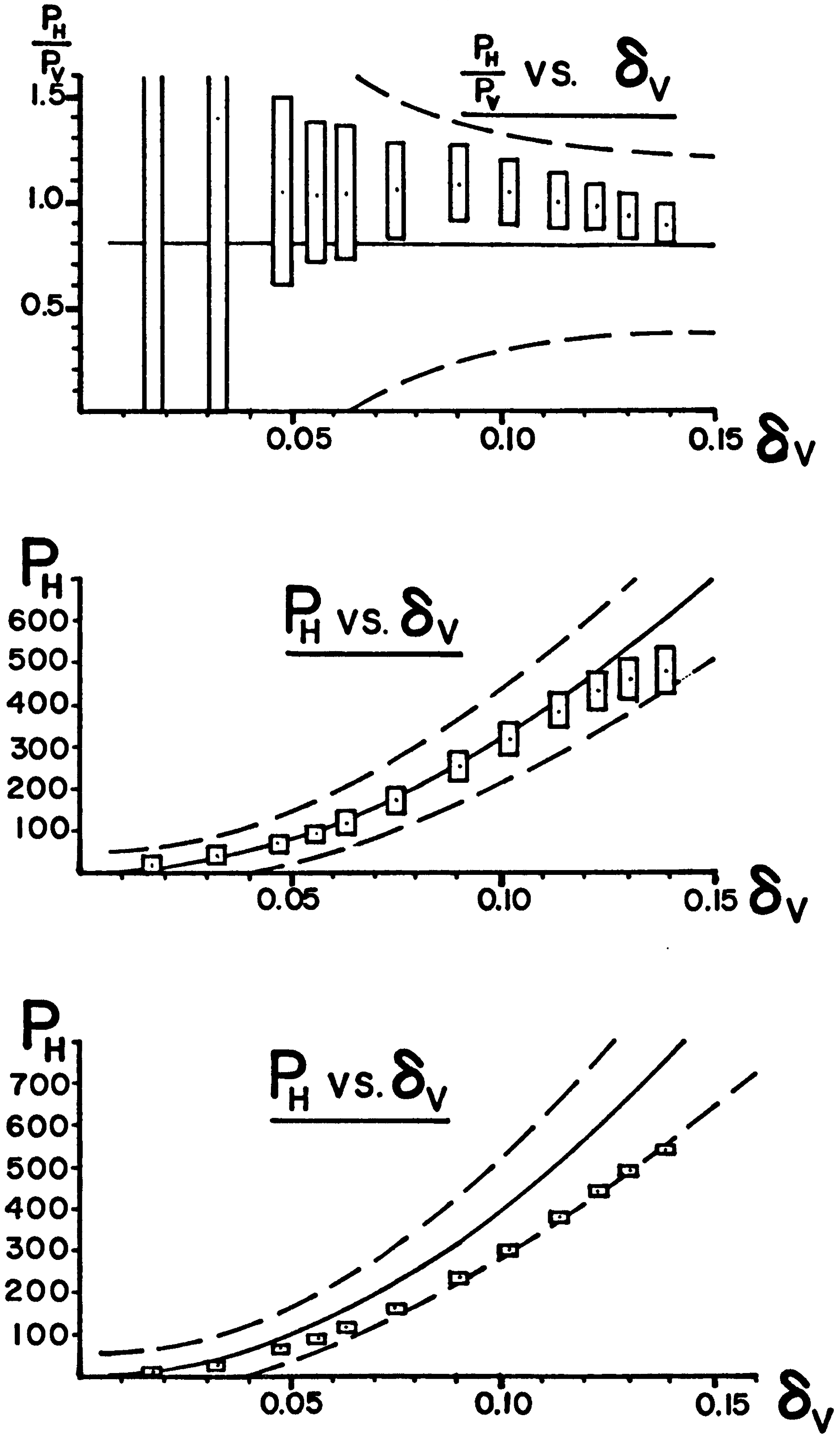

Figure F-43 Force-Deflection, Test 79 , $\beta = 30^\circ$, $\psi_x = 30^\circ$, $\psi_y = 10^\circ$

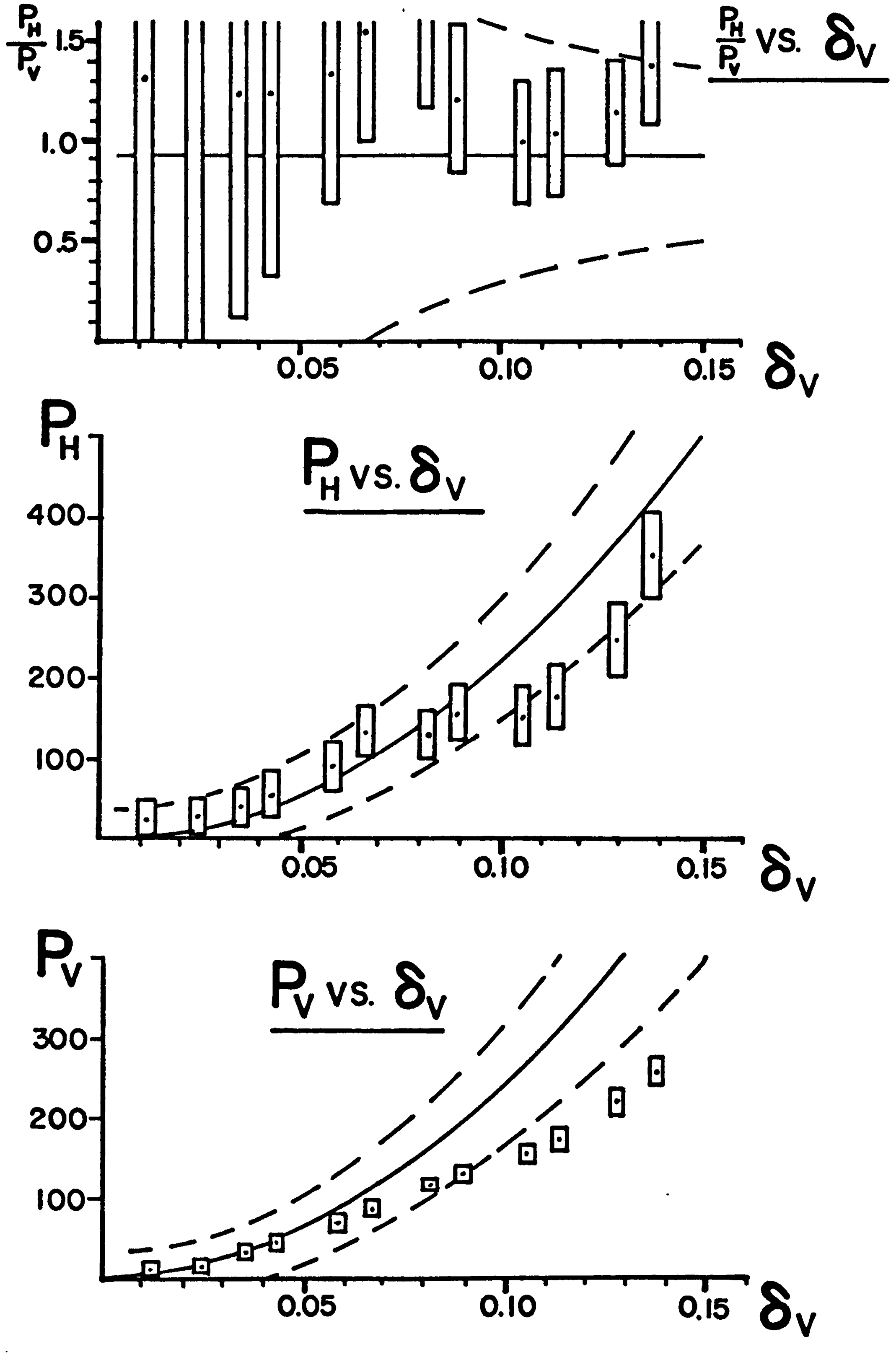

Figure F-44 Force-Deflection, Test 80, $\beta = 30^\circ$, $\psi_x = 30^\circ$, $\psi_y = 20^\circ$

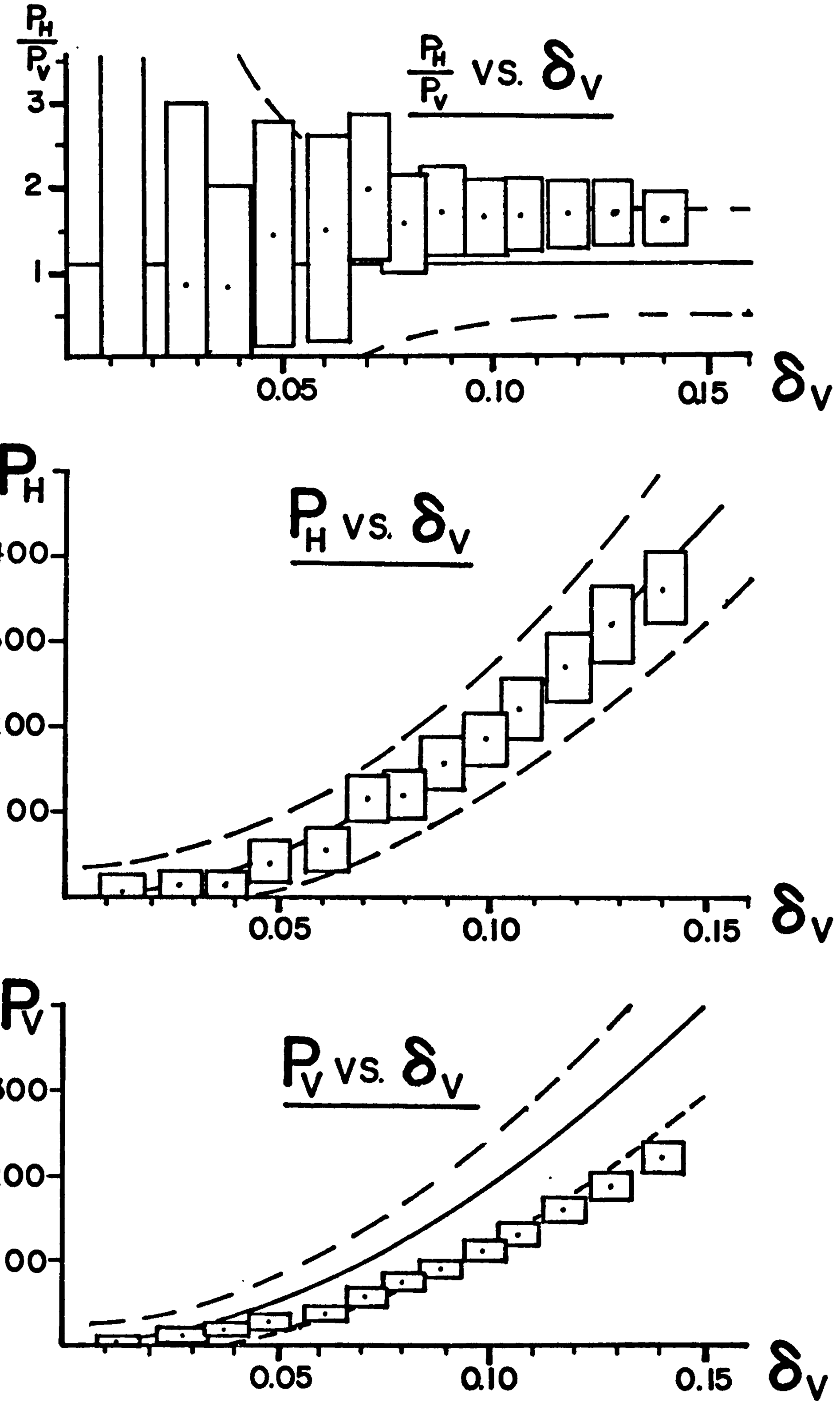

Figure F-45 Force-Deflection, Test 81, $\beta = 30^\circ$, $\psi_x = 30^\circ$, $\psi_y = 30^\circ$

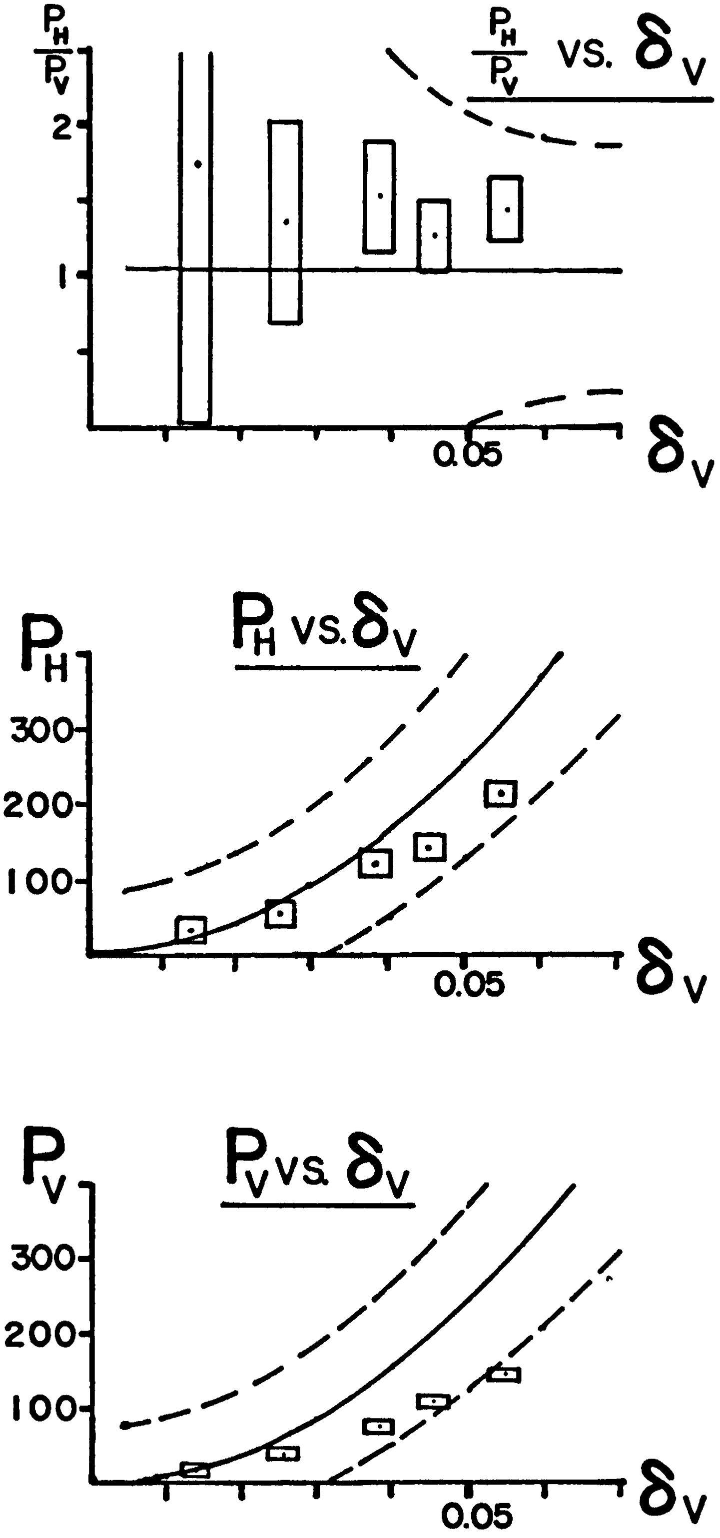

Figure F-46 Force-Deflection, Test 82, $\beta = 30^\circ$, $\psi_x = 30^\circ$, $\psi_y = 45^\circ$

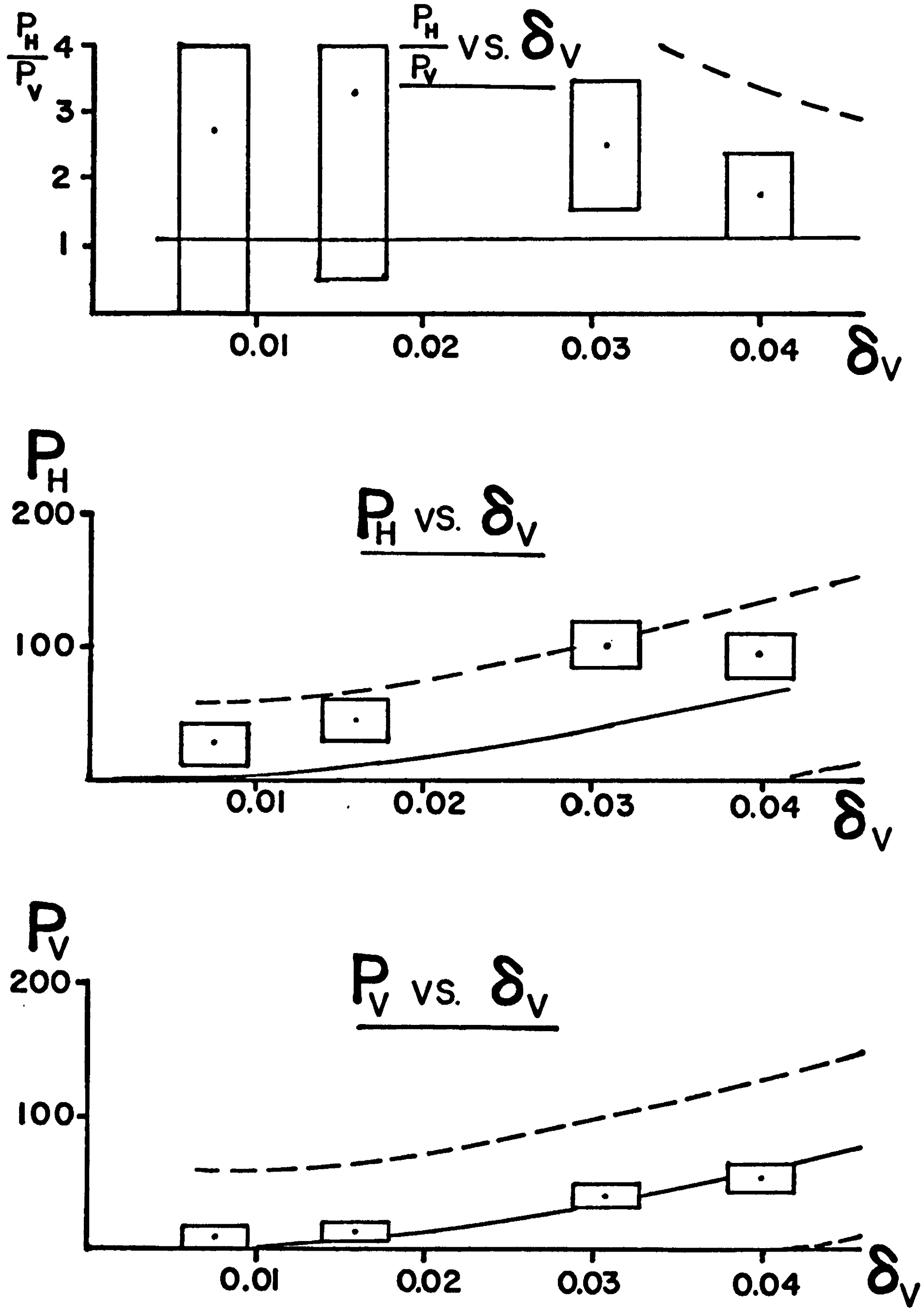

Figure F-47 Force-Deflection, Test 83 , β = 30° , ψ_x = 30° , ψ_y = 55°

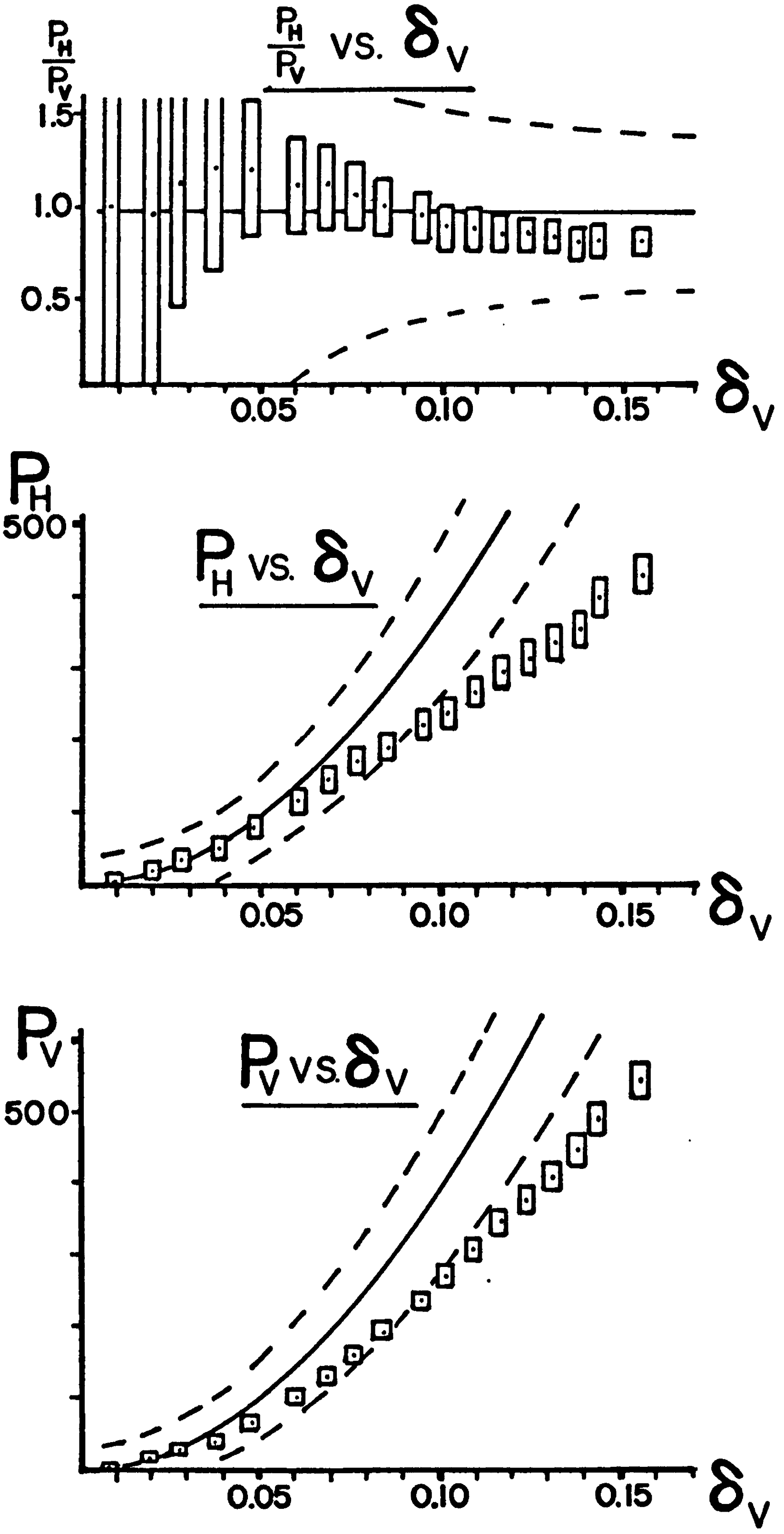

Figure F-48 Force-Deflection, Test 86, $\beta = 30^\circ$, $\psi_x = 45^\circ$, $\psi_y = 20^\circ$

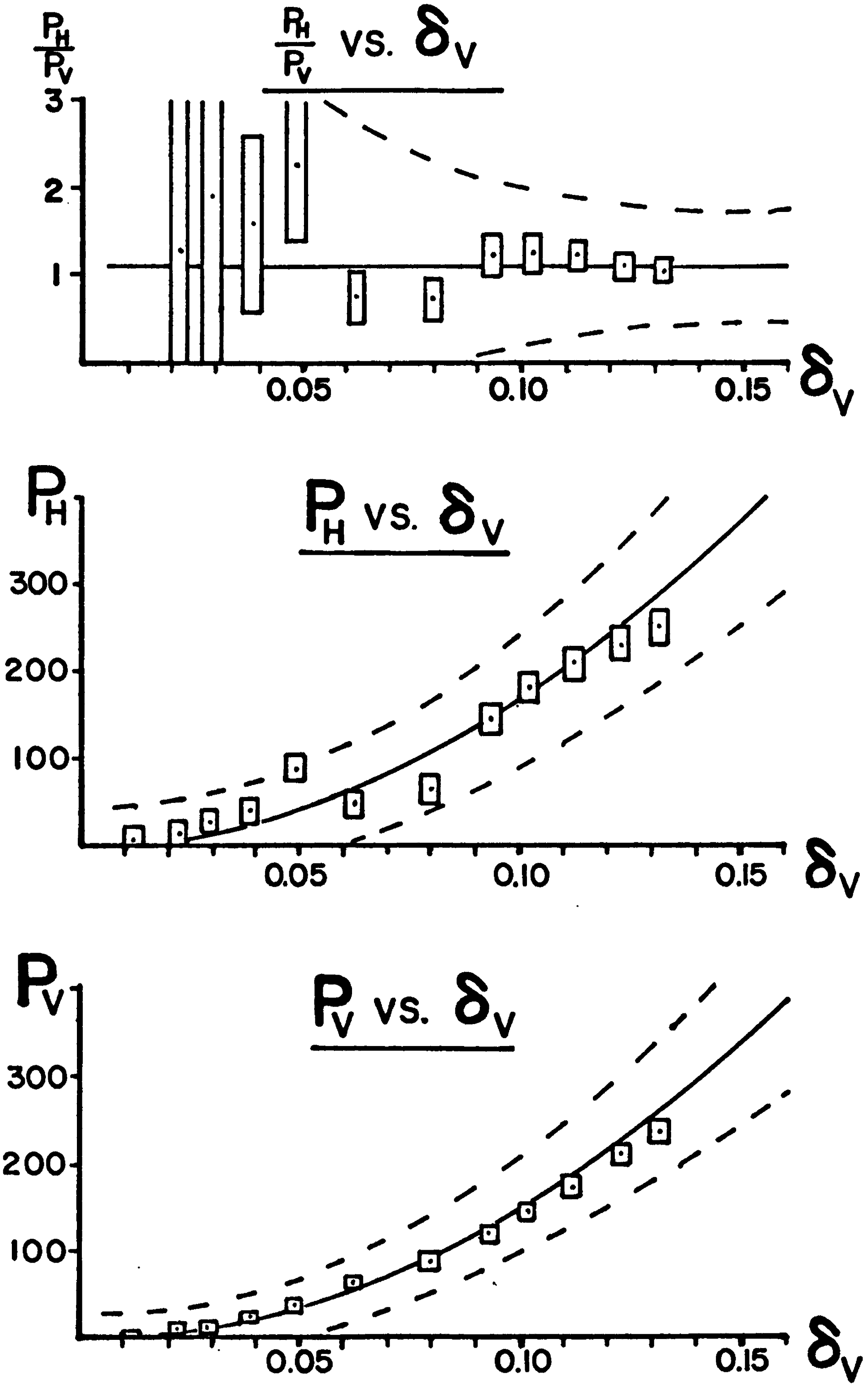

Figure F-49 Force-Deflection, Test 85, $\beta = 30^\circ$, $\psi_x = 45^\circ$, $\psi_y = 45^\circ$

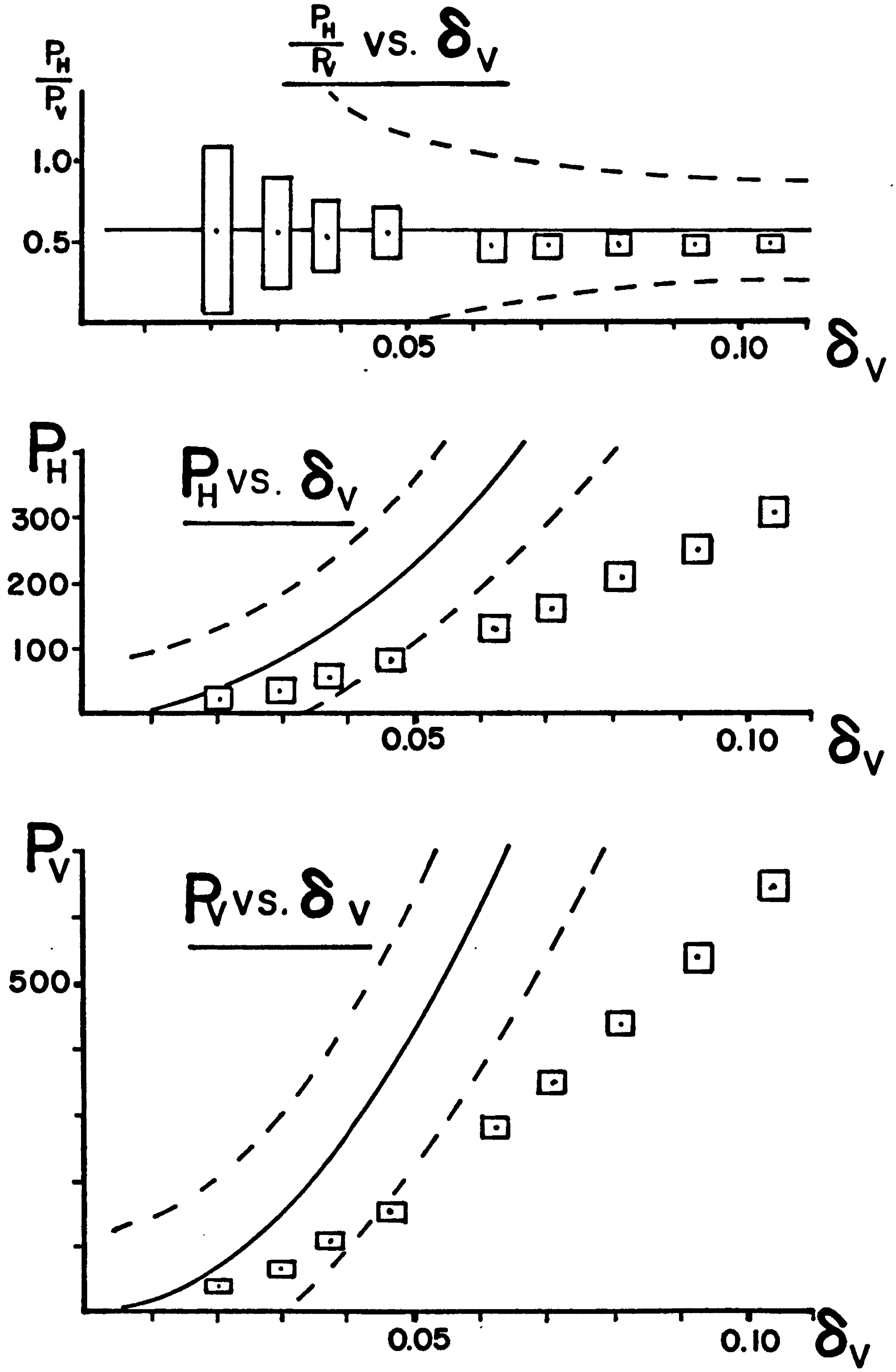

Figure F-50 Force-Deflection, Test 92, $\beta = 45^\circ$, $\psi_x = 30^\circ$, $\psi_y = 20^\circ$

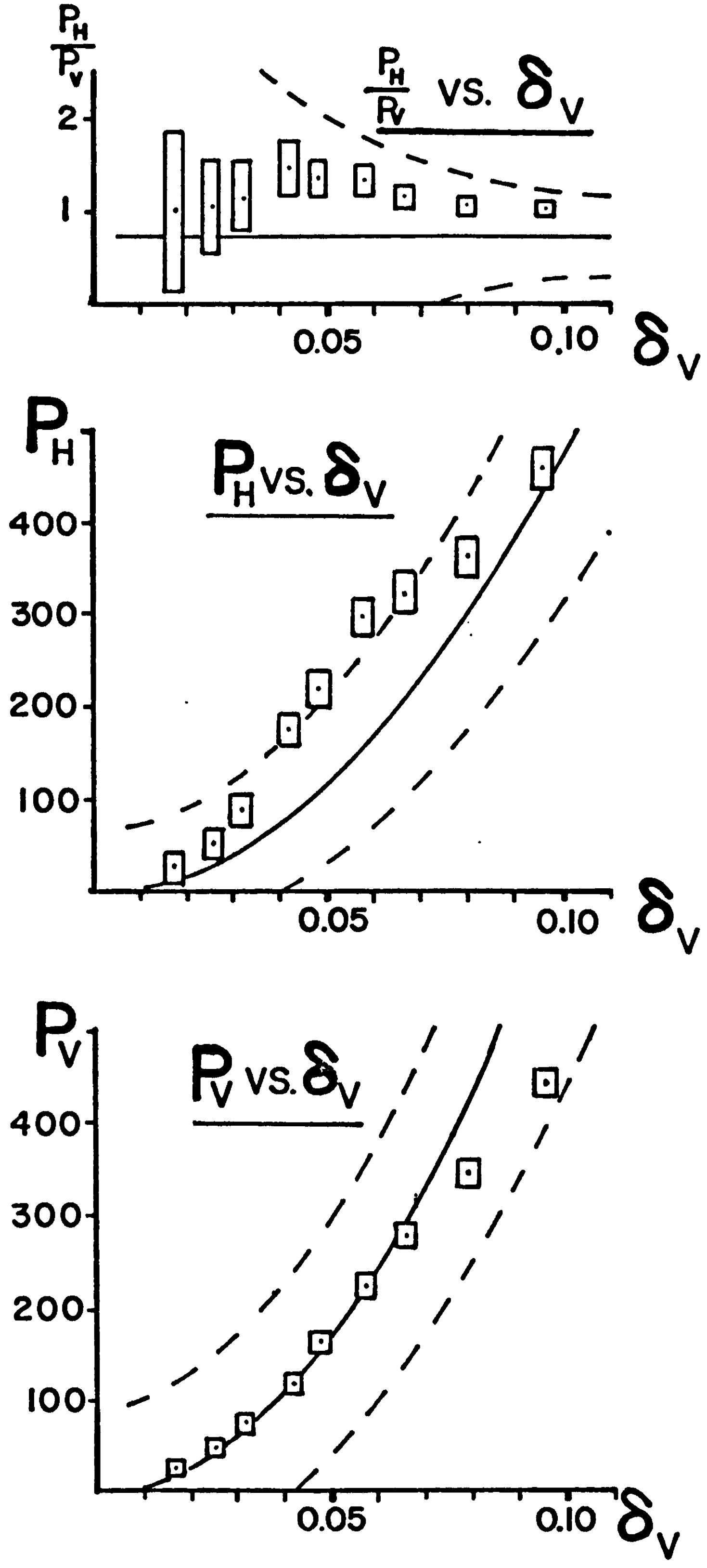

Figure F-51 Force-Deflection, Test 93, $\beta = 45^\circ$, $\psi_x = 30^\circ$, $\psi_y = 45^\circ$

References

1. Abbott, M. B., The Method of Characteristics, American Elsevier, New York, N. Y., 1966.

2. Berry, P. M., "Rock Penetration at Oblique Incidence by a Yawed Bit Tooth," Proceedings of the First Congress of the International Society of Rock Mechanics, V.2, 1966, pp. 115-118.

3. Bradley, W.B., "Deviation Forces from the Wedge Penetration Failure of Anisotropic Rock," Transactions of the ASME, Journal of Engineering for Industry, Vol. 95, November,1973, pp. 1093-1100.

4. Celle, C. C., "Anisotropic Hardening of an Initially Isotropic Porous Limestone," Unpublished M. S. Thesis, Rice University, Houston, 1975.

5. Cheatham, J. B., Jr., "Rock-Bit Tooth Friction Analysis," AIME Transactions (SPE), V. 228, 1963.

6. Cheatham, J. B., Jr., Musselman, J. A., "Plane-Strain Chip Formation in Carthage Marble," Basic and Applied Rock Mechanics - Proc. of 10th Symposium on Rock Mechanics, Ed. by K. E. Gray, AIME, New York, 1972, pp. 389-408.

7. Cheatham, J. B. Jr., Smith, M. B., "Deviation Forces Arising from Single Bit Tooth Indentation of an Anisotropic Porous Media," ASME Paper #76-PET-52, Presented at the Petroleum Mechanical Engineering and Pressure Vessels and Piping Conference, Mexico City, September 24, 1976; To be published in ASME Transactions Journal of Pressure Vessel Tech.

8. Drucker, D. C., "A More Fundamental Approach to Plastic Stress-Strain Relations," Proceedings of the First U. S. National Congress of Applied Mechanics, pp. 487-491, ASME, 1951.

9. Drucker, D. C., Prager, W., "Soil Mechanics and Plastic Analysis on Limit Design," Quarterly of Applied Mathematics, V. 10, No. 2, 1951, pp. 157-165.

10. Drucker, D. C., "Plasticity," Structural Mechanics, Proceedings of the First Symposium on Naval Structural Mechanics, Pergamon Press, New York, 1960, pp. 407-455.

11. Drucker, D. C., Chen, W. F., "On the Use of Simple Discontinuous Fields to Bound Limit Loads," Engineering Plasticity, Ed. by J. Heyman, F. A. Leckie, University Press, Cambridge, 1968, pp. 129-145.

12. Drucker, D. C., Greenberg, H. J., Prager, W., "The Safety Factor of an Elastic-Plastic Body in Plain Strain," Journal of Applied Mechanics, December, 1951, pp. 371-378.

13. Ford, H., Advanced Strength of Materials, John Wiley and Sons, New York, 1963.

14. Gnirk, P. F., Cheatham, J. B., Jr., "Indentation Experiments on Dry Rocks Under Pressure," AIME Transactions (SPE), V. 228, 1963.

15. Grunzweig, J., Longman, I. M., Petch, N. J., "Calculations and Measurements on Wedge-Indentation," Journal of the Mechanics and Physics of Solids, 1954, V. 2, pp. 81-86.

16. Hill, R., The Mathematical Theory of Plasticity, Oxford University Press, London, 1950.

17. Hill, R., Lee, E. H., Tupper, S. J., "The Theory of Wedge Indentation of Ductile Materials," Proceedings of the Royal Society of London, V. 188. A., 1947, pp. 273-289.

18. Johnson, W., Mellor, P. B., Engineering Plasticity, Van Nostran Reinhold Company, London, 1973.

19. McLamore, R. T., "The Role of Rock Strength Anisotropy in Natural Hole Deviation," Journal of Petroleum Technology, November, 1971, pp. 1313-1321.

20. Miller, T. W., "A Consistent Workhardening Theory for Porous Limestone," Unpublished Ph.D. Thesis, Rice University, Houston, 1970.

21. Pariseau, W. G., "Plasticity Theory for Anisotropic Rocks and Soils," Basic and Applied Rock Mechanics, Tenth Symposium on Rock Mechanics, edited by K. E. Gray, American Institute of Mining, Metallurgical, and Petroleum Engineers, Port City Press, Baltimore, 1972, pp. 267-295.

22. Pariseau, W. G., "Wedge Indentation of Anisotropic Geologic Media," Prepared for the 12th Symposium on Rock Mechanics, University of Missouri, Rolla, Missouri, July, 1970.

23. Pariseau, W. G., Fairhurst, C., "The Force-Penetration Characteristic for Wedge Penetration into Rock," Int. J. Rock Mech. Min. Sci., Vol. 4, Pergamon Press, 1967, pp. 165-180.

24. Prager, W., "A Geometrical Discussion of the Slip Line Field in Plane Plastic Flow," Transactions of the Royal Institute of Technology, Stockhlm, Sweden, No. 65, 1953.

25. Prager, W., "A New Method of Analyzing Stresses and Strains in Workhardening Plastic Solids," Journal of Applied Mechanics, December, 1956, pp. 493-496.

26. Prager, W., An Introduction to Plasticity, Addison-Wesley Publishing Co., Reading, Massachusetts, 1959.

27. Prager, W., Hodge, P. G., Theory of Perfectly Plastic Solids, John Wiley & Sons, New York, 1951.

28. Roark, R. J., Young, W. C., Formulas for Stress and Strain, McGraw-Hill, New York, 1975.

29. Shield, R. T., "Mixed Boundary Value Problems in Soil Mechanics," Quarterly of Applied Mathematics, V. 11, No. 1, 1953, pp. 61-75.

30. Shield, R. T., "Stress and Velocity Fields in Soil Mechanics," Journal of Mathematics and Physics, V. 33, 1954, pp. 144-156.

31. Shield, R. T., Drucker, D. C., "The Application of Limit Analysis to Punch-Indentation Problems," Journal of Applied Mechanics, December, 1953, pp. 453-460.

32. Smith, M. B., "A Parabolic Yield Condition for Anisotropic Rocks and Soils," Unpublished Ph.D. Thesis, Rice University, Houston, 1974.